Charge-carrier Dynamics in Metal Oxides and Hybrid Lead Perovskites investigated by Time-Resolved UV and X-ray Spectroscopy.

THÈSE N° 9133 (2018)

ÉCOLE POLYTECHNIQUE FÉDÉRALE DE LAUSANNE

POUR L'OBTENTION DU GRADE DE DOCTEUR ÈS SCIENCES

PAR

Thomas Charles Henry ROSSI

acceptée sur proposition du jury:

Prof. J.-E. Moser, président du jury
Prof. M. Chergui, directeur de thèse
Dr U. Staub, rapporteur
Prof. X. Zhu, rapporteur
Prof. A. Hagfeldt, rapporteur

EPFL

ÉCOLE POLYTECHNIQUE
FÉDÉRALE DE LAUSANNE

Suisse
2018

A mes parents, pour m'avoir donné la chance de vivre ces expériences,
A Laetitia, pour l'être sensible que je suis devenu…

One's dreams must be big enough so as not to lose sight of them.
– Oscar Wilde

Acknowledgements

First of all, I would like to thank Professor Majed Chergui for hosting and supervising me as a PhD student during these four years and a few months. Although I was sometimes a bit overwhelmed by the number of projects carried on in the lab, you were often available for discussion and provided helpful guidance. The LSU is a fantastic scientific environment which provides the possibility for a PhD student to build experiments around her/his centres of interest. Additionally, being able to participate to the experiments at the SLS and at the LSU gave me the opportunity to meet people from different communities which I enjoyed and broadened my interests in ultrafast optical and X-ray spectroscopies.

The LSU would be nothing without the formidable crew with which I had the chance to share this journey over the last few years. A special thank goes to Malte Oppermann who arrived not long after I moved to the 20 kHz setup and with his invaluable motivation and sense of humour, I have been able to concentrate more on the fundamental parts of the projects leaving him some technical aspects. A large part of this PhD would not exist without him. Not only in science, I am also thankful for the evenings spent at the Théâtre de Vidy.

Around the SLS, I am especially thankful to Chris Milne who supervised me during my Master project and who has always been a constant support and a constant source of help. Thanks also to the local beamline scientists and support at the MicroXAS, Phoenix, and SuperXAS beamlines.

Over the years, I had the occasion to work more closely with a number of people in the group. Many thanks to Benjamin, Boris, Camila, Chris, Dominik, Edoardo, Fabio, Giulia, James, Janina, Jakob, Jérémy, Jochen, Kevin, Lars, Lijie, Mahsa, Malte, Natalia, Oliviero and Thomas B for the good time spent in the lab. Finally, I would like to thank all current and past LSU members for all the motivating atmosphere in the lab and elsewhere. Special thanks to my officemates: Benjamin, Enrico and Gloria.

Thanks also to the three LSU secretaries I had the opportunity to bother during these four years: Annick, Annissa and Monique.

The challenging experiments performed at the LSU and the SLS require technical support. The ISIC is very lucky to rely on talented mechanical, electronic and informatic workshops. Their commitment to design, adapt, and fix our equipments is such that I can count them as collaborators in most of the experiments described in this Thesis.

Dans une vie de thésard, les moments d'euphorie alternent avec les déceptions. Il est plus facile de surmonter ces dernières avec le soutien de sa famille et de ses amis. J'ai eu la chance de compter en particulier sur le support de Mathieu, Cédric, Mireille et ma famille dans ces moments.

Finalement, je souhaite remercier tout particulièrement Laetitia qui m'a accompagné pendant la grande partie de cette thèse et sur qui je peux compter dans toutes les épreuves. La distance n'empêche rien elle invite au voyage ; le temps peut s'écouler, je vis un rêve éveillé.

More anecdotic, the years spent in Evian-Les-Bains have been an incredible source of joy and wonder at sunset and sunrise over the Leman lake which I could admire in all its magnificence from my balcony. I have spent a decent amount of time on the CGN boats to cross the lake every day and go to work. Their reliability with time and sailing removes the uncertainty one can feel in other places when taking common transport may be a random variable.

Evian-Les-Bains, le 3 Décembre 2018   T. R.

Abstract

In modern ultrafast optoelectronic technologies based on wide band gap insulators, the non-equilibrium dynamics of photogenerated charges plays a major role. Unravelling the mechanisms of interaction between these charge carriers and their environment is crucial to support the design of more efficient devices. Especially, the absorption of photons with more energy than the optical band gap generates electrons-hole pairs (EHP) whose transport and dissociation as excitons or free charge carriers is of pivotal importance for the charge separation at photovoltaic interfaces. The advent of ultrafast pump-probe optical spectroscopy in the UV provides access to the dynamics of EHP through a variety of transient modifications of the optical spectrum. In this Thesis, the cooling of electrons in ZnO and methylammonium lead bromide perovskite (MAPbBr$_3$), two broadly used direct band gap semiconductors, is tracked as they end up and accumulate at the bottom of the conduction band. In ZnO, the cooling time depends on the pump photon energy, of the order of ~1 ps, which contrasts with the theoretically predicted cooling time of a few hundreds of femtoseconds. In MAPbBr$_3$, a rather slow electron cooling time of the order of ~400 fs is measured, favorable for charge separation at interfaces as it drives the injection of hot carriers. Additionally, the high energy carried by the UV probe photons provides access to the photodynamics at different high symmetry points in the Brillouin zone. Following the study of neat ZnO and MAPbBr$_3$, these two semiconductors have been associated to other materials to form prototypical photovoltaic assemblies such as dye-sensitized (ZnO/N719) and solid-state lead perovskite sensitized (TiO$_2$/MAPbBr$_3$) interfaces. Upon electron injection into the transition metal oxide (ZnO or TiO$_2$), dramatic changes are observed in the absorption close to the optical band gap from which the timescale of electron injection is obtained. It highlights how slight screening length and chemical potential changes can generate large modifications in the optical properties through many-body effects. At both interfaces, a delayed appearance of the electron at the bottom of the conduction band is observed which may be due the electron localizing in a shallow trap. This Thesis extends beyond the band insulators to the photodynamics of NiO, a strongly correlated charge-transfer insulator. Excitation above the optical band gap generates a large photoinduced absorption below the optical band gap which is characteristic of the interplay between the electronic and the low energy bosonic excitations. The dressing of electronic excitations with bosonic modes generates low energy excitation modes on ultrafast timescales which generate a competition between itinerant and localized resonances with a high degree of tunability. The progress made in resonant X-ray based time-resolved spectroscopies allows the investigation of the degree of charge localization around specific atoms in a system. Photogenerated electron

localization in NiO is studied by time-resolved X-ray absorption spectroscopy, causing bond elongations and the formation of an electron-polaron in less than 100 ps. In a last part, the linear dichroism of the steady-state X-ray absorption spectrum of anatase TiO_2 at the K-edge is studied which provides an unambiguous assignment of the pre-edge transitions as their orbital composition is strongly anisotropic and sensitive to the crystal orientation. A complete characterization of the spectrum is provided with the support of *ab initio* calculations and analytical derivations of the angular X-ray absorption cross-section.

Résumé

Dans les applications optoélectroniques modernes basées sur des isolants à large bande interdite, la dynamique hors-équilibre des charges photogénérées joue un rôle majeur. La résolution des mécanismes d'interaction entre ces charges et leur environnement est cruciale pour appuyer le développement de technologies plus efficaces. En particulier, l'absorption de photons avec plus d'énergie que la bande optique interdite génère des paires electron-trou dont le transport et la dissociation en tant qu'excitons ou porteurs de charges libres a une importance de premier plan dans la séparation des charges aux interfaces photovoltaïques. Les avancées dans le domaine de la spectroscopie ultrarapide pompe-sonde dans l'UV fournit l'accès à la dynamique des paires electron-trou au travers d'une variété de modification du spectre d'absorption optique. Dans cette Thèse, le refroidissement des électrons dans ZnO et dans le bromure de plomb methylammonium (MAPbBr$_3$), deux semiconducteurs directs très largement utilisés, est observé jusqu'à ce qu'ils atteignent le bas de la bande de conduction et s'accumulent. Dans le cas de ZnO, un temps de refroidissement qui dépend de l'énergie du photon de pompe de l'ordre de 1 ps est mesuré qui contraste avec la prédiction théorique qu'il devrait avoir lieu en quelques centaines de femtosecondes. Pour MAPbBr$_3$, un temps de refroidissement lent de l'ordre de 400 fs, favorable pour la séparation de charges aux interfaces puisque c'est un paramètre qui oriente l'injection de porteurs de charges "chauds". En outre, l'énergie élevée portée par les photons de la sonde dans l'UV donne accès à la photodynamique à différents points de haute symmétrie dans la zone de Brillouin. Suivant létude des semiconducteurs seuls ZnO et MAPbBr$_3$, ces derniers ont été associés à d'autres matériaux pour former des prototypes d'assemblages photovoltaïques comme des interfaces sensibilisées par colorant (ZnO/N719) ou par une couche solide de perovskite au plomb (TiO$_2$/MAPbBr$_3$). Sous l'effet de l'injection d'électrons dans l'oxyde de métal de transition (ZnO ou TiO$_2$), des changements dramatiques sont observés dans l'absorption près du seuil optique à partir desquels l'échelle de temps de l'injection électronique est obtenue. Cela met en lumière comment de petites modifications de la longueur caractéristique d'écrantage et du potentiel chimique peuvent générer de larges modifications dans les propriétés optiques au travers des effets à plusieurs corps. Aux deux interfaces, l'apparition retardée des électrons au bas de la bande de conduction est observée, qui est possiblement due à la localisation des électrons dans des défauts peu profonds. Cette Thèse dépasse le cadre des isolants de bande pour s'intéresser à la photodynamique de NiO, un matériau fortement corrélé à transfert de charge. L'excitation au-dessus de la bande interdite optique génère une large absorption induite en-dessous de la bande interdite qui est caractéristique de l'intrication entre les excitations

électroniques et bosoniques de basse énergie. L'habillage des excitations électroniques avec les modes bosoniques génère des excitations de basse énergie sur des échelles de temps ultra-rapides qui déclenchent une compétition entre l'itinérance et la localisation des résonances avec un grand degré d'accordabilité. Les progrès fait dans le domaine des spectroscopies X résonantes résolues en temps permettent l'investigation du degré de localisation des charges autour d'atomes spécifiques d'un système. La localisation d'électrons photogénérés dans le NiO est étudiée par spectroscopie d'absorption X résolue en temps, causant une élongation des liaisons et la formation d'un électron-polaron en moins de 100 ps. Dans une dernière partie, le dichroïsme linéaire du spectre d'absorption X statique de l'anatase TiO_2 au seuil K est étudié ce qui fournit une attribution fiable des transitions en-dessous du seuil du fait que leur composition orbitalaire fortement anisotropique et sensible à l'orientation du cristal. Une caractérisation complète du spectre est fournie avec le support de calculs *ab initio* et la dérivation analytique des sections efficaces angulaires d'absorption X.

Contents

Contents

Contents

List of Figures

List of Figures

List of Figures

List of Tables

List of Tables

Acronyms

ADC analog-to-digital converter. 161, 163, 165

AF antiferromagnetic. 112, 115

AFM antiferromagnetic. xxiii, 91, 93, 102

APD avalanche photodiode. 163, 164

ARPES angle-resolved photoemission spectroscopy. 40, 76

BBO β-barium borate. 162, 166

BGR band gap renormalization. 11, 14, 15, 134

BM Burstein-Moss. xxvi, 41, 59, 134, 148

BZ Brillouin zone. xvii, xxi, xxix, 1, 9, 17–20, 25, 29, 30, 70

CB conduction band. xvii, xix, xxi, 1, 10–13, 18, 21, 23, 25, 28, 30, 34–38, 40, 52, 55, 59, 63, 65, 67, 68, 70–73, 76, 88, 100, 101, 138, 143, 146, 148

CCD charge-coupled device. xvii, 5, 6, 165

CS Coulomb screening. 15, 21, 30, 41, 48, 52, 62, 64, 70

CT charge-transfer. 2, 25, 70, 75, 76, 80, 85, 87, 92, 100, 102, 117

CTE charge-transfer exciton. 61, 62, 143

DAQ data acquisition system. 160, 161

DAS decay associated spectrum. xxv, 55, 138, 142

DFT density functional theory. xxiii, 36, 76, 87, 89, 91, 92, 95, 153, 157

DLS dynamic light scattering. 119

DMF dimethylformamide. xxi, xxiv, 66, 119, 120

DMFT dynamical mean-field theory. 76

Acronyms

DOF degree of freedom. 1, 37, 75, 84, 85, 88, 102

DOS density of states. xxiv, 9, 18, 37, 63, 71, 73, 89, 92, 93, 111–113, 144, 156

DSSC dye-sensitized solar cell. xxi, 34, 51, 63, 65, 71, 73

ETM electron transport material. 34, 51, 52, 59, 60, 73, 117, 123, 138, 143

EXAFS extended X-ray absorption fine structure. xxii, xxiii, 3, 87–90, 93–99, 101, 103, 105, 116, 151, 153, 157, 158, 165

FD Fermi-Dirac. 9, 11, 35, 39, 59, 144

FDM finite difference method. xxvii, 91, 105, 106, 109, 111, 112, 115, 116, 153–157

FDMNES finite difference method near-edge structure. 105, 106, 109, 116

FEL free-electron laser. 102, 118, 160

FMS full multiple scattering. xxiii, xxvi, 91, 95–97, 104, 153, 154, 158

fs femtosecond. 5, 52, 88

FWHM full width at half maximum. 29, 40, 133, 134, 148, 150, 163, 165, 166

GA global analysis. xxv, 55, 58, 138, 140, 141

GGA generalized gradient approximation. 76, 157

HOIP hybrid organic-inorganic lead halide perovskite. 17, 21, 31, 51, 61, 122, 137, 138, 143, 144

ICTC interfacial charge-transfer complex. xxi, 61, 63, 67, 70, 72, 73, 117

IPCE internal photon-to-electron conversion efficiency. 51

IPES inverse photoemission spectroscopy. 76, 88, 92

IR infrared. 52, 67, 72, 73, 84

IRF instrument response function. xviii, xx, xxv, 7, 11, 17, 18, 20, 21, 23, 25, 26, 28, 30, 42, 54, 65, 102, 129, 130

KB Kirkpatrick-Baez. 160

LA longitudinal acoustic. 9, 10

LC ligand-centred. xxiv, 64, 120

xxxii

LD linear dichroism. 105, 106, 109, 111, 116, 118

LDA local density approximation. 76, 154

LDM lifetime density method. 37

LO longitudinal optical. 10, 42, 45

LSDA local spin-density approximation. 153

MB Maxwell-Boltzmann. 37, 42, 59, 144

MLCT metal-to-ligand charge-transfer. xxi, xxiv, 2, 64, 66, 70, 120, 121

MO molecular orbital. 91, 103, 104

MS multiple scattering. 104

MT muffin-tin. 91, 153, 154, 158

N719 di-tetrabutylammonium cis-bis(isothiocyanato)bis(2,2´-bipyridyl-4,4´-dicarboxylato)-ruthenium(II). xxi, xxiv, xxix, 63–70, 72, 73, 119–121, 125, 126

NLO non-linear optics. 162

NOPA non-collinear optical parametric amplifier. 166

NP nanoparticle. xix, xxi, xxiv, xxix, 1, 2, 33, 34, 39–42, 46, 49, 61, 63–70, 72, 73, 88, 93, 94, 117, 119–121, 125, 126, 128, 163, 165

ns nanosecond. 52, 65, 138

OD optical density. xxiv, 119–121, 125, 126

PA photoinduced absorption. xviii, 2, 8, 9, 15, 18, 26, 27, 37, 41, 42, 84, 85, 117, 134

PAW projected augmented wave. 157

PB photobleach. xvii–xxii, xxiv, xxv, xxix, 2, 7–9, 12, 13, 15, 17–21, 23, 25–28, 32, 36, 37, 41–43, 45, 47–49, 51, 52, 54, 55, 58–60, 62, 64–68, 70, 73, 75, 79–82, 84, 121, 126, 129, 131, 134, 137, 145, 146

PES photoemission spectroscopy. 76, 88, 92

PL photoluminescence. 65

PLD pulse laser deposition. 123

PoD pulse-on-demand. 162

UHB upper Hubbard band. 76

UV ultraviolet. xv, xvii–xxi, xxiv–xxvi, xxix, 1, 2, 5, 9, 17–19, 21, 24, 26, 27, 29–31, 33, 34, 38–41, 44, 48, 49, 51, 52, 58–60, 62–64, 68–70, 72, 73, 78, 87, 89, 117–122, 125, 127–131, 138, 139, 143, 149, 150, 159, 166, 213, 214

VB valence band. xvii, 10, 11, 13, 14, 17, 18, 21, 23, 25, 28, 30, 34–38, 40, 45, 59, 65, 76, 88, 91, 100, 101, 146, 148

XANES X-ray absorption near-edge structure. xxii, xxiii, 3, 87–96, 98, 101–103, 105, 116, 149, 152, 153, 157, 158

XAS X-ray absorption spectrum. xvi, xxiii, xxvi, xxvii, 3, 87–98, 102–106, 109, 117, 119, 149, 152–154, 156–158

XRD X-ray diffraction. 88, 119, 123

XRR X-ray reflectivity. 123

Introduction

The interaction between light and matter is one of many ways to tune material properties by playing with the spin, lattice, orbital and/or charge degree of freedom (DOF) [18]. Especially, photons with energies above the optical band gap of semiconductors in the range of a few electronvolts can promote electrons and holes out-of-equilibrium by populating higher energy bands. The relaxation of these charge carriers occurs along different radiative and non-radiative pathways with different efficiencies depending on the topology of the band structure. The non-radiative carrier relaxation to the band extrema relies on the coupling between the charge and the lattice DOFs called the *electron-phonon* or *hole-phonon* coupling. In many optoelectronic materials, the strength of this coupling is not known accurately which would help in designing materials with better efficiencies. The deeper comprehension of the coupling and relaxation of photogenerated charges goes hand in hand with the technological progress in ultrafast optical laser sources which can readily deliver sub-100 fs pulses with high energy and high shot-to-shot stability [19].

In this Thesis, ultrafast spectroscopy techniques in the Visible, the ultraviolet (UV) and the hard X-ray spectral range are used to unravel the charge-carrier cooling, injection and localization dynamics in a range of semiconductors with different degrees of electronic correlations.

In Chapter 1, some basic concepts of semiconductor physics are presented, which are used in the following Chapters with a brief introduction to pump-probe spectroscopy in general. The different type of signals one can expect are presented and their connection to the dynamics of the photogenerated particles in the material band structure.

In Chapter 2, the electron cooling in methylammonium lead bromide perovskite (MAPbBr$_3$) thin film is investigated by differential transmission in the UV. The high energy of the photons provides a selective access to the population of the conduction band (CB) where the electrons cool down to the R-point and accumulate, which provides an accurate estimate of the cooling time. Transient optical non-linearities triggered at different high-symmetry points in the Brillouin zone (BZ) are also observed which are not directly populated upon band gap excitation but undergo many-body effects such as the screening of the exciton oscillator strength and suppression of the Coulomb enhancement.

In Chapter 3, the charge-carrier cooling in a colloidal suspension of ZnO nanoparticles (NPs),

widely used in light-emitting devices [20], is investigated by transient absorption spectroscopy in the UV. The cooling time is observed from the spectral movement of the photobleach (PB) on the high energy side of the band edge bleach which represents the population of single particle states away from the Γ-point by hot charge carriers. The results are compared with the *ab initio* calculations by Zhukov and coworkers. We find that the experimental cooling times are approximately 3 times longer than than the theretical prediction [7, 21]. The shape of the PB at different excitation densities is modelled using a simple theory developed by Banyai and Koch [22]. The incorporation of the changes in the refractive index are needed to reproduce the transient signal in the spectral region above the optical band gap.

In Chapter 4, the electron injection at the interface between MAPbBr$_3$ and anatase TiO$_2$ (a-TiO$_2$) thin films is investigated by differential transmission in the UV from selective excitation of the MAPbBr$_3$ layer. The spectral signature of an exciton bleach in the a-TiO$_2$ layer is retrieved which is only possible under electron injection. The injection timescale is very slow with the main time constant of the order of 1 ns. The formation of a bound state at the interface is a possible explanation for the slow injection rate. This calls for a better design of the interface which can screen the charges more efficiently.

In Chapter 5, the electron injection at the interface between N719 dye molecules attached to ZnO NPs is investigated by transient absorption spectroscopy in the UV under selective excitation of N719 at the metal-to-ligand charge-transfer (MLCT) transition. The electrons injected into the ZnO NPs end up at the Γ-point where they bleach the direct band gap due to phase-space filling (PSF). The injection process is slow with two time constants of 64 ps and 590 ps. The possible causes of this slow injection rate are discussed. Especially, the possibility to form an interfacial charge-transfer complex has already been invoked. However, we discuss that there should not be a significant injection rate difference between N719 and a-TiO$_2$ on one side and N719 and ZnO on the other side in this scenario while drastic differences are observed. The involvement of surface states in the formation of the bound state is one possible explanation for the delayed injection.

In Chapter 6, the transient optical response upon bang gap excitation of a benchmark charge-transfer (CT) insulator, NiO, is investigated in the spectral region of its optical band by transient reflectivity in the deep-UV. We find a significant spectral weight redistribution after excitation with a strong photoinduced absorption (PA) below the optical gap which is not observed in standard band insulators. This may be due to the dressing of the electronic excitation with the underlying bosonic field which generates quasiparticles resonant below the optical band gap. Experiments performed in differential transmission of NiO thin films show acoustic oscillations whose amplitude is related to the antiferromagnetic ordering of the material first increasing up to the Néel temperature and then decreasing.

In Chapter 7, the electron localization upon band gap excitation of NiO microcrystals is investigated by time-resolved X-ray absorption spectroscopy (TRXAS) at the Ni K-edge. The electron localization is observed through a combination of chemical shift of the band edge,

bond elongation observed both in the X-ray absorption near-edge structure (XANES) and in the extended X-ray absorption fine structure (EXAFS) and bleach of a pre-edge transition. We estimate the electron localization occurs faster than the time resolution of the experiment of the order of 100 ps.

In Chapter 8, the linear dichroism of the X-ray absorption spectrum (XAS) spectrum of a-TiO$_2$ at the Ti K-edge is investigated. The angular variation of the absorption cross-section largely affects the peak A1 in the pre-edge due to the strong orbital polarization in the final of the transition. With the support of *ab initio* calculations and the analytical derivation of the XAS angular cross-section, we provide an unambiguous assignment of the pre-edge transitions and their degree of localization or delocalization in the final state. A strong linear dichroism is also observed in the EXAFS which is due to the p-orbital polarization. Surprisingly, peak A2 exhibits a quadrupolar angular evolution. Its large amplitude shows that the angular momentum selection rule of the transition relaxes when an oxygen vacancy is formed in the vicinity of a nickel atom.

Conclusions and future directions of the topics presented in this Thesis are discussed in a last part.

1 Basic concepts of semiconductor physics and time-resolved spectroscopy

Summary

In this Chapter, we briefly introduce the concepts behind pump-probe spectroscopy and the different signals one can expect when applied on solid materials in the vocabulary of solid state physicists. Then, the concept of charge-carrier cooling in semiconductors is presented which is used in Chapters 2 and 3 of this Thesis. Also presented are the nature of two encountered quasiparticles, namely excitons and polarons.

1.1 Pump-probe spectroscopy

1.1.1 General description

Among time-resolved spectroscopy techniques, pump-probe spectroscopies are very popular because they are often easy to implement and provide femtosecond (fs) time resolution with nowadays available laser sources. In pump-probe, a first intense light pulse, called the *pump*, is shined on the system to excite it (Figure 1.1). Then, a second less intense laser pulse, called the *probe*, is shined on the system. The probe transmitted or reflected spectral intensity is measured by a spectrograph coupled to a charge-coupled device (CCD) array in the ultraviolet (UV)-Vis or a silicon diode in the X-ray regime. The experiment consists in measuring the probe intensity after interaction with the sample at different time delays between the pump and the probe alternatively with and without pump pulse. The delay can be controlled electronically by the laser (pulse delivery) or by a mechanical translation stage to change the optical path of the pump or the probe. The temporal overlap between the pump and the probe at the system position is called *time zero*. For negative time delays, the probe arrives first at the sample and nothing happens since there is no difference in the probe intensity with or without a pump pulse arriving at later times. However, for positive time delays, the pump arrives first and the probe will experience a difference between the pumped and unpumped sample. This difference depends on the time delay between the pump and the probe. Hence, pump-probe spectroscopy measures the excited state dynamics of a system

mapping both in the spectral domain (with the spectral content of the probe) and in the time domain with the control of the delay between the pump and the probe pulses.
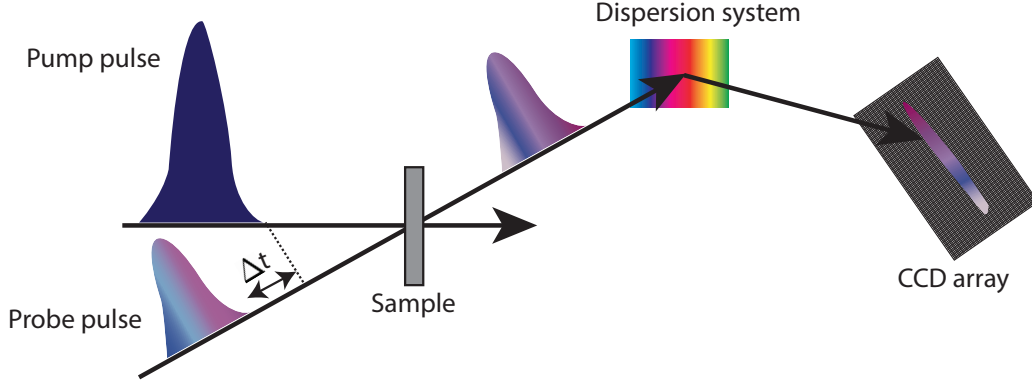
Figure 1.1 – Schematic of the pump-probe experiment in transmission around the sample position. The pump pulse is intense which brings the system out-of-equilibrium. After a controlled delay time Δt, a weaker polychromatic probe pulse arrives at the sample position which will have its spectral components transmitted depending on the system excited state. The transmitted probe pulse is dispersed and imaged into the Fourier plane by a CCD camera. An alternative geometry to the transmission is a measurement in reflectivity adapted to bulk solid samples.

Now, we focus on the type of signal measured in non-linear spectroscopy such as pump-probe spectroscopy. The energy transfer between a light pulse and a system is given by the variation of the light intensity I per unit distance dz according to,

$$-\frac{dI}{dz} = \langle \mathbf{E} \cdot \frac{\partial \mathbf{P}}{\partial t} \rangle \tag{1.1}$$

with I the intensity of the light pulse, $\mathbf{E}$ its electric field and $\mathbf{P}$ the polarization oscillating in the system at the same frequency as the light. In pump-probe spectroscopy, we look at higher order terms of the polarization $\mathbf{P}$ which can be expanded in power laws and give birth to interaction terms mixing the frequencies of the pump and the probe pulse. Following equation 1.1, the signal (light intensity variation) between the probe and the sample can be written as,

$$S = \Im \int dt \epsilon_S^* \frac{dP}{dt} \tag{1.2}$$

where ϵ_S is the probe field amplitude, $\Im$ the imaginary part and P is a polarization oscillating at the same frequency as the probe and including different interactions between the pump and probe photons depending on the interaction order. At first order for instance, only ϵ_S at frequency ω_S is included in P which is the usual absorption process where the pump photon frequency plays no role. The second order polarization proportional to the second order rank electric susceptibility tensor $\chi^{(2)}$, plays no role since it is zero in most samples

but most important is the fact that one cannot create an oscillating polarization at the probe frequency ω_s at second order. At third order, one term plays a role which relies on ϵ_S, ϵ_P and ϵ_P which oscillates at the frequency $\omega_S = \omega_S + \omega_P - \omega_P$ with an automatic phase-matching $k_S + k_P - k_P = k_S$ for the wavevectors of the pump pulse k_p and the probe pulse k_S. This is the pump-probe signal which can be expressed following equation 1.2 as,

$$S = \omega_s \Im \int dt \epsilon_S^*(t) P_S^{(3)}(t) \tag{1.3}$$

with $P_S^{(3)}$ the third order polarization field. A set of Feynman diagrams are associated to the third order polarization which show that when the pump and probe do not temporally overlap, only population terms play a role in the expression of the transient signal [23]. This is straightforward to interpret, the pump excites the molecule or the solid and the probe arriving at later time measures the system state in which excited populations have evolved. However, when the pump and probe pulses temporally overlap, there can be an interaction between the electronic fields which can give an important contribution to the signal, called the coherence term [24]. In practice, if the pump and the probe are spectrally non-degenerate, one can show that the ratio between the population and coherence term is of the order of the ratio between the pulse duration and the coherence relaxation time. This ratio is often very large and the coherence effect is negligible. If the pump and the probe contain the same frequencies (degenerate case), the population and coherence term have equal amplitudes at time zero which means that the signal measured close to time zero does not reflect the dynamics of the system, it is called the *coherent artifact*.

In most cases, equation 1.3 does not give an analytical formula. However, in the situation where the probe pulse is a gaussian in time and the population term decays exponentially, the convolution product gives an analytical formula involving the error function, a gaussian and an exponential decay. The width of the gaussian is called the instrument response function (IRF) and represents the convolution product of pump and probe temporal envelopes without resonant interaction in the sample. It can be measured separately from the pump-probe experiment by measuring the transient optical response of a medium with the same thickness and similar refractive index as the sample. For liquid systems, this can be a measurement of the pure solvent while for thin films, a piece of substrate of the same thickness as for the sample of interest can be used. The separate measurement of the IRF is useful to disentangle the actual signal coming from the system close to time zero from the response due to the non-resonant modulation of the system optical properties.

1.1.2 Type of signals

A typical pump-probe signal of a band semiconductor after above band gap excitation can contain three types of contributions as sketched in the transient transmission signal in Figure 1.2. The absorption spectrum is shown with a dotted line which has a sharp rise at the optical band gap reaching a local maximum at the exciton resonance if any (*vide infra*).
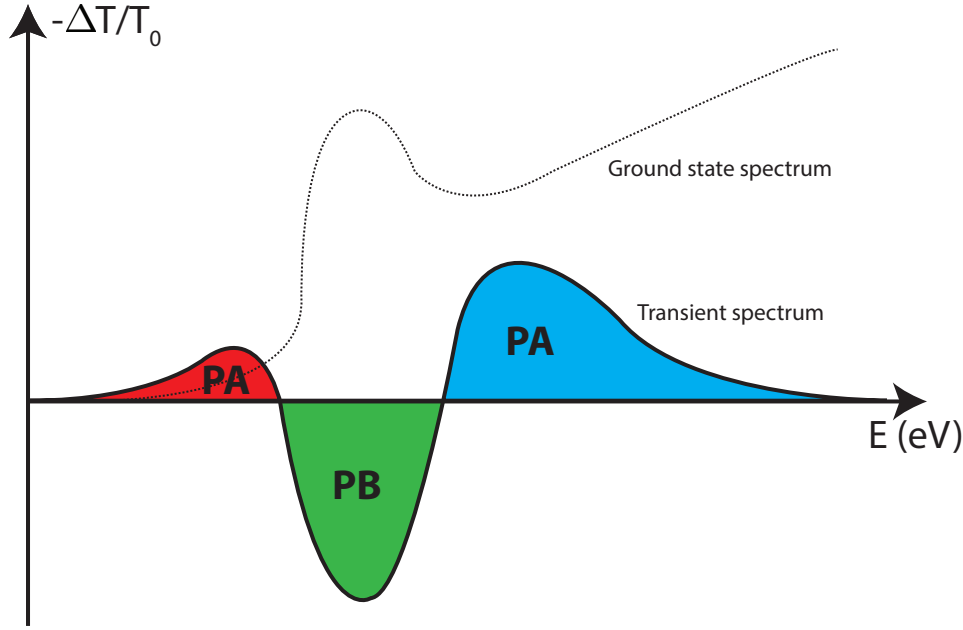
Figure 1.2 – Schematic of a transient spectrum measured in differential transmission $(-\Delta T/T_0)$ at the optical band edge of a semiconductor after above band gap excitation. The ground state spectrum is shown with dots. The transient exhibits three regions with two photoinduced absorption (PA) above and below the band gap while a photobleach (PB) appears at the exciton line.

The photobleach (PB) close to the absorption maximum at the optical gap corresponds to an induced transparency. This is the consequence of a filling of the states involved in the formation of the exciton which decreases the absorption coefficient. In the language of solid-state physics, the expression phase-space filling (PSF) is often used to describe the filling of the single particle states involved in an optical transition which leads to its blocking (bleaching). It is a consequence of the Pauli exclusion principle which cannot put two electrons with the same spin at the same energy position and crystal momentum in reciprocal space. In contrast, the photoinduced absorption (PA) on both sides of the PB (red and blue parts) correspond to an increase of the absorption coefficient. In the context of a semiconductor transient optical response, these two PAs have different origins. The red PA is due to the renormalization of the band gap which generates empty states below the band gap on ultrafast timescales. These states can be transiently populated before the cooling of the charge carrier is completed [25]. It is thus an increased absorption of the light at the corresponding probe photon energy due to the formation of new states. The blue PA does not correspond to the formation of new states but is usually due to the increase of the semiconductor refractive index [26, 27]. Since the quantity measured is a transient transmission, any increase in the sample reflectivity will translate into a decreased transmission which can be misleadingly interpreted as a PA of photogenerated charges in the excited state. Finally, not shown in Figure 1.2 is the possibility that the electromagnetic radiation can stimulate an emission from the

excited state. Stimulated emission is observed as an induced transparency with the same sign as a PB. It occurs efficiently in some semiconductors which have large Einstein B_{21} coefficients [28]. Stimulated emission and PB are usually close in energy at the optical absorption edge of the semiconductor and not easily disentangled [29].

In band insulators or semiconductors such as MAPbBr$_3$, TiO$_2$ or ZnO, a description of the optical transition in terms of electron and hole excitation between single particle states at a given crystal momentum in the band diagram is preferred. In this context, stimulated emission, PB and PA can be represented as vertical arrows in the band diagram of the solid. The probe photons connect different points in the band diagram from which the transient population with photogenerated charges can be monitored by transient absorption spectroscopy (TAS). The probe photon is more sensitive to crystal momenta with high density of states (DOS) which usually occur at high symmetry points of the Brillouin zone (BZ) (the so-called Van Hove singularities [30]). An example of the sensitivity of TAS to different high symmetry points is given in chapter 2 where high energy probe photons in the deep-UV have been used to access higher order interband transitions and high symmetry points away from the band gap minimum in reciprocal space.

1.2 Charge carrier cooling in band semiconductors

The illumination of a semiconductor with photons carrying more energy than the single particle band gap results in the generation of a large non-equilibrium carrier density with elevated temperatures as high as a few thousand of degrees [31]. The dynamics of transient populations affect the optical properties of the system in different manners which can be investigated by pump-probe spectroscopy with femtosecond time resolution.

Following the optical excitation, electrons and holes undergo a spatial (ballistic and diffusive) and temporal evolution with characteristic times which depend on the various relaxation pathways [32]. Initially, the pump photon energy is entirely transferred to carriers with specific momentum states depending on the energy difference between the bands matching the photon energy (Figure 1.3). The initial rise in the electron (hole) temperature depends on the excess energy which is the difference between the absorbed pump photon energy and the band gap E_g. As the system evolves towards equilibrium, there is a momentum and energy relaxation which depends on the topology of the band structure. Momentum relaxation or randomization occurs on a few femtoseconds timescale via elastic and inelastic scattering with the consequence that the average particle momentum becomes zero in isotropic bands [33]. On the same timescale, the carrier-carrier scattering of the electrons (holes) results in thermalization and the charges energy can be described by a Fermi-Dirac (FD) distribution with average temperature T_e (T_h). Because the hole effective mass is often larger than the electron [34], electrons carry more of the excess energy and the electron temperature is larger than the hole. Electron-hole scattering eventually brings the two distributions into thermal equilibrium to set a common carrier temperature ($T_e = T_h$).
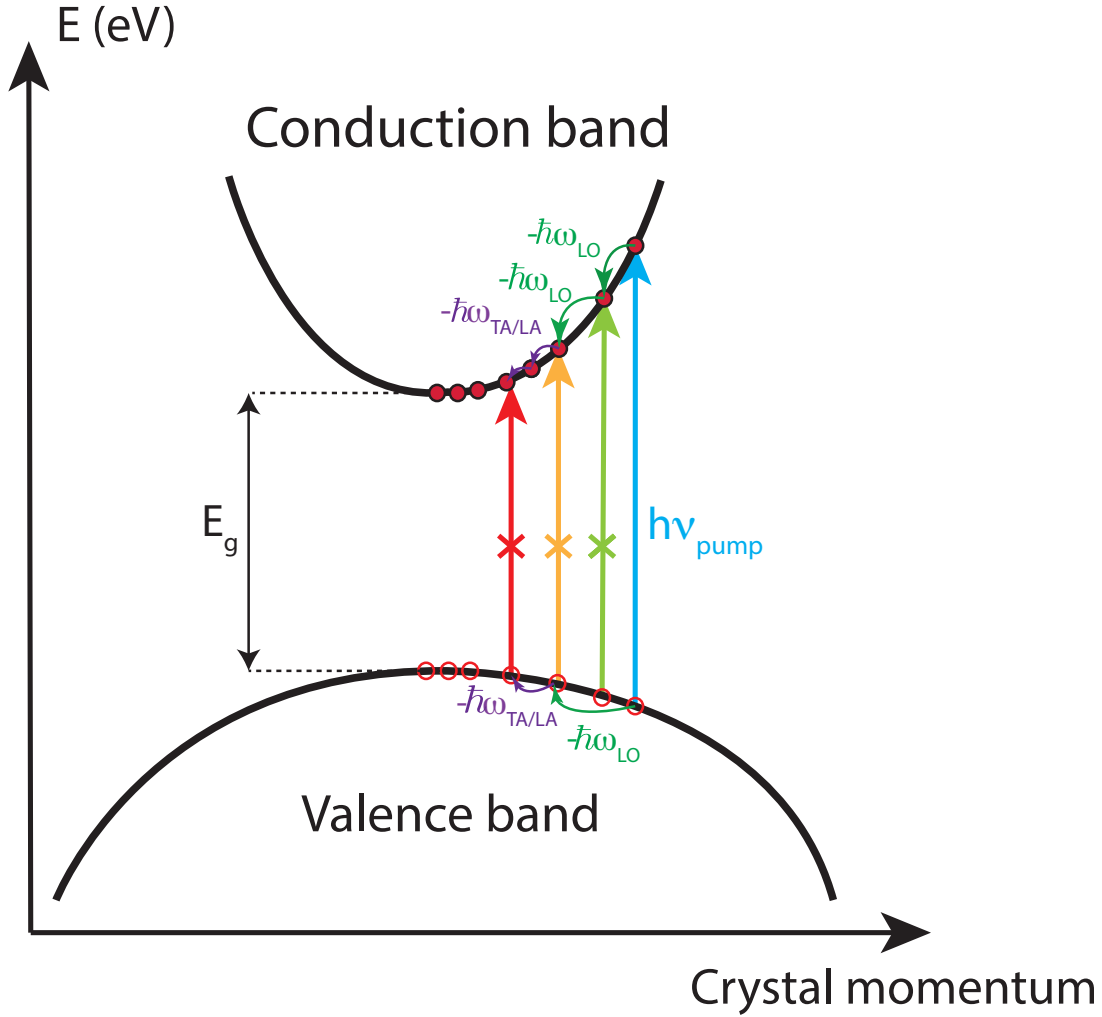
Figure 1.3 – Schematic of the cooling of electrons and holes in the valence band (VB) and conduction band (CB) of a band insulator or semiconductor.

Energy relaxation occurs primarily via the emission of optical phonons. All optical phonons generated eventually decay into two or more lower energy phonons (longitudinal acoustic (LA)+LA, LA+longitudinal optical (LO), etc...) via multiphonon processes associated with lattice anharmonicity. The time necessary for the phonons to reach an equilibrium distribution associated to a lattice temperature varies from ~10 ps at cryogenic temperatures to ~4 ps or less at room temperature [35]. Because the phonon equilibration can be longer than the carrier-optical phonon cooling time, large non-equilibrium optical phonon populations can be generated during the carrier energy relaxation called *hot phonons* [36, 37]. This is especially important in lead halide perovskites in which this effect called the "hot phonon bottleneck" can slow down significantly the carrier cooling time due to the reabsorption of phonons [38, 39].

On a timescale greater than 100 ps (depending on the carrier density), electron-hole recombination occurs according to a second order kinetic law or at high carrier densities via three-body Auger processes following a third order law. Other recombination processes can take place on even longer timescales[1] and therefore are considered negligible in the femtosecond to picosecond regime investigated in most of this Thesis.

Because the excitation beam is focused on a narrow region of the sample surface, one has also to consider the spatial behavior of the various microscopic processes in addition to the temporal aspect of the laser pulse excitation which are related to the diffusive and ballistic transport of the carriers [35]. Most of the charge carriers are generated in a small region close to the sample surface which is especially important for experiments performed on single crystals such as NiO in Chapter 6. This leads to carrier diffusion which is one mechanism for the excited system to go back to equilibrium. The diffusion of electrons and holes can differ significantly, leading to a dominant charge in one spatial region at the sample surface. The initial rise in temperature of the charge carriers leads to a large increase in diffusion coefficient which causes the carriers to move away from the interaction region. As the carriers lose their excess kinetic energy and the system returns to equilibrium, the diffusion coefficient also returns to its ambient value. In most semiconductors, this diffusion coefficient enhancement lasts the time it takes for the carrier to lose their excess kinetic which corresponds to the carrier-phonon cooling time in a few picoseconds.

Laser pulses contain a large number of photons generating very dense electronic excitations. For such high densities, the carriers cannot be considered as behaving independently and *many body* effects are often not negligible [40]. Some of these effects are exciton screening [41, 42, 43] (see section 1.3) and band gap renormalization (BGR) [44] encountered in this Thesis. The latter is related to the normalization of the particles self-energies as the exchange and correlation terms are modified by the changes in the Coulomb potential upon excitation (which includes a screening length factor in solids[2]) [46].

The cooling of the charge carriers to their equilibrium state can be readily monitored by TAS. The transient absorption signal depends proportionally on the occupation number of electrons and holes at a given probe photon energy and crystal momentum[3]. In the process of charge carrier relaxation, the thermalization of the charge carriers has to be distinguished from the cooling of the charge carriers [47]. While the former is related to carrier-carrier scattering processes setting up a thermalized carrier temperature on a few femtoseconds timescale, the latter exchanges energy between the carriers and the lattice degrees of freedom which allows the relaxation to the band edges. In the context of this Thesis, the IRF of our

---

[1]This includes the oxidation of the solvent molecules at photovoltaic interfaces studied in this Thesis which is relevant in applied systems.

[2]See for instance the work by Yukawa to include the corrections due to the excited carrier density to the Coulomb potential in solids [45].

[3]The absorption coefficient α at probe photon energy E for an excited density of electron-hole pairs n is related to the ground state absorption coefficient α_0 by $\alpha(E, n) = \alpha_0(E)[f_V(E_C, n) - f_C(E_V, n)]$ with f_V, f_C the VB and CB FD distributions, and E_V, E_C the energy of the VB and CB extrema [25]. This expression is averaged over all crystal momenta.

setups is of the order of 100 fs which is longer than the thermalization time. The consequence is that the probed charge distribution is already thermalized which for low excitation densities populates the band edges at the time zero of the experiment. Hence, the cooling of the charge carriers in the following will only refer to the electron-phonon coupling mechanism due to the the insensitivity of our experimental techniques to thermalization. While the photogenerated electrons and holes cool down to their band extrema, they occupy single particle states in momentum space which are resonant with optical frequencies contained in the probe pulse. In that case, the probe pulse has a decreased probability of absorption after the excitation with the pump pulse which gives a negative signal in TAS corresponding to a PB. This effect is illustrated in Figure 1.3 in which, while the electron and hole cool down, optical transitions which are lower and lower in energy (colored arrows) are blocked by the particle occupation. This translates into a PB which is spectrally moving to lower photon energies (see Chapter 3, Figure 3.8). An alternative way to look at this process is to observe the rise of the PB at the band edge. The slower the carrier-phonon cooling process, the longer it takes for the PB to reach its maximum amplitude. This is illustrated in Figure 1.4 for PbSe quantum dots (QDs), a semiconductor with a band gap of ~0.9 eV in which an increase in pump photon energy leads to slower cooling time and thus longer rise time for the bleach at the optical band edge [1]. The effect is enhanced in the example given in Figure 1.4 because the bands are partially discretized in QDs, slowing down the cooling even more when the pump photon energy increases. Note that other effects can slow down the cooling time of charge carriers such as polaron formation [48] of intervalley scattering [49].

As just explained, after the charge carriers have cooled down to the band extrema, a PB peaked at the optical band gap is observed. Its amplitude is related to the excited densities of electrons and holes. Since the hole effective mass is usually an order of magnitude larger than the electron ($m_h^*/m_e^* \sim 6$ in CdSe [50]) and the VB degeneracy is usually more than the CB, there is a large difference between the hole and electron density at the band edges [51]. The consequence is that the photogenerated holes occupy single particle states which extend to larger crystal momenta than the electrons. Since the amplitude of the PB at the band edge is proportional to the density of electrons and holes in a narrow range of momenta around the band extrema, the asymmetric band dispersion contains a larger density of electrons causing the PB to be more sensitive to the photogenerated electrons than holes [52]. This has been experimentally observed in CdSe [53, 54]. However, in the semiconductors investigated in this Thesis such as ZnO and MAPbBr$_3$, the electron and hole effective masses are of the same order of magnitude or almost equal in MAPbBr$_3$ [55]. This implies that the contribution of holes to the transient signal cannot be neglected and that the observed cooling is due to an interplay of electron and hole dynamics.

For a more detailed description of the charge-carrier cooling in semiconductors, a few review papers provide a detailed formalism [27, 56] and examples investigated by pump-probe spectroscopy [1, 33, 57].
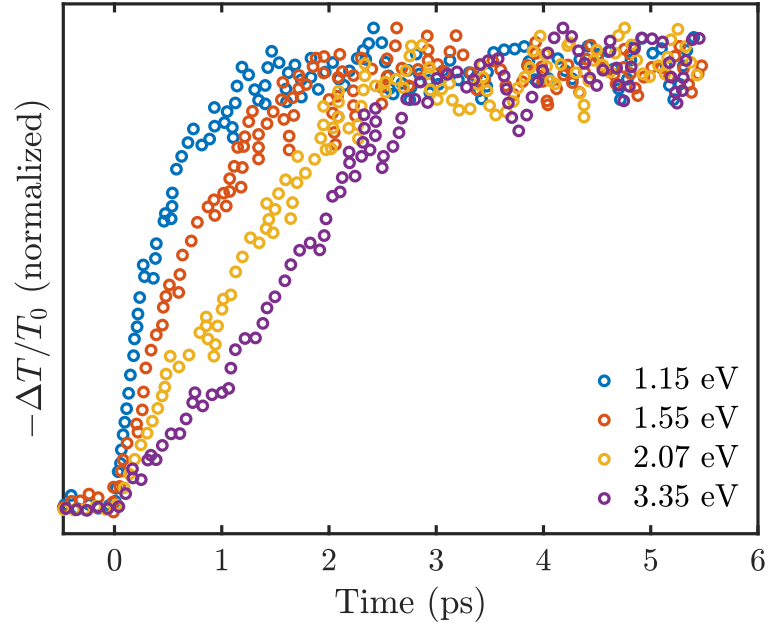
Figure 1.4 – Evolution of the carrier cooling at the optical band edge of PbSe under different pump photon energies at 1.15 eV (blue), 1.55 eV (orange), 2.07 eV (yellow) and 3.35 eV (purple). The larger the pump photon energy, the slower the cooling due to the larger number of electron-phonon scattering processes required for the electron to cool down in the CB. Reproduced from [1] (Figure under Creative Common License).

1.3 Excitons in solids

The Coulomb interaction between the photogenerated electron and hole can form bound states called *excitons*. They are resonant below the energy gap of the semiconductor. As the net charge of the electron-hole pair is zero, excitons do not contribute to the electric conduction but can be excited by electromagnetic fields and contribute to the optical absorption of a system.

In an isotropic semiconductor, the electron-hole interaction is described in a similar way as for the hydrogen atom. The Coulomb interaction is screened by the static background dielectric constant $\epsilon_{\omega \to 0} = \epsilon_r \epsilon_0$ of the semiconductor. Both the hole and the electron can be represented by spherical wavefunctions and the energy of the bound state follows a geometric progression given by,

$$E_n = E_g - \frac{e^4 \mu}{2\hbar^2 \epsilon_{\omega \to 0}^2 n^2} \tag{1.4}$$

where $n = 1, 2, 3, \ldots$ is the exciton principal quantum number and μ the reduced electron-hole effective mass $\mu^{-1} = m_e^{*-1} + m_h^{*-1}$. The spatial extension of the exciton in the ground state ($n = 1$) can be estimated by similarity with the hydrogen atom problem and is called the

exciton Bohr radius as,

$$a_B = \frac{\epsilon_{\omega \to 0} \hbar^2}{e^2 \mu}$$ (1.5)

For small band gap semiconductors, the static dielectric constant $\epsilon_{\omega \to 0}$ is correspondingly large and the spatial extension of the exciton is large going beyond several unit cells. This is the Wannier exciton limit [58] with a low binding energy (typically a few meV) possibly ionized at room temperature [59]. In wide band gap semiconductors or insulators, the dielectric constant is smaller and the exciton remains confined within a unit cell with a large binding energy which corresponds to the Frenkel exciton limit [60]. It is common in alkali halides systems [61]. Extrinsic effects can significantly increase the exciton binding energy such as the spatial confinement of the electron and hole wavefunctions so that they are "forced" to interact. This is typically the case in quantum dots [1], nanorods [62], quantum wells [63] or monolayers [64] which exhibit robust excitons at room temperature.

Equation 1.4 describes the energy of an exciton at rest. The motion of the electron-hole pair can be decomposed into the relative motion around the centre of mass and the motion of the centre of mass itself. The latter is equivalent to a free particle with a total mass $m_e^* + m_h^*$ and in the effective mass approximation has a translation motion with kinetic energy following,

$$E_{kin} = \frac{\hbar^2 \mathbf{K}^2}{2(m_e^* + m_h^*)} = \frac{\hbar^2 (\mathbf{k}_e + \mathbf{k}_h)^2}{2(m_e^* + m_h^*)}$$ (1.6)

This parabolic dispersion is similar to the free charge dispersion with a larger mass. The excitonic progression forms sharp lines in the absorption spectrum below the band gap of semiconductors at low temperature [65]. As the temperature increases, the progression gets broader and is usually not resolved at room temperature for low band gap semiconductors.

The sensitivity of the excitons to the Coulomb field in the semiconductor provides a high degree of tunability of these optical resonances [41]. Exciton screening refers to the process where increasing carrier concentration makes the resonant exciton absorption broader and eventually disappears because the screening length becomes comparable to the exciton Bohr radius. In that latter case, the electron-hole interaction is fully screened and a bound state cannot be formed which means that the charge carriers after excitation only exist as free charge carriers (Mott transition) [66].

The transient optical properties of the excitons have been investigated in detail by Chemla and coworkers in GaAs quantum wells [2]. In Figure 1.5, the ground state absorption spectrum (red curve) shows two prominent absorption lines corresponding to excitons formed at the heavy-hole (peak at 1.46 eV) and light-hole (1.47 eV) VBs. Upon continuous laser irradiation with photon energy above the band gap, a strong damping of the exciton lines is observed together with an increased absorption below the band gap (blue curve) as a result of the broadening of the exciton lines and a slight energy shift of the spectrum to the red (BGR). The difference spectrum between the irradiated and non-irradiated sample is depicted as a black line which
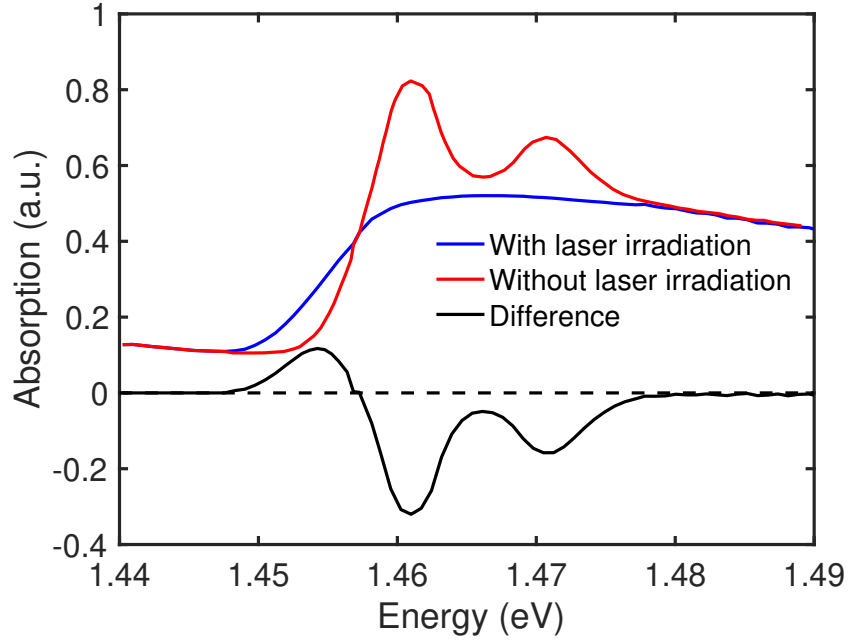
Figure 1.5 – Evolution of the absorption spectrum of GaAs/AlGaAs quantum wells under laser irradiation at 35 meV above the heavy-hole exciton (peak at 1.46 eV). Adapted from [2].

gives negative signals (PB) at the energy positions of the excitons and a positive signal (PA) below the optical gap. Although the difference spectrum is obtained by continuous irradiation (quasi-equilibrium), it corresponds to the typical transient signal observed around the exciton lines upon above band gap excitations with light pulses [2, 67]. The exciton PB and broadening occurs immediately after excitation which shows that the screening of the exciton due to the photogenerated free charge carriers occurs in less than 100 fs [68]. From these first studies, theoretical developments have quantified the contribution from the PSF and the Coulomb screening (CS) to the PB of the excitonic lines [69]. In direct band gap semiconductors, PSF is usually the dominant mechanism of exciton PB. In more recent studies on indirect band gap semiconductors such as anatase TiO_2, the effect of CS on the exciton bleaching can compete with PSF [43, 70]. In the eighties, a simple theory has been developed by Banyai and Koch to describe the modification of the optical spectrum under irradiation with a continuous-wave laser (quasi-equilibrium) with great success on low band gap semiconductors such as GaAs and CdSe [22, 71]. The theory is presented in more details in Chapter 3 to model the transient absorption spectrum in the ZnO spectral region of the exciton. The theory typically takes into account the change in electron and hole chemical potential (PSF), BGR and screening length to compute the optical spectrum in the excited state for a given photogenerated density of electron-hole pairs.

1.4   Polarons

The term *polaron* often refers to the quasiparticle ensemble of a trapped carrier and the associated lattice displacement out of its equilibrium position. More generally, a polaron defines the movement of a charge carrier with the associated lattice deformation due to the modification of the Coulomb potential [72]. The polaron can have very different mobility coefficients depending on the strength of the interaction with the lattice. In the weak-coupling regime, the polaron has an effective mass slightly larger than the bare carrier mass while it is much larger for a strongly coupled polaron. The coupling strength affects the spatial localization with large polarons extending over several unit cells while *small* polarons typically involve the few atoms linked to a single site. The formation of polarons in optoelectronic systems affect the charge transport properties and are thus of fundamental importance for a lot of applications among which photovoltaics. Although the polaron effective mass is larger than the bare carrier which decreases its mobility [73], it prevents the carrier to interact with other particles in the system. This effect can be viewed as a sort of protection in which the coupling with the bosonic modes screens the charge from the surroundings [74, 75]. It has recently been shown that the formation of electron polarons in lead halide perovskites can explain the slow electron cooling time since it competes with the electron cooling [75].

Due to the lattice deformation they induce, the formation of polarons can be conveniently detected with ultrafast techniques which are sensitive to bond distances around the specific atoms where the localization occurs. Time-resolved X-ray absorption spectroscopy (TRXAS) provides the sensitivity to both the change in geometry and electronic structure of specific atoms. It has been recently used to track the decay of polarons in inorganic lead halide perovskites [76, 77, 78]. In this Thesis, a similar method is used which tracks the formation of small electron polarons in NiO microcrystals and the lattice extension of ~7% induced by the electron localization around the Ni centres (Chapter 7).

2 Photodynamics in methylammonium lead bromide perovskite (MAPbBr$_3$)

Summary

In this Chapter, the photodynamics of charge carriers in MAPbBr$_3$ thin films is studied by femtosecond differential transmission spectroscopy in the ultraviolet (UV). The electron and hole dynamics are disentangled by probing higher energy interband transitions in the Brillouin zone (BZ), similarly to the strategy implemented for MAPbI$_3$ [3]. The differential transmission exhibits three photobleaches (PBs) with different rise times. The PB around 3.47 eV is sensitive to the electron cooling in the M-R valley of the BZ and provides a cooling time of ~400 fs with 3.1 eV excitation. This is half the cooling time usually reported in transient absorption spectroscopy (TAS) experiments with Visible probe looking at the optical band gap [79, 80, 81, 82] meaning that the hole is limiting the overall cooling of the charge-carriers. It is consistent with the results on other hybrid organic-inorganic lead halide perovskites (HOIPs) [83] where slow hole cooling is reported which may explain the efficiency of hole extraction for this class of perovskite [84]. Part of this Chapter has been published in a proceedings [85].

Introduction

HOIP with formula MAPbX$_3$ (MA stands for methylammonium, X=Cl, Br, I) are very promising materials for applications in photovoltaic [86, 87], light-emitting [88], sensor devices [89] or actuators [90]. They can be easily synthesized with cheap production costs [91]. Among HOIP, MAPbBr$_3$ can generate high open circuit voltages which are promising for photovoltaic applications [92, 93].

Excitation above the band gap of MAPbBr$_3$ (E_g = 2.3 eV at room temperature [94]) generates electron-hole pairs in the $R - M$ valley of the BZ (thick purple arrow in Figure 2.1). The excess energy prevents the formation of excitons which dissociate on a sub-10 fs timescale [82, 95] such that the photogenerated charges behave as free electrons and holes [96]. The thermalization of the charge carriers occurs on ultrafast timescales within the instrument response function (IRF) of our setup which populates the extrema of the valence band (VB) and the con-

duction band (CB) in less than 100 fs [97, 98, 99]. After thermalization, the charges cool down to the *R*-point (pink circles in Figure 2.1) via electron-phonon and hole-phonon scattering where they recombine or get trapped [100]. The charge-carrier dynamics in MAPbBr$_3$ with above band gap excitation has been intensively investigated by femtosecond TAS in the Visible [39, 81, 82, 101]. Carrier cooling times around 1 ps are reported with 3.1 eV pump photon energy (0.8 eV excess energy) [39] similar to other bulk polar semiconductors like CdS [102] or GaAs [103] in which the charge-phonon Fröhlich coupling is dominant [104]. The cooling time increases to several picosecond (ps) in MAPbBr$_3$ quantum dot (QD) [101] as previously observed in CdSe QD [51, 105] due to the discretization of the bands into energy levels. This slow cooling is beneficial to achieve efficient charge injection into acceptor materials or molecules [101, 106]. However, TAS at the optical band gap does not distinguish between the type of charge carrier since electron and hole have similar effective masses [107] and thus density of states (DOS) at the CB and VB extrema. The consequence is that electron and hole populations are expected to contribute similarly to the transient spectrum at the optical band gap so that they cannot be easily disentangled [108]. This contrasts with other polar semiconductors such as CdSe in which the large ratio between the electron and hole effective masses ($m_e^*/m_h^* = 0.3$ [109]) leads to TAS being more sensitive to the electron population changes. It calls for ultrafast spectroscopy strategies which can access selectively the dynamics of electrons or holes.

In this Chapter, using femtosecond UV differential transmission with 150 fs time resolution from 3.45 eV to 4.55 eV [110, 111], higher order interband transitions can be reached in MAPbBr$_3$, from which we specifically observe the electron dynamics. In addition, a broader phase-space can be sampled with optical transitions at the *M* and *X*-points in the BZ.

2.1 Results

In this Chapter, the pump-probe experiments measure the differential transmission of MAPbBr$_3$ thin films from Prof. T. F. Guo in Taiwan (the sample synthesis is described in Appendix A.4). The sample characterizations are provided in Appendix (section C.1) which includes the UV-Vis and emission spectra as well as the analysis of the absorptive properties with the Elliott formalism to determine the band gap and exciton binding energy [112]. A characterization of the setup IRF is provided in Appendix (Figure C.3a). The differential transmission signal is plotted with a negative sign ($-\Delta T/T_0$) so that the PB appear as negative and the photoinduced absorption (PA) is positive.

Figure 2.2b shows the pseudo-color coded differential transmission energy-time map of MAPbBr$_3$ thin films excited at 3.1 eV (400 nm, excitation density 1.3×10^{17} cm^{-3}) and probed in the deep-UV. The transient signal exhibits three PB centred at 3.47, 3.87 and 4.57 eV labelled PB2 to PB4 in the following (we keep PB1 for the optical band edge bleach at 2.3 eV). PB2 and PB3 correspond to specific features in the imaginary part of the dielectric constant (Figure 2.2a). The PB energies agree with the resonances retrieved in previous spectroscopic ellipsometry studies [4, 113, 114, 115, 116] and summarized in Appendix (Table C.2). Stimulated emission
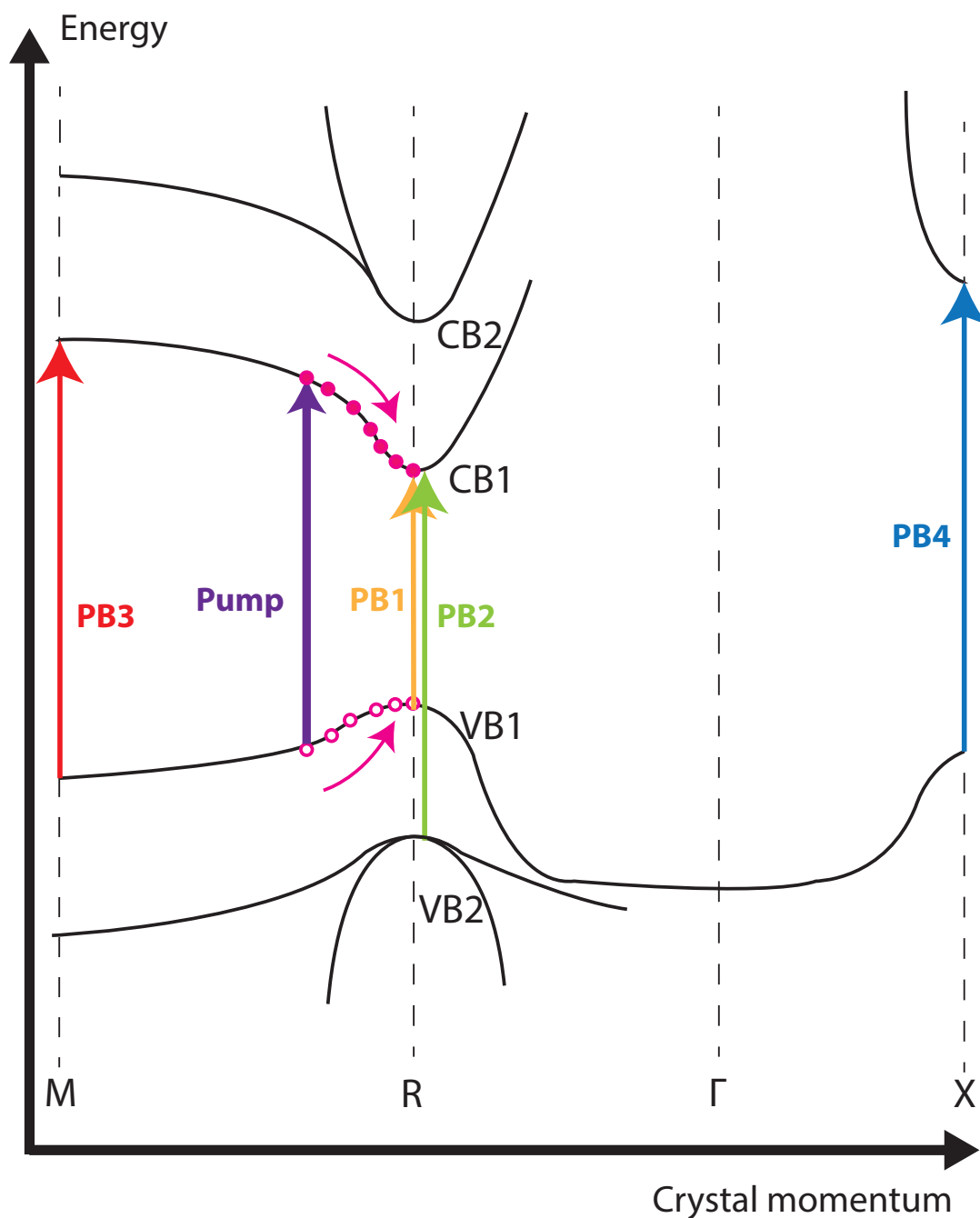
Figure 2.1 – Schematic band structure of MAPbBr$_3$ BZ. The pump excitation (3.1 eV) is represented by a thick violet arrow. The optical transitions involved in the PB measured in the deep-UV are represented with thin arrows at the R-point (PB2, green), at the M-point (PB3, red) and at the X-point (PB4, blue). The PB at the optical band edge in the Visible (PB1) is shown with a yellow arrow.

is excluded since the pump photon energy is lower than the probe. In order to rule out a contribution from the change of refractive index to the differential transmission, we performed a transient reflectivity experiment shown in Appendix (Figure C.4). Both detection modes give the same signal shape which means that the observed transient transmission signal originates from changes in the absorption coefficient only[1] [25]. This is in turn related to the changes in the band populations in the BZ and to many-body effects [68].
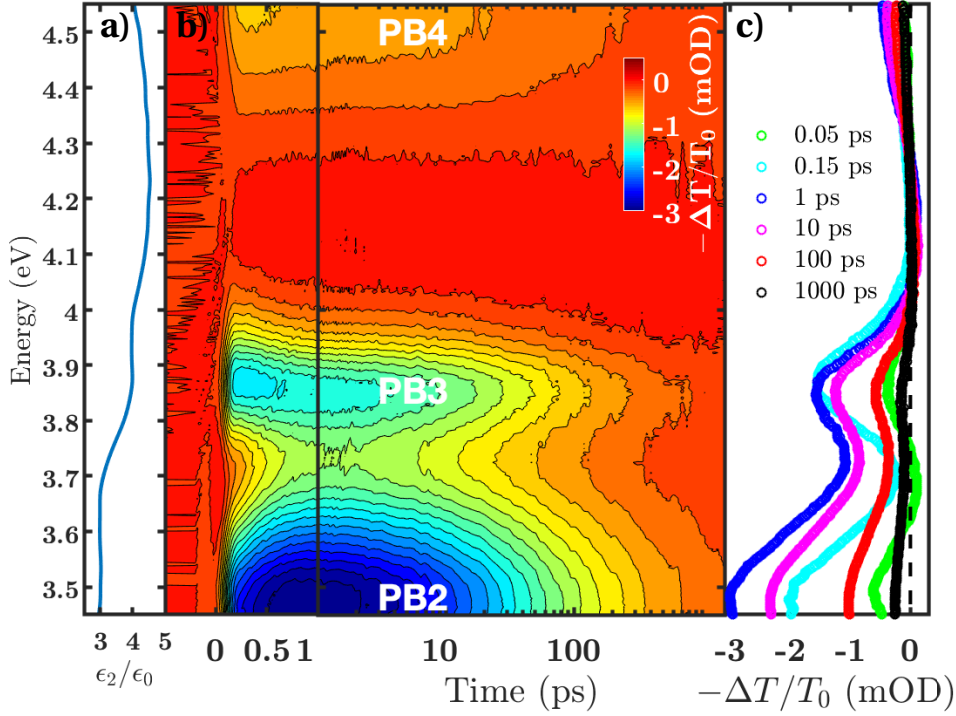
Figure 2.2 – a) Imaginary part of the dielectric constant of MAPbBr$_3$, b) Differential transmission of MAPbBr$_3$ following 3.1 eV excitation (density 1.3×10^{17} cm^{-3}), c) Spectral traces at different time delays.

Spectral traces at different time delays are shown in Figure 2.2c. At time delays within the setup IRF (< 150 fs, green circles), PB3 exhibits weak positive wings with the low energy one at 3.7 eV quickly overwhelmed by PB2. A red shift of the PB3 minimum is observed between time 0 and 1 ps (cyan and blue circles in Figure 2.2c) while PB1 and PB3 minima remain at the same energy.

Time traces at the PB minima are shown in Figure 2.3 from 1 ps to 1 ns. They are best fitted with a third order kinetic law which shows that Auger recombination dominates at our excitation

---

[1]The differential transmission and transient reflectivity signals are proportional to both the change in refractive index Δn and absorption coefficient $\Delta \alpha$. However, they depend differently on the change of refractive index so that a similar pump-probe signal in transmission and in reflectivity shows that only the change in absorption coefficient $\Delta \alpha$ is present in the signal.

density. However, the actual kinetics is likely a mixture of second and third order law similarly to previous works [117, 118].

Band integrals[2] normalized at time 0 centred at the PB minima are depicted in Figure 2.4 together with the IRF (time traces at single probe wavelengths are given in Appendix Figure C.3b for comparison). PB2 (green curve) and PB3 (red curve) have similar decays while PB4 decay is slower (blue curve). At short time delays (inset in Figure 2.4), PB3 and PB4 reach their maximum absolute amplitude within the IRF while PB2 follows a bimodal rise with a prompt bleach within the IRF followed by a further bleach in ~0.4 ps. Such bimodal rise is also reported for the optical band edge bleach in the Visible and has been attributed to charge-carrier phonon cooling (*vide infra*) [81, 82]. The IRF-limited PB over a wide spectral range in the UV is related to the ultrafast suppression of the Coulomb enhancement [27] due the screening of the electron-hole pair interaction by free charge carriers in MAPbBr$_3$ [82].

To complement the differential transmission experiments in the deep-UV, we have also repeated the measurements in the Visible following 3.1 eV excitation of MAPbBr$_3$. Since these results are not novel [39, 81, 82, 101], they are described in Appendix D.2. They will be used in the Discussion (section 2.2) to compare the kinetics at the optical band edge in the Visible and in the UV, the latter involves higher energy interband transitions and portions of the band diagram away from the R-point.

2.2 Discussion

2.2.1 Assignment of the photobleaches

We first discuss the assignment of the PB in the differential transmission signal of MAPbBr$_3$ by comparing with previous TAS measurements performed on other HOIP systems such as MAPbI$_3$. This is a reasonable starting point since the UV-Vis spectra of methylammonium lead perovskites with different halogens look similar with an energy shift of the spectrum which depends on the halogen composition (see Figure 2b in Ref. [4] for comparison). This way, we can expect a direct correspondance between the PB in MAPbBr$_3$ and MAPbI$_3$ which is given in Table 2.1 and serves as a basis for the assignment of the optical transitions underlying the PB in MAPbBr$_3$. In the measurements by Sum et al. on MAPbI$_3$ [3, 119, 120, 121], two PB are observed in the region of the optical band edge at ~1.63 eV (PB1) and above the band edge at ~2.61 eV (PB2) under 2.1 eV excitation in the $R - M$ valley as shown in Figure 2.5B. PB1 is due to a combination of Coulomb screening (CS) and phase-space filling (PSF) [81, 82, 118, 122]. Both PB have similar decays (Figure 2.5C). Since PB1 and PB2 are at different energies, they involve different interband transitions. The similar decay times show that they have a band in common which is either the VB or the CB so that they are sensitive to the recombination rate of the same particle (electron or hole) [3, 123]. While PB1 is sensitive to both the electron and

---

[2]See Appendix section D.9 for the mathematical definition of a band integral. It is a useful analytical tool which can detect the onset and evolution of state filling without reference to specific structures in the transient spectrum [82].
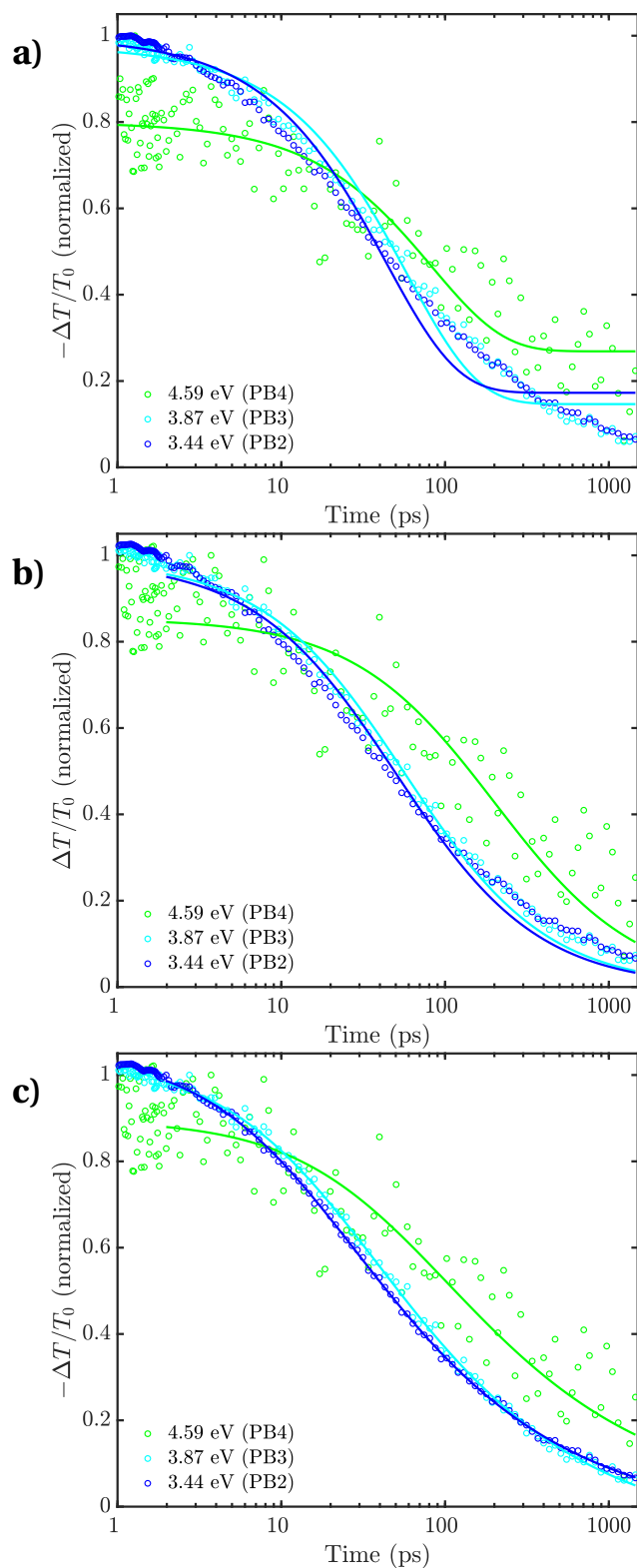
Figure 2.3 – Kinetic models at PB2 (blue), PB3 (cyan) and PB4 (green) on MAPbBr$_3$: a) first order law, b) second order law and c) third order law. Experimental data are circles and fits are continuous lines.
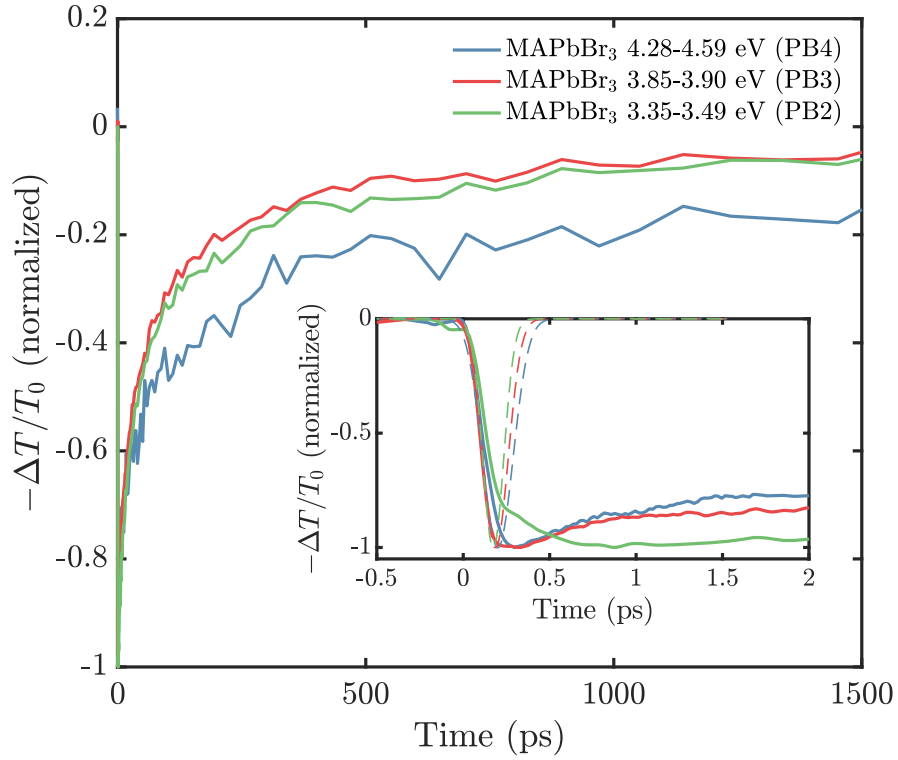
Figure 2.4 – Band integrals from the differential transmission of MAPbBr$_3$ following 3.1 eV excitation in the spectral region of PB2 (green), PB3 (red) and PB4 (blue). The IRF for each range of probe energies is given by the thin dashed lines.

hole dynamics at the R-point after optical excitation in the $R - M$ valley, PB2 is sensitive to only one type of charge carrier, electron or hole, if it involves the CB or the VB, respectively. Based on complementary experiments with electron and hole extraction layers in contact with MAPbI$_3$, the authors find that PB2 is compatible with a transition from the second VB[3] to the CB at the R-point. In addition, they performed one measurement with an increased pump photon energy at 3.1 eV above the PB2 energy to excite directly the corresponding interband transition. Time traces are reproduced in Figure 2.6 with pump photons above (upper pannel) and below (lower pannel) PB2 energy. A new fast decay of ~400 fs appears with the pump photon energy higher than PB2 (black curve in Figure 2.6A) which is compatible with hot-hole scattering between VB2 and VB1 (confirmed in [124]) when holes populate directly VB2, scatter and cool down in VB1. This is longer than in most organic semiconductors in which the hot-hole scattering occurs in ~100 fs [125]. PB1 has a consistent delayed rise time of the same ~400 fs as the hot-hole scattering time (red curve in Figure 2.6A). However, we note that the hot hole fast decay has also been observed elsewhere with the pump photon energy tuned in between the two PB energies [123]. Three important conclusions can be drawn from this

---

[3]the second VB (labelled VB2 in the following) refers to the band located at a lower energy than the VB at the R-point (called VB1 in the following). See Figure 2.1 for an illustration.
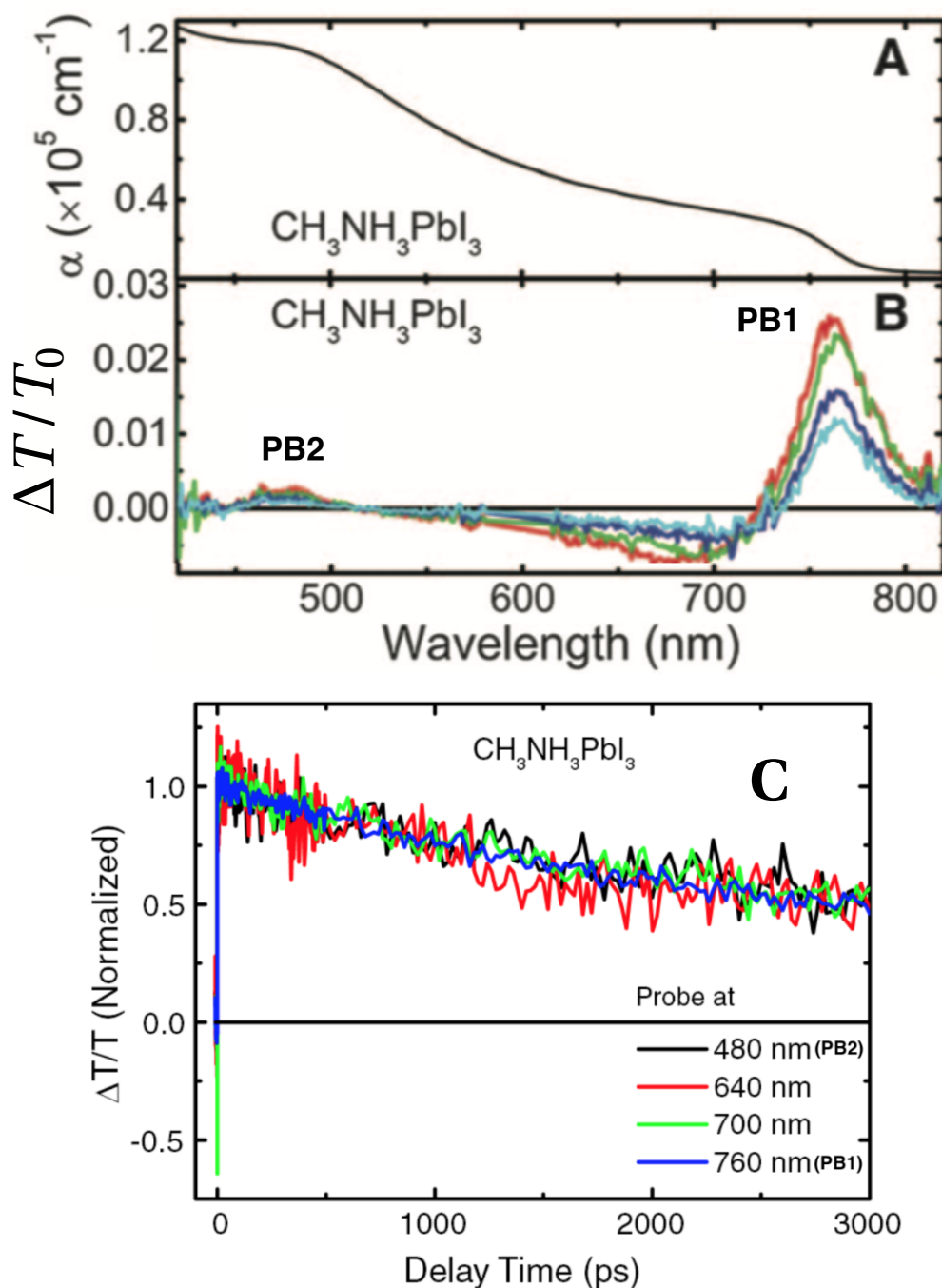
Figure 2.5 – (A) UV-Visible absorbance spectrum of a pure MAPbI$_3$ layer. (B) Differential transmission spectra of MAPbI$_3$ films in vacuum under excitation at 600 nm (2.1 eV) at different time delays: red (1 ps), green (100 ps), blue (500 ps), and cyan (1 ns). (C) Normalized time traces at different wavelengths of MAPbI$_3$ film in vacuum following excitation at 600 nm. The signals at 640 nm and 700 nm have been sign-flipped for better comparison. Adapted with permission from [3], Copyright American Association for the Advancement of Science.

study which are interesting for the parallel made with MAPbBr$_3$. First, PB2 in MAPbI$_3$ is due to a transition between VB2 and CB1 at the *R*-point. Second, the hole cooling limits the rise time of PB1 at the optical band edge. Third, PB2 rise time gives direct access to the electron cooling time at the R-point since it is sensitive to VB1. From this last point, the authors have not observed a significant delayed rise of PB2 increasing the pump-photon energy which means the electron cooling is expected to be in < 200 fs within their IRF consistent with recent studies [126]. The photodynamics in the PB2 spectral region has been further investigated by Manser, Kamat and coworkers [122] which confirmed the assignment by Xing et al. More recently, the formation of a charge-transfer (CT) complex has been invoked to explain PB2 [127].

Table 2.1 – Correspondance between the PB observed in the transient spectra of MAPbBr$_3$ and MAPbI$_3$ and assignment of the corresponding interband transitions in MAPbI$_3$. The letter subscript gives the high-symmetry point of the optical transition in the BZ.

MAPbBr$_3$ PB	MAPbI$_3$ PB	assignment in MAPbI$_3$
PB2 (3.5 eV)	PB2 (2.58 eV)	(VB2→CB1)$_R$ [3, 5, 122]
PB3 (3.86 eV)	PB3 (3.1 eV)	(VB1→CB2)$_R$,(VB1→CB1)$_M$ [114]

Following the pioneering work by Sum and coworkers, two studies have investigated in more details the origin of PB2 in MAPbI$_3$ [5, 128]. Anand and coworkers managed to access three PB in MAPbI$_3$ (labelled PB1 to PB3) extending the spectral bandwidth of the probe pulse in the Visible up to 3.55 eV (Figure 2.7). The energy positions of the PB are in agreement with ellipsometry data [107] and theory including spin-orbit coupling (SOC) [129]. All PB are observed with the lowest pump energy of 2.5 eV (550 nm) which populates only the VB and CB at the optical band gap of MAPbI$_3$. They investigated the changes in kinetics of the PB upon different pump photon energies which is illustrated in Figure 2.8. For every pump photon energies of 2.5, 3.1 (not shown) and 4.1 eV, PB1 at the optical band edge has a slow rise (red curve) while PB2 and PB3 (green and blue curves) reach their maximum within the IRF. In contrast, a faster initial decay of PB2 and PB3 appears when the pump photon energy is tuned above PB2 (green and blue circles) which is consistent with the results by Sum and coworkers of the hot-hole scattering [3]. Comparatively, a slower rise of PB1 is observed due to the delayed hole cooling. These results are compatible with a multiband picture at the *R*-point in which PB2 is due to the transition between VB2 and CB1. The authors propose that PB3 is either due to a transition from VB3 to CB1 or from VB1 to CB2 at the *R*-point. We already note a striking similarity between the rise times of PB2 and PB3 in MAPbI$_3$ (Figure 2.7) which is not observed in MAPbBr$_3$ (*vide infra*). In their work, Appavoo and coworkers have investigated the changes in the transient absorption response of MAPbI$_3$ upon temperature change through the different structural phases of the material (tetragonal and orthorhombic) [128]. PB2 at 2.6 eV splits in energy in the low temperature orthorhombic phase. From a symmetry analysis of the energy levels under symmetry lowering at the phase transition, the authors assign PB2
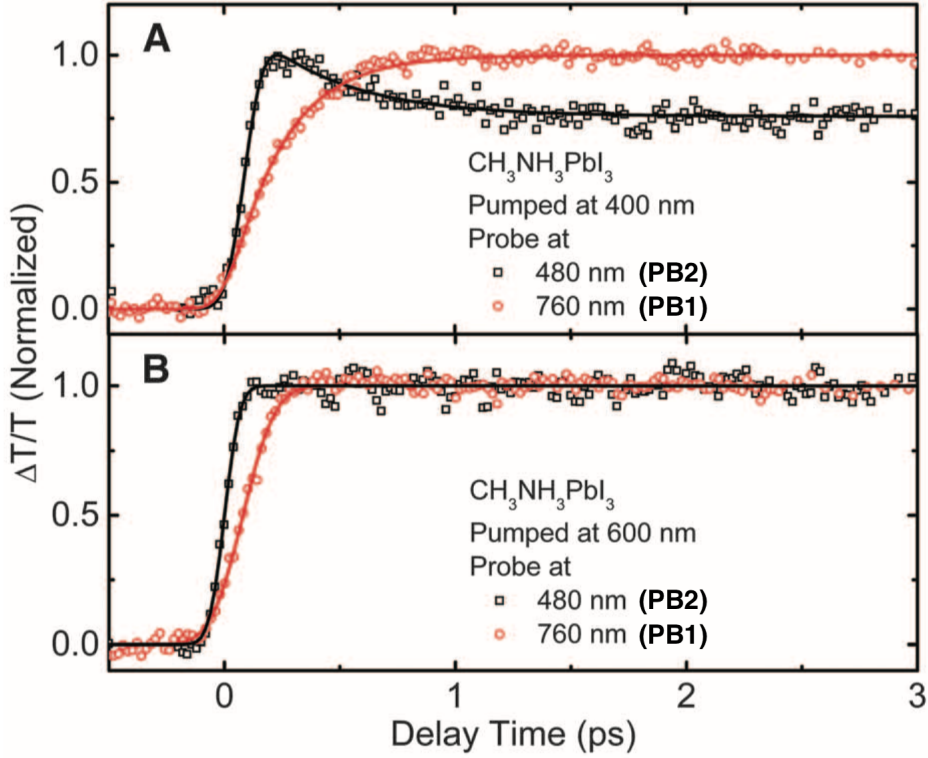
Figure 2.6 – Normalized PB kinetics at 480 nm (PB2) and 760 nm (PB1) in a short time range show the intervalence band hot-hole cooling for MAPbI$_3$ film (in vacuum) after excitation at (**A**) 400 nm (3.1 eV) and (**B**) 600 nm (2.1 eV). Reproduced from [3] with permission, Copyright American Association for the Advancement of Science.

to an almost degenerate transition from VB2 to CB1 at the R-point with a small contribution from VB1 to CB1 at the M-point (the energy difference between the two transitions is ~50 meV at room temperature).

In summary, previous TAS experiments on MAPbI$_3$ show that the electron and hole dynamics can be disentangled by probing higher energy transitions at the R-point by TAS which is the strategy we aim at implementing in MAPbBr$_3$ where these transitions fall in the UV.

We have chosen the PB labelling such that a natural analogy can be drawn between the MAPbI$_3$ and MAPbBr$_3$ transient responses. In Figure 2.9, the UV-Vis and differential transmission spectra of MAPbBr$_3$ (blue curve) and MAPbI$_3$ (red curve) are overlapped. PB2 in MAPbBr$_3$ and MAPbI$_3$ coincides with the local maximum in the UV-Vis spectrum at ~3.44 eV in MAPbBr$_3$ and ~2.58 eV in MAPbI$_3$ so that we naturally assign PB2 in MAPbBr$_3$ to a transition from VB2 to CB1 at the R-point. While in MAPbI$_3$ the PA is observed between PB2 and PB3 at 2.9 eV, it appears in MAPbBr$_3$ (3.7 eV) only at short time delays within the setup IRF (Figure 2.2C). Besides, PB3 is at the energy position of a shoulder in the MAPbBr$_3$ UV-Vis spectrum
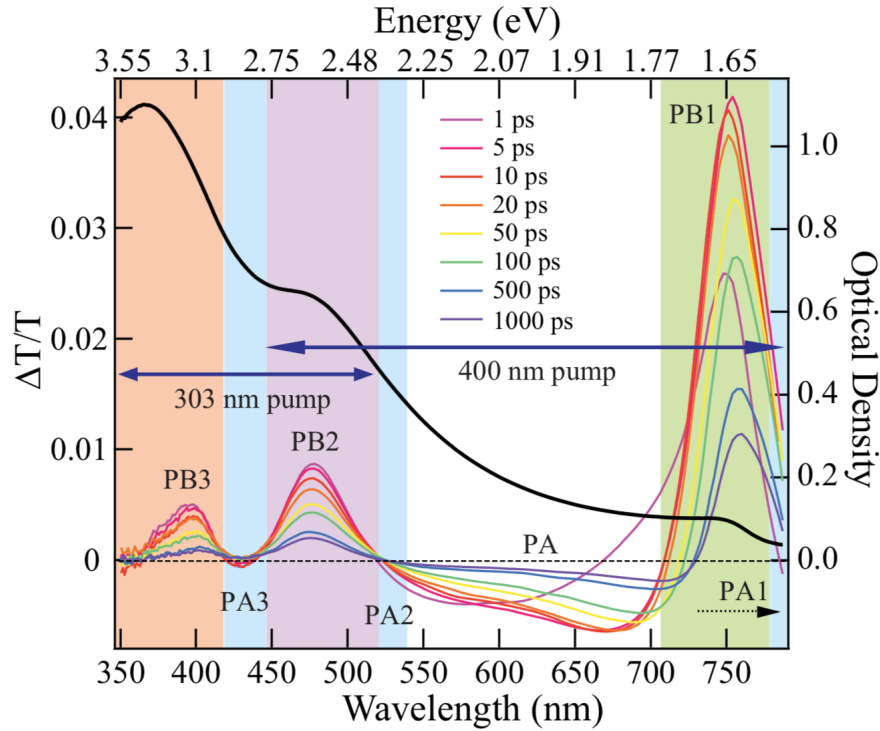
Figure 2.7 – Transient spectra measured in the $350-800$ nm probe range for different time delays between pump and probe beams on MAPbI$_3$. Visible and near-UV parts of the spectrum here are taken with different excitation densities and matched to each other at the PB2 peak for ≥ 1 ps time delays to account for differences in photoexcitation levels. The colored bands are used to indicate the positions of various features: bleaches PB1 (green), PB2 (purple), PB3 (orange), the broad long-lived PA (white) and the short-lived PA signals (blue) adjacent to PB bands. Also shown is the steady-state UV-Vis linear absorption spectrum (black curve referring to the vertical right axis). Reproduced with permission (License # RNP/18/SEP/007900).

while in MAPbI$_3$, PB3 does not correspond to any particular feature. This is supported by the ellipsometry data of MAPbI$_3$ where no resonance is found between the two local maxima of the UV-Vis spectrum at ~2.58 and 3.4 eV [4, 114, 130]. However, a transition is possibly at this energy position in MAPbI$_3$ which does not have a large oscillator strength based on its energy position between the two local maxima of the UV-Vis spectrum similarly to PB3 in MAPbBr$_3$. PB4 has not been observed in any experiment on MAPbI$_3$ so far because of the lack of high probe photon energy in the deep-UV.

We now compare the kinetics of the PB in MAPbI$_3$ and MAPbBr$_3$. The kinetics of PB1 and PB2 in MAPbI$_3$ reported in the literature are inconsistent: Xing and coworkers find similar decays [3] while Anand and coworkers find a significantly longer decay time for PB1 than PB2. We compare the kinetics of PB1 and PB2 in MAPbBr$_3$ in Figure 2.10. A slower decay is observed for PB1 when normalized at time zero (Figure 2.10a). However, the same decay time is observed
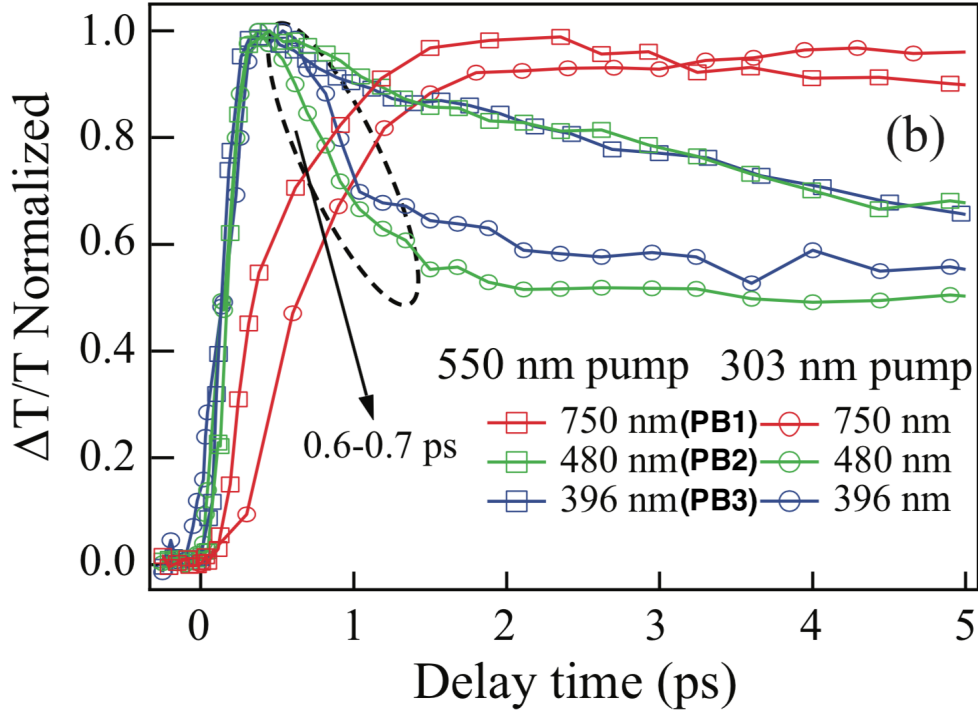
Figure 2.8 – Normalized kinetics at the PB extrema following excitation with different pump photon energies. The PB labelling is the same as in Figure 2.7. Reproduced with permission (Licence # RNP/18/SEP/007901).

on the long time delays when the time traces are normalized on the nanosecond timescale (Figure 2.10b). This is fully consistent with the results by Anand on MAPbI$_3$ [5]. Such behaviour shows that PB1 and PB2 in MAPbBr$_3$ are sensitive to electron-hole recombination at the band gap which is given by the longest time constant they have in common. As shown earlier, PB2 in MAPbBr$_3$ has a bimodal rise (green curve in Figure 2.4) which indicates a sensitivity to charge-carrier cooling while PB2 in MAPI$_3$ exhibits a prompt rise independent of the pump photon energy (green curve in Figure 2.8). Since PB2 in MAPbI$_3$ has been consensually assigned to the transition VB2→CB1 at the R-point [3, 122], it is surprising that no electron cooling has been observed so far from the rise time. This is consistent with the recent results by Richter and coworkers which show that electron thermalization in MAPbI$_3$ populates the VB and CB extrema in less than 85 fs with a pump photon energy at the band gap (~1.7 eV) and becomes sub-10 fs at ~2.1 eV [126]. This is within the IRF of the experiments performed earlier by others which may explain the insensitivity of PB2 to electron cooling [3, 5]. In our study of MAPbBr$_3$, the bimodal rise of PB2 is due to a slow electron cooling time to the R-point in ~ 400 fs (green curve in Figure 2.4 inset). This result shows a fundamental difference between MAPbBr$_3$ and MAPbI$_3$ with respect to the electron cooling mechanism in the CB while high pump photon excess energies have been used in some experiments on MAPbI$_3$ [5] which do not show a slow electron cooling. These results pave the way to a more systematic study of the electron cooling
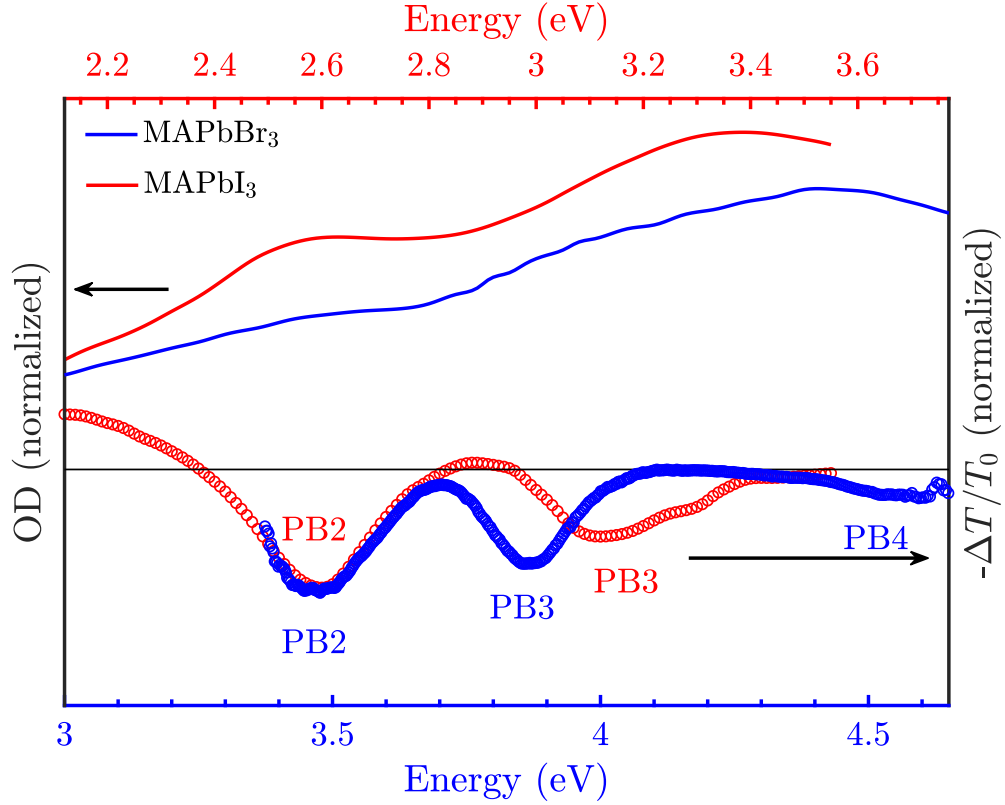
Figure 2.9 – Overlap of MAPbI$_3$ (red) and MAPbBr$_3$ (blue) UV-Vis spectra and differential transmission. Continuous lines are UV-Vis spectra and circles are differential transmission spectra ($-\Delta T/T_0$) 1 ps after excitation (normalized at PB2 minimum). The UV-Vis spectrum of MAPbI$_3$ is adapted from [4]. The differential transmission spectrum of MAPbI$_3$ is reproduced from [5].

time in MAPbBr$_3$ at different pump photon energies and excitation densities thanks to the sensitivity of PB2 to electron cooling. It is also promising in the field of photovoltaics where a slow charge carrier cooling is needed to drive the charge injection at interfaces.

The assignment of the transition involved at PB3 in MAPbBr$_3$ can be clarified in the light of recent temperature dependent ellipsometry measurements by Chi and coworkers [6] (Figure 2.11). The energy position of PB3 in the differential transmission of MAPbBr$_3$ is shown with a vertical dashed line. A resonance is found at PB3 which undergoes a pronounced narrowing when the temperature decreases similarly to the resonance at the optical band gap around 2.3 eV. This is compatible with the predicted evolution of the full width at half maximum (FWHM) of an exciton-phonon optical transition with temperature and shows a similar coupling mechanism and that an exciton may be present at PB3 [6]. Previous ellipsometry studies by Leguy and coworkers supported by quasiparticle self-consistent GW calculations have assigned the transition at PB3 to VB1→CB1 at the M-point which is a saddle point in the BZ [114]. This transition has an excitonic phase [131] of $\sim \pi/2$ compatible with the formation of
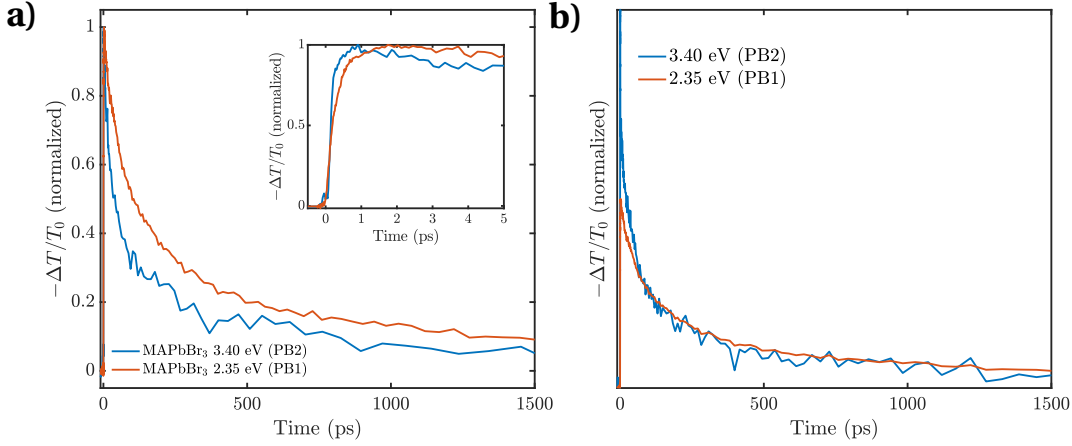
Figure 2.10 – a) Comparison of the time traces at the optical band edge in the Visible (PB1 at 2.35 eV, orange) and in the UV (PB2 at 3.40 eV, blue) with excitation at 3.1 eV at the same fluence (excitation density 1.3×10^{17} cm^{-3}). b) Comparison of the time traces normalized on the longest time constant. The sign of the time traces has been flipped for convenience.

an exciton[4] [114]. PB3 exhibits positive wings within the IRF in the differential transmission (Figure 2.2b) which resemble CS of an excitonic transition, compatible with this interpretation. In addition, PB3 should not involve states which are populated by the pump at 3.1 eV since its prompt rise time indicates that it is not sensitive to PSF and carrier cooling which excludes a transition at the R-point. Hence, these studies and our results support that PB3 is related to an exciton, formed at the M-point between VB1 and CB1 as suggested in other works [114, 116]. PB3 itself is then the bleaching and screening of an excitonic transition which recovers with the same kinetics as the electron-hole pair recombination at the band gap as observed in Figure 2.4 (red and green curves). Since the single particle states involved in the exciton formation are not populated at our pump energy, PB3 is due to the damping of the exciton oscillator strength from the CS induced by the photogenerated charge carriers [81, 82].

PB4 is expected to have a small excitonic contribution according to the critical point analysis of the ellipsometry data [114]. Previous calculations have assigned this transition between VB1 and CB1 at the X-point in the BZ [114, 116]. We can only observe a weak bleach in Figure 2.2 because PB4 involves single particle states which are not directly populated upon 3.1 eV excitation. However, the underlying exciton oscillator strength can be damped due to CS which leads to PB4 within the IRF of the setup similar to PB3. The fact that PB4 recovers more slowly than PB2 and PB3 may be due to hot holes scattering from the $\Gamma - R$ valley ending in the X valley (Figure 2.1). In fact, the topology and energy of this valley is not really well known because of the lack of accurate theoretical calculations in this region of the BZ.

---

[4]The excitonic phase provides information about the topology of the bands close the energy minimum between them [132, 133]. When for instance the CB and VB reach their minimum and maximum respectively at the same point in the BZ, this is a favorable band dispersion for the formation of an exciton with similar hole and electron group velocities. The associated excitonic phase in this band configuration is $\pi/2$.
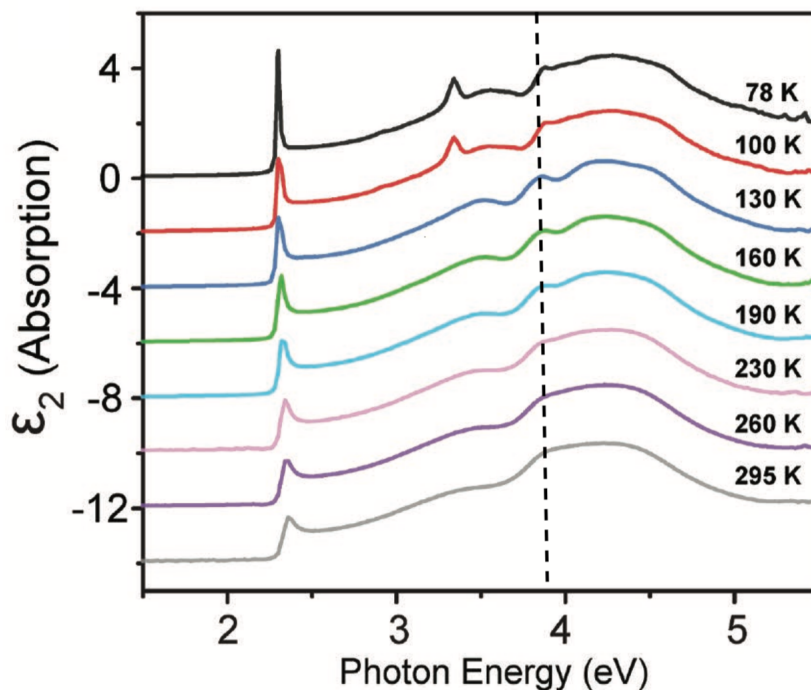
Figure 2.11 – Imaginary part of the dielectric constant in MAPbBr$_3$ single crystal measured at different temperatures. The energy position of PB3 in MAPbBr$_3$ is shown by a vertical dashed line. Adapted with permission from [6] (Licence # 4432070660202).

2.2.2 Absence of first order decay rate

The fact that first order kinetics does not fit the data shows that exciton recombination and trapped-assisted recombination are negligible in our MAPbBr$_3$ thin film. The former is due to an ultrafast screening of electron-hole pairs which prevents the formation of excitons [82] while the latter is due to the low defect density which renders these HOIP attractive for optoelectronic applications [101, 134].

Conclusion

In conclusion, we have been able to assign the high energy interband transitions of MAPbBr$_3$ by differential transmission in the deep-UV. The transition at ~3.5 eV is due to the interband transition from VB2 to CB1 at the R-point, the transition at ~3.9 eV is due an exciton formed between VB1 and CB1 at the M-point. We have assigned the transition at ~4.5 eV to an exciton at the X-point with a weak oscillator strength. The summary of our assignment of these transitions involved in PB2, PB3 and PB4 in MAPbBr$_3$ is provided in the schematic band structure of Figure 2.1. In Chapter 4, the MAPbBr$_3$ perovskite layer is put in contact with an electron acceptor, namely mesoporous anatase TiO$_2$. Although charge injection

is unambiguously observed from the PB in anatase TiO$_2$, PB2 and PB4 recovery times are unchanged so that the injection cannot be used to infer the assignment provided in this chapter.

3 Photodynamics in colloidal suspensions of ZnO nanoparticles

Summary

In this Chapter, the charge carrier-phonon cooling in ZnO nanoparticles (NPs) is investigated under different pump photon excess energies and fluences. The charge-phonon cooling time is compared with the *ab initio* calculations performed by Zhukov and coworkers [7, 8, 21]. The transient spectrum after the cooling shows a strong dependence with excitation fluence when free charge carriers are generated above the band gap while no dependence is observed when excitons are resonantly generated. This is in agreement with the orders of magnitude difference in Coulomb screening between free charge carriers and excitons. The shape of the transient absorption spectrum under different photoexcitation densities above the optical band gap is modelled with the theory developed by Banyai and Koch in the eighties [22] which provides an excellent agreement.

Introduction

ZnO is a II-VI direct band gap insulator with a single particle band gap of ~3.37 eV at room temperature which exhibits a bound exciton with a binding energy of ~60 meV in the bulk [135]. This is the largest binding energy in the II-VI compounds but by far not the largest for all semiconductors since for example, CuCl and CuO have exciton binding energies around 190 and 150 meV respectively [136]. Materials with band gaps falling in the ultraviolet (UV) have triggered interest since they can be used as transparent optoelectronic materials in the Visible [137, 138]. Among them, the ZnO wurtzite polymorph discussed in this Chapter occurs naturally at room temperature and has been widely applied in photovoltaics [139] and light-emitting devices [140] among other applications [141].

Wurtzite ZnO has a hexagonal lattice with the zinc atoms tetrahedrally coordinated to oxygens. The Zn-O bond has a considerable degree of polarity which is caused by the strong electronegativity of the oxygen together with the rather low electronegativity of zinc. The bond ionicity is 0.616 on the Phillips scale [142]. Therefore, the zinc and oxygen atoms in ZnO may well be

considered as ionized Zn^{2+} and O^{2-} although the bond covalence is not negligible.

The conduction band (CB) close to the Γ-point has s-symmetry because it arises from the empty $4s$ levels of Zn^{2+} and from the lowest antibonding sp^3 states [143]. The valence band (VB) originates from the occupied $2p$ states of O^{2-} or the energetically highest bonding sp^3 states. The VB is energy split due to the crystal-field and the spin-orbit coupling which have the same order of magnitudes [144]. This becomes clear in low temperature spectroscopy experiments on single crystals [145] while the experiments performed at room temperature in this Chapter are insensitive to this effect.

As an electron or a hole is promoted to an excited state in ZnO, its dynamics is relevant for a range of optoelectronic applications including photocatalysis [146] and photovoltaics [147]. Historically, ZnO has played a key role in the development of dye-sensitized solar cells (DSSCs) as electron transport material (ETM) [148]. However, it is not as used as anatase TiO_2 because of the difficulty to control precisely its stoichiometry in the NP form [149] leading to rather large defect densities.

In this Chapter, the transient optical response of a colloidal suspension of ZnO NPs is investigated by transient absorption spectroscopy (TAS) in the UV under above band gap and resonant excitation. In particular, the effect of the pump photon energy on the charge carrier cooling time is observed as well as the effect of generating increasingly large populations of excitons or free charge carriers on the transient response in the spectral region of the optical gap.

3.1 Mechanism and theory of electron cooling

In transition-metal oxide (TMO) insulators, the main mechanism of excited electron (hole) energy-loss is due to the electron-phonon coupling contrary to metals in which the available phase-space at the Fermi level allows efficient electron-electron scattering [7]. According to Fermi's golden rule [150], the probability per unit time of the electron (hole) transition between two states i and j mediated by the electron-phonon (hole-phonon) coupling is determined by the equation [151],

$$P^{\nu}_{k,i;k,\mathbf{k}+\mathbf{q},j} = \frac{2\pi}{\hbar} |\langle \mathbf{k}, i | \Delta V_{\mathbf{q},\nu} | \mathbf{k}+\mathbf{q}, j \rangle|^2 \delta(e_{\mathbf{k}+\mathbf{q},j} - e_{\mathbf{k},i}) \tag{3.1}$$

with $|\mathbf{k}, i\rangle$ and $|\mathbf{k}+\mathbf{q}, i\rangle$ the electronic states participating in the transition at crystal momentum $\mathbf{k}$ accompanied by the absorption or emission of a phonon with momentum $\mathbf{q}$ and polarization ν. The operator $\Delta V_{\mathbf{q},\nu}$ measures the variation of the self-consistent potential in the crystal caused by the displacement mode of the phonon. The methods of calculation of this matrix element have been extensively discussed elsewhere [152]. In equation 3.1, the energy of the phonon is neglected since it is small compared to the energies of the electronic states $e_{\mathbf{k}+\mathbf{q},j}$ and $e_{\mathbf{k},i}$, the so-called "quasi-elastic approximation". The integration over all crystal momenta of equation 3.1 provides the probability of an electron (hole) to leave the state $|\mathbf{k}, i\rangle$ by losing

the energy $\hbar\omega_{\mathbf{q}}^{\nu}$ of the released phonon,

$$\phi_{\mathbf{k},i}(\omega) = \frac{2\pi}{\hbar} \sum_j \sum_i \int_{BZ} \delta(\omega_{\mathbf{q}}^{\nu} - \omega) |\langle \mathbf{k}, i | \Delta V_{\mathbf{q},\nu} | \mathbf{k} + \mathbf{q}, j \rangle|^2 \delta(e_{\mathbf{k}+\mathbf{q},j} - e_{\mathbf{k},i}) d^3\mathbf{q} \tag{3.2}$$

The function $\phi_{\mathbf{k},i}(\omega)$ differs only by a constant from the Eliashberg function $\alpha^2 F_{\mathbf{k},i}(\omega) = \frac{\hbar\phi_{\mathbf{k},i}(\omega)}{2\pi}$ which determines the electron-phonon (hole-phonon) strength parameter [153],

$$\lambda_{\mathbf{k},i} = 2 \int \frac{\alpha^2 F_{\mathbf{k},i}(\omega)}{\omega} d\omega. \tag{3.3}$$

The integration of expression 3.2 in frequency ω from 0 to the maximum phonon frequency provides the rate of electron-phonon (hole-phonon) relaxation,

$$\Gamma_{\mathbf{k},i} = \int d\omega \phi_{\mathbf{k},i}[1 + 2n(\omega, T) + f(\omega + e_{\mathbf{k},i}, T) - f(\omega - e_{\mathbf{k},i}, T)] \tag{3.4}$$

which includes phonon emission and absorption, $n(\omega, T)$ is the Bose-Einstein function for phonons and $f(\omega, T)$ is the Fermi-Dirac (FD) function for electrons (holes). The inverse of $\Gamma_{\mathbf{k},i}$ is the time of electron (hole) relaxation $\tau_{\mathbf{k},i} = \hbar/\Gamma_{\mathbf{k},i}$ which means that $\tau_{\mathbf{k},i}$ measures the time an electron (hole) can reside in the state $|\mathbf{k}, i\rangle$ before it moves to another single-particle state due to phonon emission or absorption.

Another important parameter of the cooling process is the energy loss time τ_{en} which is the time necessary for an electron (hole) to fall down to the bottom of the CB (top of the VB) via the repeated emission of phonons. For a state $|\mathbf{k}, i\rangle$, it is determined by the first moment of the probability function $\phi_{\mathbf{k},i}$,

$$\Delta e_{\mathbf{k},i} = \int d\omega \phi_{\mathbf{k},i}(\omega)\omega[2n(\omega, T) + 1]. \tag{3.5}$$

For the TAS experiments, we are sensitive to the energy and not to the crystal momentum $\mathbf{k}$ so that the relevant physical quantities are momentum averaged which provides for the electron-phonon (hole-phonon) coupling parameter,

$$\lambda(\epsilon) = \frac{1}{N(\epsilon)} \sum_i \int d^3\mathbf{k} \delta(e_{\mathbf{k},i} - \epsilon) \lambda_{\mathbf{k},i}/\Omega_{\mathbf{k},i} \tag{3.6}$$

the relaxation rate,

$$\Gamma(\epsilon) = \frac{1}{N(\epsilon)} \sum_i \int d^3\mathbf{k} \delta(e_{\mathbf{k},i} - \epsilon) \Gamma_{\mathbf{k},i}/\Omega_{\mathbf{k},i} \tag{3.7}$$

and the energy loss,

$$\Delta e(\epsilon) = \frac{1}{N(\epsilon)} \sum_i \int d^3\mathbf{k} \delta(e_{\mathbf{k},i} - \epsilon) \Delta e_{\mathbf{k},i}/\Omega_{\mathbf{k},i} \tag{3.8}$$

with $N(\epsilon)$ the density of electronic states at the energy ϵ and with the probability normalization integral $\Omega_{\mathbf{k},i} = \int d\omega \phi_{\mathbf{k},i}(\omega)$. From $\Gamma(\epsilon)$ and $\Delta e(\epsilon)$, one can calculate the rate of energy loss as $\Delta e(\epsilon)/\tau(\epsilon) = \Delta e(\epsilon)\Gamma(\epsilon)$. Finally, the time to release the total excess energy (which is defined as the energy of the excited electron (hole) with respect to the CB minimum (VB maximum)) is,

$$\tau_{en}(\epsilon) = \int_0^\epsilon \frac{dE}{\Delta e(E)\Gamma(E)} \tag{3.9}$$

The energy loss time $\tau_{en}(\epsilon)$ and the time of electron (hole) relaxation $\tau(\epsilon)$ are the two important physical quantities that describe the cooling time of electrons in a given material[1]. The former measures the time it takes for an electron or hole to transfer all its excess energy ϵ into the phonon bath while the latter measures the time an electron (hole) remains on average in a single particle state with excess energy ϵ.

Zhukov and coworkers have computed $\tau(\epsilon)$ and $\tau_{en}(\epsilon)$ for the electrons in ZnO by *ab-initio* density functional theory (DFT) calculations in a series of articles which we briefly summarize here [7, 8, 21]. In the articles [7] and [8], the authors identified two electron-phonon cooling regimes depending on the electron excess energy with respect to the highest phonon energy. At high electron excess energies, the whole phonon dispersion will act on the electron cooling[2] while below the cutoff of the highest energy phonon, only phonons which have a lower energy than the electron excess energy will play a role in the cooling. Figure 3.1 presents the average electron relaxation and energy-loss time in these two situations where the electron excess energy is less (Figure 3.1a) or exceeds (Figure 3.1b) the highest phonon energy involved in the cooling. For high electron excess energies (panel b), the energy loss-time spans from 100 to 500 fs depending on the excess energy. In contrast, for electron excess energies in the range of a few tens of meV (panel a), the energy loss time can span a very large range from sub-100 fs up to 10 ps with a rapid increase below an excess energy of ~20 meV due to the reduction of the available phonon phase-space. The differential transmission experiments presented in this Chapter are with an excess energy of several hundreds of meV which falls into the high excess energy regime above the cutoff (panel b). The conditions of low excess energy are difficult to achieve in ZnO since both free electron-hole pairs and excitons are generated close to the optical band edge, the latter not being accounted for in the model. The energy loss time in ZnO is rather long with respect to other TMOs such as anatase TiO_2 in which the cooling occurs in less than 50 fs with an excess energy of ~0.85 eV [154] in contrast to the ~200 fs predicted for ZnO at the same excess energy. In their latest article [21], the authors have computed the cooling time of the holes which is typically 3 times faster than the electron cooling time meaning that they do not limit the overall cooling time of the system

Now, we establish a connection between the relaxation and energy-loss times and the spectro-

---

[1] The radiative recombination of charges is not considered here while it is a mechanism of energy release for the electrons. Our interest is only on the electron-phonon cooling timescale which is of the order of the picosecond while the radiative recombination of electrons and holes acts on the 100 ps timescale and can be neglected during the cooling time.

[2] At the condition that the modes have the correct symmetry.
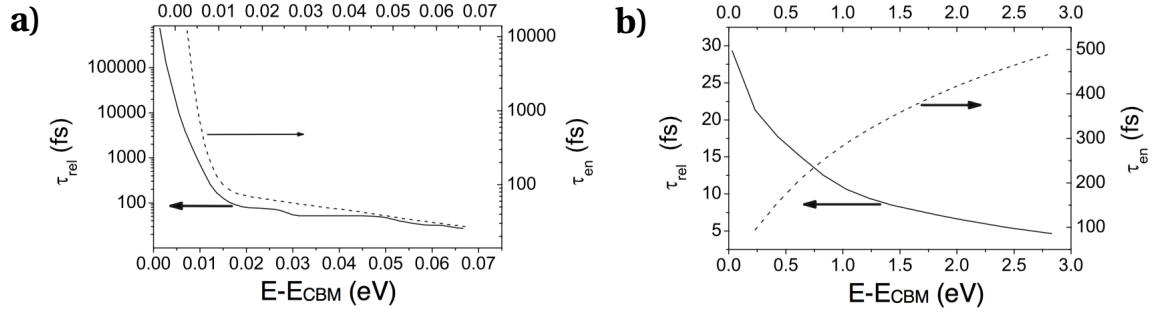
Figure 3.1 – Dependence of the energy relaxation τ_{rel} and energy-loss time τ_{en} on the excess energy of an excited electron with respect to the CB minimum ($E - E_{CBM}$) of ZnO. Reproduced with permission from [7].

scopic observables in TAS. After excitation and thermalization, a distribution of hot electrons sets up in the CB of the semiconductor which gives rise to a high-energy tail photobleach (PB) close to the optical band gap as observed in GaAs [155], MAPbI$_3$ [25], MAPbBr$_3$ [101] (see Figure 3.9a for an illustration of the high energy tail PB due to hot carriers in ZnO). It corresponds to the high energy tail photoluminescence observed in typical semiconductors such as GaAs during the carrier cooling because of the hot electron-hot hole radiative recombination [156]. In the parabolic band approximation, which is appropriate for ZnO [157], the probe photon is sensitive to the population of electrons in the CB around the Γ-point[3]. In this simple band topology, a single probe photon energy connects single particle states in the VB and in the CB with a unique crystal momentum modulus[4]. This means that a time trace at a single probe photon is sensitive to the charge population at a specific crystal momentum modulus in reciprocal space. Thus, the time constant of the decay is connected to the electron or hole *relaxation rate* since the corresponding probe photon is bleached as long as electrons or holes remain in this single particle state[5]. In practice, the relaxation rate it rather difficult to obtain by TAS since thermalization occurs on sub-100 fs timescales which already populates many of the band states before the cooling occurs.

The electron-phonon coupling leads to the excess energy to be transferred from the electrons and holes to the lattice degrees of freedom (DOFs). Hence, the charge-carrier *energy loss rate* is related to the time taken by the PB minimum to move from its initial position at the pump photon energy to the optical band edge where the carriers accumulate before they recombine. There are several methods to estimate the energy loss rate from this spectral movement in the TAS. A few groups have fitted a Maxwell-Boltzmann (MB) distribution to the high energy tail of the PB which gives access to the average carrier temperature over time

---

[3]At large crystal momentum, the joined density of states (DOS) between the VB and the CB becomes low which provides negligible TAS signals. In general, the transient signal is strong in the region of van Hove singularities.

[4]Along a given reciprocal space direction from the Γ-point, a photon with energy $\hbar\omega$ can only be absorbed at crystal momenta $+k$ and $-k$ so that the condition $E_{CB}(+k/-k) - E_{VB}(+k/-k) = \hbar\omega$ can be fulfilled.

[5]Under the assumption that there is no photoinduced absorption (PA). See Figure 1.3 for an illustration, the bleached probe photons are more and more towards the red while the electron and hole populations cool down to their band extrema.

[101, 158]. However, this approach becomes rather unreliable at low excitation densities for which the contribution of the MB distribution is more difficult to identify. More recently, lifetime density method (LDM) provided a way to estimate the time constants of the decays and spectral movements in broadband TAS [159, 160]. The main difficulty is that the fitting procedure with a large number of time constants at the core of the method relies on the use of penalty parameters for the algorithm to converge which may be difficult to determine accurately in practice [161]. Instead, we have used a much simpler approach in which we follow the transient signal of constant amplitude to provide an estimate of the cooling time (energy-loss rate). This approach is valid as long as the electron-hole recombination does not compete with the cooling. Previous time-resolved photoluminescence studies on ZnO have measured the radiatiave recombination rate of the order of 300 ps [162, 163]. Since we observe cooling times shorter than 2 ps, this method is applicable to determine the *energy-loss time* at different pump photon energies and compare the results with the prediction by Zhukov and coworkers [7, 21] (see section 3.3.3).

3.2 Evolution of the optical spectrum under electron-hole pair excitation: quasi-equilibrium regime

After the cooling, the electrons and holes have accumulated at the band extrema around the Γ-point and get trapped or recombine. This is similar to a quasi-equilibrium regime on the timescale of several tens of picoseconds. A simple theory has been developed by Banyai and Koch in the eighties to model the evolution of the UV-Vis spectrum of a semiconductor under continuous laser irradiation above the optical gap [22, 26, 27]. The excited state absorption spectrum represents the optical response of the quasi-equilibrium electron and hole distribution in the system and is derived from the Elliott formalism [112]. In this section, we briefly summarize the important steps to compute the excited state absorption spectrum which we use to model the spectral traces of ZnO in the UV after cooling of the carriers.

The absorptive properties of the material are given by the imaginary part of the dielectric constant (ϵ_2) which depends on the exciton principal quantum number n, the exciton binding energy E_R and the excitation density N through the screening parameter g according to [22],

$$\epsilon_2 = \bar{\epsilon} \tanh\left(\frac{1}{2}\left(\frac{\widetilde{\omega}}{\widetilde{T}} - \widetilde{\mu}_e - \widetilde{\mu}_h\right)\right) \sum_{l=1}^{g^{1/2}} \pi \delta_{\widetilde{\Gamma}}\left(\widetilde{\omega} + \left(\frac{1}{l} - \frac{l}{g}\right)^2\right) \times$$

$$\frac{2(g-l^2)(2l^2-g)}{l^3 g^2} \prod_{n=1,n\neq l}^{\infty} \frac{n^2[n^2l^2-(g-l^2)^2]}{(n^2-l^2)(n^2l^2-g^2)} + \int_0^{\infty} dx\, x^{1/2} \prod_{n=1}^{\infty}\left(1 + \frac{2gn^2-g^2}{(n^2-g)^2+n^2g^2x}\right)\delta_{\widetilde{\Gamma}}(x-\widetilde{\omega})$$

(3.10)

with $\bar{\epsilon} = \frac{r_{cv}^2}{2\pi a_0^3 E_R}$, $\widetilde{\omega} = (\hbar\omega - E_g)/E_R$, $\widetilde{T} = k_B T/E_R$, $\widetilde{\Gamma} = \Gamma/E_R$, $\widetilde{\mu}_{e/h} = (\mu_{e/h} - E_g/2)/k_B T$ and $g = 12/\pi^2 a_0 \kappa$. In equation 3.10, r_{cv} is the dipole matrix element between the VB and the CB which is considered as independent on the k-point, a_0 is the exciton Bohr radius, $\alpha = h, e$ for

the hole or the electron respectively. The screening length κ which provides g is determined from,

$$(a_0\kappa)^2 = \frac{4}{\pi}\widetilde{T}^{1/2}\int_0^\infty dx\,x^{1/2}\sum_\alpha \widetilde{m}_\alpha^{3/2}f(x-\widetilde{\mu}_\alpha)[1-f(x-\widetilde{\mu}_\alpha)], \tag{3.11}$$

where $\widetilde{m}_\alpha = m_\alpha/m$ and $m^{-1} = m_e^{-1} + m_h^{-1}$. The chemical potential μ_α is that of an ideal Fermi gas which is connected to the excitation density N as,

$$\frac{1}{2\pi^2}(\widetilde{T}\widetilde{m}_\alpha)^{3/2}\int_0^\infty dx\,x^{1/2}f(x-\widetilde{\mu}_\alpha) = a_0^3 N_\alpha \tag{3.12}$$

with $f(x-\widetilde{\mu}_\alpha) = 1/(e^{\beta(\widetilde{\epsilon}_\alpha(\mathbf{k})-\widetilde{\mu}_\alpha)} + 1)$ the FD distribution and $\epsilon_\alpha(\mathbf{k}) = \hbar^2 k^2/2m_\alpha + E_g^0/2$ the electron or hole energy. The energy gap E_g in this context is given by the renormalized band gap energy which, in the Hulthen approximation below the Mott density, is given by [164],

$$\frac{E_g - E_g^0}{E_R} = -1 + (1 - \frac{1}{g})^2 \tag{3.13}$$

The computed excited state spectrum is broadened by the hyperbolic function $\delta_{\widetilde{\Gamma}}(x) = 1/(\pi\widetilde{\Gamma}\cosh(x/\widetilde{\Gamma}))$ to account for the experimental temperature and sample morphology effects on the spectrum. From the binding energy and the ground state band gap E_g^0 determined by the fitting with the Elliott formula in section 3.3.1, we can model the evolution of the UV-Vis spectrum with various excitation densities at quasiequilibrium (Figure 3.4a). This in turn provides a simulation for the transient transmission spectrum. The difference in absorption coefficient between the ground state and the excited state $\Delta\alpha$ is obtained directly from ϵ_2 in equation 3.10. The change in refractive index Δn is obtained by Kramers-Kronig transformation of the dielectric constant [165]. Finally, the differential transmission $\frac{-\Delta T(E)}{T_0(E)}$ at probe photon energy E is computed as [25],

$$\frac{-\Delta T(E)}{T_0(E)} = -l\Delta\alpha(E) + 2\frac{n_g - n(E)}{[n(E)^2 + n(E)][n_g + n(E)]}\Delta n(E) \tag{3.14}$$

where l is the sample thickness and n_g the solvent refractive index (in our case ethanol, $n_g = 1.36$ on average in the spectral range of interest [166]). Simulations based on the differential transmission computed with equation 3.14 are performed in section 3.3.2 and compared to the experimental spectral traces following excitation at 4.66 eV at different fluences.

3.3 Results

3.3.1 Ground state optical properties of ZnO - Elliott formula

The UV-Vis spectrum of a colloidal suspension of ZnO NPs suspended in ethanol (~100 mM concentration) is shown in Figure 3.2a (blue circles). It exhibits an absorption maximum around 3.45 eV which corresponds to a bound exciton resonance. We have applied the convo-

luted Elliott formula C.2 to determine the band gap and the exciton binding energy in the ZnO NPs (red curve in Figure 3.2a). The fitted parameters are given in Table 3.1. At the absorption edge, the experimental spectrum is sharper than in the fitting while a broader exciton line is observed in the experimental spectrum. There are two possible reasons for this effect which we did not account for in our fitting. The first reason is that ZnO is anisotropic and gives birth to two excitonic progressions at the optical band gap which may broaden the experimental exciton line [167]. We have tried including a second exciton oscillator in the Elliott formula used for the fitting but we obtained unphysical exciton binding energies. The other possibility is that there are other sources of broadening that we did not account for by a single experimental convolution with the *sech* function. For instance, the retrieved larger exciton binding energy of 89 meV than in single crystals [168, 169, 170] shows that we are in a regime where the exciton resonance depends on the NP size [171] and that the width of the resonance is expected to follow the inhomogeneous distribution of NP sizes[6]. The exciton Bohr radius is of the order $1.8 - 2.2$ nm [172, 173] which excludes quantum confinement for our size of NPs. To explain the larger binding energy, the effect of the surface screening properties is more important which increases the average exciton binding energy [174].

We note that the Elliott formula gives an excellent agreement with the experimental UV-Vis spectrum in the region above the band gap (Figure 3.2a). This shows that the VB and CB of ZnO do not deviate from the ideal parabolicity even at crystal momentum points which are rather far from the Γ-point in agreement with angle-resolved photoemission spectroscopy (ARPES) studies[7] [176, 177].
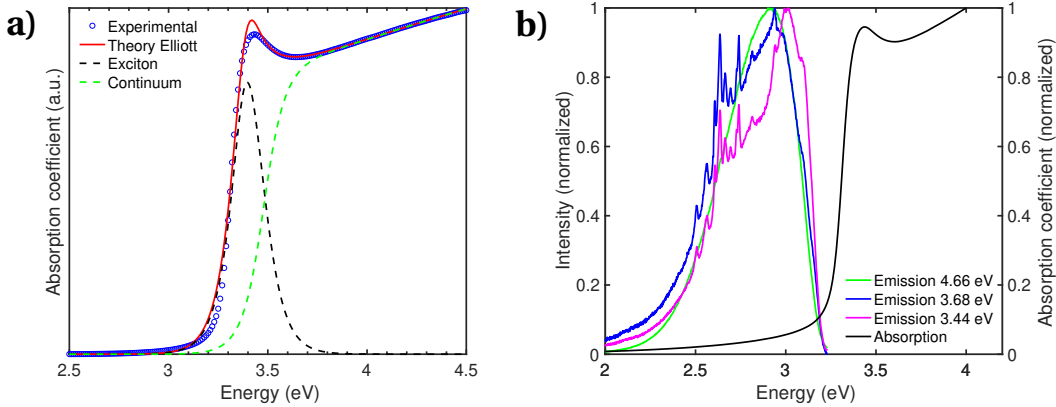
Figure 3.2 – a) Absorption coefficient of ZnO NPs (blue circles) with the fitting obtained from the convoluted Elliott formula C.2 (red line). The fitted absorption coefficient is decomposed into the excitonic (black dashed line) and continuum (green dashed line) contributions. b) Absorption coefficient (black curve) and emission spectra (colored curves) at the different pump photon energies used in the TAS experiments.

---

[6]See for instance the Ref. [149] in which the same batch of NPs with average radius 16.5 nm and size dispersion of 8.8 nm full width at half maximum (FWHM) has been characterized which contributes to the exciton broadening.

[7]Compare for instance with the lead perovskite spectrum for which the fitting with the Elliott formula deviates from the experimental spectrum approximately 0.2 eV above the optical gap due to the non-parabolicity of the VB and CB [117, 175].

Table 3.1 – Parameters of the Elliott formula used for the fitting of the ZnO NPs absorption coefficient in Figure 3.2 with the Elliott formula. E_b is the exciton binding energy, E_g the band gap energy and Γ the broadening.

parameter	E_b (meV)	E_g (eV)	Γ (meV)
value	89 ± 1	3.478 ± 0.002	68 ± 1

The absorption and emission spectra of the ZnO NPs are overlapped in Figure 3.2b. The sharp lines in the emission spectra are due to the cold lines of the emission lamp. The emission spectra are measured at the same pump photon energies as in the TAS experiments in section 3.3.3. For every excitation photon energy, a broad emission is observed below the optical gap with a large Stokes shift of ~0.5 eV. For the excitation resonant with the exciton at 3.44 eV, a pronounced narrowing of the emission is observed which is consistent with an excitonic emission becoming dominant over the free electron-hole recombination [135, 178].

3.3.2 Effect of the pump fluence with 4.66 eV pump photon energy

Transient absorption spectra measured in colloidal suspensions of ZnO NPs are shown in Figure 3.3 for increasing excitation densities with 4.66 eV pump photons. At the lowest excitation density (Figure 3.3a), the PB at the exciton resonance (~3.35 eV) exhibits a positive wing on the high energy side. Upon increasing excitation densities (Figure 3.3b,c), the PB minimum shifts to higher energies (dynamic Burstein-Moss (BM) shift) while the positive wing disappears to become a pure PB at the highest excitation density. We have modelled the evolution of the PB with the Banyai-Koch theory presented in section 3.2. The input parameters used for the modelling are summarized in Table 3.2[8]. We have reused the binding energy (E_b = 89 meV) and bare band gap (E_g = 3.478 eV) determined from the Elliott fitting of the UV-Vis spectrum (Table 3.1). We plot in Figure 3.4 the computed evolution of the absorption coefficient at different excitation densities in the range investigated here. When the excitation density increases, the amplitude of the exciton line decreases and a negative absorption coefficient appears on the low energy side of the optical gap. The former is due to the decrease of the oscillator strength upon Coulomb screening (CS) by the free charge carriers [179, 180] while the latter is due to the gain created by the population inversion at the band edge. The exciton also broadens due to CS which gives a weak increase of the absorption coefficient at higher energies than the exciton absorption. The difference in absorption coefficient between a given excitation density and the calculated ground state spectrum is plotted in Figure 3.5a. The amplitude of the PB at the exciton transition increases when the excitation density increases while a weak PA wing is observed on the high energy side which is progressively overwhelmed by the PB. The ratio between the PB minimum and the PA maximum does not match the

---

[8]For the parameter values, we have used the weighted values along the ordinary and extraordinary axes (2/3 for the former and 1/3 for the latter) which differ slightly because of the wurtzite ZnO anisotropy.

experimental differential transmission in which the PA is more pronounced at low excitation densities (Figure 3.3). We have computed the refractive index from the calculated absorption coefficient by Kramers-Kronig transformation and plot the change in refractive index in Figure 3.5b. The differential transmission $-\Delta T/T_0$ computed from the change in absorption coefficient and refractive index is plotted in Figure 3.4. We have performed the calculations at the excitation densities used in the experiment and show that they can reproduce the experimental transients with increasing fluences at 266 nm excitation (Figure 3.6). A sample thickness of 110 nm (determined experimentally by SEM [181]) has been used which affects the relative contribution of the change in refractive index and absorption coefficient to the differential transmission. The experimental PA on the high energy side cannot be reproduced without accounting for a change in refractive index as observed elsewhere [25, 182, 183]. At high excitation densities, a kink in the PB cannot be reproduced in the region of 3.5 eV. At this energy, ZnO single crystals exhibit an exciton-longitudinal optical (LO) phonon replica distant from the excitonic resonance by the LO phonon energy [168, 184, 185]. This replica is less pronounced and appears at a different energy in quantum wells [186], hence it is expected to be present also in ZnO NPs and is not accounted for in the model.

Table 3.2 – Parameter values used in the modelling of the transient spectra of ZnO NPs. ϵ_r is the relative dielectric constant, m_e^* and m_h^* are the electron and hole effective masses, m_0 is the electron bare mass and a_B is the exciton Bohr radius.

parameter	ϵ_r	m_e^*/m_0	m_h^*/m_0	a_B (nm)
value	7.8	0.28	0.59	1.8
reference	[187]	[173]	[173]	[188]

3.3.3   Effect of the pump photon energy

Transient absorption experiments performed with different pump photon energies are depicted in Figure 3.7. Increasing the pump photon energy generates a high energy tail to the PB which extends more and more into the blue. With 3.44 eV pump photons (Figure 3.7c), no excess energy is given to the charge carriers and the high energy tail is almost absent which shows the absence of population and cooling from states above the band edges. In principle, one can extract the electron and hole average cooling time (energy loss time) from the fitting of the high energy tail of the PB with a MB distribution. This has proven to be a successful method in several systems [101, 158]. Alternatively, a slow rise of the PB close to the band gap gives the average time constant of charge carrier cooling, similarly to chapter 2. However, in this study the instrument response function (IRF) of the measurement differs significantly between the different pump photon energies which prevents the use of this method[9]. Instead, we have extracted the energy-time coordinates of points with a constant PB amplitude which

---

[9]The IRF is typically around 80 fs with 4.66 eV pump photons and around $150-180$ fs with lower pump photon energies.
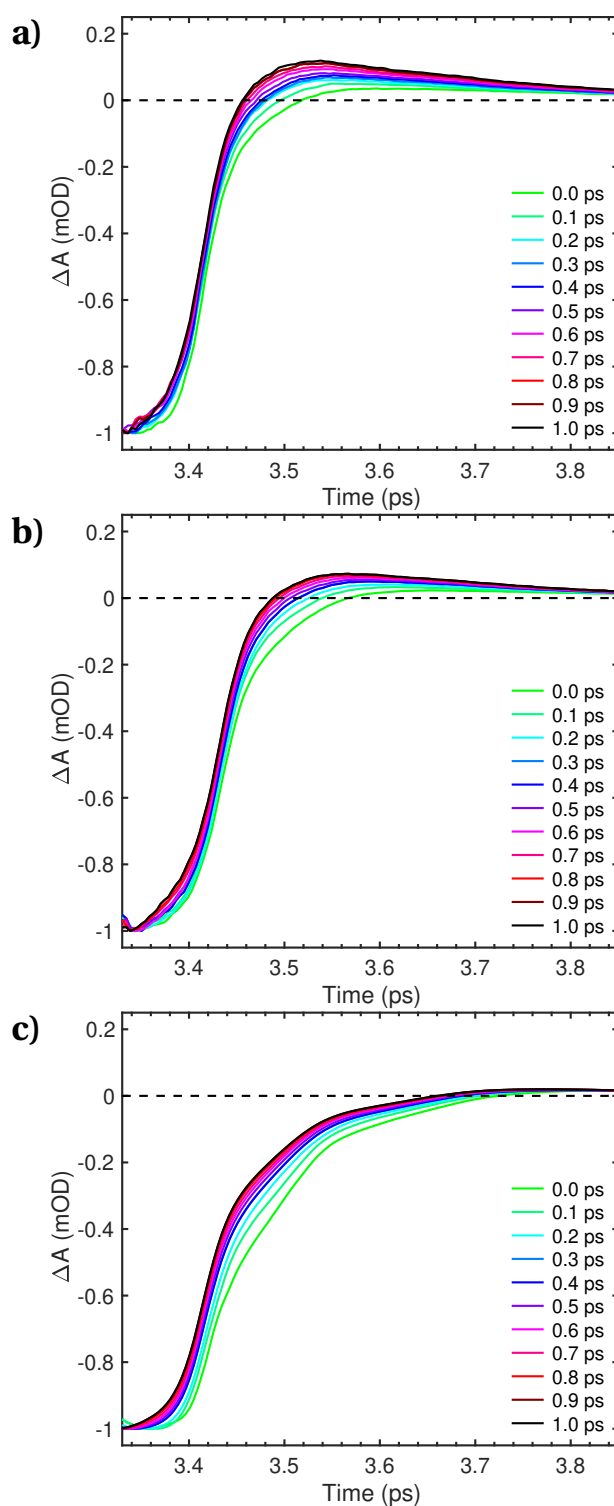
Figure 3.3 – Evolution of the normalized spectral traces at the PB minimum during the first picosecond after excitation at 4.66 eV with increasing pump excitation densities a) 10^{17} cm^{-3}, b) $2 \cdot 10^{17}$ cm^{-3} and c) $3.5 \cdot 10^{17}$ cm^{-3}.
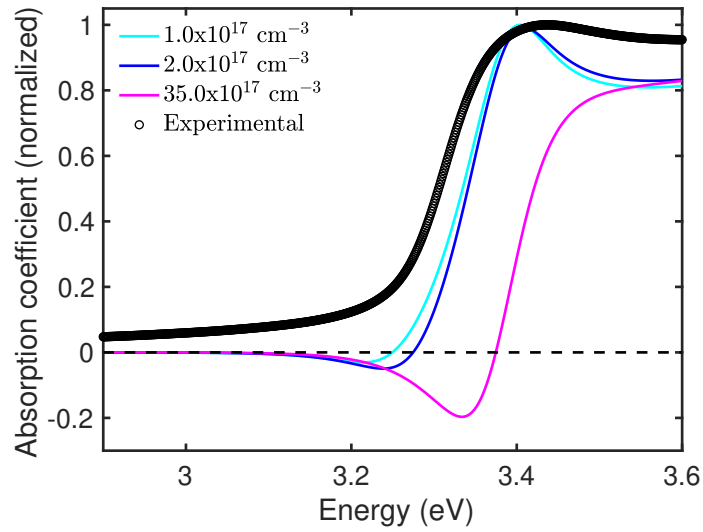
Figure 3.4 – Evolution of the absorption coefficient at the excitation densities used in the differential transmission experiment with 4.66 eV pump photons according to the Banyai-Koch theory (colored curves). The ground state spectrum calculated in the Banyai-Koch theory for a zero excitation density is shown in green. The UV-Vis spectrum of the colloidal suspension is shown with black circles.
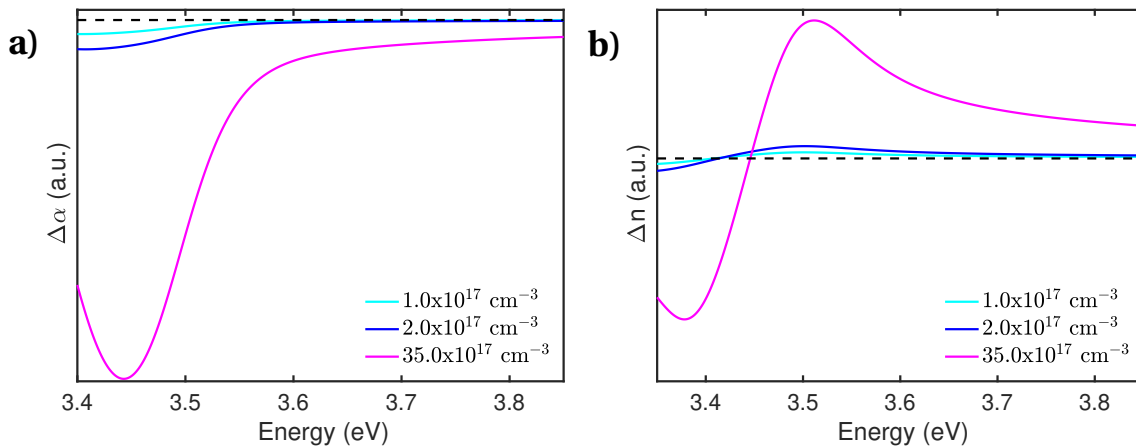
Figure 3.5 – Variation of a) the absorption coefficient, b) the refractive index under different pump excitation densities according to the Banyai-Koch theory.
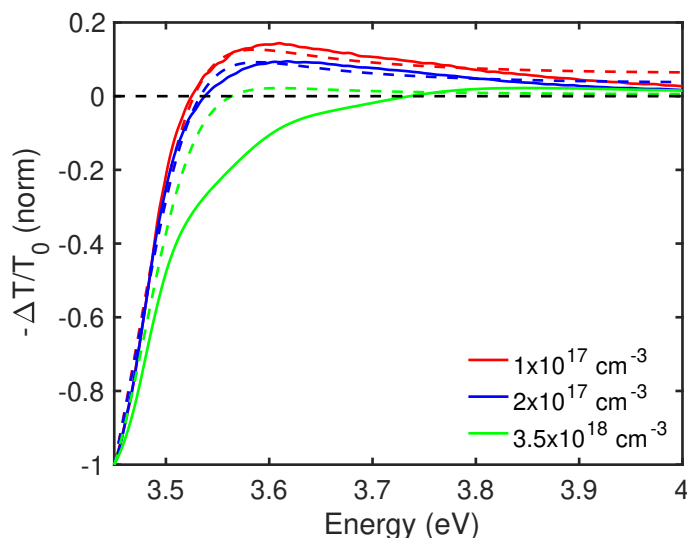
Figure 3.6 – Comparison between the calculated differential transmission spectra (dashed lines) at the excitation densities of the experimental differential transmission with 4.66 eV pump photon energy (continuous lines).

is representative of the spectral movement of the PB high energy tail while the charges cool down. The corresponding energy loss curves are plotted in Figure 3.8a for the three pump photon energies investigated here. The three experiments have been performed at similar excitation densities (~4×10^{18} cm^{-3}) so that the expected difference between the experiments comes from the effect of the photon excess energy while the fluence remains sufficiently low to prevent a hot-phonon bottleneck [189]. An exponential energy loss over time is expected in the dominant carrier-LO phonon emission regime [47, 190, 191, 192, 193]. Indeed, a monoexponential can fit the curves in Figure 3.8a whose time constants are depicted in Figure 3.8b together with the estimated electron cooling time by Zhukov and coworkers [7, 21][10].

We find that the cooling time constant estimated with this method is ∼ 3 times larger than in the prediction. However, the trend of increasing cooling time when the pump photon energy increases is reproduced. This method is reliable in the limit that the electron-hole recombination is much longer than the cooling time. The cooling time observed here is in agreement with the works of Yamamoto and coworkers who have found a cooling time of 1 ps with an almost zero excess energy [194], Hendry and coworkers who found a cooling time of 1.5 ps with 1.3 eV excess energy [195] and 800 fs found by Wen and coworkers with 1.2 eV excess energy [196]. Although there is a difference between the determined cooling time and the theory, we believe the electron cooling time is still limiting the overall cooling time of the system because of the stronger hole-phonon coupling in the VB [21]. The slow electron cooling time in ZnO contrasts with the recent ultrafast cooling observed in anatase TiO$_2$ [154]. Such slow electron cooling time is beneficial for a range of applications since the excess energy

---

[10]The time constants are independent of the fixed amplitude chosen to draw the curves in Figure 3.8a.
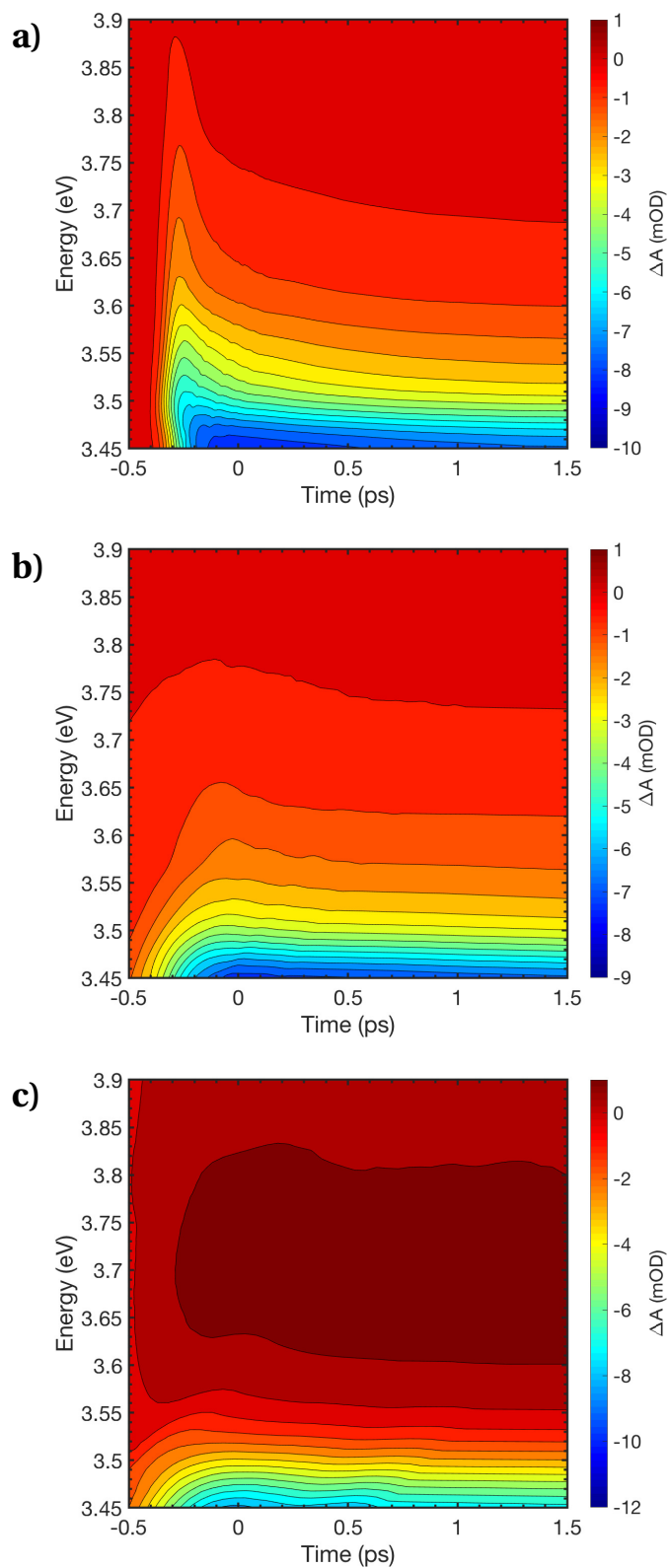
Figure 3.7 – Energy-time transient absorption signal of ZnO NPs with pump photon energies of a) 4.66 eV, b) 3.68 eV, c) 3.44 eV.
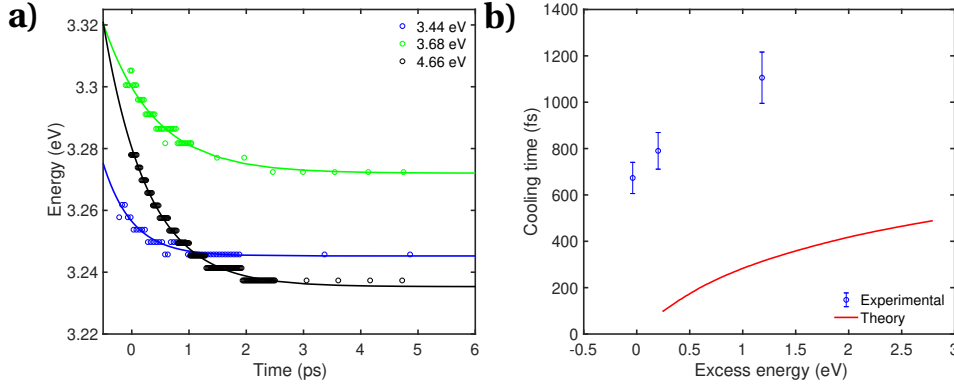
Figure 3.8 – a) Evolution of the energy of the points with a fixed PB amplitude of −1 mOD against time at different pump photon energies (circles). Monoexponential fits are shown with continuous lines whose time constant provide the energy loss time (cooling time). b) Comparison of our estimated cooling times with the *ab initio* estimate by Zhukov and coworkers [7, 8].

given to the charge carriers is not transferred efficiently to the lattice bath. Possible reasons for the discrepancy between the theory and the experiment may be the occurrence of many-body effects which are not included in the original model. Exciton and free carrier screening affect the charge-phonon scattering cross-section which may delay the cooling. Additionally, the formation of polarons is also possible in ZnO [197, 198, 199].

3.4 Exciton and free carrier screening

We performed a fluence dependence at a time delay of 5 ps after the cooling is completed with pump photons resonant with the exciton line at 3.45 eV and above the band gap at 3.68 eV. The former generates a large population of excitons resonantly while the second generates free charge carriers with excess kinetic energy. Normalized spectral traces at the PB minimum are depicted in Figure 3.9a,b. The excitation at 3.68 eV (panel a) shows a PB minimum blue-shifting and getting broader on the high energy side of the PB when the excitation density increases. In contrast, exciting resonantly the excitons (panel b) generates a PB whose lineshape does not depend on the excitation density. At both pump photon energies, the amplitude of the PB minimum evolves linearly over the large range of excitation densities investigated here up to 8×10^{20} cm^{-3} (Figure 3.9c,d). The different behavior with the pump photon energy is related to the screening properties of the quasiparticles generated by the pump. Exciton-exciton screening generated with 3.45 eV pump is ∼3 orders of magnitude less efficient than free carrier screening generated with 3.68 eV pump [200, 201]. This requires to achieve high excitation densities pumping excitons resonantly before the system exhibits a non-linear behavior or reaches the Mott density [195]. Hence we interpret the difference in PB lineshape by the difference in screening properties of the two types of generated particles. This is also clear from section 3.3.2 where the PB is affected by the change in screening length

κ when the excitation density of free charge carriers increases. The linear evolution of the PB minimum amplitude is promising for optoelectronic applications since a photoinduced transparency can be generated very efficiently in ZnO in the spectral region of the exciton due to its sensitivity to both phase-space filling (PSF) and CS.
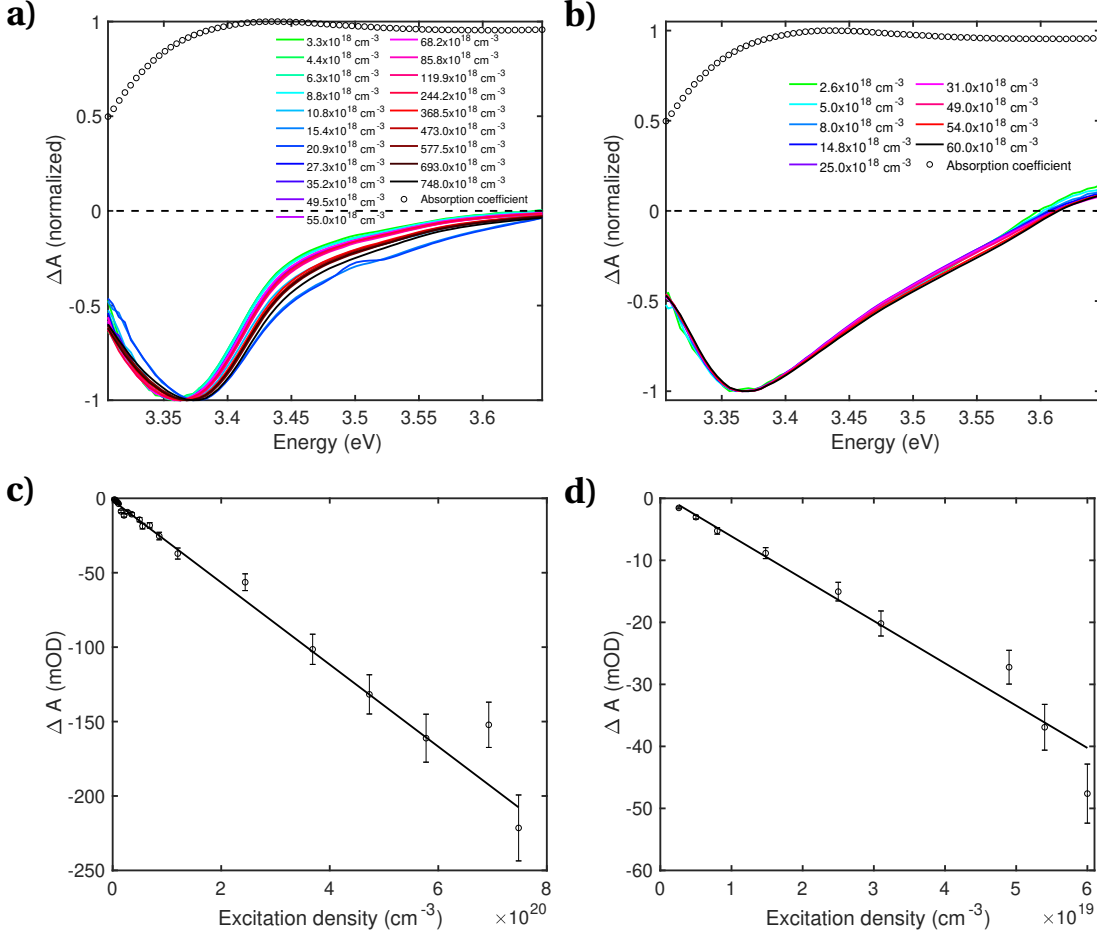
Figure 3.9 – Evolution of the normalized spectral traces for different excitation densitites with a) 3.68 eV and b) 3.44 eV pump photon energy (continuous lines). UV-Vis spectrum of the colloidal suspension of nanoparticles (black circles). Evolution of the PB minimum amplitude with respect to pump excitation density at c) 3.68 eV and d) 3.44 eV pump photon energy.

3.5 Discussion

In order to corroborate the exceptionally long cooling times observed in this Chapter, we performed complementary fluorescence up-conversion measurements [202] which look at the radiative recombination of electron-hole pairs. With 4.66 eV pump photons, we are able to resolve a bimodal rise of the fluorescence maximum below the absorption edge (3.18 eV) of the order of 1 ps (Figure 3.10, red curve) consistent with the cooling time retrieved by TAS. Experiments are ongoing that can investigate the cooling of the charge carriers by 2D-UV

spectroscopy [203] and fluorescence up-conversion at several pump photon energies.
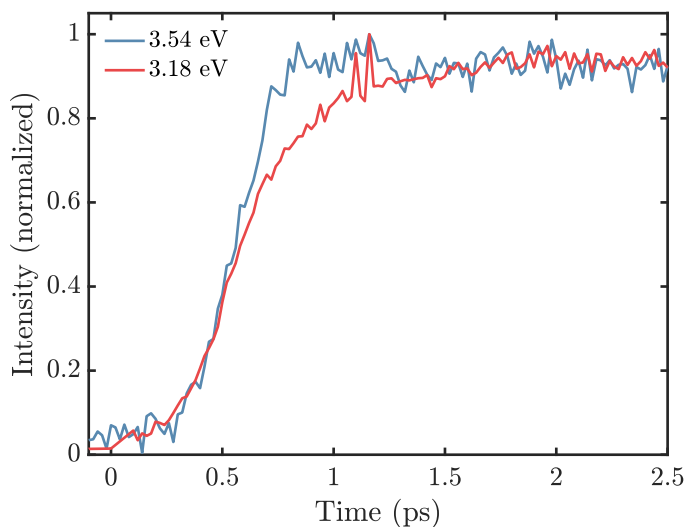
Figure 3.10 – Time traces from fluorescence up-conversion following 4.66 eV excitation and probe at 3.54 eV on the high energy side of the emission and at 3.18 eV at the maximum of the emission.

Conclusion

In this Chapter, different aspects of the photophysics of photogenerated charge carriers in ZnO NPs have been investigated by TAS in the deep-UV. We find that the electron cooling is approximately 3 times longer than theoretically predicted for different pump photon energies. The evolution of the PB after cooling under increasing excitation densities above the optical band gap are reproduced using a theory accounting for the changes in screening properties of the material after photoexcitation. Finally, a different behavior in the PB shape at the optical band gap is observed if the pump is tuned to the exciton resonance to generate an exciton gas and above the band gap to generate free charge carriers. We find the PB under resonant excitation of the exciton to behave linearly with the excitation due to the weak exciton-exciton screening [200, 201].

4 Electron injection at the methylammonium lead bromide perovskite MAPbBr$_3$ - anatase TiO$_2$ interface

Summary

In this Chapter, electron injection at the methylammonium lead bromide perovskite (MAPbBr$_3$) and anatase TiO$_2$ (a-TiO$_2$) interface is investigated by femtosecond differential transmission in the ultraviolet (UV). Injected electrons into a-TiO$_2$ lead to the photobleach (PB) of the exciton transition at ~3.85 eV [43, 70] where MAPbBr$_3$ also has a strong PB. From the comparison of the kinetics in bare MAPbBr$_3$ and MAPbBr$_3$/a-TiO$_2$, we are able to isolate the spectral signature of the injected electrons into a-TiO$_2$ and find injection time from hundreds of picoseconds to nanoseconds. The slow injection time is discussed in the context of the formation of a bound state at the interface. This slow injection time may be detrimental for the performances of the solar cell using a-TiO$_2$ as electron transport material (ETM). This study shows that the electron transport likely occurs in the perovskite layer itself instead of within a-TiO$_2$ as usually assumed.

Introduction

Anatase TiO$_2$ (a-TiO$_2$) is a popular ETM which is currently used in dye-sensitized solar cells (DSSCs) [204, 205]. More recently, the advent of solid-state solar cells based on hybrid organic-inorganic lead halide perovskites (HOIPs) raised the question of the appropriate ETM to extract the electrons from the HOIP layer. Probably because of the popularity of a-TiO$_2$ in DSSCs, mesoporous a-TiO$_2$ is the ETM used in a number of studies on perovskite solar cells [206, 207]. The role of mesoporous a-TiO$_2$ in solid-state solar cells involving HOIP has been recently questioned by Snaith and coworkers [86, 88, 208] since similar internal photon-to-electron conversion efficiency (IPCE) can be obtained by replacing a-TiO$_2$ with a spectator Al$_2$O$_3$ meso-superstructure as a inert substrate of HOIP.

Previous studies investigating the timescale of charge-injection between HOIP and a-TiO$_2$ looked at the photodynamics close to to the perovskite optical band gap by transient absorption spectroscopy (TAS) [80, 209, 210, 211]. In this spectral range, the strategy to infer charge

injection is to monitor the decay time of the PB at the optical band edge upon band gap excitation with and without ETM. The effect of electron injection is to accelerate the decay time of the PB on the femtosecond (fs) to picosecond (ps) timescale because of the decrease of phase-space filling (PSF) at the conduction band (CB) minimum [212, 213, 214]. It is not often mentioned that this should also lead to a long-lived component of the PB on the nanosecond (ns) timescale or longer because of the charge separation preventing electron-hole recombination. Such a method has been applied successfully on CsPbI$_3$ quantum dot (QD) [214], CsPbBr$_3$ [106], MAPbI$_3$ [3] and MAPbBr$_3$ [80] thin films which show electron injection into a-TiO$_2$ on a subpicosecond timescale. Alternative methods to infer electron injection on the fs or ps timescale are (i) TAS in the infrared (IR), which can access the response of free electrons in the CB of the ETM [84], (ii) TAS in the terahertz (THz), sensitive to the density and mobility of charge carriers which decreases significantly upon injection [215, 216], (iii) time-resolved photoluminescence, which is quenched upon charge separation at the interface [217], (iv) transient microwave photoconductance [218], or (v) modelling of the carrier temperature with the average temperature decreasing faster upon injection of hot charges [101].

In this Chapter, we investigate the electron injection at the MAPbBr$_3$/a-TiO$_2$ interface from the change in decay kinetics of MAPbBr$_3$ in the UV with and without a-TiO$_2$ in contact. The MAPbBr$_3$ layer is excited selectively with 3.1 eV pump photons which is below the optical band gap of a-TiO$_2$ [43]. The photodynamics of neat MAPbBr$_3$ in the UV has been discussed is Chapter 2 while the expected transient response of a-TiO$_2$ upon electron injection has been discussed elsewhere [43, 70].

4.1 Results

Details about the sample synthesis can be found in Appendix A.4 as well as the UV-Vis spectra of the MAPbBr$_3$, MAPbBr$_3$/a-TiO$_2$ and a-TiO$_2$ thin films (Figure A.4).

The strategy to characterize the electron injection at the MAPbBr$_3$/a-TiO$_2$ interface is to monitor the changes in decay times of the PBs in MAPbBr$_3$ in the UV with and without a-TiO$_2$ layer in contact. The differential transmission results are shown in Figure 4.1 for (a) MAPbBr$_3$, (b) MAPbBr$_3$/a-TiO$_2$ and (c) a-TiO$_2$. Bare MAPbBr$_3$ exhibits three PBs labelled PB2 to PB4 which have been assigned in Chapter 2. From a first look at the color-coded differential transmission energy-time maps of (a) MAPbBr$_3$ and (b) MAPbBr$_3$/a-TiO$_2$, almost no difference can be observed with the three PBs having similar relative amplitudes in both systems. The main differences are a broader PB3 with a slower decay in MAPbBr$_3$/a-TiO$_2$ on the ns timescale which can be observed from the spectral traces in Figure 4.1 (right panels). Two PBs are observed in a-TiO$_2$ upon above band gap excitation (Figure 4.1c) in agreement with previous results [43, 70, 154] which correspond to direct excitons parallel and perpendicular to the **c**-axis [43]. The PBs in a-TiO$_2$ are expected to appear in the differential transmission of MAPbBr$_3$/a-TiO$_2$ after electron injection due to the screening (Coulomb screening (CS)) of the exciton resonance [219]. Unfortunately, the strongest PB in a-TiO$_2$ appears at 3.84 eV which
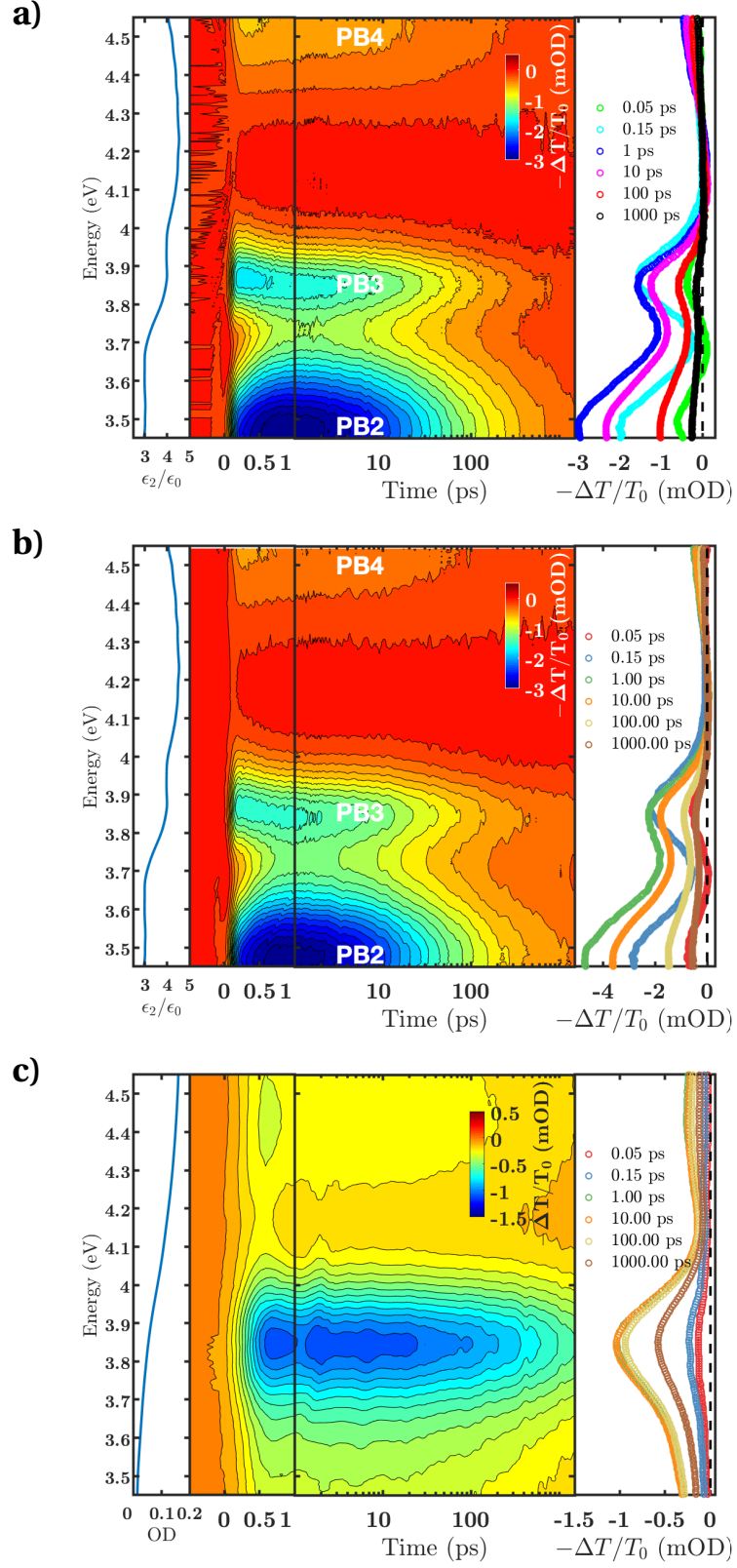
Figure 4.1 – Differential transmission on a) MAPbBr$_3$, b) MAPbBr$_3$/a-TiO$_2$ following 3.1 eV excitation (density 1.3×10^{17} cm^{-3}) and c) a-TiO$_2$ following 3.87 eV.

overlaps with PB2 in MAPbBr$_3$ while the weak PB at 4.44 eV in a-TiO$_2$ overlaps partially with PB4 in MAPbBr$_3$. Hence, there is no spectral window to isolate the photodynamics of a-TiO$_2$ in MAPbBr$_3$/a-TiO$_2$ which requires a deeper analysis. Overall, there is clearly not a strong signature of the PB of a-TiO$_2$ in the differential transmission of MAPbBr$_3$/a-TiO$_2$ in Figure 4.1b.
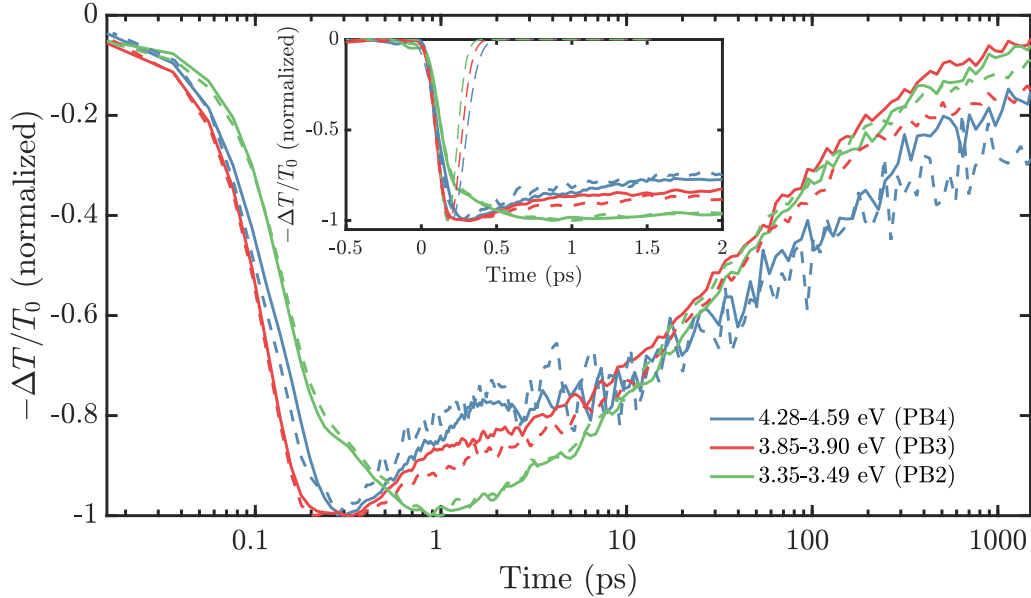
Figure 4.2 – Comparison of the time traces between MAPbBr$_3$ (continuous lines) and MAPbBr$_3$/a-TiO$_2$ (thick dashed lines) in the spectral region of PB1 (green lines), PB2 (red lines) and PB3 (blue lines). Inset shows the time traces up to 2 ps after excitation (instrument response function (IRF) is shown with thin dashed lines).

Band integrals in the spectral region of the PB for MAPbBr$_3$ and MAPbBr$_3$/a-TiO$_2$ are depicted in Figure 4.2 (a more detailed comparison of the time traces is available in Appendix, Figure D.13). No difference is observed in the rise time and initial decay up to ∼0.3 ps after excitation (inset of Figure 4.2) for every PBs. This remarkable overlap between the time traces shows that the experiment has been performed at the same fluence and with the same time resolution for the two systems. Since PB2 (green curve) has identical decay times with and without a-TiO$_2$ layer up to 1 ns, it shows that the differential transmission in that spectral window is intrinsic to MAPbBr$_3$ and can be used as reference to identify the changes in the other parts of the spectrum. This result is expected from the weak contribution of a-TiO$_2$ in the PB2 spectral region upon band gap excitation (Figure 4.1c). The decay times at PB2 (green curve) and PB4 (blue curve) are unchanged between the bare and combined perovskite systems while it gets longer for PB3 (red curve) in MAPbBr$_3$/a-TiO$_2$. We noticed that it was not possible to fit accurately PB3 with a third order kinetics contrary to bare MAPbBr$_3$ (Appendix Figure D.5c) which means that an additional component appears at PB3 when a-TiO$_2$ is present. We use PB2 as a reference to enhance the differences with the other parts of the transient spectra. We have then renormalized the spectral traces to the minimum of PB2 in MAPbBr$_3$

and MAPbBr$_3$/a-TiO$_2$ at different time delays which are depicted in Figure 4.3.

For MAPbBr$_3$ (Figure 4.3a), the normalized spectral traces show little evolution between 1 and 100 ps which means that the differential transmission decays with similar time constants at PB2 and PB3 on this timescale with only a weak deviation. In contrast, MAPbBr$_3$/a-TiO$_2$ (Figure 4.3b) shows a pronounced evolution at PB3 after 10 ps while the evolution at PB4 is the same as in bare MAPbBr$_3$. This points to an additional bleach in the PB3 region in MAPbBr$_3$/a-TiO$_2$ which grows over time. This additional PB is absent up to 10 ps which means that the dynamics before this time delay is intrinsic to MAPbBr$_3$. Spectrally, it does not follow the PB3 lineshape with one part of the PB extending to the red down to ~3.65 eV.

We isolated the evolution and spectral shape of this additional PB by taking the difference between the normalized spectral trace of Figure 4.3b at time delay t and the spectral trace at 1 ps which represents the transient response of MAPbBr$_3$. The energy-time color-coded map obtained from this procedure is plotted in Figure 4.4 (bottom panel) as a difference of differential transmission ($-\Delta\Delta T/T_0$). The PB has an asymmetric lineshape centred at 3.85 eV with a longer tail on the red side while the rest of the map gives zero signal within the noise level. This confirms that the additional PB grows over time and has a lineshape and central energy position similar to the PB in a-TiO$_2$ upon band gap excitation (Figure 4.4, top panel). We performed the same procedure on bare MAPbBr$_3$ and plotted the reconstructed $-\Delta\Delta T/T_0$ in Appendix (Figure D.14). Spectral cuts of the PB isolated from this procedure in MAPbBr$_3$ and MAPbBr$_3$/a-TiO$_2$ are overlapped in Figure 4.5a together with the PB in a-TiO$_2$ at 100 ps and 1 ns. There is a clear difference between the PB isolated in MAPbbr$_3$ and MAPbBr$_3$/a-TiO$_2$ since the former is weak and has a first derivative lineshape with similar positive and negative amplitudes while a clear bleach appears in the latter with a similar lineshape than the PB in a-TiO$_2$. This is an unambiguous spectral signature of injected electrons into a-TiO$_2$. It shows that the difference in kinetics observed at PB3 is unlikely due to a change of MAPbBr$_3$ kinetics upon electron injection but an overlapping spectral signature of a PB in a-TiO$_2$. We plot in Figure 4.5b the time trace corresponding to the minimum of $-\Delta\Delta T/T_0$ extracted from MAPbBr$_3$/a-TiO$_2$. A biexponential fitting provides time constants of $\tau_1 = 150 \pm 10$ ps (16%) and $\tau_2 > 1.5$ ns (84%). The PB upon electron injection into a-TiO$_2$ appears immediately after the injection of free carriers due to an ultrafast cooling time to the CB minimum [154], hence the time constant τ_1 and τ_2 correspond directly to the electron injection time from MAPbBr$_3$ to a-TiO$_2$. We discuss the exceptionally long injection time in the next section. Note that due to the contribution of a-TiO$_2$, the band integral at PB3 (red curves in Figure 4.2) has a slower decay in MAPbBr$_3$/a-TiO$_2$ than in bare MAPbBr$_3$. If the kinetics at PB3 was only from MAPbBr$_3$, the injected electrons would reduce the PSF and a faster decay would be observed first while a longer time constant would be observed on longer timescales due to the charge separation at the interface. This is consistent with the unchanged kinetics at PB2 which is purely related to electrons in CB1 (chapter 2), while electrons are injected.

We have tried to extract the PB of a-TiO$_2$ in the MAPbBr$_3$/a-TiO$_2$ transient by other methods such as global analysis (GA) (Appendix section D.4). The decay associated spectra (DASs) do
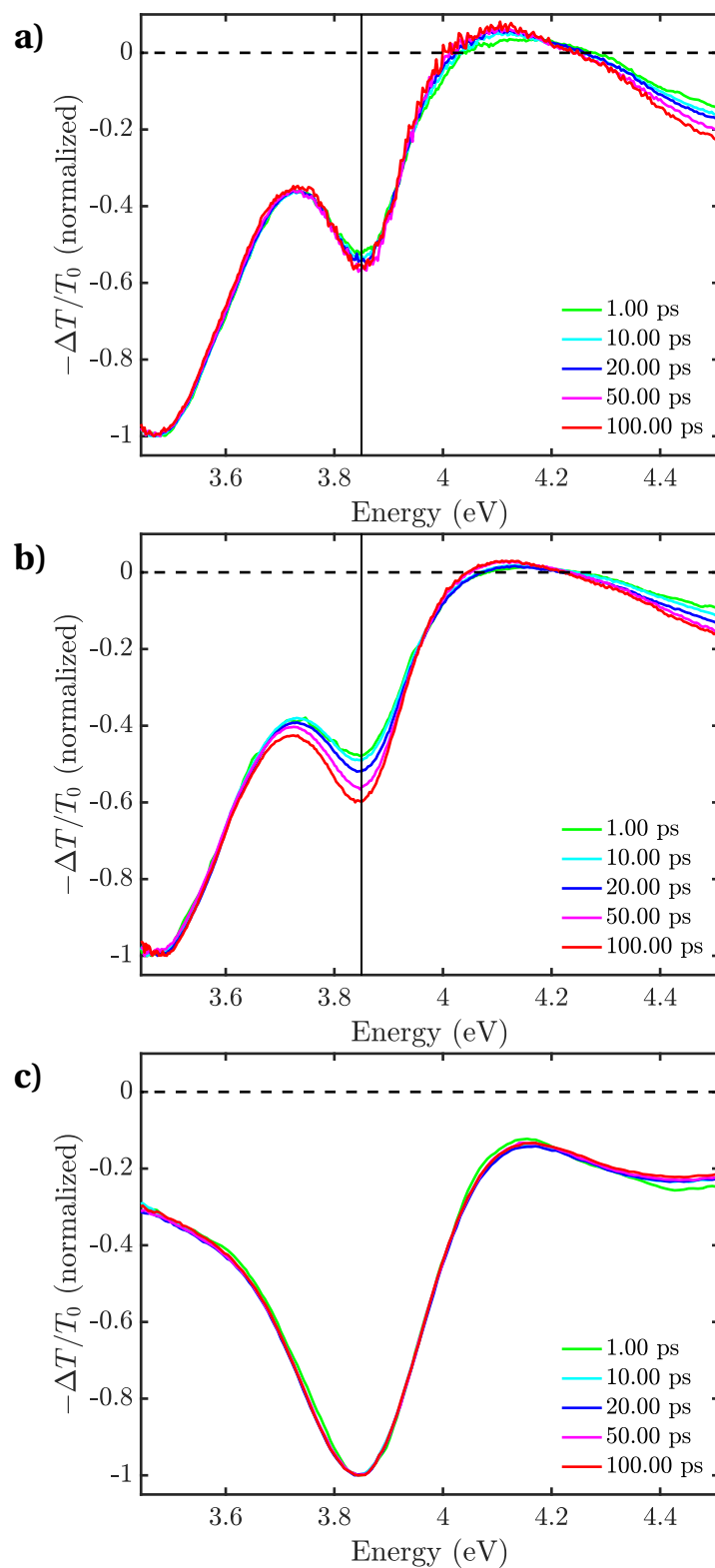
Figure 4.3 – Normalized spectral traces at PB2 minimum for a) MAPbBr$_3$, b) MAPbBr$_3$/a-TiO$_2$. In c) normalized spectral traces at the minimum for a-TiO$_2$. The continuous vertical black line is a guide to the eye at 3.85 eV.
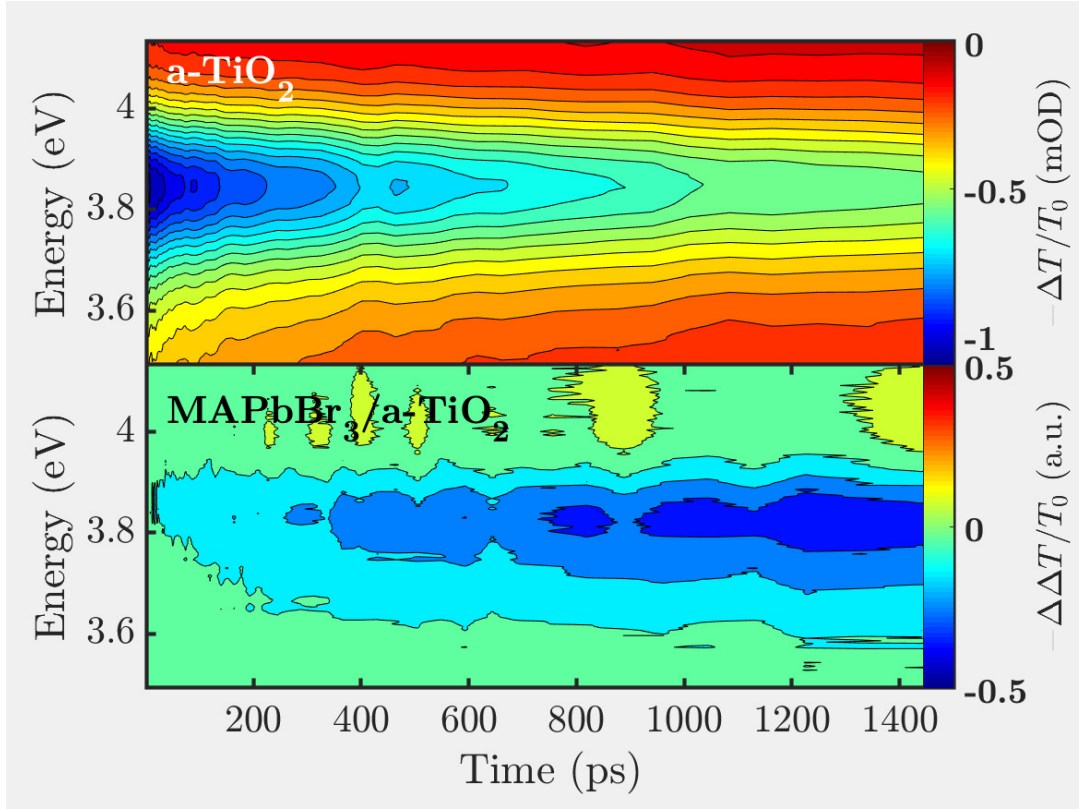
Figure 4.4 – Transient transmission signal of (top) neat a-TiO$_2$ following 3.87 eV excitation and (bottom) reconstructed signal of a-TiO$_2$ in MAPbBr$_3$/a-TiO$_2$ following 3.1 eV excitation according to the normalization procedure described in the text.

not resemble the a-TiO$_2$ PB. This is likely due to the fact that electron injection cannot be considered as a simple parallel mechanism to the electron-hole recombination which would be a scenario in which GA applies.

The experiments in the UV are complemented by differential transmission in the Visible detailed in Appendix D.5 with the same excitation conditions (pump 3.1 eV, density 1.3×10^{17} cm^{-3}). Time traces at the PB minimum in the Visible (PB1) for the two systems are depicted in Figure 4.6a. We observe a slightly longer decay time in MAPbBr$_3$/a-TiO$_2$ on the nanosecond timescale consistent with the effect of charge separation delaying electron-hole recombination[1]. The similarity between the two time traces shows they have been measured at similar pump fluences since dramatic changes in the decay time are observed increasing the pump fluence on the ~100 ps timescale while it is very similar for MAPbBr$_3$ and MAPbBr$_3$/a-TiO$_2$ (Figure 4.6b, Table 4.1[2]). However, the kinetics in the first 2 ps differ significantly (inset in Figure 4.6a).

---

[1] We note however that Deng and coworkers have reported a significantly faster decay in the presence of a-TiO$_2$ [79, 80] which they claim is an effect of sample morphology at the interface assisting the electron-hole recombination in MAPbBr$_3$/a-TiO$_2$.

[2] The faster decay time observed with increasing excitation densities is in agreement with other works [97, 220].
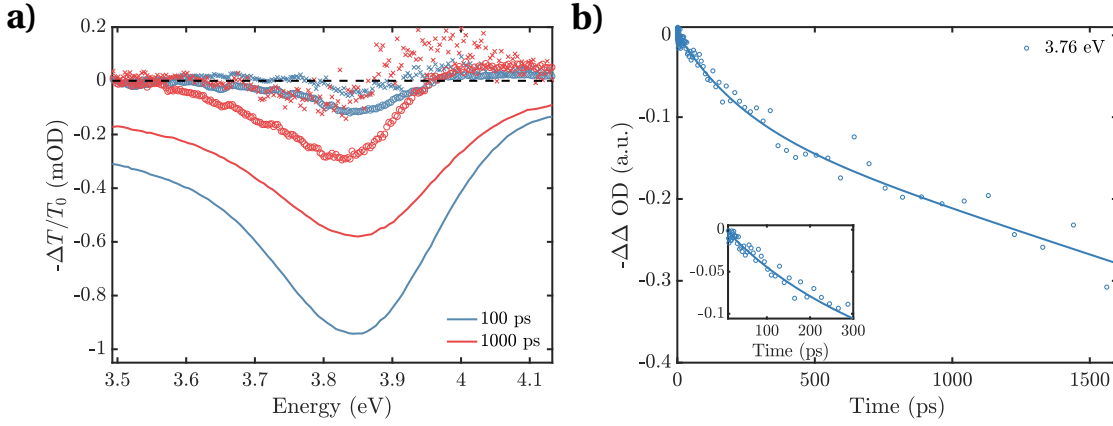
Figure 4.5 – a) Spectral traces retrieved from the difference signal in Figure 4.4 for MAPbBr$_3$ (crosses) and MAPbBr$_3$/a-TiO$_2$ (circles) and spectral traces of a-TiO$_2$ thin film (continuous line) at different time delays. b) Time trace corresponding to the retrieved a-TiO$_2$ PB in the transient signal of MAPbBr$_3$/a-TiO$_2$. The continuous lines is a biexponential fitting.

Especially, PB1 rise time in MAPbBr$_3$/a-TiO$_2$ is systematically faster than in MAPbBr$_3$ at all the investigated pump fluences (Figure 4.7a). A pronounced bimodal rise appears in both MAPbBr$_3$ and MAPbBr$_3$/a-TiO$_2$ for increasing pump fluences with the slowest component due to charge carrier cooling [81, 82] (see Chapter 2). The amplitude of this second rise is systematically smaller in MAPbBr$_3$/a-TiO$_2$ than in MAPbBr$_3$ for similar pump fluences. This seems to indicate that fewer hot charge carriers contribute to the cooling when a-TiO$_2$ is present which is compatible with the injection of hot-carriers. However, we find that the spectral traces measured at this slow rise during the cooling (0.3 ps) and after the cooling (2 ps) compared in Figure 4.7b do not corroborate this interpretation[3]. During and after the cooling (blue and red curves respectively), there is a difference in the PB1 broadening with the high energy tail extending more into the blue in MAPbBr$_3$/a-TiO$_2$ (dotted lines) while the position of the PB1 minimum is unchanged between the two samples. The position of the PB minimum after the cooling (2 ps) is related to the filling of the valence band (VB) and CB with photogenerated charges which leads to a dynamic Burstein-Moss (BM) shift [221, 222]. This effect has been investigated in detail by Manser and Kamat in MAPbI$_3$ [122]. The dynamic BM leads to an increase in the apparent band gap E_g of a semiconductor. We have analyzed the Burstein-Moss shift in MAPbBr$_3$ and MAPbBr$_3$/a-TiO$_2$ and detail the results in Appendix D.10. The band gap shift upon increasing excitation densities is proportional to the 2/3rd power of the excitation density as expected but the analysis shows that the amplitude of this shift is more important in MAPbBr$_3$/a-TiO$_2$ than in MAPbBr$_3$. This is inconsistent with the effect of electron injection where the amplitude of the BM shift is expected to decrease in MAPbBr$_3$/a-TiO$_2$ contrary to the observation.

During the cooling, the high energy tail of PB1 is related to the carrier temperature through the Fermi-Dirac (FD) distribution of the hot carriers in the VB and CB after thermalization

---

[3]The origin of the different parts of the spectral trace is explained in detail in the Appendix D.2.
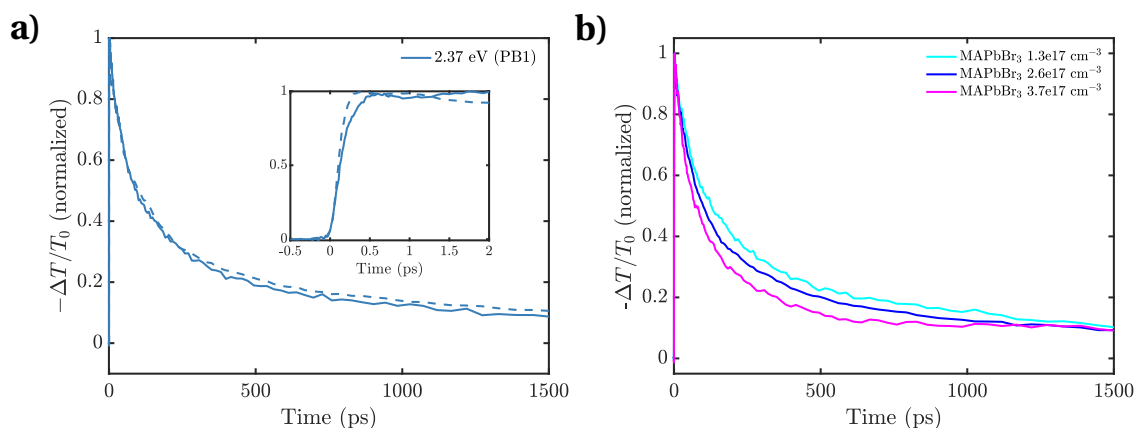
Figure 4.6 – a) Comparison between the time traces at PB1 minimum (2.37 eV) for MAPbBr$_3$ (continuous line) and MAPbBr$_3$/a-TiO$_2$ (dashed line). The excitation density is 1.3×10^{17} cm^{-3}. b) Time traces at PB1 minimum for MAPbBr$_3$ at different excitation densities. The sign of the time traces has been flipped for convenience.

[101, 158]. The fitted lineshape in this spectral region with an approximate Maxwell-Boltzmann (MB) distribution provides the evolution of the average carrier temperature (electron and hole) over time. Following this procedure, Li and coworkers have shown subpicosecond electron injection from MAPbBr$_3$ into an organic ETM from the spontaneous decrease of the average temperature absent in the bare perovskite [101]. Our dataset exhibits the opposite effect where the high energy tail of PB1 is broader in MAPbBr$_3$/a-TiO$_2$ at 0.3 ps during the cooling (Figure 4.7, red curve). An analysis of the average carrier temperature with a MB distribution provides a higher temperature over time in MAPbBr$_3$/a-TiO$_2$ than in MAPbBr$_3$ during the cooling step which is inconsistent with the injection of hot carriers.

Table 4.1 – Time constants obtained from the global analysis of the energy-time maps of MAPbBr$_3$ and MAPbBr$_3$/a-TiO$_2$ at different excitation densities.

Sample (excitation density $\times 10^{17}$ cm^{-3})	MAPbBr$_3$ (1.3)	MAPbBr$_3$/a-TiO$_2$ (1.3)	MAPbBr$_3$ (2.6)	MAPbBr$_3$ (3.7)
τ_1 (ps)	0.34	0.2	0.38	0.53
τ_2 (ps)	10.6	10.0	10.9	10.6
τ_3 (ps)	94.4	95.8	87.9	76.8
τ_4 (ps)	> 1500	> 1500	> 1500	> 1500

Thus, neither the analysis of the BM shift or the average carrier temperature allows an unambiguous proof of electron injection. Instead, differential transmission in the UV allows access to spectral signatures of electrons into the ETM, namely a-TiO$_2$, which is an unambiguous fingerprint of injection. In the next section, we discuss the unchanged kinetics at PB2 upon injection and the slow electron injection time.
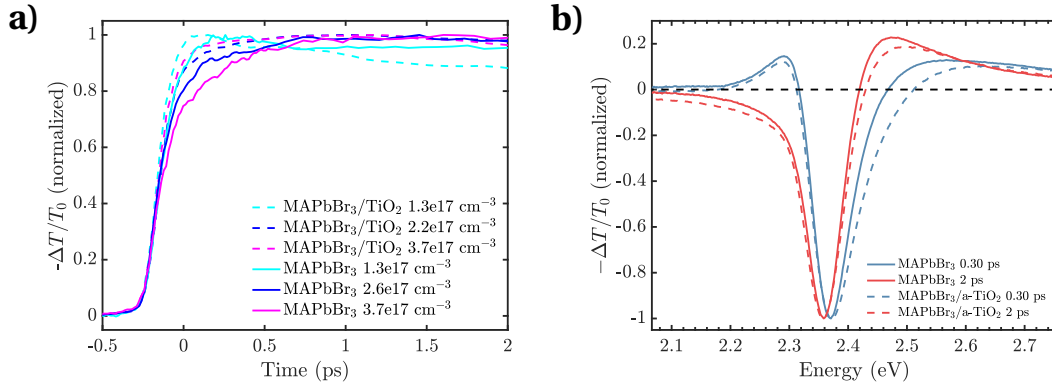
Figure 4.7 – a) Comparison between the rise times at PB1 minimum (2.37 eV) for MAPbBr$_3$ (continous line) and MAPbBr$_3$/a-TiO$_2$ (dashed line). The sign of the time traces has been flipped for convenience. b) Comparison between the normalized spectral traces of MAPbBr$_3$ (continuous line) and MAPbBr$_3$/a-TiO$_2$ at PB1 minimum 0.3 ps (blue curve) and 2 ps (red curve) after excitation at 3.1 eV (density $\sim 1 \times 10^{17}$ cm^{-3}).

4.2 Discussion

4.2.1 Unchanged kinetics at PB2

We observed the same time traces at PB2 in the UV (rise time and decay) for MAPbBr$_3$ and MAPbBr$_3$/a-TiO$_2$ (green curve in Figure 4.2). In Chapter 2 we have assigned the optical transition at PB2 to a transition from VB2 to CB1 at the R-point, sensitive to the electron cooling. Although we demonstrated charge injection takes place, it leaves the kinetics at PB2 unchanged. Since the overall electron injection seems to be inefficient giving a rather weak PB in a-TiO$_2$, it is likely that the low density of injected charges does no trigger any change in the recombination dynamics within the MAPbBr$_3$ layer and leave he kinetics at PB2 unchanged.

4.2.2 Long injection time - Formation of charge-transfer excitons

The exceptionally long injection time with the main component beyond 1 ns has been already reported in MAPbBr$_3$ nanoparticles (NPs) [80, 210], CsPbI$_3$ QD [214], CsPbBr$_3$ QD [106] and is in contradiction with the sub-100 fs time constants reported by Grancini and coworkers [84], Piatkowski and coworkers [124] and Marchioro and coworkers [123, 218] from the signature of Drude electrons in a-TiO$_2$ upon electron injection. Li and coworkers have identified subpicosecond electron injection from the decrease of the average carrier temperature in MAPbBr$_3$ QD [101]. Ponseca and coworkers have shown subpicosecond electron injection from the mobility drop of the charge-carriers upon injection by pump-probe in the THz [215] with other injection timescales spanning hundreds of picoseconds to several nanoseconds [216]. Instead of a prompt electron injection, we observe a progressive injection on the nanosecond timescale. An effect of stochastic diffusion of the photogenerated electrons to the interface can be excluded because of the diffusion time of the electron to the interface for a perovskite

layer of ~30 nm is of the order of 10 ps[4] with the electron mean free path being larger than the sample thickness such that the electron trajectory can be approximated by a straight line [224]. Once the electron has crossed the interface, its diffusion towards the bulk enters the regime of a drifting charge because of the electrostatic potential which builds up at the MAPbBr$_3$/a-TiO$_2$ interface. This process involves the charge mobility in the a-TiO$_2$ layer which is rather large and should not limit the movement of charge carriers towards the bulk [225] although the mobility strongly depends on the material morphology [226].

The slow injection kinetics is similar to the case of ZnO/N719 presented in Chapter 5 which is either due to the formation of an interfacial charge-transfer complex (ICTC) (also called charge-transfer exciton (CTE)) or the shallow trapping of electrons at the surface. A CTE is an electrostatically bound electron-hole pair at a junction or domain boundary which needs to overcome its binding energy to generate free charge carriers. The formation of CTE has been claimed at boundaries in mixed halide perovskites [227], between MAPbBr$_3$ nanoplatelets [228] and heterostructures [229], and in MAPbI$_3$ with a mixture of structural phases [230]. Hence, HOIPs have a propensity to form interfacial charges which keep interacting via Coulomb forces. This scenario could explain our observation of the delayed electron injection at the MAPbBr$_3$/a-TiO$_2$ which calls for the formation of a bound state at the interface. Since the CTE formation can alter the performances of photovoltaic devices, the methodology developed in this Chapter provides a way for the community to estimate the efficiency of the electron injection and design interfaces which can screen the electron-hole interaction leading to more efficient charge injection. Work is already in progress in this respect [206, 213].

Conclusion

In this Chapter, we have been able to develop a methodology to monitor electron injection from MAPbBr$_3$ to a-TiO$_2$ thin films under selective excitation of the perovskite layer. It is based on the exciton PB in a-TiO$_2$ which happens due to the PSF and CS of the injected electrons. Although the transient signal of MAPbBr$_3$ is overwhelming in the deep-UV, we have been able to extract the a-TiO$_2$ exciton PB and the electron injection timescale from hundreds of picoseconds to nanoseconds. This is an unambiguous proof of electron injection on these timescales. We suspect the slow electron injection is due to the formation of a CTE at the MAPbBr$_3$/a-TiO$_2$ interface but may also be due to the shallow trapping of electrons at the interface. This calls for a better design of the interface to screen the Coulomb interaction and gain in injection efficiency. The current study confirms the generality of the method of TAS in the deep-UV [70] to investigate charge injection into wide band gap semiconductors at solid-state interfaces even when the injection efficiencies are low like in this chapter system of interest.

---

[4]The electron mean free path L_e is of the order of 100 nm and the electron diffusion coefficient approximately 0.20 cm^2 s^{-1} in MAPbBr$_3$ [223] which yields a diffusion time of $\tau_e = L_e^2/D_e = 11$ ps which is an order of magnitude shorter than the injection time constant.

5 Charge injection between N719 and ZnO

Summary

In this Chapter, the electron injection at the interface between a prototypical dye molecule (di-tetrabutylammonium cis-bis(isothiocyanato)bis(2,2´-bipyridyl-4,4´-dicarboxylato)ruthenium-(II) (N719)) and ZnO nanoparticles (NPs) is studied by femtosecond transient absorption spectroscopy (TAS) in the ultraviolet (UV). A part of this chapter has been published in Ref. [70] which compares the injection kinetics between N719 and anatase TiO_2 or wurtzite ZnO NPs. The characterization of the NPs in the colloidal suspension has been published in a separate paper [149].

The current results confirm the formation of a bound state at the interface which delays the injection of charges into the ZnO NP bulk. The possible formation of an interfacial charge-transfer complex (ICTC) is discussed which shows that the electronic coupling, the conduction band (CB) density of states (DOS) and the static dielectric screening cannot separately account for the differences in injection kinetics between TiO_2/N719 and ZnO/N719. The involvement of surface states in the formation of the ICTC may be the main difference between ZnO and TiO_2.

Introduction

Dye-sensitized solar cells (DSSCs) have been an intense topic of research over the past two decades. The efforts devoted to design photovoltaic materials with cheap building processes bear fruits with the discovery of DSSCs by Gratzel and O'REgan [231] in the nineties. The working principle of a DSSC is depicted in Figure 5.1. Briefly, dye molecules (organic or molecular complexes) harvest the most intense part of the solar spectrum in the Visible (step 1) and inject the photoexcited electron into the CB of mesoporous transition-metal oxide (TMO) assemblies such as anatase TiO_2 or wurtzite ZnO (step 2). The photogenerated electric current is collected at the anode in contact with the TMO NP (step 3) which flows to the cathode where it reduces the electrolyte (step 4) and ultimately, regenerates the ground state

of the light harvesting dye molecule after diffusion (step 5). In this cycle, step 2 is a key step where the electron is injected from the dye molecule to the electron acceptor, namely the TMO NP embedded in the mesoporous film, which is the focus of this Chapter. The optimization of the dye and TMO has been the topic of a number of works with, nowadays, little understanding of the driving force leading to electron injection. Hereby, we propose the investigation of charge injection from a prototypical molecular complex, the dye N719, into wurtzite ZnO NPs by femtosecond broadband TAS in the UV. We show that this technique is substrate specific since it can access the transient optical non-linearities triggered by the electron injection in the spectral region of the semiconductor band gap. A similar study has been performed between N719 and anatase TiO$_2$ which can be found in Refs. [70] and [219].

The optical properties of ZnO NPs have been discussed in Chapter 3. In this Chapter, it is useful to remember that ZnO is a direct band gap semiconductor at the Γ-point with E_g = 3.26 eV at room temperature. An exciton with a large binding energy of ~60 meV is formed at the band gap [169, 232, 233]. The UV-Vis spectrum of the ZnO NP colloidal solution is largely influenced by the size of the material with a pronounced blue shift of the band gap down to the middle of the UVA region (~3.4 eV) for NP of ~10 nm radius due to quantum confinement [149, 234]. Under laser excitation above the optical band gap of ZnO NPs, a pronounced photobleach (PB) is observed in the region of the optical band gap which has been assigned to the bleaching of the band gap transition [235] and/or Coulomb screening (CS) of the exciton resonance [194] (Chapter 3). In the current experiment, the detection of a transient bleach in the spectral region of the ZnO optical band gap is used to monitor charge injection from N719 to ZnO.

Details about the sample preparation are given in Appendix A.1, A.2 and A.3 with the UV-Vis spectra of the solutions. The experimental conditions for each experiment are summarized in Appendix B (Table B.1).

5.1 Results

Figure 5.2a presents the energy-time pseudo-color map of ZnO NPs following 295 nm excitation (above the optical band gap of ZnO NPs). Figure 5.2d and g present the maps of N719 and ZnO/N719 respectively, following 550 nm excitation resonant with the singlet metal-to-ligand charge-transfer (MLCT) of N719.

In the experiment on bare N719 (Figure 5.2d,e), a prominent PB appears between 295 and 325 nm, which corresponds to the bleach of the ligand-centred (LC) transition. It is a consequence of the depopulation of the ground state by the pump pulse. The spectral regions to the blue and the red side of this bleach are positive. All features (positive or negative) exhibit a long recovery time beyond 1 ns (Figure 5.2f). The photodynamics of N719 following the excitation of the ^{1}MLCT is well established. The system undergoes ultrafast vibrational cooling and intersystem crossing into the triplet ^{3}MLCT state in less than 30 − 40 fs [236, 237] in which it remains for around 20 ns [238]. The positive wings to the main bleach involve excited state absorption of the ^{3}MLCT state. The fast and weak evolution of the signal over the first 100 fs is
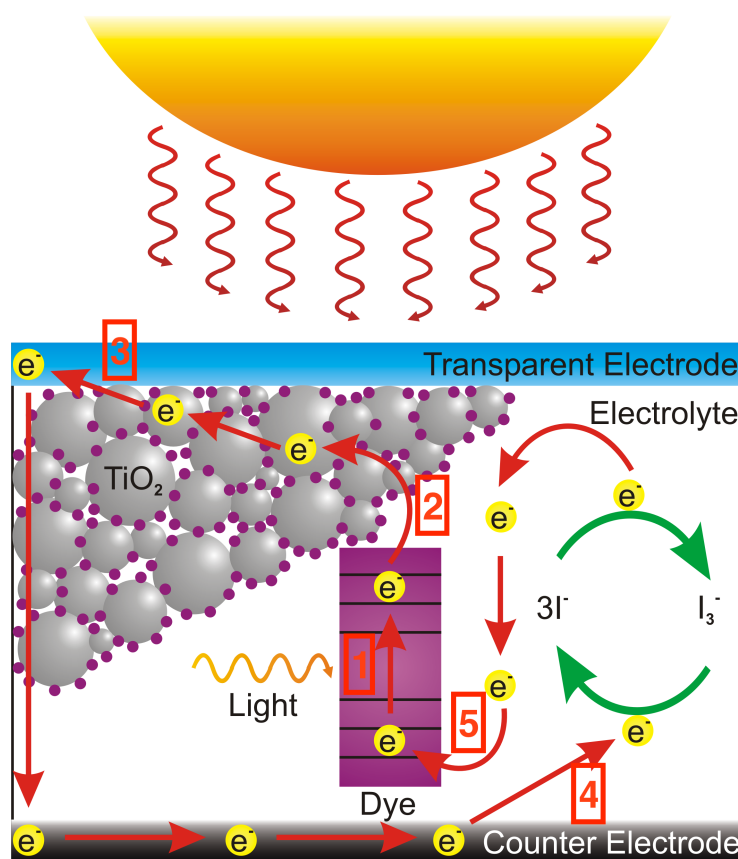
Figure 5.1 – Schematic working principle of a DSSC. (1) A photon is absorbed by the dye which excites an electron into higher energy orbitals, (2) the electron is injected into the CB of the TMO acceptor, (3) the electron is collected at the anode interface, (4) the electron reduces the electrolyte at the cathode interface and (5) the reduced electrolyte regenerates the electronic ground state of the dye after diffusion. The photodynamics of step (2) is studied in this Chapter at the interface between N719 and ZnO NPs. Image under CC licence.

due to vibrational cooling [239].

In the experiment on bare ZnO NPs (Figure 5.2a,b), the PB exhibits a Lorentzian line shape centred at the exciton resonance around 365 nm. The bleach is prompt, within the instrument response function (IRF) of the setup (< 100 fs), and follows a multiexponential recovery with fitted time constants of $\tau_1 = 1.1 \pm 0.1$ ps, $\tau_2 = 87.6 \pm 1.0$ ps and $\tau_3 = 3.9 \pm 0.4$ ns (Figure 5.2c). In the picosecond (ps) regime, the photogenerated electrons and holes trigger a PB in the region of the exciton which is due to phase-space filling (PSF) of the single particle states involved in the formation of the exciton at the energy extrema of the valence band (VB) and the CB (Chapter 3). The ps time constant τ_1 has been already reported in terahertz (THz) [195], photoluminescence (PL) [163] and transient reflectivity [240] spectroscopy, commonly assigned to the cooling of the charge-carriers. The electron-hole recombination occurs within τ_2. The longest time constant τ_3 goes beyond several nanosecond (ns) in agreement with PL
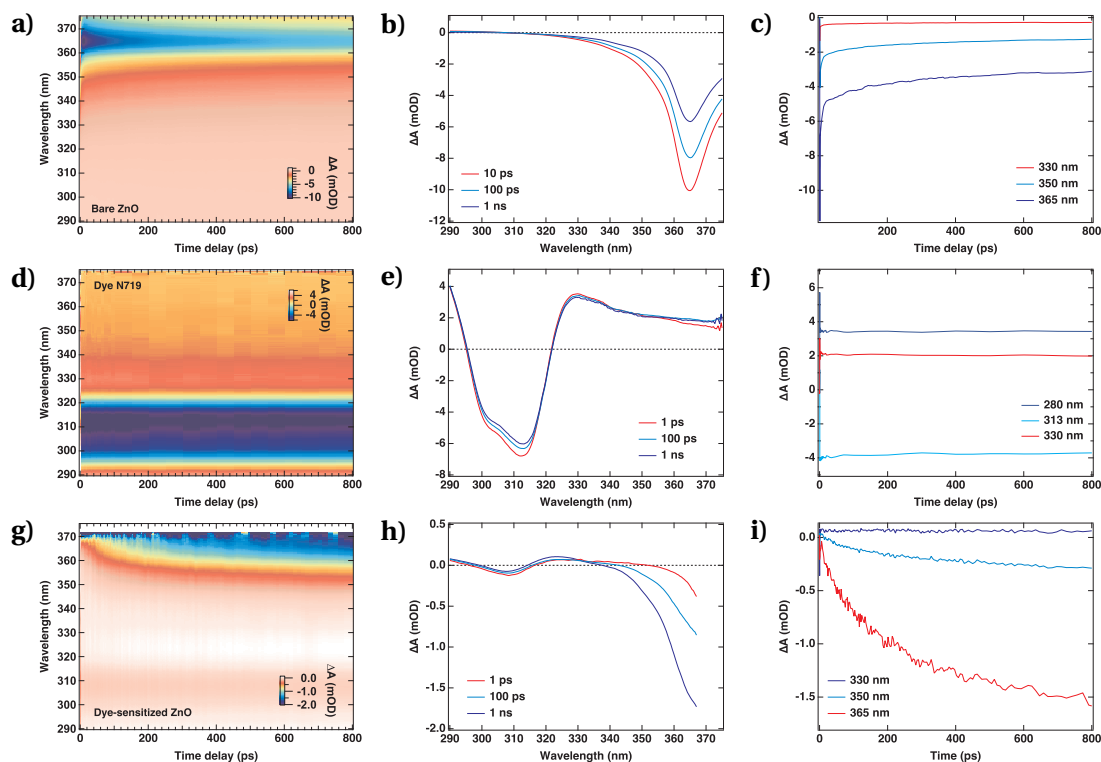
Figure 5.2 – Transient absorption on (a,b,c) bare ZnO NP following 295 nm excitation (fluence 63 μJ/cm^2), (d,e,f) N719 in dimethylformamide (DMF) following 550 nm excitation (fluence 40 μJ/cm^2), and (g,h,i) ZnO/N719 following 550 nm excitation (fluence 740 μJ/cm^2). Spectral cuts are given in b), e) and f). Time traces are given in c), f) and i).

[241, 242] and time-resolved X-ray absorption spectroscopy (TRXAS) studies [243, 244] and is due to trapped charges.

Before moving to the excitation of the ZnO/N719 ensemble at 550 nm (below the optical band gap of ZnO), a blank experiment was performed on bare ZnO NP to show that no electron-hole pairs could be generated at this pump photon energy. The spectral traces are presented in Figure 5.3a for different pump fluences. A weak PB of < 0.1 mOD in the spectral region of the exciton could be observed at a fluence 3.5 times larger than the one used for the experiment on ZnO/N719 in Figure 5.2g,h,i. This PB has a positive wing which differs from the one observed upon direct band gap excitation where the signal is only negative (black circles in Figure 5.3a). Such a PB is obtained at low excitation densities (see Figure 3.3 in Chapter 3) where the change in refractive index provides a positive signal on the high energy side of the PB which disappears progressively when the excitation density increases. We found the amplitude of the PB to evolve linearly with the pump fluence which excludes two-photon absorption (Appendix Figure A.3).

Finally, the ensemble ZnO/N719 is excited at 550 nm, resonant with the ^{1}MLCT state of N719 (Figure 5.2g,h). The transient signal exhibits a PB centred at 310 nm with positive wings due to
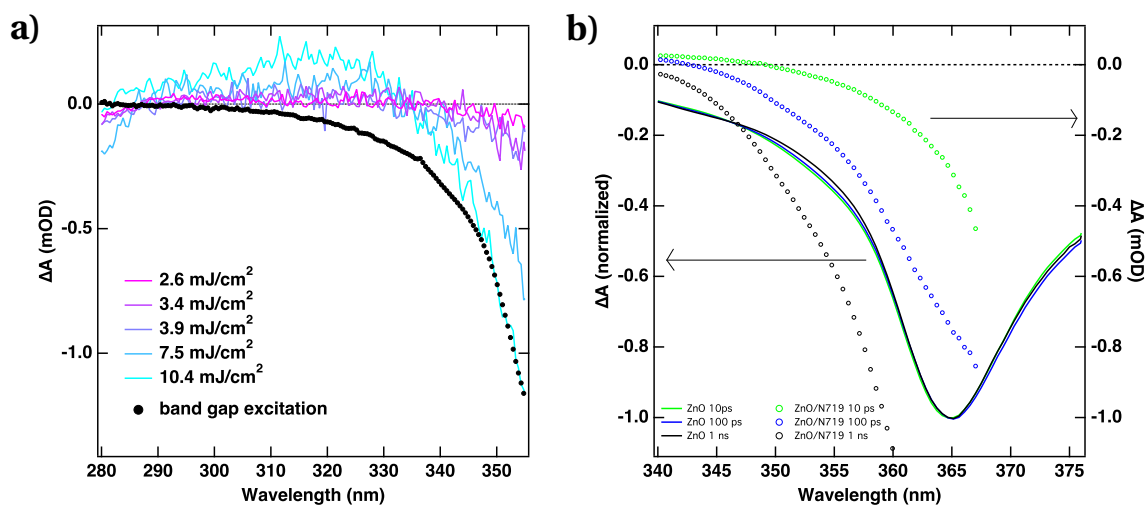
Figure 5.3 – a) Evolution of the transient absorption of ZnO nanoparticles in ethanol following excitation at 550 nm at different fluences (continuous lines). The spectral traces are taken 1 ps after excitation. The spectral trace upon band gap excitation at 295 nm after 1 ps is shown for comparison (black circles). b) Overlap between the normalized spectral traces acquired on bare ZnO following 295 nm excitation (lines, left vertical axis) and spectral traces on ZnO/N719 following 550 nm excitation (circles, right vertical axis). The position of the PB maximum is shifted between bare ZnO and ZnO/N719.

the N719 contribution. Indeed, time traces at 290, 305 and 330 nm show the same kinetics as free N719 molecules (Figure 5.4). The PB observed around 365 nm coincides with the PB in bare ZnO NPs upon above band gap excitation (Figure 5.2b). Spectral traces of N719, ZnO and ZnO/N719 are compared in Figure 5.5a[1]. A similar PB is observed at the exciton resonance between ZnO and ZnO/N719 which can only be due to the electron population of the ZnO CB in the latter. This is an unambiguous proof of charge injection into ZnO NPs. The PB kinetics differ between ZnO and ZnO/N719 (Figure 5.5b). In the latter, the PB amplitude slowly increases on a time scale of several tens to hundreds of ps while bare ZnO undergoes a prompt PB and a recovery over hundreds of femtoseconds and picoseconds. A multiexponential fit provides rise times of $\tau_1 = 64$ ps (33%) and $\tau_2 = 590$ ps (67%) for the PB in ZnO/N719.

Such slow bimodal rise of the PB due to injected electrons into ZnO NPs has been already reported by THz [245], mid-infrared (IR) [246] and near-IR [247, 248, 249, 250] spectroscopy with different sensitizers. The formation of an ICTC at the ZnO/N719 interface has been invoked to explain the delayed injection into the NP bulk [246, 247, 249, 251, 252, 253]. The maximum amplitude of the PB 1 ns after excitation is approximately one order of magnitude smaller than in bare ZnO, in line with our estimate of the number of injected electrons relative to the bare nanoparticle case (see Appendix B for the calculation of the excitation densities). In addition, the PB in ZnO/N719 undergoes a progressive broadening as the amplitude of the

[1]Due to the strong absorption of N719 from 365 nm to higher wavelengths in ZnO/N719, the number of transmitted probe photons drops significantly so that we cannot resolved the exciton PB on the red side.
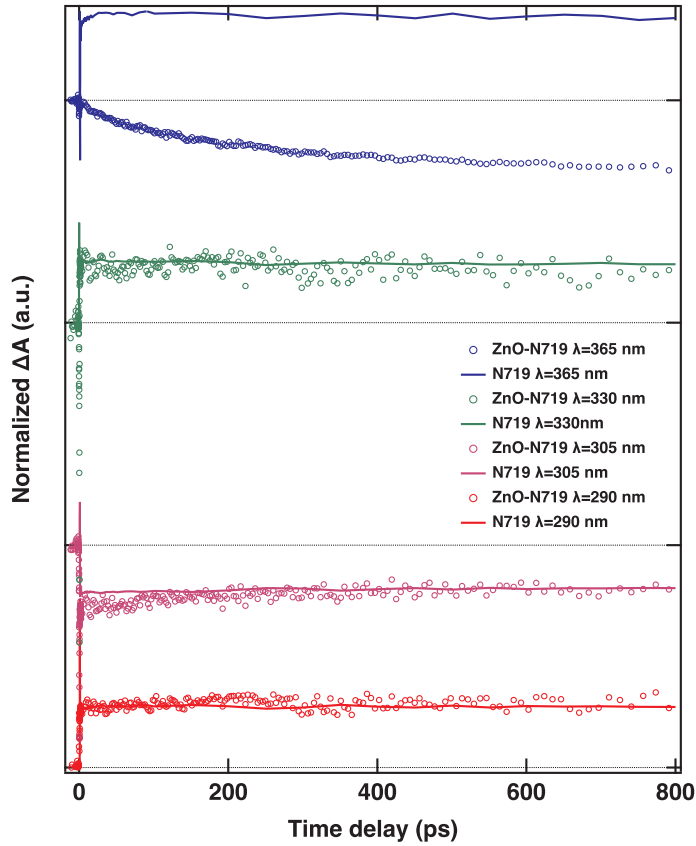
Figure 5.4 – Overlap between the time traces of bare N719 (continous) and ZnO/N719 (circles) at 290 (red), 305 (purple), 330 (green) and 365 nm (blue) probe wavelength following 550 nm excitation.

bleach grows over time, illustrated in Figure 5.2g. This is explained by the progressive filling of single particle states at higher and higher energies on the sides of the Γ-valley at the bottom of the CB. In contrast, the PB in bare ZnO has a constant bandwidth which means that all single particle states involved in the PB recover with the same kinetics. A red shift of the PB maximum with respect to the bare ZnO case is observed (Figure 5.3b) while the position of the exciton and the band gap is unchanged between ZnO and ZnO/N719 (see UV-Vis spectra in Figure A.1). This is in stark contrast with other accepting semiconductor materials for which the bleach appears at the position of the exciton following charge injection, such as in CdSe [254, 255]. We simulated the PB of n-doped ZnO NPs from the available literature of Ga:ZnO UV-Vis spectra [9, 10] (Figure 5.6). For a doping concentration of ~10^{17} cm^{-3} similar to the estimated injected electron density (Appendix B), the PB maximum appears 27 meV below the exciton maximum which corresponds to a PB maximum at 368 nm in our experiment on ZnO/N719 consistent with our results (Figure 5.3b). Increasing the n-doping concentration blue shifts the PB which coincides with the energy position of the PB in bare ZnO NP (Figure 5.3b) and the progressive blue shift of the PB minimum upon increasing excitation densities
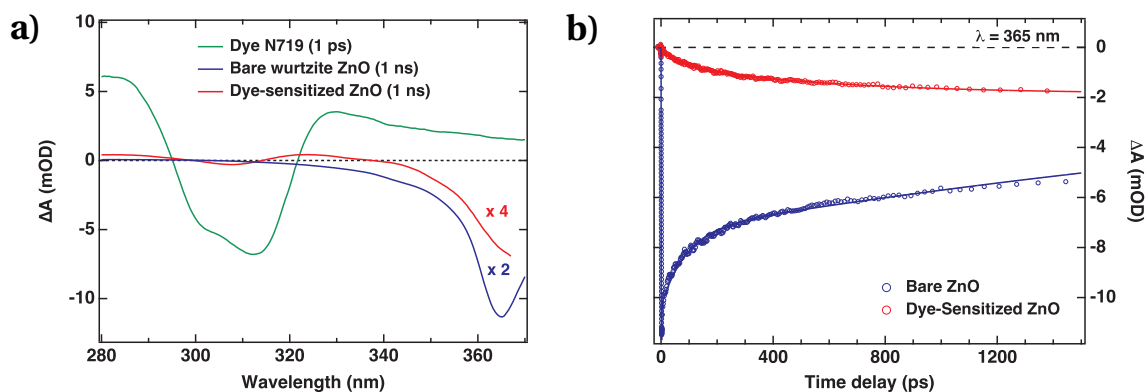
Figure 5.5 – a) Comparison of the spectral traces measured in the three separate experiments of Figure 5.2. The transient spectrum of N719 is in green (1 ps after excitation). The transient spectra of bare and dye-sensititized ZnO NPs are given 1 ns after excitation in blue and red respectively. b) Comparison of the time traces measured at 365 nm in the case of bare ZnO NPs under 295 nm excitation (blue curve) and N719 dye-sensitized ZnO NPs under 550 nm excitation (red curve). Dots represent experimental data; lines are multiexponential fits.
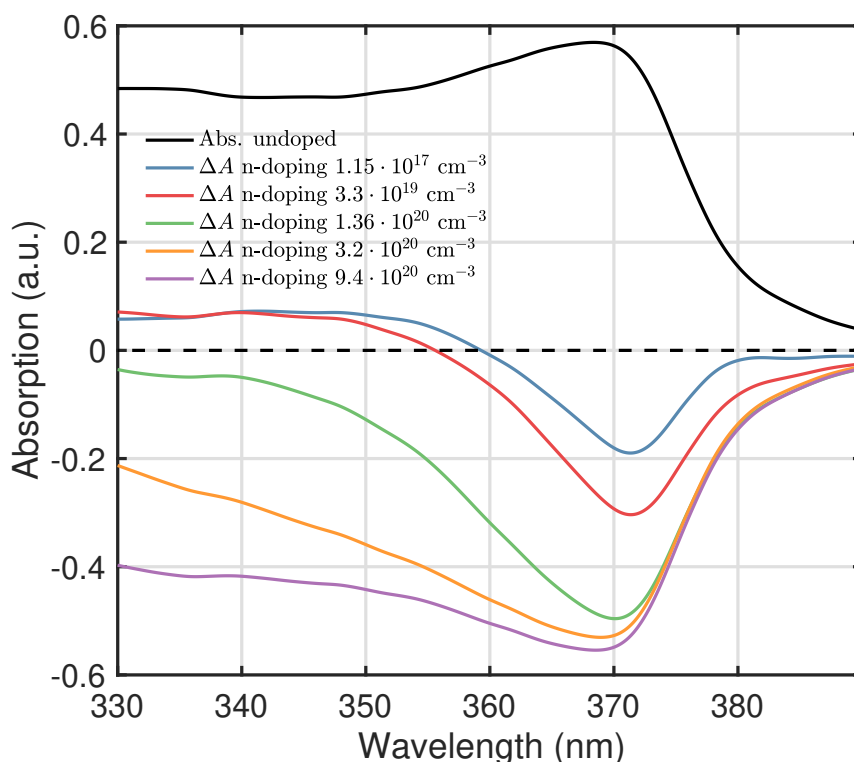
Figure 5.6 – Simulated transient spectra of n-doped ZnO NPs from the UV-Vis spectra of Ga:ZnO taken from Ref. [9] for doping densities $<10^{20}$ cm^{-3} and from Ref. [10] for doping densities $>10^{20}$ cm^{-3}.

in chapter 3 (Figure 3.3). The blue shift of the PB upon increasing excitation densities is due to an interplay between the CS of the electron-hole interaction which decreases the exciton binding energy as well as a reduction of the oscillator strength due to PSF which dominates over band gap renormalization after a few picoseconds [194].
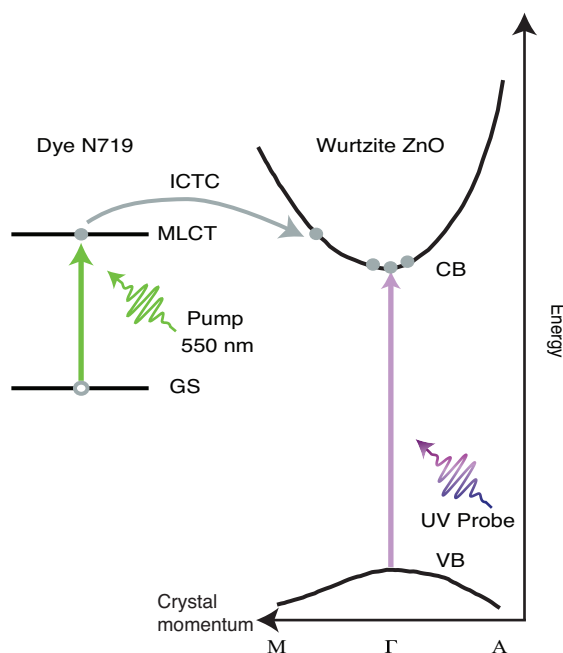
Figure 5.7 – Schematic representation of the UV based detection of the electron transfer in dye-sensitized ZnO NPs. The pump photon at 550 nm (green arrow) excites the ^{1}MLCT state of the N719 dye, which forms an ICTC at the wurtzite ZnO surface. The broadband UV pulse (violet arrow) probes the sharp exciton resonance at 365 nm coming from the Γ-point of the Brillouin zone (BZ). The band structure of wurtzite ZnO has been adapted from Ref. [11].

In summary, a schematic representation of the electron injection in dye-sensitized ZnO is given in Figure 5.7.

5.2 Discussion

The mechanisms of formation and dissociation of an ICTC at the ZnO NP surface remains elusive and deserve a discussion. More specifically, we would like to interpret the difference in electron injection rates between ZnO and TiO_2 in $10-100$ ps for the former and < 100 fs for the latter [70]. The model often used to predict the charge-transfer (CT) rate is derived from Marcus theory [256] with the additional ingredient that the electron acceptor contains a continuum of states to model the CB of the TMO NP [257]. Briefly, starting from the original expression of the electron transfer between discrete donor and acceptor states, the electron

transfer rate k_{et} is given by [258],

$$k_{et} = k_e \nu_{eff} e^{-E^*/k_B T} \tag{5.1}$$

where k_e is the electronic transmission factor through the activation energy barrier E^* and ν_{eff} is the effective frequency of motion along the reaction coordinate. The transmission factor is related to the Landau-Zener coefficient for curve crossing [256],

$$k_e = \frac{2P_0}{1+P_0}, \; P_0 = 1 - \exp\left(\frac{-|V|^2 \pi^{3/2}}{h\nu_{eff}}\sqrt{k_B T \lambda}\right) \tag{5.2}$$

where V is the electronic coupling matrix element and λ the total reorganization energy. In the limit of weak coupling of interest here (non-adiabatic limit), the probability P_0 can be expanded and truncated at second order leading to the usual expression for non-adiabatic electron-transfer rate,

$$k_{et} = \frac{2\pi}{\hbar} \frac{|V|^2}{\sqrt{4\pi\lambda k_B T}} \exp\left(-\frac{(\lambda + \Delta G^o)^2}{4\lambda k_B T}\right) \tag{5.3}$$

with ΔG^o the energy difference between the donor and acceptor energy levels and λ the reorganization energy. As explained before, this expression is derived for the electron transfer between two discrete energy levels. The total electron transfer rate K_{et} is obtained from the integral over all possible CB states with which the donor level can couple [250],

$$K_{et} = \frac{2\pi}{\hbar} \int_0^\infty dE \rho(E) |V(E)|^2 \frac{1}{\sqrt{4\pi\lambda k_B T}} \exp\left(-\frac{(\lambda + \Delta G^o - E)}{4\lambda k_B T}\right) \tag{5.4}$$

where ΔG^o is the energy difference between the CB edge and the redox potential of the adsorbate excited state, $\rho(E)$ is the density of states at energy E from the CB energy minimum and λ is the total reorganization energy. From equation 5.4, the injection transfer rate depends on four parameters namely, the reorganization energy λ, the electronic coupling matrix element V, the free enthalpy ΔG^o and the density of acceptor states $\rho(E)$. Other parameters can play a role in the full DSSC [259] which are not considered here because of the relatively short time scales investigated and the absence of electrolyte [260]. In addition, quantum confinement effect may also play a role since the discretization of the TMO CB is not considered in the model [261].

Since ZnO and TiO$_2$ have similar CB energy minima with respect to the vacuum level [245, 262], the free energy ΔG^o cannot account for the strong discrepancy in the injection rate. The effective electron mass m_e^* in ZnO is approximately one order of magnitude lower than in TiO$_2$. Since the DOS is proportional to $m_e^{*3/2}$ for an isotropic band dispersion, the electron transfer rate is expected to be ~30 times slower in ZnO than in TiO$_2$ from the difference in the density of acceptor states $\rho(E)$ [245, 246, 263][2]. This is not large enough to explain the

---

[2]The difference in effective mass originates from the different orbitals involved in the formation of the CB. In TiO$_2$, the CB is made of weakly dispersed 3d-t$_{2g}$ orbitals with large effective masses while it is made of highly

difference in injection rate by two to three orders of magnitude between TiO_2 and ZnO. The different orbitals involved in the CB formation affect the electronic coupling $V(E)$ with the donor excited state. Indeed, the 3d-t_{2g} states in the CB of TiO_2 can hybridize with the π^* orbitals of the dye leading to an increase in $|V|^2$ [245, 264] which can also contribute to the increase in injection rate. However, this parameter is not expected to vary by several orders of magnitude between ZnO and TiO_2 because of the similarity of the chemical bonding between N719 and the NP surface for both TMO. Hence, the difference in ΔG^o, $\rho(E)$ and $V(E)$ cannot account for the large difference in injection rate between ZnO and TiO_2.

In Marcus theory, the fact that the electron injection occurs from an ICTC (also called exciplex) is not considered. This mechanism has gained credibility recently with the ability to monitor both ICTC by TAS and free electron formation by THz/mid-IR spectroscopy [246]. In TAS, the appearance of spectral signatures of the dye cation is observed on a ~100 fs timescale [265] while the appearance of the Drude response of injected electrons in the THz or mid-IR appears on the ~10 ps timescale [264]. This leads to the conclusion that an intermediate state is involved between the charge injection and the formation of a free electron in the NP core. In some studies, the formation of a spectral signature of the ICTC has been found in the range from 900 to 1300 nm, decaying on the same timescale than free carrier formation [252, 266, 267].

The formation of a bound ICTC closely relies on the properties of the acceptor material to screen the injected charge via the zero frequency (static) dielectric constant $\epsilon_{\omega=0} = \epsilon(0)$. The literature reports a difference by a factor ~ 2 to 6 between ZnO ($\epsilon_{\perp,ZnO}(0) = 7.40$, $\epsilon_{\parallel,ZnO}(0) = 8.49$ [268]) and TiO_2 ($\epsilon_{\perp,TiO_2}(0) = 43$, $\epsilon_{\parallel,TiO_2}(0) = 13$ [269, 270]) static dielectric constants significantly lower than the difference invoked by Nemec and coworkers to interpret the formation of the ICTC [247]. We noticed that the reported static dielectric constant can vary by one order of magnitude depending on the chemical synthesis of the NP and $\epsilon_{TiO_2,\omega=0} > 100$ has already been reported [271, 272]. Such large differences in static dielectric constant lead to Debye screening lengths of the electron plasma of ~11 nm for ZnO and ~37 nm for anatase TiO_2 at our injected electron densities which are not very different because of the square root dependence of the screening length with the static dielectric constant. Hence, it is unlikely that the static dielectric constant alone can account for the formation of an ICTC in ZnO while free charges are directly formed upon injection in anatase TiO_2. The ICTC has the form of an ionized exciplex with a fully positive charge localized on the dye molecule and a fully negative charge within the TMO as recently shown by time-resolved photoemission spectroscopy in the XUV [251, 273]. An estimate of the binding energy of the ICTC of ~400 meV has been determined with the same technique probing within the ZnO gap after photoexcitation [253] in agreement with Monte Carlo simulations [247]. Recent studies have shown that moving away the dye cation from the NP surface with a spacer did not prevent the formation of the ICTC and that the Coulombic interaction cannot fully account for the difference in injection kinetics between ZnO and TiO_2. Instead, surface states may be involved, weakly coupled

---

dispersed 4s and 3p orbitals in ZnO.

with the bulk states [264] which supports our interpretation that the weaker screening of the injected electron into ZnO cannot explain the ICTC formation alone. In ZnO, surface states are formed upon anchoring dye molecules to Zn^{4+} cations which has not been found upon sensitization of TiO_2 [246] but can also be naturally present because of the unsaturated atoms at the NP surface [274].

In a recent work by Virkki and coworkers, the role of the slow formation of free charges in dye-sensitized ZnO has been investigated. They wonder if the slow injection rate may compete with charge recombination and decrease the DSSC performances in ZnO-based DSSCs while TiO_2-based DSSCs may not undergo this effect. Instead, they observed a larger electron-hole recombination rate at the interface in TiO_2 leading to larger injection efficiencies for ZnO from 20 ps after excitation and at later times [275]. Possible explanations for this effect are the 7 orders of magnitude larger drift mobility of electrons in ZnO [276, 277] than in TiO_2 [278] leading to a more efficient charge separation.

Conclusion

From our study, we managed to monitor charge-injection and ICTC formation at the ZnO/N719 interface via the exciton PB at the band gap of ZnO NPs. The formation of the ICTC leads to a delayed PB with progressive accumulation of the electrons at the bottom of the CB upon ICTC dissociation on the 10 to 100 ps timescale. TAS in the UV is an alternative method to THz or IR spectroscopy techniques looking at the Drude electrons upon injection. However, it is a substrate specific technique which offers interesting opportunities to investigate complex electron transport materials (ETMs) such as the recent record combination of SnO_2 and TiO_2 in perovskite solar cells [279, 280], which exhibit excitons at different energies in the UV and the deep-UV. We discuss the possible reasons for the formation of ICTC in ZnO and the difference with anatase TiO_2. The electronic coupling, the CB DOS and the static screening cannot separately account for the formation of the ICTC in ZnO and its absence in TiO_2. Possible reason for this is the involvement of surface states in the electron injection as recently demonstrated in anatase TiO_2 by TRXAS [281, 282] due to lattice disorder at the NP surface whose electronic structure may play a role in the injection efficiency.

6 Transient reflectivity in the deep-UV of a prototypical charge-transfer insulator: Nickel Oxide (NiO)

Summary

In this Chapter, the transient optical response of NiO single crystals and thin films is investigated after above band gap excitation. A fast lattice heating is observed on the ~10 ps timescale which shows the strong charge-phonon coupling in this system. The decay of the spectrum close to the main photobleach (PB) at the absorption maximum follows a third order kinetic law (Auger-like). The effect of crystal surface orientation and pump photon energy is investigated which shows a strong dependence of the optical response in the spectral and in the time domain. Finally, acoustic waves are detected in the differential transmission spectrum of NiO thin films which shows an amplitude enhancement closer to the Néel temperature. The energy transfer from the electronic to the bosonic degrees of freedom (DOFs) is discussed by comparison with the extensively investigated charge-transfer (CT) cuprate systems. The results presented in this Chapter are preliminary and some sections are limited to the description of the experimental data which are presented to provide material for discussion.

Introduction

Nickel oxide (NiO) is nowadays a widely used semiconductor in ceramics [283], hydrogenation catalysts [284], switching memory devices [285], electrochromic coating [286] or active material in gas sensors [287]. It is composed of nickel ions with electronic structure $[Ar]4s^03d^8$ in a +2 oxidation state. NiO has a rocksalt structure which exhibits a CT insulating gap ($E_g \sim 4$ eV) and an antiferromagnetic ground state at room temperature ($T_N = 525$ K) [288]. The optical spectrum first measured by Chrenko et al. shows a rich structure with a sharp optical absorption edge at ~4 eV characteristic of a wide band gap semiconductor and a manifold of peaks in the Visible region which are due to crystal field multiplets centred on Ni ions in the lattice [289].

The nature of the insulating gap in NiO has been historically controversial. It was first assigned to a Mott gap [290] but Sawatzky and Allen identified the role of the oxygen ligand in the

75

single particle gap energy and the CT character on the basis of complementary photoemission spectroscopy (PES)/inverse photoemission spectroscopy (IPES) experiments [291, 292].

The band structure of NiO has been characterized in the nineties by angle-resolved photoemission spectroscopy (ARPES) and the effect of the correlation on the band structure has clearly been observed by a splitting of the Ni 3d and O 2p bands [293, 294]. A set of theoretical calculations are now available which reproduce the band structure via cluster [295, 296], density functional theory (DFT)-local density approximation (LDA) [297], DFT-(LDA or generalized gradient approximation (GGA))+U [298, 299, 300], DFT-GW-LDA [301] and dynamical mean-field theory (DMFT)-LDA [302, 303, 304]. We briefly describe here the consensus reached about the electronic structure of NiO close to its optical band gap. The valence band (VB) maximum comes from the hybridization of oxygen 2p and Ni 3d(t_{2g}) orbitals while the conduction band (CB) minimum is almost made of pure Ni 3d(e_g) orbitals. The orbital mixture in the VB questions the CT nature of the insulating gap since it would be more accurately described as a mixture of Mott and CT insulator [305]. In fact, NiO falls into the intermediate regime of the Zaanen-Sawatzky-Allen classification which supports this observation [306].

The modelling of the optical spectrum from the NiO band structure is possible using the Bethe-Salpeter equation [307] which has been performed by Rödl and coworkers [300]. They show that the optical band gap is due to transitions from Ni(t_{2g}) to Ni(e_g) states which would correspond to a Mott insulator [308].

Despite the elusive CT or Mott character of the band gap, most studies on NiO nowadays consider a CT insulator whose band gap excitation transfers electrons from the oxygen 2p band to the upper Hubbard band (UHB) [309]. This point has been strengthened recently by resonant X-ray emission spectroscopy (RXES) experiments focusing on the CT [310, 311] from which the charge-transfer energy Δ, the Hubbard U and hybridization parameter W could be estimated in agreement with a CT gap. Due to the strongly correlated nature of the electron in the UHB and its low mobility, a convenient picture is to consider that under optical excitation, an electron is transferred from one oxygen atom to a neighbor Ni with an energy cost $\Delta \sim 4$ eV, the so-called CT gap.

In this Chapter, we investigate the transient optical properties in the spectral region of the NiO optical band gap after above gap excitation. The experiments are performed in transient reflectivity of NiO single crystal and differential transmission of NiO thin film with subpicosecond time resolution.

6.1 Results

6.1.1 Ellipsometry

A NiO (001) single crystal was purchased from Mateck. The absorption coefficient determined by spectroscopic ellipsometry is depicted in Figure 6.1 (blue curve) overlapped with the
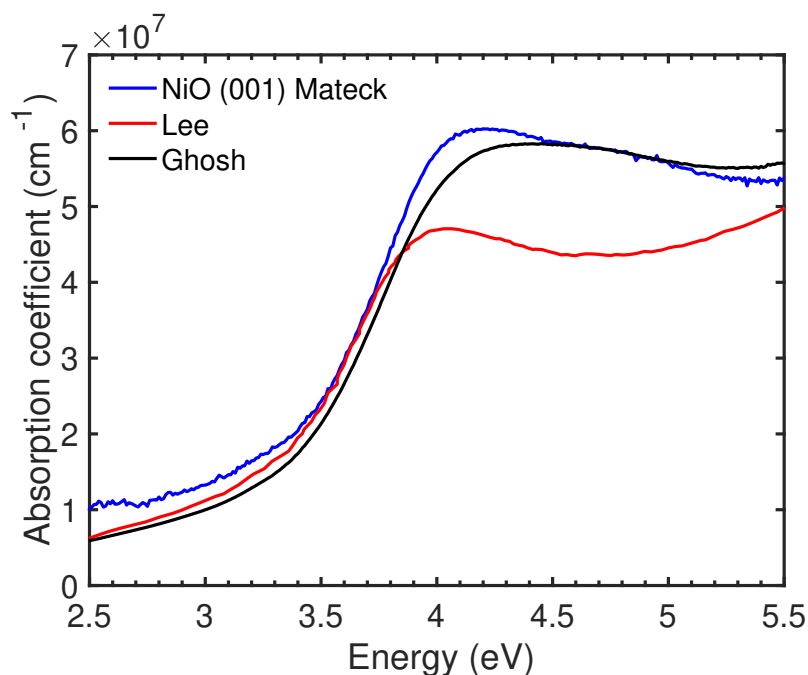
Figure 6.1 – Absorption coefficient determined by us using spectroscopic ellipsometry from NiO (001) (blue curve). Traces from the studies of Lee and coworkers [12] (red curve) and Ghosh and coworkers [13] (black curve) are also shown.

results from other studies [12, 13]. The absorption coefficient of NiO is characterized by a rapid increase around the optical band gap at ~3.6 eV which reaches a maximum around 4 eV followed by a decrease to higher photon energies.

The real and imaginary part of the dielectric constant are fitted with a sum of two Tauc-Lorentz oscillators[1] and one Lorentz oscillator[2] in Figure 6.2a showing an excellent agreement with the experiment (see Appendix H.2 for the details of the fitting). The fitting parameters are given in Table 6.1. In the expression of the Tauc-Lorentz oscillator, E_0 represents the oscillator resonance energy and E_g the material band gap. From the fit, the main peak at 4 eV is due to the overlap of one Tauc-Lorentz resonance at 3.86 eV and one Lorentz resonance at 4.68 eV. The second Tauc-Lorentz oscillator is used to model the increase of the imaginary part of the dielectric constant between 1 and 3.1 eV below the optical gap which has been assigned to a transition from the oxygen $2p$ orbitals to the Ni $4s$ orbitals [13]. Indeed, while most calculations ignore the role played by the $4s$ orbitals of Ni, GW calculations show that these orbitals are dispersed with an energy minimum within the optical gap [312] which gives rise to a first optical gap in the sub-1 eV region [13]. The temperature dependence of the imaginary of the dielectric constant is reproduced from Ref. [13] and depicted in Figure 6.2b. Upon temperature increase, some spectral weight is transferred from the region near the maximum

---

[1]See Appendix H.2 for the mathematical expression of the Tauc-Lorentz oscillator.
[2]We have used one Lorentz oscillator less than in a recent ellipsometry study over the same spectral range [13].
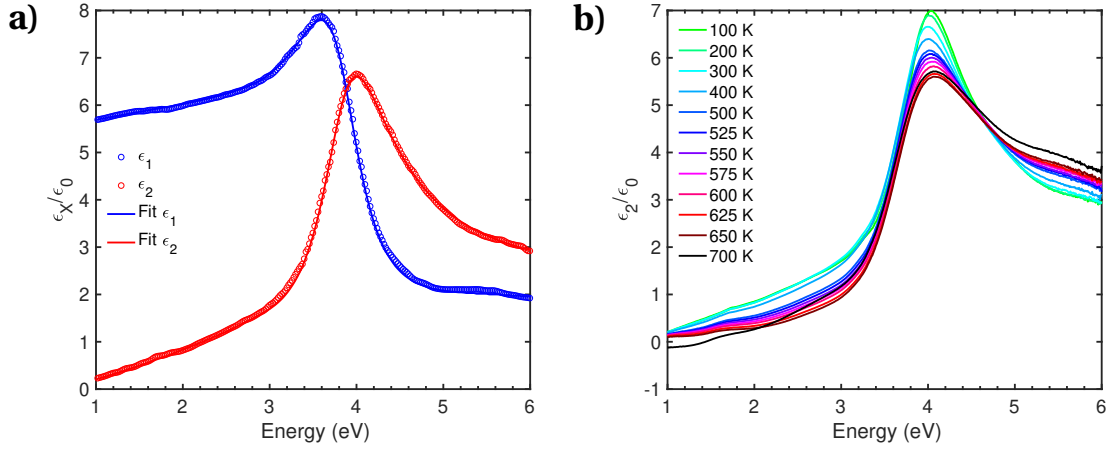
Figure 6.2 – a) Fit of the real (blue) and imaginary part (red) of the dielectric constant of NiO (001) with a sum of two Tauc-Lorentz oscillators and one Lorentz oscillator. b) Temperature dependence of the imaginary part of the dielectric constant (reproduced with permission from [13]).

at 4 eV to the above band gap region with an isosbestic point at 4.7 eV between 100 to 650 K.

Table 6.1 – Parameters of the fitting of the dielectric constant of NiO (001) with two Tauc-Lorentz oscillators and one Lorentz oscillator. Γ refers to the oscillator broadening, E_0 to the oscillator energy and E_g to the band gap.

oscillator	plasma frequency (eV)	Γ (eV)	E_0 (eV)	E_g (eV)
Tauc-Lorentz 1	54.8	0.86	3.86	2.95
Tauc-Lorentz 2	27.8	12.94	8.54	0.50
Lorentz	3.17	2.04	4.68	

In the following, we focus on the general behaviour of NiO in transient reflectivity in the region of its optical band gap at 4 eV in the deep-ultraviolet (UV).

6.1.2   Transient reflectivity upon above band gap excitation

The energy-time color-coded map obtained following 4.28 eV excitation is shown in Figure 6.3a (fluence 210 µJ/cm^2, 13 nJ per pulse). The transient exhibits a prompt negative signal at the position of the absorption coefficient maximum at 4.0 eV which decays over time. A positive signal appears on the low energy side centred at 3.6 eV on the ~10 ps timescale. Spectral traces at different time delays are plotted in Figure 6.3b which show the evolution of the transient reflectivity over time. The negative signal exhibits a kink around 3.9 eV.

In order to identify the possible contribution of a refractive index change to the transient reflectivity, we have performed measurements in transmission of a NiO (001) thin film (35 nm
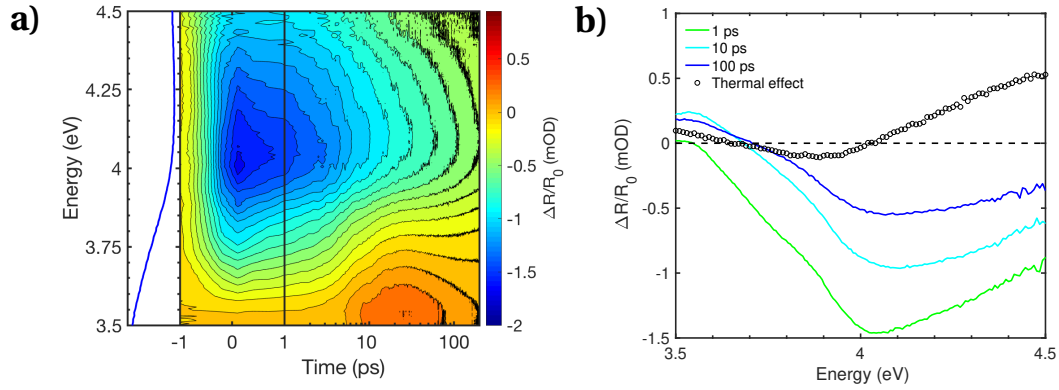
Figure 6.3 – a) Transient reflectivity following 4.28 eV excitation (fluence 210 μJ/cm²). b) Spectral traces at different time delays (colored lines). The change in reflectivity from a temperature increase from 300 to 400 K is shown with black circles.

thickness on MgO) which are shown in Figure 6.4a. The signal shape is the same as in reflectivity which shows that only changes in the absorption coefficient are observed. The positive modulation at short time delays in differential transmission is due to the self-phase modulation of the probe through the substrate by the pump pulse (Figure 6.4a). Time traces from the differential reflectivity are taken in the PB region and depicted in Figure 6.4b. The decay times are the same between 4.2 and 4.4 eV on the high energy side of the PB while an additional component appears progressively below 4.2 eV.
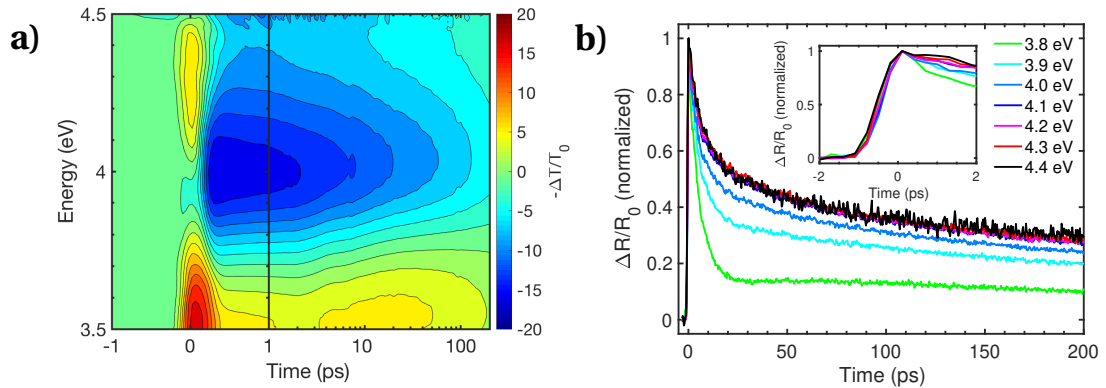
Figure 6.4 – a) Differential transmission measured on NiO (001) following 4.66 eV excitation. b) Time traces in transient reflectivity taken in the PB region of the differential reflectivity on NiO (001) 4.66 eV excitation. The time traces have been sign flipped for convenience.

On the picosecond timescale, the effect of lattice heating can be modelled from the temperature dependent ellipsometry data published by Ghosh and coworkers (Figure 6.2b) [13]. Only large temperature jumps of 100 K are available in the range close to room temperature so we have modelled the effect of the transient reflectivity under a lattice temperature increase of 100 K from 300 to 400 K and overlap the simulated transient in Figure 6.3b. It is clear that the signal shape at the optical band gap is not reproduced by a lattice temperature increase.

However, the kink observed on the low energy side of the main PB and the positive signal progressively appearing around 3.5 eV can be well described by the effect of the lattice temperature increase on the sample reflectivity. It is the consequence of the strong coupling between the charges and the lattice. This seems to be rather general in strongly correlated materials where efficient coupling to the bosonic fields have been demonstrated in cuprates [313, 314, 315, 316]. We discuss in more details this effect in section 6.2.
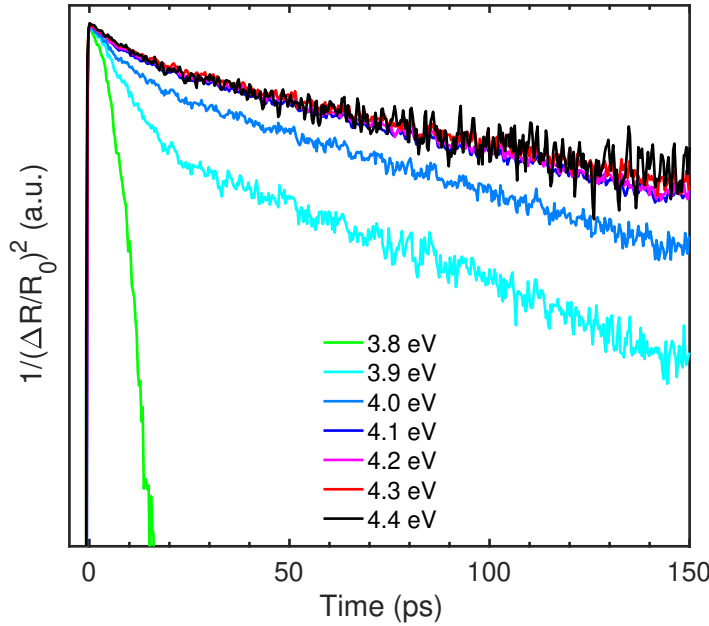
Figure 6.5 – Evolution of the transient reflectivity depicted as the squared inverse following a third order kinetic law.

The recovery of the electronic excitations in the CT insulators is expected to occur with a first order law exponentially [317]. However, we find that a third order law (Auger-like) is necessary to describe the temporal behaviour of the system from the plot of the squared inverse of the transient reflectivity over time (Figure 6.5). Over the first 150 ps, two decay kinetics can be clearly identified with a rather sharp transition from the first to the second around 20 ps.

6.1.3 Effect of the crystal surface orientation

We checked the influence of the NiO single crystal surface orientation on the dynamics over short timescales in transient reflectivity. The color-coded energy-time maps for the (001) and (101) orientations are depicted in Figure 6.6a,b following 4.28 eV excitation (fluence $210\,\mu J/cm^2$, 13 nJ per pulse). Normalized time traces are plotted in Figure 6.6c around the PB maximum. A faster decay time is observed for NiO (001) over the first few picoseconds but on longer timescales, we can guess that NiO (101) exhibits a faster recovery since the time traces seem to cross between the two surface orientations. Normalized spectral traces are plotted in Figure 6.6d. It shows that the spectral shape is the same on the low energy side of the PB
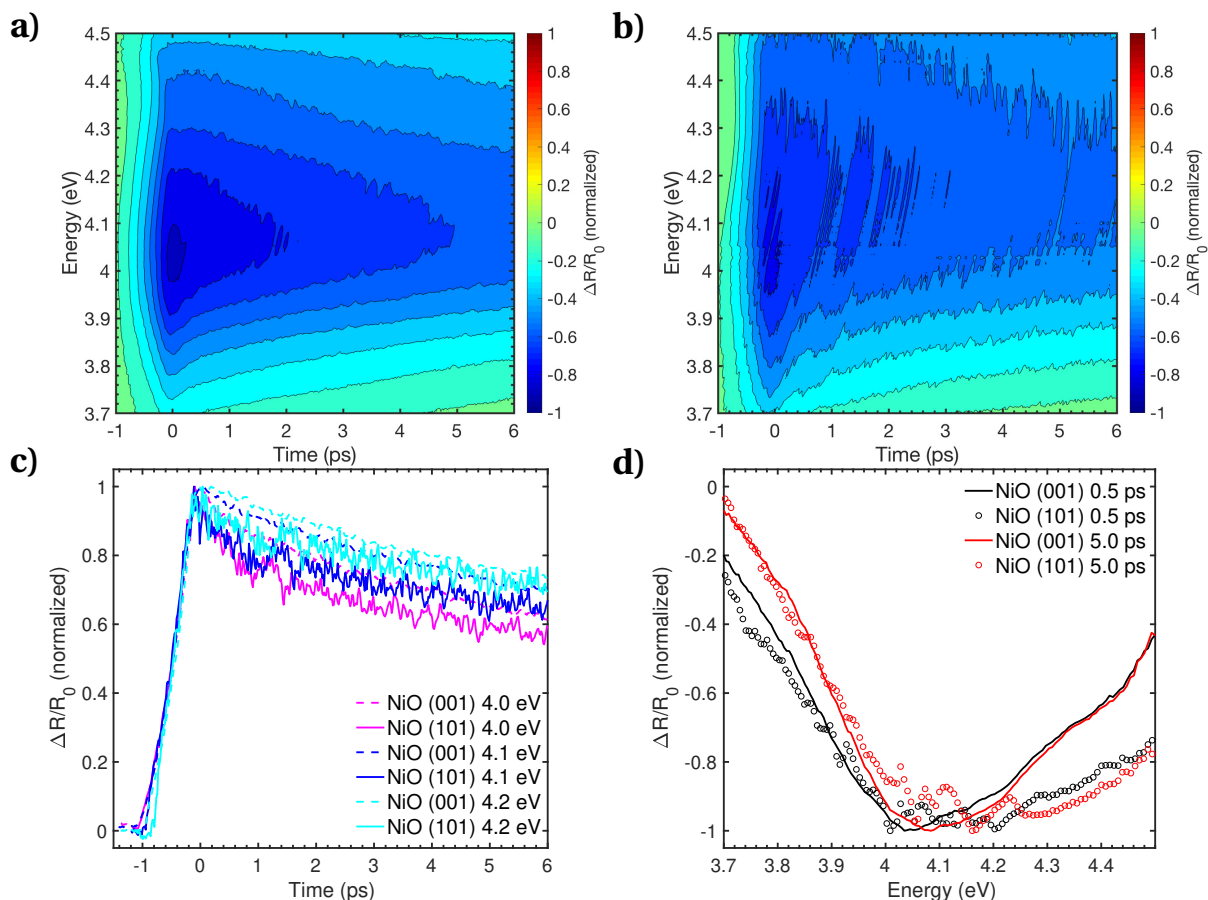
Figure 6.6 – Normalized transient reflectivity energy-time color-coded map for NiO a) (100) and b(101) oriented following 4.28 eV excitation. c) Time traces around the PB maximum for NiO (001) (dashed lines) and NiO (101) (continuous lines) at 3.9 (black) 4.0 eV probe photon energy. The sign of the time traces has been flipped for convenience. d) Spectral traces at 0.5 (black) and 5 ps (red) for NiO (001) (continuous lines) and NiO (101) (circles).

for both surface orientations while the PB is broader on the high energy side for NiO (101) at 5 ps. Since the ellipsometry gives the same absorption coefficient for both single crystal orientations, this is a transient effect.

6.1.4 Effect of the pump photon energy

Three pump photon energies have been used on NiO (001) in transient reflectivity at 3.54, 3.97 and 4.28 eV which are at the optical band gap onset, at the absorption maximum and above the optical band gap, respectively. For every pump photon energies, the same incidence fluence of 210 μJ/cm^2 is used. The energy-time color-coded maps are depicted in Figure 6.7. Note that the excitation at the optical gap onset at 3.54 eV generates the same signal shape than with higher pump photon energies which shows that an electronic excitation occurs at
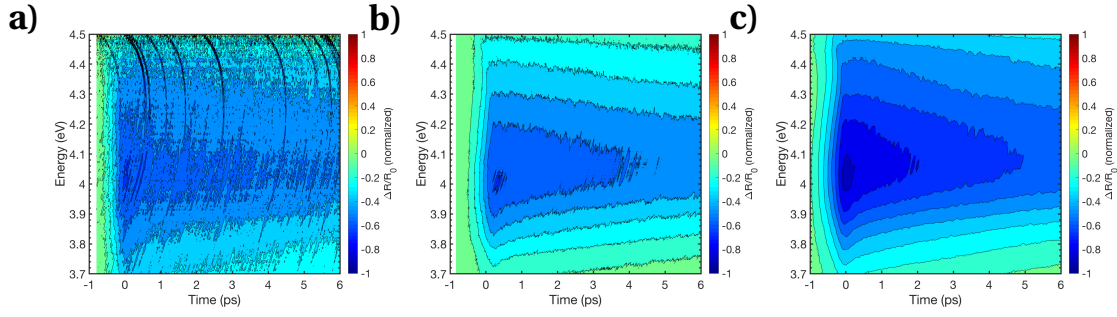
Figure 6.7 – Normalized transient reflectivity color-coded energy-time map following a) 3.54 eV, b) 3.97 eV and c) 4.28 eV pump photon energy excitation.

this pump photon energy we have used for the time-resolved X-ray absorption spectroscopy (TRXAS) experiment in chapter 7. Time traces are compared close to the PB maximum at 4.1 eV in Figure 6.8a. We observe that decreasing the pump photon energy seems to slow down the decay. Spectral traces at 5 ps are shown in Figure 6.7b. Between 3.97 and 4.28 eV excitation above the gap, the shape of the PB is the same on the low energy side but differs on the high energy side. The pump at the absorption onset (3.54 eV) generates a broad PB. Hence, the pump photon energy has a rather dramatic effect both in the time and in the spectral domain.
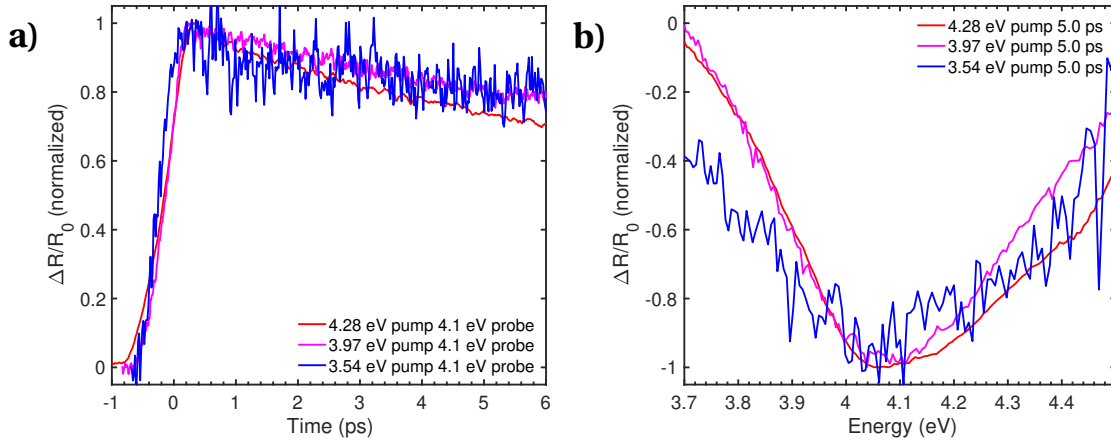
Figure 6.8 – Effect of the pump photon energy on a) the kinetics at 4.1 eV, b) the spectral traces at 5 ps. The time traces have been sign flipped for convenience.

6.1.5 Effect of the lattice temperature

Differential transmission were also performed on NiO (001) thin films deposited onto MgO (001) following 4.66 eV excitation at different lattice temperatures. The color-coded energy-time maps are depicted in Figure 6.9. We observe a strong variation of the signal amplitude between 495 K and 600 K where the Néel temperature is found (T_N = 525 K). Time traces at the PB maximum are depicted in Figure 6.10a. Close to time zero, a strong positive signal is observed which is due to self-phase modulation in the film. Oscillations are observed at later
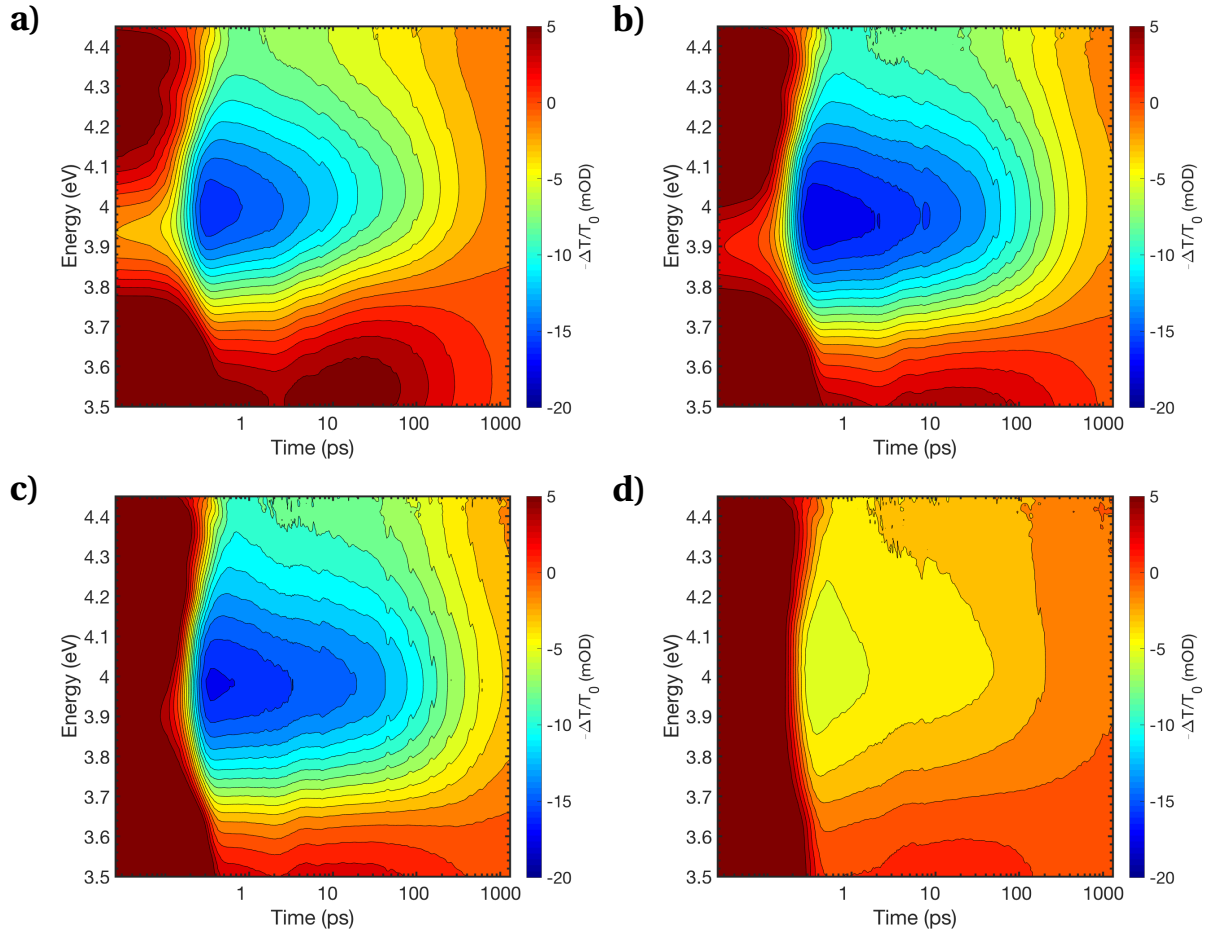
Figure 6.9 – Differential transmission measured on NiO (001) thin film following 4.66 eV at a) 350 K, b) 450 K, c) 495 K and d) 600 K. The overwhelming positive signal close to time zero (dark red color) is due to self-phase modulation.

times at 350, 450 and 495 K which are strongly quenched at 600 K. We have fitted the time traces at 3.54 eV and plot the residuals in Figure 6.10b to show the oscillations. We observe an amplitude increase from 350 to 450 K and a significant decrease at 600 K. This anomalous behavior seems correlated with the phase transition at the Néel temperature (T_N = 525 K) with the amplitude of the oscillations increasing up to T_N and decreasing afterwards. The period of the oscillations is ~5 ps[3]. This is in excellent agreement with the acoustic period of a 35 nm thin film with a sound velocity of 7.1 km/s [318, 319]. However, it is surprising that the amplitude of the acoustic wave depends in a non monotonic way on the lattice temperature. In the seventies, one study has identified an anomalous variation of the acoustic loss in NiO around the Néel temperature which reaches its maximum at T_N [320]. It is the opposite behavior to the evolution of the amplitude of the oscillations we observe, which reach their maximum amplitude closer to the Néel temperature.

---

[3]The oscillatory pattern becomes multimodal above the Néel temperature (600 K). Not enough oscillations are visible that would allow for a Fourier transform.

a)

b)
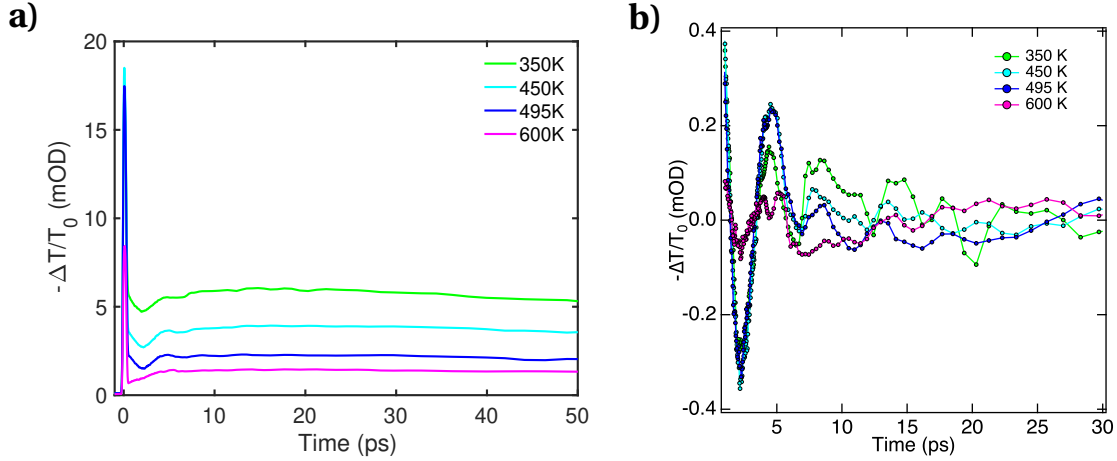
Figure 6.10 – a) Evolution of the time traces at 3.54 eV following 4.66 eV at different temperatures. b) Residuals of a multiexponential fitting showing the oscillations.

6.2 Discussion

The effect of above band gap excitation on the appearance of a broad photoinduced absorption (PA) band below the gap has been the subject of a number of studies on cuprate systems[4]. Okamoto and coworkers have studied the undoped cuprates Nd_2CuO_4 and La_2CuO_4 and observed a PA below the optical gap which corresponds to a temperature jump of ~50 K, 1 ps after excitation [313, 314]. The energy transfer from the electronic to the bosonic degrees of freedom is exceptionally fast in these systems which is a general manifestation of the entanglement between the electronic and lattice DOFs in strongly correlated materials. The PA goes together with a strong PB in the region of the absorption maximum similar to our observations in NiO. A recent study by the same group shows that the dressing of the electronic excitation into a magnetic polaron occurs on the 10 fs timescale [321]. Novelli and coworkers have observed the same effect on $La_2CuO_{4+\delta}$ pumping above and below the optical gap in the mid-infrared (IR) where polaronic excitations exist and couple to the electronic DOFs [315][5]. The strong coupling between the DOFs can also be investigated in the time domain where Raman impulsive mode are triggered by the band gap excitation into a coherent lattice fluctuation [323, 324].

In this Chapter, the appearance of a PA on the low energy side of the band gap of NiO after above band gap excitation is observed with a weak evolution between ~10 and 100 ps. We expect that some of the PA contribution comes from a lattice temperature increase due to the similarity between the energy position of the zero crossing of the transient reflectivity with the modelled change in reflectivity (Figure 6.3). However, this PA reaches is delayed with respect to the cuprates [313, 314]. Possible reasons for this effect are a weaker electron-phonon coupling

---

[4]Note that this is drastically different from the Drude response of electrons since the corresponding PA has a maximum while the contribution from Drude electrons to the transient signal evolves as λ^2.

[5]A review article covering the out-of-equilibrium dynamics of cuprates at the optical band gap region has been written [322].

strength although the temperature dependence of the absorption edge shows that NiO falls into the self-trapped exciton regime [325] described by Toyozawa [132] which involves a rather strong coupling. We know from chapter 7 that electron localization occurs in NiO in less than 100 ps which generates the reduction of Ni centres associated to bond elongation. This would be in agreement with the dressing of the electronic excitation that generates the PA below the optical band gap.

Conclusion

In this Chapter, we obtained preliminary results of the optical response of NiO, a benchmark CT insulator, after band gap excitation. The system shows a response which depends on the crystal surface orientation and pump photon energy both in the spectral and the time domain. The lattice heating predicted from temperature-dependent ellipsometry occurs in ~10 ps which is longer than in the cuprate systems. This shows the strong coupling between the electronic and lattice DOFs in this system which seems general in strongly correlated transition-metal oxide (TMO) systems. Differential transmission on NiO thin films at different temperatures shows acoustic waves whose amplitude is temperature dependent and seems to reach their maximum at the Néel temperature (T_N). Further experiments are on going to investigate this effect closer to T_N.

7 Electron localization upon optical band gap excitation in NiO microparticles investigated by time-resolved X-ray absorption spectroscopy at the Ni K-edge

Summary

In this chapter, the electron localization in NiO microparticles following optical band gap excitation is studied by time-resolved X-ray absorption spectroscopy (TRXAS) at the Ni K-edge. First, the X-ray absorption spectrum (XAS) of a particle suspension is measured. It reproduces the spectrum of NiO single crystals which shows the bulk-like structure of the particles. The X-ray absorption near-edge structure (XANES) is modelled with *ab initio* density functional theory (DFT) calculations to provide an assignment of the pre-edge peak. The TRXAS is measured 100 ps after optical excitation at the charge-transfer (CT) gap onset at 355 nm. The transient is modelled with a combination of chemical shift analysis and *ab initio* calculations in the XANES and in the extended X-ray absorption fine structure (EXAFS). The results are consistent with an electron localization in the antibonding Ni $3d$ orbitals which triggers a Ni-O bond elongation of ~7%. This is consistent with the formation of an electron-polaron already witnessed in other strongly correlated materials such as cuprates [315, 316] and band insulators such as anatase TiO_2 [326].

Introduction

NiO has been extensively investigated over the last few years because of its efficient hole transport properties [327, 328, 329] promising for solid-state photovoltaic applications [330]. Recent examples of its implementation include dye-sensitized [331] and perovskite solar cell heterojunctions [332, 333]. However, little is known about the mobility of the electrons in this material which can be generated from an optical excitation in the deep-ultraviolet (UV) (chap-

ter 6). NiO is a strongly correlated material whose electronic structure has remained enigmatic over the past few decades and has also more recently become a topic of textbooks in solid state physics [334] and review articles [335, 336, 337]. From complementary photoemission spectroscopy (PES)/inverse photoemission spectroscopy (IPES) experiments [338, 339, 340], it is well admitted that it is a wide band gap insulator ($E_g \sim 4$ eV at room temperature) whose valence band (VB) is made essentially of oxygen $2p$ states and conduction band (CB) made of nickel antibonding $3d$ states (see chapter 6) [304].

Photogenerated charge carriers in conventional semiconductors without strong correlations have rather large mobilities which can drop upon charge trapping or polaron formation. Typical timescales of charge trapping are on the femtosecond (fs) [282, 326] to picosecond (ps) timescale [240]. The formation of polarons can also occur on ultrafast timescales which depends on the phonon emission rates or the ability of the material to deform around photogenerated charges to trap them (self-trapped excitons). Hence, lattice modifications are observed as trapped charge or polaron form around specific atoms from which fundamental knowledge about lattice defects (trapping case [244]) or quasiparticle shape (polaron case [341]) can be obtained. An ideal technique to study this effect is time-resolved X-ray diffraction (TRXRD) or time-resolved electron diffraction (TRED) which is sensitive to bond distance modifications (structure factor) and to lattice parameter changes (Bragg peak position) [342, 343]. Although diffraction based techniques are powerful to observe the structural changes, they remain blind to the change in the material electronic properties[1]. In contrast, TRXAS is a powerful technique to probe the localization of photogenerated charge carriers around a given chemical element giving access to both electronic and structural information at the picosecond timescale provided by third-generation synchrotrons. We have already shown the capability of this technique to probe trapped electrons at undercoordinated Ti centres in anatase [281, 282] and rutile [78] TiO_2 nanoparticles (NPs), trapped holes at oxygen vacancies in ZnO [243, 244] and polaron formation in the inorganic lead halide perovskite $CsPbBr_3$ NPs [77, 78].

In this chapter, TRXAS is used to follow charge localization upon band gap excitation of suspended NiO microcrystals at the Ni K-edge. The Ni $3d$ orbitals form a weakly dispersed CB where photogenerated electrons get strongly localized in real space. The effect of the localization on the change in Ni−O bond distances is observed in the XANES and in the EXAFS while the filling of the Ni $3d$ states is observed in the pre-edge.

The chapter is divided as follows. First, experimental details about the XAS and TRXAS measurements are briefly presented. Then, the XAS spectrum of the NiO microcrystals is described with *ab initio* modelling in the XANES. The TRXAS results are presented in the main result part and are modelled in the following section with a combination of chemical shift and *ab initio* calculations in the XANES (XSpectra package) and in the EXAFS (FDMNES package). The observations of the TRXAS in the pre-edge, XANES and EXAFS converge to the picture of

---

[1]Although resonant X-ray diffraction (XRD) can give access to electronic degrees of freedom (DOFs) information [344].

an electron-polaron formed in less than 100 ps which is discussed in a last part.

7.1 Experimental details

The XAS and TRXAS experiments have been performed at the MicroXAS (X05LA) and SuperXAS (X10DA) beamlines of the Swiss Light Source (SLS). The pump pulse is made of the third harmonic of a Nd:YAG laser fundamental (1064 nm, Duetto, Time Bandwidth) at 355 nm. The X-ray beam is monochromatized in the spectral region of the Ni K-edge (~8.35 keV) with Si(111) and the detection of the absorption cross-section is performed in total fluorescence yield (TFY). Details about the sample preparation, UV-Vis spectrum of the solution and TRXAS experimental parameters are provided in Appendix E.1 and E.2. Briefly, NiO microcrystals powder has been purchased from Sigma-Alrich (325 mesh). A suspension is made in MilliQ water by sonication of the powder agglomerate for half an hour. The same sample has been studied in detail elsewhere which shows that the microcrystals are bulk-like [15]. The NiO concentration in the suspension is ~170 mM. The TRXAS setup and the sample delivery are detailed in Appendix G.4 also published elsewhere [17]. The X-ray energy calibration has been performed with a Ni foil and is detailed in Appendix E.3.

7.2 XAS of NiO microparticles at the Ni K-edge

7.2.1 Experimental spectrum

The XAS of the NiO microcrystals suspension at the Ni K-edge is depicted in Figure 7.1a for the XANES and Figure 7.1b for the EXAFS (blue lines). The spectrum exhibits a pre-edge peak at 8334 eV (labelled **A**) and shoulders in the edge at 8338 (labelled **B**), 8343 and 8347 eV with the maximum of the absorption coefficient at 8350 eV. The spectra in the XANES and in the EXAFS reproduce previously published spectra of NiO single crystals [14, 15, 345] (red lines in Figure 7.1) which shows that the NiO microparticles used in this study have the same electronic structure and lattice parameters than NiO single crystals.

7.2.2 Ab-initio XANES calculations

We performed *ab-initio* DFT calculations of the density of states (DOS) and XANES cross-section of bulk NiO at the Ni K-edge to find the orbitals involved in the underlying transitions, especially in the pre-edge. Such calculations in NiO are complicated by the strongly correlated nature of the material (see chapter 6). We summarize here the theoretical developments related to the description of the XANES spectrum of NiO at the Ni K-edge.

Zaanen, Sawatzky and Allen have shown that the ground state (Ψ_{GS}) of nickel ions in NiO can be described as a linear superposition of multiplets involving the Ni $3d$ orbitals and the oxygen $2p$ orbitals (labelled L in the following) due to the strong hybridization of these orbitals
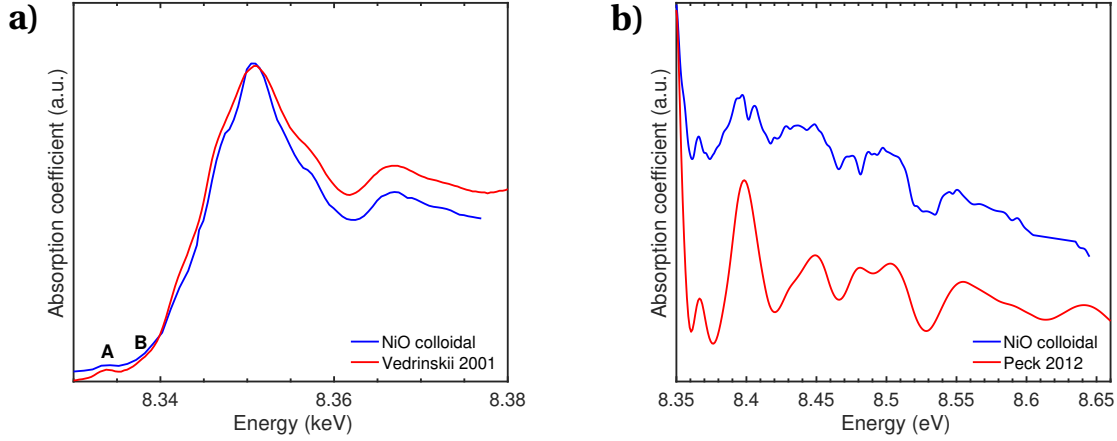
Figure 7.1 – a) XANES and b) EXAFS of NiO microparticles suspension at the Ni K-edge measured in TFY (blue curve). Overlapped are the measured XANES in [14] and EXAFS in [15] on NiO single crystals (red curve).

[346, 347],

$$|\Psi_{GS}\rangle = a_0\,|3d^8\rangle + a_1\,|3d^9\underline{L}\rangle + a_2\,|3d^{10}\underline{L}^2\rangle \tag{7.1}$$

where $\underline{L}$ stands for an oxygen $2p$ hole and $3d^X$ the filling of the Ni $3d$ orbitals with X electrons. The amplitudes a_i $(i = 0, 1, 2)$ of the different electronic configurations are 0.73, 0.21 and 0.06 respectively in the ground state [346, 347] which shows the large degree of hybridization between the orbitals redistributes the electron density from the ground state atomic configurations. These amplitudes strongly correlate with the electronegativity of the ligand (the larger the electronegativy, the less the amplitudes of a_1 and a_2) as was shown for cobaltites [348] and nickelates [349]. This shows the strong hybridization in the ground state of NiO. The effects of hybridization and correlation need to be considered in the calculations, the latter being related to the energy cost to put two electrons of opposite spin in the same orbital (*vide infra*).

The origin of the pre-edge peak **A** at 8334 eV has been debated and remains elusive. Garcia and coworkers claim that it originates from a dipole allowed transition to $O(2p) - Ni(3d)$ hybridized states supported by the correlation of the pre-edge peak amplitude to the degree of orbital mixing in a family of nickelates [349]. This is a general effect observed in transition-metal oxides (TMOs) at the metal K-edge in which pre-edge peaks are due to metal $3d$ and oxygen $2p$ mixed final states [350, 351]. Others claim that this pre-edge peak is due to a quadrupole transition to Ni $3d$ states forming an exciton with binding energy of $\sim$ 4 eV supported by experimental XAS [14, 352], resonant Auger spectroscopy [352], K-edge resonant X-ray scattering [353] and calculations [14, 16, 354]. More recent calculations have shown that this peak contains a weak dipolar component originating from the hybridization of the core-hole attracted Ni $3d$ orbitals with oxygen $2p$ orbitals [16] which supports the first assignment by Garcia and coworkers [349].
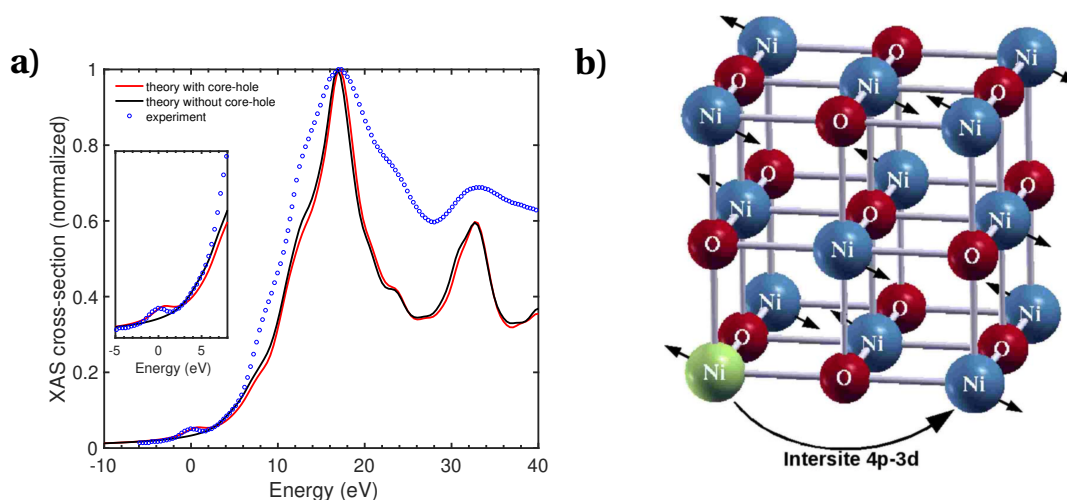
Figure 7.2 – a) Calculated XAS cross-section in the XANES region using DFT+U and a pseudopotential approach. Both calculations with the core-hole included in the pseudopotential (red curve) and without the core-hole (black curve) are overlapped with the experimental spectrum of NiO single crystal in Ref. [16] (blue circles). The zero energy is set at the Fermi level. b) Schematic of the off-site transition between the $1s$ orbital of the absorbing Ni atom and the $3d$ orbital of a neighbor Ni via $3d - 4p$ orbital hybridization. The absorbing Ni atom is in green with a majority up spin. The excited electron has a spin up due to Pauli blocking in the antiferromagnetic (AFM) phase.

Ab initio calculations of the NiO XANES at the Ni K-edge have followed the progress made in the theoretical description of the XAS. The early molecular orbital (MO) theory including core-hole effects reproduces the pre-edge peak which is assigned to a transition to Ni $3d$ states [350]. Rapidly, good agreement between the theoretical and experimental spectra has been reached with monoelectronic calculation techniques [355]. In this respect, important contributions are from Kuzmin and coworkers with finite difference method (FDM) and full multiple scattering (FMS) calculations in the muffin-tin (MT) approximation [354, 356, 357, 358, 359] although they did not focus on the pre-edge. The full-potential is not required for an accurate description of the XANES of NiO because of its cubic phase [359]. FMS with partial screening and spin-polarized potential to account for the majority spin on the Ni centre has been implemented in [14]. The self-consistency was added with many-body effects and complex energy-dependent self-energy in [360]. More recently, Gougoussis and coworkers have implemented a pseudopotential-based method that reproduces the XANES spectrum of NiO with very high fidelity [16]. The pre-edge peak **A** at 8334 eV is assigned to on-site quadrupolar excitations to Ni $3d$ states. Interestingly, they predict that the shoulder **B** at 8338 eV is due to a non-local dipolar excitation to a neighbor Ni atom $3d$ orbital via hybridization with the Ni $4p$ orbitals of the absorbing atom (Figure 7.2b). They further investigated the effect of introducing holes at the top of the oxygen $2p$ VB upon doping with lithium ions. The effect is to open an excitation channel from the Ni $1s$ orbital to the top of the VB as illustrated in Figure 7.3 where the appearance of a peak below peak **A** is observed which is due the hole

doping. Since this peak corresponds to a transition to the top of the oxygen $2p$ band and the shoulder **B** at 8338 eV is a transition to a neighbor Ni atom $3d$ orbital, the energy difference between these two peaks gives the CT gap (red double arrow in Figure 7.3). The authors find a CT gap of ~4.2 eV in NiO in agreement with complementary PES/IPES experiments [361] larger than the optical band gap of ~4 eV [289] due to excitonic effects. This shows the reliability of the assignment of **B** in [16] and provides an alternative method to look at the evolution of the CT gap amplitude. Finally, the *ab initio* calculation techniques presented here above are performed under the single-particle approximation which is justified most of the time at the metal K-edge due to the high kinetic energy of the photoelectron. However, a recent work by Calandra and coworkers has shown that a more accurate prediction of the XAS spectrum above the maximum absorption peak in the XANES can only be obtained including many-body effects such as shake-up transitions [362] which has been further developed more recently [363, 364]. The many-body description of the NiO XAS spectrum is out of the scope of this study.
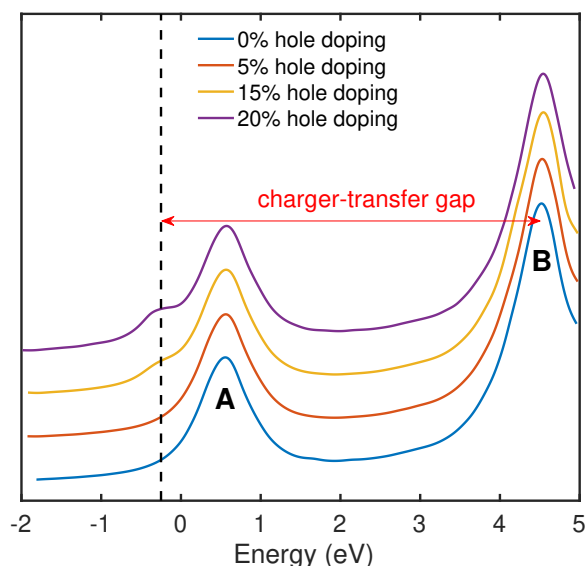
Figure 7.3 – Calculated influence of hole doping in $Li_xNi_{1-x}O$ on the pre-edge XAS (adapted from [16]). The spectrum is not convoluted to the experimental resolution. The zero energy is set at the Fermi level. Spectra are shifted vertically for clarity. The labels **A** and **B** correspond to those in the experimental XAS in Figure 7.1a.

For the purpose of the interpretation of the TRXAS data, we need an accurate theoretical description of the steady-state XANES of NiO so that the excited state spectrum after optical excitation can be modelled in a second time from the change of a set of parameters. In this respect, DFT+U based calculations of the DOS and XAS cross-section are performed on NiO at the Ni K-edge following a procedure developed elsewhere [16]. Details about the calculations are given in Appendix F.2. We arbitrarily set a majority spin up on the absorbing Ni atom. Calculations with and without core-hole effects are presented in Figure 7.2a with the zero energy set at the Fermi level. An excellent agreement is achieved between the experiment and the

calculation within the discrepancy of the experimental spectrum broadening. The core-hole has a dramatic improvement on the agreement between the experimental spectrum and the calculation in the pre-edge (inset in Figure 7.2a) and minor effect on the rest of the spectrum. Based on this calculation, the XAS cross-section can now be decomposed into dipolar and quadrupolar components. The final states involved in each transition is determined from the DOS of the different orbitals. The analysis of the XAS cross-section in terms of projected DOS onto specific orbitals (Lowdin projection [365]) shows that the pre-edge peak is due to a mixture of a quadrupolar and dipolar transition [16]. The former is from the Ni $1s$ to the Ni $3d$ orbitals of the absorbing atom (the excited electron is with spin down) while the latter corresponds to a transition to the O $2p$ - Ni $3d$ hybridized orbitals. Consequently, the pre-edge peak is sensitive to the Ni-O bond distance from its dipolar component and to the filling of the Ni $3d$ orbitals from its quadrupolar component. Noteworthy, the pre-edge structure **B** at 8338 eV would be dramatically affected without AFM ordering since both spin up or spin down could be transferred to a Ni nearest neighbor in this case [16]. Since we observe peak **B** in the experimental XAS spectrum of the NiO microparticles, the AFM ordering is conserved. It shows that the sample used in this study has a bulk-like structure based on the conservation of the AFM ordering and the similarity with the XANES and EXAFS measured on NiO single crystals (Figure 7.1). This supports the observation of the robustness of the AFM ordering even in NiO NPs [366]. The rest of the NiO XANES spectrum is purely dipolar and is due to transitions from the $1s$ to the p-DOS [16].

7.3 TRXAS of NiO microparticles at the Ni K-edge
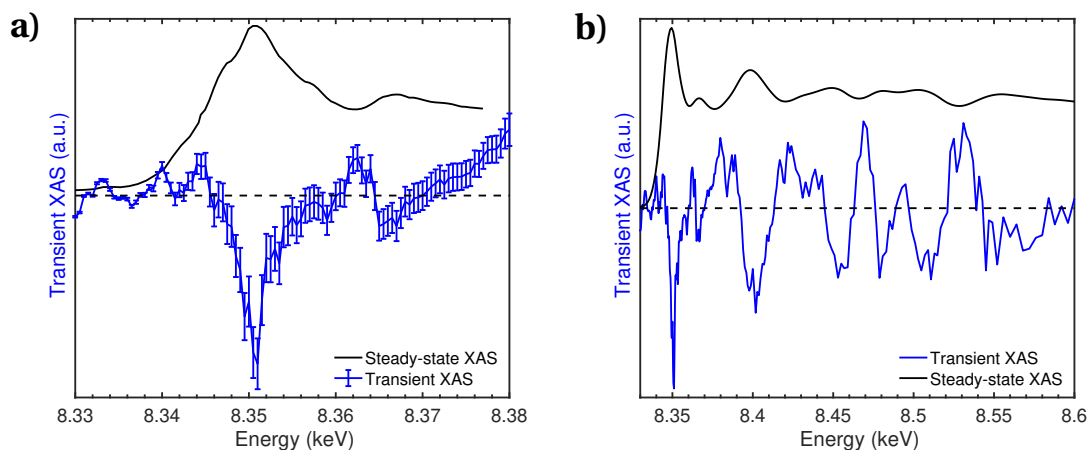
Figure 7.4 – TRXAS data from the NiO microparticles following 355 nm excitation and probing at the Ni K-edge (blue curve) a) in the XANES, b) in the EXAFS. The steady-state spectrum is shown for comparison (black curve). The dashed black line corresponds to the zero transient signal.

Transient spectral traces 100 ps after excitation of the colloidal suspension of NiO microparticles at 355 nm (3.49 eV) are depicted in Figure 7.4 in the XANES (panel a) and in the EXAFS (panel b) corresponding to the average of 30 scans. The transient shows a pronounced bleach

at the XAS maximum around 8350 eV. Strong modulations are observed in the EXAFS whose maxima and minima correspond to minima and maxima respectively of the steady-state XAS spectrum. This indicates a substantial change in bond lengths around Ni atoms in the structure after excitation. A similar pattern for the EXAFS transient spectrum has been reported in ZnO NPs which is modelled by a Zn-O bond elongation around an oxygen vacancy upon hole trapping [244]. In the pre-edge, although the error bars are small, we usually get non-zero signals which are due large fluctuations of the transient in this region not averaging to zero while the error bar is small because of the low number of detected photons [77]. Thus no conclusion is drawn and we measured specifically at the pre-edge peak at 8334 eV and acquired ~500 transient spectra which are averaged in Figure 7.5b. The transient shows that the pre-edge peak **A** amplitude decreases upon optical excitation on its low energy side. The evolution of the transient spectrum at different time steps in the XANES is given in Appendix (Figure E.3a). It shows that the negative transient signal at the XAS maximum (8350 eV) has positive wings which seem to recover more slowly than the bleach. A time trace taken at 8350 eV is shown in Figure 7.6. A biexponential decay is required to fit the time trace (blue curve) with time constants $\tau_1 = 90 \pm 10$ ps (37%) and $\tau_2 = 19 \pm 2$ ns (63%) in the investigated time window. A fluence dependence of the transient signal is reported in Appendix (Figure E.2a) which shows that all transient features in the XANES persist at fluences down to ~50% the one used for the experiment presented in this chapter. In addition, Figure E.2b shows that the amplitude of the negative transient signal at the XAS maximum is linear in the range of investigated fluences. The pump photon energy has been increased to 266 nm (4.67 eV) which provides the same transient signal than with 355 nm excitation showing that the TRXAS is likely independent on the pump photon energy on the investigated 100 ps timescale (Appendix Figure E.3b).
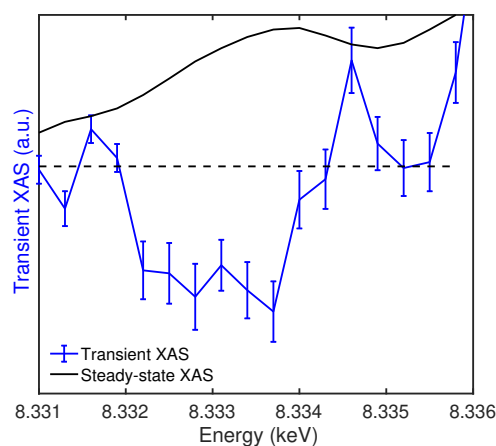
Figure 7.5 – Transient XAS in the pre-edge of NiO following 355 nm excitation and probing at the Ni K-edge (blue curve). The steady-state spectrum is shown for comparison (black curve). The dashed black line corresponds to the zero transient signal.
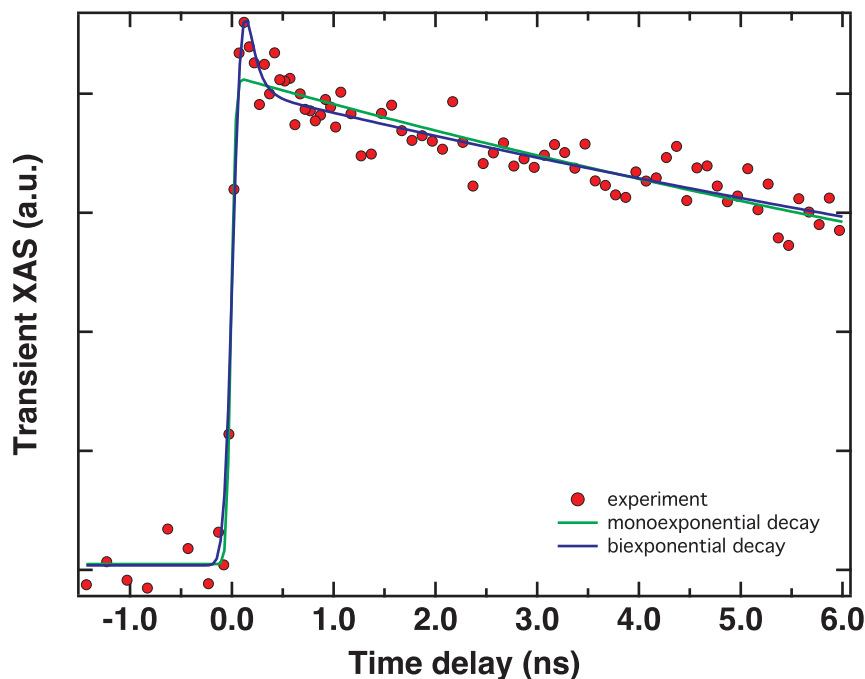
Figure 7.6 – Time trace at 8.35 keV of NiO colloidal suspension following 355 nm excitation (red dots). A monoexponential decay cannot reproduce the time trace in the first 500 ps. A biexponential decay provides $\tau_1 = 90 \pm 10$ ps (37%) and $\tau_2 = 19 \pm 2$ ns (63%) in the investigated time window.

7.4 Modelling of the TRXAS

In order to explain the transient signal observed at the Ni K-edge in NiO we rely on chemical shift models we have already used in the past [77, 78, 281] and *ab-initio* calculations in the XANES (DFT+U with XSpectra) and in the EXAFS (FMS with FDMNES).

7.4.1 Chemical shift

When a photoexcited electron or hole localizes around a specific atom in the lattice, the energy levels can be drastically affected due to the change in screening properties after reduction or oxidation [367]. The effect on the XANES is to red or blue-shift the spectrum upon reduction or oxidation respectively, providing a first derivative lineshape in the transient spectrum. This has already been shown after band gap excitation of anatase [77, 281] and rutile [78] TiO$_2$ where electrons get trapped at pentacoordinated titanium atoms which is similar to a reduction of the titanium oxidation state. Figure 7.7 shows the simulated transient XAS spectra upon reduction or oxidation of the nickel atoms with different chemical shifts. None of the simulated transient reproduces the transient XAS spectrum where the bleach is more pronounced than the positive wings which shows that a reduction or oxidation alone cannot

95

account for the transient. Overall, a better agreement is achieved upon reduction (red shift of the steady-state XAS spectrum) especially for the two positive wings on the low and high energy side of the main negative signal at 8350 eV.
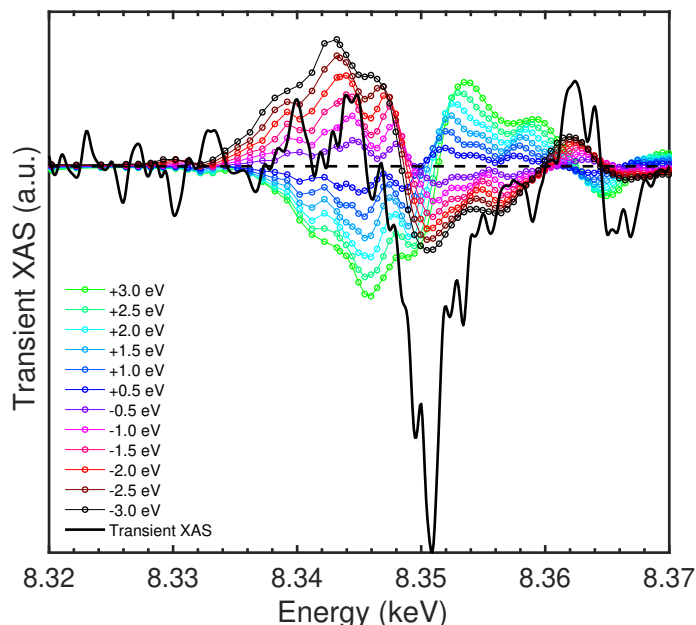
Figure 7.7 – Simulation of the transient XAS in the XANES region based on a rigid shift of the steady-state XAS spectrum by a given energy amount. Blue shifts (positive energy shifts) correspond to Ni oxidation and red shifts (negative energy shifts) correspond to Ni reduction.

7.4.2   *Ab-initio* calculation in the EXAFS

Before modelling the TRXAS in the EXAFS, an accurate description of the ground state EXAFS is required. We have performed FMS calculations in the $F_{m\bar{3}m}$ cubic phase of NiO as implemented in the FDMNES package developed by Y. Joly (details of the calculation in Appendix F.3.1) [368, 369]. The calculated and experimental EXAFS spectra are depicted in Figure 7.8. A good agreement is achieved for lattice parameters $a = b = c = 4.1684$ Å which is 0.2 % shorter than the reported lattice parameter of NiO single crystal [370, 371]. Although the relative amplitudes of the extrema differ between the experiment and the theory, they occur at the same energies. Some features are more pronounced in the computed spectrum while the experimental spectrum damps more rapidly to higher energies because of the amplitude reduction factor of the photoelectron with increasing kinetic energy [372] which is not considered in the calculation. Hence, we expect the transient spectrum computed by FMS not to reproduce quantitavely the amplitude of the oscillations of the TRXAS but the sign of the transient signal and the energy position of the extrema should be captured.

In order to simulate the TRXAS, we need to narrow down the number of parameters to play with in the calculations by guessing how the system has evolved ~100 ps after excitation.
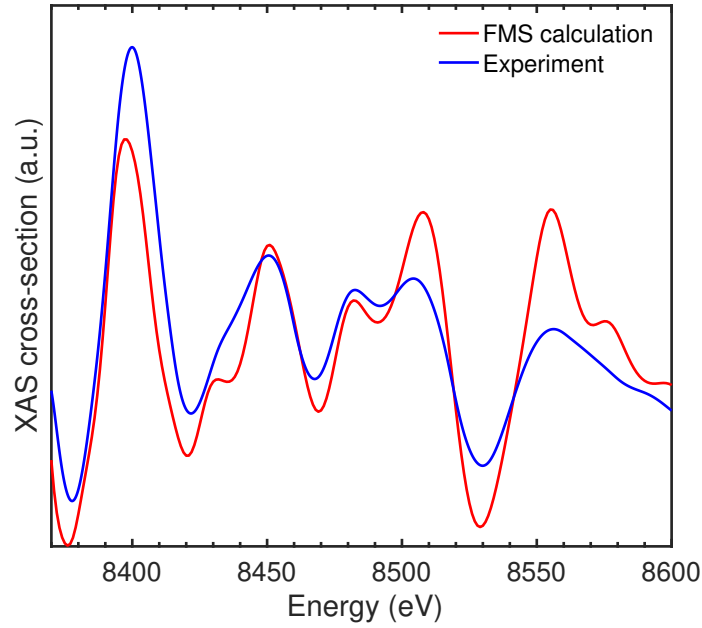
Figure 7.8 – Overlap between the experimentally measured EXAFS on NiO at the Ni K-edge (blue curve) and the computed spectrum with FMS (red curve).

In the EXAFS, single scattering events of the photoelectron dominate which provide direct information about the bond distances [373]. Thus, a transient in the EXAFS can be either due to a change in the bond distance (elongation or contraction) or to an increased Debye-Waller factor[2] which damps the XAS with photoelectron momentum k following $e^{-k^2 \langle \mathbf{u}(T) \rangle /3}$ with $\langle \mathbf{u}(T) \rangle$ the thermal average atomic position [376]. The change in EXAFS due to the Debye-Waller factor with increased temperature can be simulated with the FDMX package associated to FDMNES [377]. However, the effect is similar to bond elongations since the average bond distance increases upon temperature increase.

We have modelled the TRXAS in the EXAFS with *ab-initio* FMS simulations of the transient EXAFS upon bond elongations and contractions around Ni atoms in the structure keeping the cubic symmetry. The Ni-O bond distance is changed by a fixed amount all over the structure which corresponds to a homogeneous lattice parameter change along the three orthogonal lattice vectors. A change of the lattice parameter corresponds to twice the Ni-O bond length change in the face-centred unit cell of NiO. From the calculated EXAFS spectrum with bond length change (excited state, A_{ES}) and the calculated ground state spectrum A_{GS}, the photoexcitation yield f is required to model the transient spectrum ΔA according to,

$$\Delta A = f(A_{ES} - A_{GS}) \tag{7.2}$$

---

[2]The Debye-Waller factor decreases the oscillation amplitudes because of the thermal disorder introduced in the atomic distribution and the increase of the average bond distance [374, 375]

We have fitted the experimental TRXAS (ΔA) from the calculated A_{GS} and A_{ES} leaving the photoexcitation yield as a free parameter (see Appendix F.3.1 for further details). Figure 7.9 shows the computed transient spectra for bond elongations (panel a) and contractions (panel b) by different amounts of the ground state lattice parameter. A very good agreement is achieved when the Ni-O bond expands with the best agreement for a relative lattice parameter increase by 15% from the ground state (based on the R goodness-of-fit parameter). In the case of bond contraction, the fitted photoexcitation yields gives negative values which means that it gives an unreasonable description of the NiO excited state. We then plot the modelled transient with a fixed positive excitation yield of 2% in Figure 7.9b for comparison. It is clear that bond contraction is inaccurate to describe the TRXAS spectrum from the energy position of the extrema in the modelled transient. Hence, the best agreement is obtained for a Ni-O bond elongation of ~7% which corresponds to a fitted excitation yield of ~1.8%. This is in agreement with our upper limit estimate based on the experimental parameters (Appendix E.4).

7.4.3 *Ab-initio* calculation in the XANES

In order to corroborate the Ni-O bond extension from the analysis of the transient EXAFS, we simulated the effect of the bond extension on the XANES spectrum. In that respect, we calculated the XANES spectrum with XSpectra similarly to the ground state spectrum (Figure 7.2a) with pseudopotentials including dipolar and quadrupolar matrix elements as well as core-hole effects [16]. The simulated transients for different relative lattice parameter expansions are depicted in Figure 7.10 leaving the photoexcitation yield as a free parameter similarly to the previous section. In contrast to the EXAFS, the agreement with the experimental transient is not excellent in the XANES likely due to the overlap of electronic and lattice effects in this part of the XAS. However, the main bleach around 8.35 keV (10 eV in relative energy scale) is reproduced as well as the positive wing on the high energy side. An additional negative contribution from the electronic response is probably missing around 8.35 keV which would rescale the relative amplitude of the bleach and the positive wings to get a better agreement with the experimental transient. The simulated transients give zero signal at the pre-edge peak which means that it is insensitive to bond elongation and that the transient response observed experimentally in Figure 7.5b is not an electronic response related to the lattice parameter change. The same calculations are performed for the lattice contraction and given in Appendix (Figure F.3) which disagree with the experimental transient. Hence, both the transient XANES and EXAFS point to a Ni-O bond elongation following the pump excitation. Nevertheless, the EXAFS is more appropriate than the XANES to estimate the bond elongation of ~7% due to the overlapping electronic and lattice contributions in the XANES.

7.4.4 Transient at the pre-edge peak

The transient at the pre-edge peak **A** is negative (Figure 7.5) which means that the corresponding bound transition has a lower cross-section after optical excitation. In the previous section,
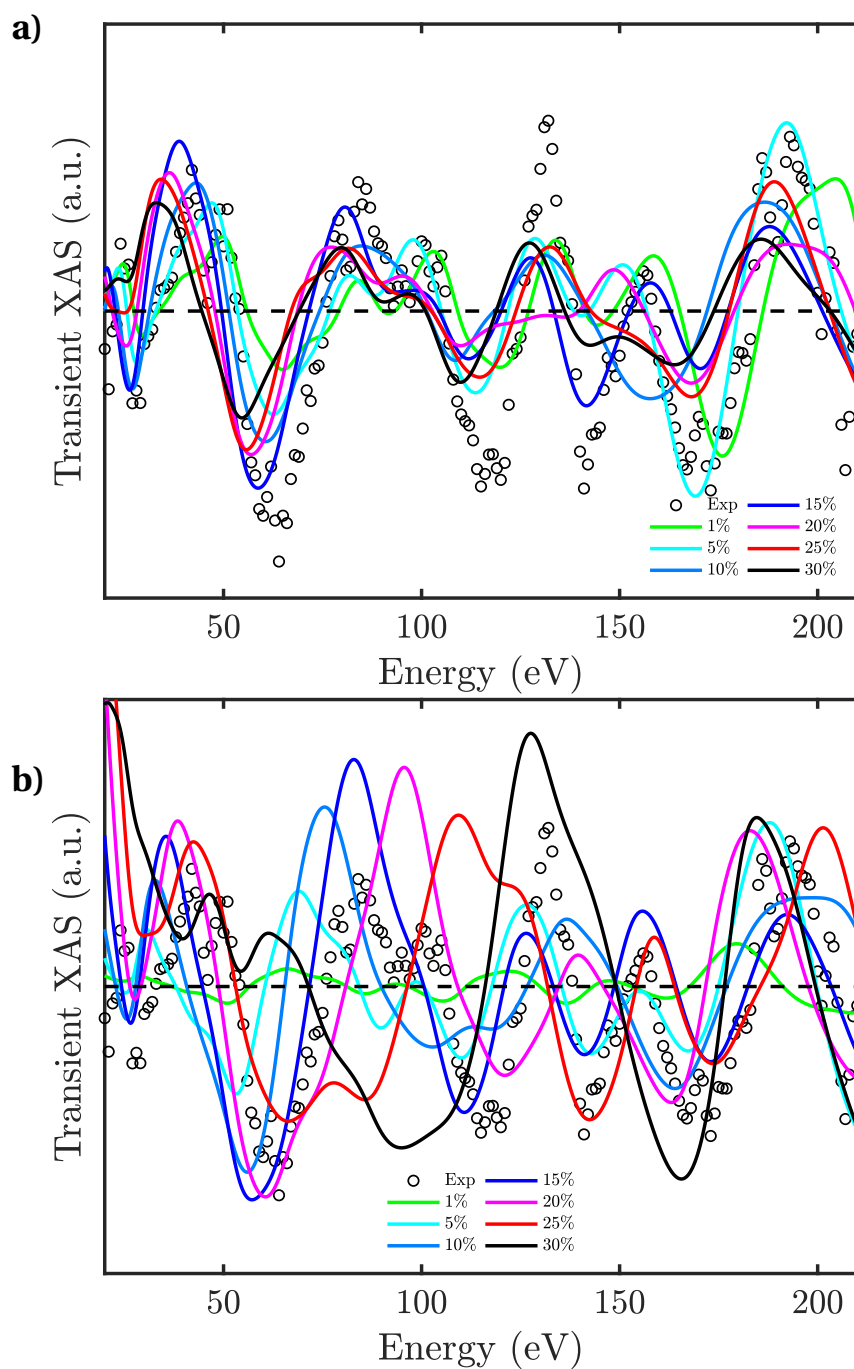
Figure 7.9 – Simulated transient spectra in the EXAFS at different amount of Ni-O a) bond elongations and b) bond contractions (colored curves). The percentage refers to the amount of elongation relatively to the Ni-O bond length in the ground state. In b), The excitation yield is kept constant at 2% because of the lack of convergence of the fitting. The zero energy is set at the Fermi level. The experimental TRXAS is shown with black circles.
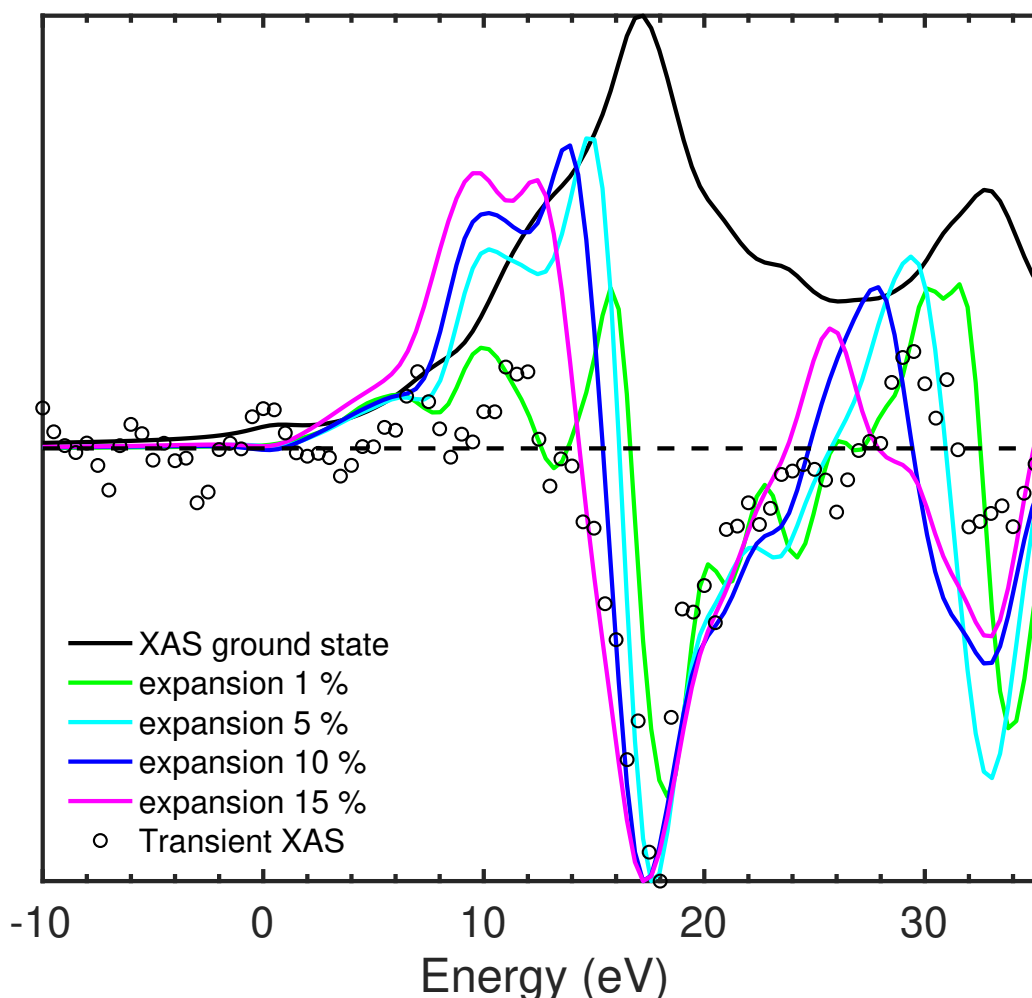
Figure 7.10 – Simulation of the transient spectrum with different relative lattice expansions (colored curves) overlapped with the transient spectrum (black circles). The calculated ground state spectrum is shown with the thick black line for reference. The Fermi energy is set to zero.

the *ab initio* calculations have shown that the change in Ni-O bond length does not affect the pre-edge peak amplitude. Since this peak corresponds to a mixture of on-site quadrupolar excitation to the Ni $3d$ states and dipolar excitation to hybridized $O(2p)$-$Ni(3d)$ final states, a contribution from the dipolar component can be excluded since a change in Ni-O bond length would lead to a change in the dipole cross-section. A contribution from the holes can also be excluded since the introduction of holes by chemical doping does not affect the amplitude of the pre-edge peak itself (Figure 7.3), the negative transient observed experimentally is thus due to the electrons.

NiO is a CT insulator in which the excitation at the optical band gap transfers electron population between oxygen $2p$ orbitals in the VB to Ni $3d$ orbitals in the CB. Upon this electron transfer, the probability of X-ray absorption promoting an electron from the Ni $1s$ to $3d$ states

at the K-edge on the same atom as the optical excitation has occurred (quadrupolar transition) becomes less which leads to a negative transient signal in agreement with our observation.

The calculations performed by Gougoussis and coworkers introducing holes in the VB upon doping of NiO with lithium (Figure 7.3) shows that a new peak appears on the low energy side of peak **A** due to the opening of the excitation from the Ni 1s to the VB maximum [16]. This means that the hole left at the VB maximum by the optical excitation may generate a positive transient signal on the low energy side of the pre-edge peak. We did not observe this positive transient which may be due to our low excitation yield. Alternatively, this may be due to a difference in hole localization between lithium doped NiO (as in the calculations by Gougoussis [16]) and the photogenerated hole in our experiment. The hole localization in Li$_x$Ni$_{1-x}$O has been widely debated with claims that the hole is localized on the nickel [378, 379, 380] or on the oxygen atom [381, 382, 383, 384]. In the first case, a hole localizing on the nickel atom differs from the optical excitation triggered in NiO which generates holes in the oxygen 2p band. In the second case, localization of a hole on the oxygen atom may influence its electronic structure and affect bond distances. In both cases, the localized hole generated by chemical doping may be of different nature than the photogenerated hole which is expected to be delocalized in the oxygen 2p band in the latter case. For a delocalized hole, the effect on the local electronic structure of the nickel atom may be too weak to be observed by TRXAS at the Ni K-edge.

Now that we have isolated the contribution of the photogenerated electron in the transient spectrum in the pre-edge, a possible connection can be established with the bond elongations observed in the modelling of the transient XANES and EXAFS. The Ni 3d orbitals involved in the formation of the CB are antibonding which can lead to bond elongation upon excitation. At the timescales investigated here, the effect of the electronic excitation is likely to have already triggered a lattice response [326, 342]. In the next section, we discuss the effects of electron localization, chemical shift, orbital population and bond elongation together.

7.4.5 Discussion

From the bond elongations observed in the XANES and in the EXAFS and the filling of Ni 3d orbitals observed in the pre-edge, these results together are consistent with an electron localization at a Ni site 100 ps after optical excitation. The localization should reduce the nickel centre and trigger a red shift at the Ni K-edge which is consistent with the chemical shift modelling (section 7.4.1). In addition, the lattice relaxes upon localization with a Ni-O bond elongation by ~7% (sections 7.4.2 and 7.4.3). This is consistent with the formation of a small polaron which has been shown in NiO [385, 386]. The bleach of the pre-edge peak is also consistent with electrons populating the Ni 3d orbitals (section 7.4.4). Since the CB of NiO is made of antibonding 3d orbitals, the electron localization in one of these orbitals is expected to trigger bond elongations consistent with our observations [302, 304]. This process forms a Ni 3d^9 centre which can undergo a Jahn-Teller distortion [387, 388]. However,

this typically leads to bond-elongations in a single plane which is inconsistent in contrast to the homogeneous bond elongation along the crystallographic axes observed in our study. The time trace measured at the XAS maximum where the contribution of bond elongation dominates the XANES shows that the lattice change occurs within the instrument response function (IRF) of our setup in less than 100 ps. The difficulty in this study is the probable overlap between electronic and lattice changes in the transient response of NiO in the XANES. Work is ongoing to implement these two DOFs in a single theoretical *ab initio* framework.

In Mott-Hubbard theory, the formation of an electron pair in one Ni $3d$ orbital is called a doublon [389]. These quasiparticles have large effective masses and low mobilities in the AFM phase [390]. However, this theoretical description is not associated with lattice distortion hence we think the electron-polaron picture is a more appropriate description of the actual excitation in NiO on the 100 ps timescale. These quasiparticles form bands in the strongly interacting electron-phonon regime [391]. The recent study on cuprates by Fausti and coworkers have witnessed the formation of bosonic dressed quasiparticles upon excitation just below the band gap [315] which are compatible with the formation of electron-polarons. This seems to be the case for a variety of strongly correlated systems [392, 393, 394] on ultrafast timescales in the femtosecond regime [316]. Especially, our pump excitation at the onset of the absorption spectrum may populate directly these states so that the electron-polaron is immediately localized. We think the bulk-like structure of the NiO microparticles in this study prevents the defect-assisted localization of photogenerated charges (extrinsic) [15]. More studies are required in this respect. Especially, the advance of femtosecond free-electron lasers (FELs) may be a useful tool to investigate the formation of electron-polarons with the chemical, electronic and structural sensitivity of the X-rays [395].

Conclusion

TRXAS on a suspension of NiO microcrystals upon excitation at the onset of the CT gap shows that photogenerated electrons get localized at Ni sites in antibonding $3d$ orbitals in less than 100 ps. The charge localization triggers a large Ni-O bond elongation of ~7% which is consistent with the formation of an electron-polaron [72, 396]. The absence of transient positive signal on the low energy side of the pre-edge peak indicates no hole localization at the Ni sites which has implications for the use of NiO as efficient hole transport materials in solid-state solar cells [330].

8 XAS linear dichroism at the Ti K-edge of anatase TiO$_2$ single crystal

8.1 Introduction

Titanium dioxide (TiO$_2$) is one of the most studied large-gap semiconductor due to its present and potential applications in photovoltaics [397] and photocatalysis [398]. The increasingly strict requirements of modern devices call for sensitive material characterization techniques which can provide local insights at the atomic level [399, 400]. K-edge X-ray absorption spectrum (XAS) is an element specific technique, that is used to extract the local geometry around an atom absorbing the X-radiation, as well as its electronic structure [401]. A typical absorption K-edge is usually composed of three parts: (i) at high energy above the absorption edge (typically > 50 eV), the extended X-ray absorption fine structure (EXAFS) contains information about bond distances. Modelling of the EXAFS is rather straightforward, as the theory is well established [401]. (ii) The region of the edge and slightly above (< 50 eV) represents the X-ray absorption near-edge structure (XANES), which contains information about bond distances and bond angles around the absorbing atom, as well as about its oxidation state. In contrast to EXAFS, XANES features require more complex theoretical developments due to the multiple scattering events and their interplay with bound-bound atomic transitions; (iii) the pre-edge region consists of bound-bound transition of the absorbing atom. In the case of transition metals, the final states are partially made of d-orbitals. Pre-edge transitions thus deliver information about orbital occupancies and about the local geometry because the dipole-forbidden s-d transitions are relaxed by lowering of the local symmetry. The Ti K-edge absorption spectrum of anatase TiO$_2$ (a-TiO$_2$) exhibits four pre-edge features labelled A1, A2, A3 and B (see Figure 8.2), while rutile TiO$_2$ only shows three [402, 403]. These have been at the centre of a long debate, which is still going on, especially in the case of the anatase polymorph [404, 405, 406]. A summary of the assignment of pre-edge transitions from previous works is given in Table 8.2.

Early theoretical developments to explain the origin of pre-edge features in a-TiO$_2$ were based on molecular orbital (MO) theory [350, 407, 408] which showed that the first two empty states in TiO$_2$ are made of antibonding t_{2g} and e_g orbitals derived from the 3d atomic orbitals

of Ti. Transitions to these levels have, respectively, been assigned to the A3 and B peaks while its absorption edge is made of Ti t_{1u} antibonding orbitals derived from Ti $4p$ atomic orbitals. Although MO theory can predict the energy position of the transitions accurately, it cannot compute the corresponding cross-sections and does not account for the core-hole to which quadrupolar transitions to d-orbitals at the K-edge are extremely sensitive [405]. The corresponding transitions are usually blue shifted by the core-hole and appear as weak peaks on the low energy side of the pre-edge. In a-TiO$_2$, peak A1 contains a significant quadrupolar component [405] which explains the inaccuracy of MO theory to predict this transition. full multiple scattering (FMS) is a suitable technique to treat large ensemble of atoms and obtain accurate cross-sections [404, 406, 408, 409]. A consensus has emerged assigning A1 to be of partial to pure quadrupolar character, A3 a mixture of dipolar and quadrupolar character with t_{2g} orbitals and B, a purely dipolar transition involving e_g states [408, 410]. However, as correctly pointed out by Ruiz-Lopez [408], this simple picture of energy split t$_{2g}$ and e_g levels becomes more complicated in a-TiO$_2$ because of the local distorted octahedral environment (D$_{2d}$ symmetry) which allows local $p-d$ orbital hybridization [411]. In that case, the dipolar contribution to the total cross-section becomes dominant for every transition in the pre-edge [412]. In addition, the cluster size used for the FMS calculations has a large influence on the A3 and B peak intensities showing that delocalized final states (off-site transitions) play a key role in the pre-edge absorption region [408]. Finally, the local environment around Ti atoms in anatase is strongly anisotropic and Ti-O bond distances separate in two groups of apical and equatorial oxygens which cannot be correctly described with spherical muffin-tin potentials as implement in FMS.

Empirical approaches have been used by Chen and co-workers [413] and Luca and co-workers [403, 414, 415] to establish correlations between the Ti K pre-edge transitions in a-TiO$_2$ and sample morphologies, showing that bond length and static disorder contribute to the change in pre-edge peak amplitudes [413] and that the A2 peak is due to pentacoordinated Ti atoms [403, 414, 415]. Farges and co-workers confirmed this assignment with the support of multiple scattering (MS) calculations [409]. The recent works by Zhang et al. [416] and Triana et al. [410] have shown the strong interplay between the intensity of pre-edge features and the coordination number and static disorder, in particular in the case of the A2 peak.

The clear assignment of the pre-edge features is important in view of recent steady-state and ultrafast XAS [281, 282, 326] and optical experiments [43]. In our picosecond XAS experiments on photoexcited a-TiO$_2$ nanoparticles, we observed a strong enhancement of the A2 peak in particular and a red shift of the edge. This was interpreted as trapping of the electrons transferred to the conduction band at defects that are abundant in the shell region of the nanoparticles [281]. We further measured the trapping time with femtosecond resolution and concluded that the trapping occurs in < 200 fs, immediately at or near the unit cell where it is created [282]. Further to this, the trapping sites were identified as being due to oxygen vacancies (O$_{vac}$) in the first shell of the reduced Ti atom. These O$_{vac}$'s are linked to two Ti atoms in the equatorial plane and one Ti atom in the apical position which induces two different responses at the Ti K-edge when a charge gets trapped at an O$_{vac}$ [78, 282]. However, these hy-

potheses await for confirmation based on further experimental and theoretical studies, which for the steady-state case, we present in this article. In particular, the study of photoexcited single crystals is planned in which the first transition at the optical gap has been identified as a 2-dimensional (2D) exciton in the 3D lattice of the material [43]. The robustness of this transition with respect to defects hinted to possible applications in relation to energy and/or charge transport. The time-resolved XAS study of single crystals with a controllable amount of O_{vac}'s would be important to clarify this transport.

Recently, there have been two main developments in the computation of XANES spectra. The first is based on band structure calculations (LDA, LDA+U,...), which compute potentials self-consistently before the calculation of the absorption cross-section with a core-hole in the final state [16, 412]. This approach provides excellent accuracy but is limited to the few tens of eV above the absorption edge due to the computational cost of increasing the basis set to include the EXAFS. The second one, the finite difference method near-edge structure (FDMNES) implemented by Joly [369, 417], overcomes the limitations of the muffin-tin approximation in order to get accurate descriptions of the pre-edge transitions especially for anisotropic materials. The recent theoretical work by Cabaret and coworkers combining GGA-PBE self-consistent calculations with FDMNES [412] concluded that in a-TiO_2, peak A1 is due to a mixture of quadrupolar (t_{2g}) and dipolar transitions ($p - t_{2g}$), A3 to on-site dipolar ($p - e_g$), off-site dipolar ($p - t_{2g}$) and quadrupolar (e_g) transitions, while B is due to an off-site dipolar transition ($p_z - e_g$). However, experimental support to the pre-edge assignments is still lacking, and is unambiguously provided in this work using linear dichroism (LD) XAS at the Ti K-edge of a-TiO_2 with the theoretical support of ab-initio full potential FDMNES calculations and spherical harmonics analysis of the XAS cross-section. We show that A1 is mainly due to dipolar transitions to on-site hybridized $p_{x,y} - (d_{xz}, d_{yz})$ final states which gives a strong dipolar LD to the transition with a weak quadrupolar component from ($d_{xz}, d_{yz}, d_{x^2-y^2}$) states. The A3 peak is due to a mixture of dipolar transitions to hybridized $p_{x,y,z} - (d_{xy}, d_{z^2})$ final states as a result of strong hybridization with the $3d$ orbitals of the nearest Ti neighbour with a small quadrupolar component. The B peak is purely dipolar (p final states) and is an off-site transition. Finally, we experimentally observe a quadrupolar evolution of the A2 peak amplitude, in qualitative agreement with the finite difference method (FDM) calculations. We argue that the amplitude of this transition may strongly depend on atomic vacancies which allow orbital mixing via lowered symmetries. This explains the relatively intense A2 peak in amorphous TiO_2 [416] or after photoexcitation of anatase or rutile TiO_2 [78, 281, 282].

8.2 Experimental setup

8.2.1 Linear dichroism

The LD measurements are performed at the SuperXAS and MicroXAS beamlines of the SLS in Villigen, Switzerland using a Si(311) crystal monochromator to optimize the energy resolution. Energy calibration is performed from the first derivative of the XAS spectrum of a thin Ti foil.

We used an unfocused square-shaped X-ray beam of $200 \times 200 \ \mu m^2$. The XAS spectrum is obtained in total fluorescence yield with a Ketek Axas detector system with Vitus H30 SFF and ultra-low capacitance Cube-Asic preamplifier (Ketek Gmbh).

The sample consists of a (001)-oriented crystalline anatase TiO$_2$ thin film (thickness ~ 30 nm, see Appendix A.5 for the sample growth method and characterizations). The incident X-ray beam is p-polarized at the sample surface and defines the orientation of the electric field $\hat{\epsilon}$.

A fixed rotation axis ($\hat{x}$) is set at the sample surface and is orthogonal to the incident X-ray beam and aligned with the target point of the X-ray at the sample surface (Figure 8.1). By convention, a set of spherical coordinates are fixed to the sample surface as defined by the anatase space group [418]. θ measures the angle between the X-ray wavevector $\hat{k}$ and the [001] crystal direction ($\hat{z}$ axis of the sample frame) orthogonal to the surface. ϕ measures the angle between the electric field $\hat{\epsilon}$ and the sample rotation axis $\hat{x}$ and is always 90°. In principle, a third angle ψ is necessary to fix the position of the wavevector in the orthogonal plane to the electric field but here $\psi = 0°$. The angles θ reported in the experimental datasets are with an uncertainty of $\pm 1°$ due to the calibration of the sample surface orientation in the orthogonal plane to the incident X-ray beam. The precision of $\pm 0.01°$ of the rotation stage is negligible with respect to the angular uncertainty.

LD is usually studied with the sample rotated in the plane orthogonal to the incident X-ray beam [419]. Here, the sample is rotated in an unconventional way around $\hat{x}$ and the X-ray footprint onto the sample surface changes with the incidence angle θ. However, we clearly show in this paper that this procedure does not introduce spectral distortions because the effective penetration depth of the X-rays through the material (between 2 and 15 μm across the absorption edge of anatase TiO$_2$ for the largest $\theta = 70°$ used here [420]) is kept constant as the sample is much thiner than the attenuation length at the Ti K-edge. Instead, the total amount of material probed by the X-rays changes due to the larger X-ray footprint when θ increases and a renormalization over the detected number of X-ray fluorescence photons is required. This is done with the support of the FDMNES calculations since a few energy points have θ-independent cross-sections (*vide infra*). With this renormalization procedure performed at a single energy point (4988.5 eV), we could obtain a set of experimental points with θ-independent cross-sections at the energies predicted by the theory confirming the reliability of the method. Hence, crystalline thin films with suitable thicknesses with respect to the X-ray penetration depth offer more possibilities to study LD effects than single crystals and prevent the usual self-absorption distortion of bulk materials when using total fluorescence yield detection [421].
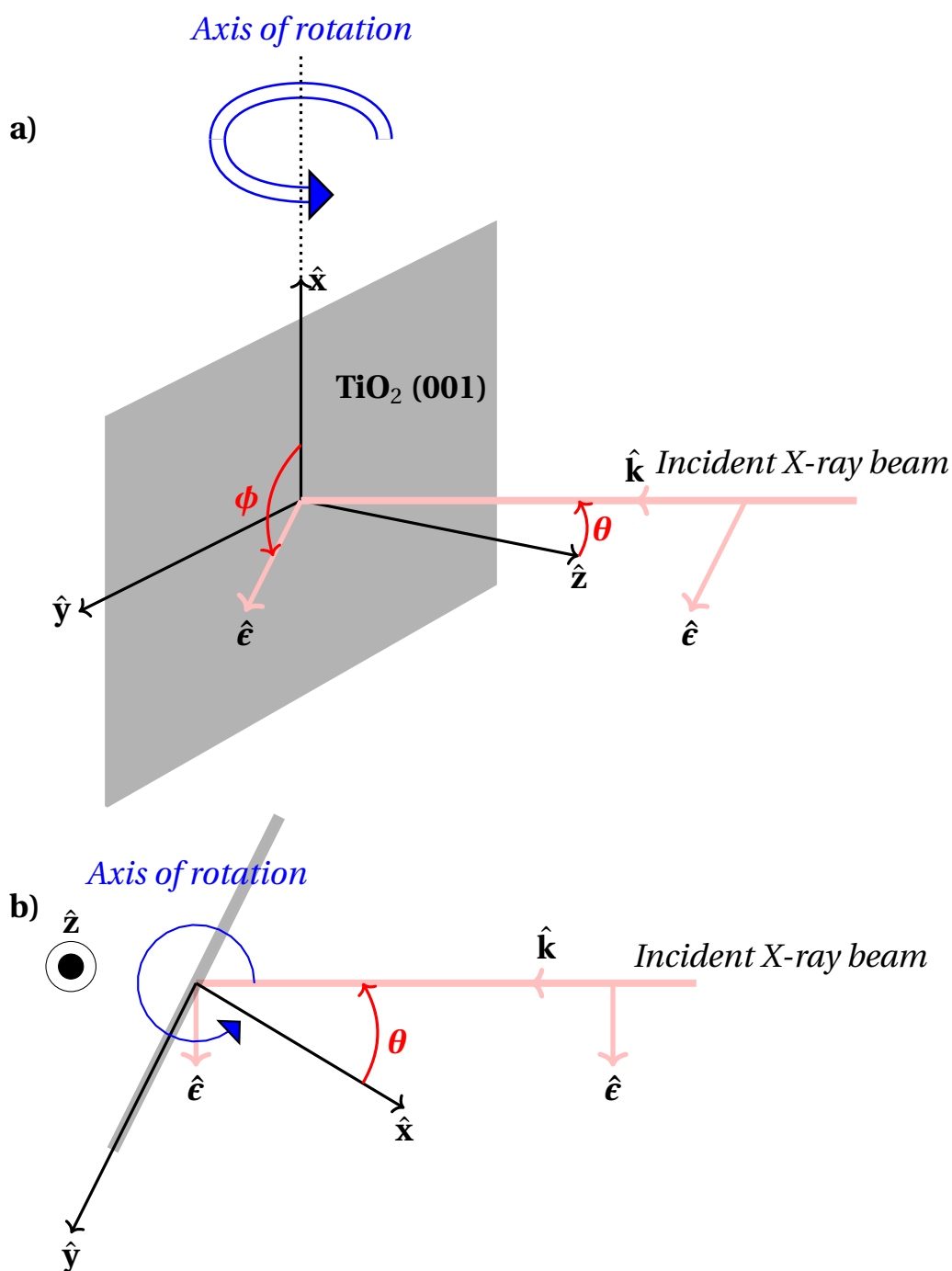
Figure 8.1 – Linear dichroism experiment with side view (a) and top view (b). The sample surface is in grey while the incident X-ray beam is in pink. A set of spherical coordinates (θ, ϕ, ψ) is used to orient the electric field $\hat{\epsilon}$ and wavevector $\hat{k}$ of the incident X-ray beam with respect to the sample surface.

8.3   Theory

8.3.1   Finite difference *ab-initio* calculations

The *ab-initio* calculations of the XAS cross-section were performed with the full potential FDM as implemented in the FDMNES package [368, 369]. A cluster of 7.0 Å was used for the calculation with the fundamental electronic configuration of the oxygen atom and an excited state configuration for the titanium atom (Ti: $[Ar]3d^14s^24p^1$) meaning that the calculation was not performed self-consistently (not recomputing the potential at every iteration and re-estimating the Fermi energy). We checked the convergence of the calculation for increasing cluster sizes and found minor evolution for larger cluster radiuses than 7.0 Å (123 atoms). The Hedin-Lundqvist exchange-correlation potential is used [422]. Since the calculation is not performed self-consistently, a minor adjustment of the screening properties of the $3d$ levels needs to be used to match the energy position of the pre-edge features with the experiment. We found the best agreement for a screening of 0.85 for the $3d$ electrons. A constant experimental gaussian broadening of 0.095 eV is applied to the calculated spectrum to account for the experimental resolution of the experiment and get the closest agreement with the broadening of the pre-edge peaks.

8.3.2   Spherical tensor analysis of the dipole and quadrupole cross-sections

Analytical expressions of the dipole and quadrupole cross-sections ($\sigma^D(\hat{\epsilon})$ and $\sigma^Q(\hat{\epsilon}, \hat{k})$ respectively) are obtained from the expansion into spherical harmonics components [419, 423]. The expressions of $\sigma^D(\hat{\epsilon})$ and $\sigma^Q(\hat{\epsilon}, \hat{k})$ depend on the crystal point group which is D_{4h} ($4/mmm$) for anatase. The dipole cross-section is given by:

$$\sigma^D(\hat{\epsilon}) = \sigma^D(0,0) - \frac{1}{\sqrt{2}}(3\cos^2\theta - 1)\sigma^D(2,0) \tag{8.1}$$

and the quadrupole cross-section by:

$$\sigma^Q(\hat{\epsilon}, \hat{k}) = \sigma^Q(0,0) + \sqrt{\frac{5}{14}}(3\sin^2\theta\sin^2\psi - 1)\sigma^Q(2,0)$$
$$+ \frac{1}{\sqrt{14}}[35\sin^2\theta\cos^2\theta\cos^2\psi + 5\sin^2\theta\sin^2\psi - 4]\sigma^Q(4,0) \tag{8.2}$$
$$+ \sqrt{5}\sin^2\theta[(\cos^2\theta\cos^2\psi - \sin^2\psi)\cos 4\phi - 2\cos\theta\sin\psi\cos\psi\sin 4\phi]\sigma^{Qr}(4,4)$$

with θ, ϕ and ψ as defined in a spherical coordinate system with the $\hat{z}$ axis following the conventions of the International Crystallography Tables [418] and $\sigma(l, m)$ the spherical tensor with the rank and the projection of the tensor l and m, respectively. Although some terms of $\sigma^D(\hat{\epsilon})$ and $\sigma^Q(\hat{\epsilon}, \hat{k})$ may be negative, the total dipolar and quadrupolar cross-sections must be positive putting constraints on the values of $\sigma^D(l, m)$ and $\sigma^Q(l, m)$. In the case of a-TiO$_2$, the $\hat{z}$ axis is along the crystallographic c-axis and the θ, ϕ and ψ angles are those defined in §8.2.1.

The electric field $\hat{\epsilon}$ and wavevector $\hat{k}$ coordinates are given by:

$$\hat{\epsilon} = \begin{pmatrix} \sin\theta\cos\phi \\ \sin\theta\sin\phi \\ \cos\theta \end{pmatrix}, \; \hat{k} = \begin{pmatrix} \cos\theta\cos\phi\cos\psi - \sin\phi\sin\psi \\ \cos\theta\sin\phi\cos\psi + \cos\phi\sin\psi \\ -\sin\theta\cos\psi \end{pmatrix} \tag{8.3}$$

Hence the detail of the cross-section angular dependence requires the estimate of the spherical tensors $\sigma^D(l,m)$ and $\sigma^Q(l,m)$ as performed elsewhere [424]. The XAS cross-section measured experimentally is an average over inequivalent Ti atoms under the symmetry operations of the crystal space group in the lattice. The analytic formula representing this site-averaged cross-section requires the crystal symmetrization of the spherical tensors provided in Supplementary Information (SI) §2. From this analysis, we conclude that Ti sites are all equivalent in a-TiO$_2$ so that the crystal symmetrized spherical tensors $\langle\sigma(l,m)\rangle_X$ and spherical tensors $\sigma(l,m)$ are the same to a constant pre-factor. Assuming pure $3d$ and $4p$ final states in the one-electron approximation, analytical expressions are provided for $\sigma^D(\hat{\epsilon})$ and $\sigma^Q(\hat{\epsilon},\hat{k})$ whose angular dependence is given in Table 8.1. The full expressions of the cross-sections are provided in SI §3. Since anatase TiO$_2$ has a tetragonal unit cell and all Ti sites are equivalent, the XAS cross-sections along $\hat{x}$ and $\hat{y}$ are equal. In this paper, we analyze the angular dependence of the pre-edge peak intensities and assign them to specific final states corresponding to Ti-$3d$ or $4p$ orbitals with the support of both FDM and spherical tensor analysis.

Table 8.1 – Angular dependence of the dipole and quadrupolar X-ray absorption cross-sections according to the final state of the transition.

final state	$\sigma^D(\hat{\epsilon})$ or $\sigma^Q(\hat{\epsilon},\hat{k})$ θ-dependence
p_x, p_y	$\cos^2\theta$
p_z	$-\cos^2\theta$
d_{z^2}, d_{xy}	$\sin^2\theta \cdot \cos^2\theta$
$d_{xz}, d_{yz}, d_{x^2-y^2}$	$-\sin^2\theta \cdot \cos^2\theta$

8.4 Results

The evolution of the Ti K-edge spectra with θ is depicted in Figure 8.2a. The spectra are normalized at 4988.5 eV where the cross-section is expected to be θ-independent according to FDMNES calculations (shown by a black arrow in Figure 8.2b). From this normalization procedure, a series of energy points with cross-section independent of the θ angle appear in the experimental dataset, as predicted by the theory (black arrows in Figures 8.2a,b) showing the reliability of the normalization procedure. In the pre-edge, the amplitudes of peaks A1 and A2 are dramatically affected by the sample orientation. In the post-edge regions, significant changes are observed as well.
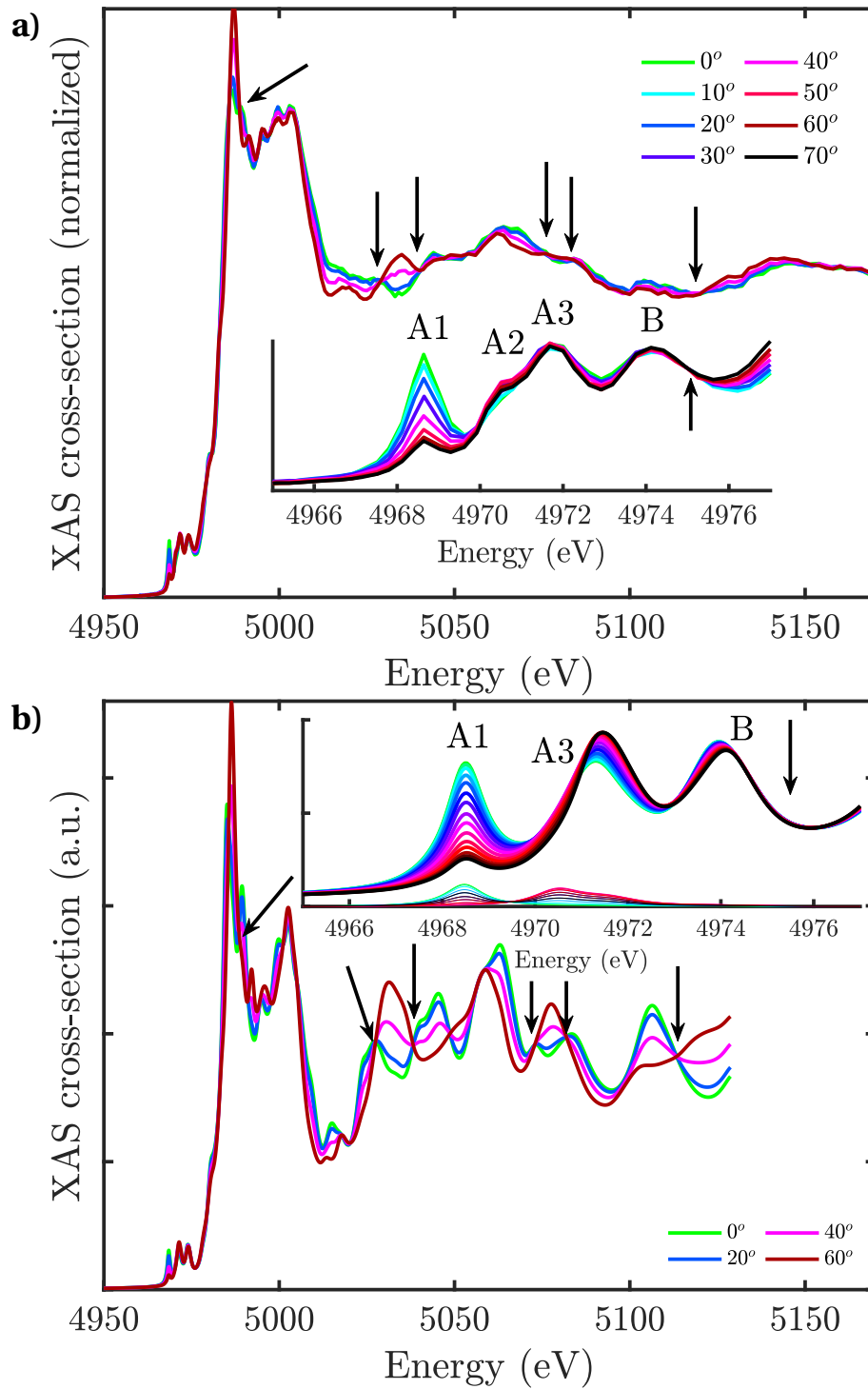
Figure 8.2 – a) Experimental and b) calculated XAS spectra for different incidence θ angles with the sum of dipolar and quadrupolar components (thick lines) and with quadrupolar components only (thin lines in the inset of b)). Points with θ-independent cross-sections are marked with black arrows.

Ab-initio FDM calculations of total XAS cross-section (dipolar and quadrupolar) are presented in Figure 8.2b for the same angles of incidence θ as in the experiment. In the pre-edge region, the trends for peak A1 are nicely reproduced. For peak A3, the agreement is of lesser quality but the absence of peak A2, which originates from defects [403, 413, 414, 415] that are not included in our perfect crystal modelling, may be one of the reasons. In the post-edge region, a good agreement is found especially for the isosbestic points. This shows that a strong LD remains well above the edge in this material.

In order to describe the origin of the LD and assign the pre-edge resonances, the projected density of states (DOS) of the final states for the pre-edge and post-edge region is depicted in Figure 8.3 (we drop the term "projected" in the following for simplicity). Due to the large differences between the DOS of s, p and d states, a logarithmic scale is used vertically and normalized to the orbital having the largest DOS contributing to the final state among s, p and d orbitals. For peaks A1, A3 and B, most of the DOS comes from d-orbitals while s- and p-DOS are comparable. However, due to the angular momentum selection rule, the spectrum resembles the p-DOS as witnessed by the similarity between the integrated p-DOS and the calculated spectrum (black line in Figure 8.3e). Importantly, peak A1 has only (p_x, p_y) contributions meaning that this transition is expected to have a much weaker intensity when the electric field gets parallel to the $\hat{z}$ axis, in agreement with the observed decrease of its amplitude when θ increases (Figure 8.2). The d-DOS at peak A1 involves d_{xz}, d_{yz} and $d_{x^2-y^2}$ orbitals, among which the first two can hybridize with the (p_x, p_y) orbitals and relax the selection rules. The dipolar nature of A1 is also seen from the monotonic decrease of its amplitude from $\theta = 0°$ to $\theta = 90°$, inconsistent with a quadrupolar allowed transition with 90° periodicity. Following the same analysis, peaks A3 and B do not undergo a strong change in amplitude under rotation because (p_x, p_y) and p_z contribute similarly to the DOS for these transitions although FDM calculations show that A3 should evolve in intensity with θ due to a ~20% larger DOS for p_z than for p_x, p_y. From the integrated d-DOS along (x, y) and z (Figure 8.4), we notice the inconsistency between the peak amplitudes in the theory and the experiment, which shows that they are essentially determined by the p-DOS.

For a more quantitative description of the dipolar and quadrupolar components in the pre-edge, we extracted the quadrupolar cross-section from FDM calculations. It is depicted as thin lines in the inset of Figure 8.2b. The quadrupolar contributions are limited to peaks A1 and A3 with a small contribution in the spectral region of peak A2. At peak A1, the quadrupolar amplitude is maximum for $\theta = 0°$ and $\theta = 90°$ and the total cross-section becomes mainly quadrupolar for $\theta = 90°$ while the quadrupolar component contributes ~ 15% of the peak amplitude for $\theta = 0°$. From the development of the cross-section into spherical harmonics (Table 8.1), the cross-section of dipolar transitions to $p_{x,y}$ final states is expected to vary as $\cos^2\theta$ while transitions to p_z vary as $-\cos^2\theta$ (see Figure 8.5a). The fitted evolution of the dipolar cross-section of peak A1 from FDM calculations is compatible with a transition to $p_{x,y}$ (green line in Figure 8.6a). The quadrupolar component (red line in Figure 8.6a) is compatible with a transition to $d_{xz}, d_{yz}, d_{x^2-y^2}$ due to its $-\sin^2\theta\cos^2\theta$ predicted (Table 8.1 and Figure 8.5b). The overlap between the experimental and theoretical amplitudes of peak

A1 (Figure 8.6a) gives a satisfactory agreement further confirming that the A1 transition is mostly dipolar to $p_{x,y}$ final states. Following the same analysis, we find that the evolution of A3 and B amplitudes are compatible with a dominant p_z-DOS for the former and $p_{x,y}$-DOS for the latter. The weak quadrupolar character of A3 with maximum at $\theta = 45°$ is compatible with d_{z^2}, d_{xy}-DOS.

As pointed out earlier, the quadrupolar cross-section has a doublet structure in the region of peak A2 and A3 (inset of Figure 8.2b). The most intense of the two peaks is in the spectral region of peak A2 where the transition involving defects is expected in real crystals. This quadrupolar component reaches its maximum amplitude for $\theta = 45°$. A closer look at the evolution of the A2 amplitude with θ shows a quadrupolar evolution with maximum value at $\theta = 45°$ (Figure 8.6b). It indicates that although the amplitude of A2 is underestimated in the FDM calculation, the consensus that A2 originates from undercoordinated and disordered samples may be more complicated, as discussed in section 8.5.2.

From this combined experimental and theoretical analysis, we emphasize that consecutive peaks in the pre-edge are not due to the energy splitting between t$_{2g}$ and e$_g$ as previously invoked [412]. In the case of a-TiO$_2$, this splitting is more complicated than the usual octahedral crystal field because of the strong hybridization between p and d orbitals in a lowered symmetry environment which affects the relative ordering between the transitions. The consistent results between experiment, FDM calculations and spherical tensor analysis show the reliability of the assignment provided in this work. A summary of the previous assignments of peaks A1 to B is provided in Table 8.2 together with our results.
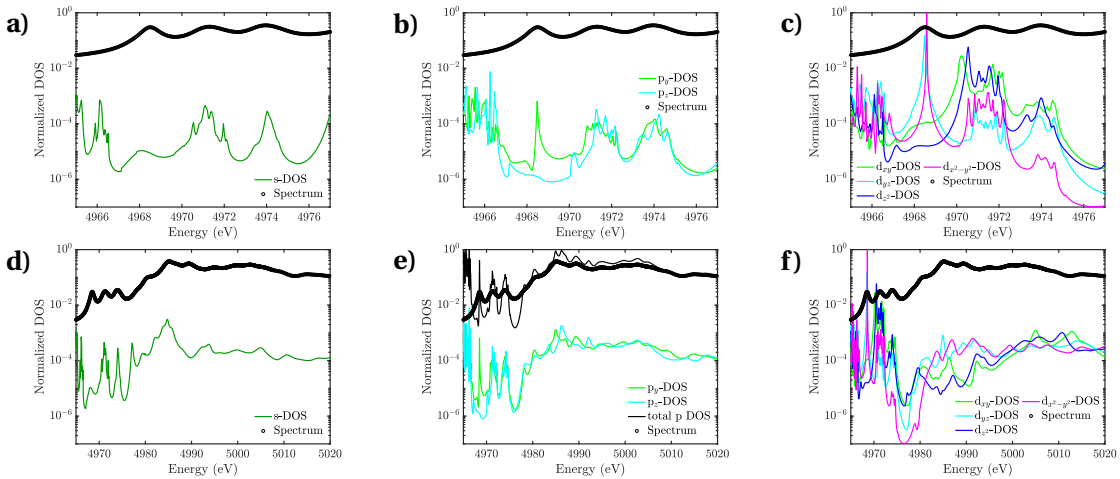
Figure 8.3 – Calculated projected final state DOS for each type of (a,d) s-, (b,e) p- and (c,f) d-final state orbitals in the pre-edge (top) and post-edge regions (bottom). Reported spectra (black circles) are calculated for $\theta = 0°$. The total p-DOS is given in e) (black line).
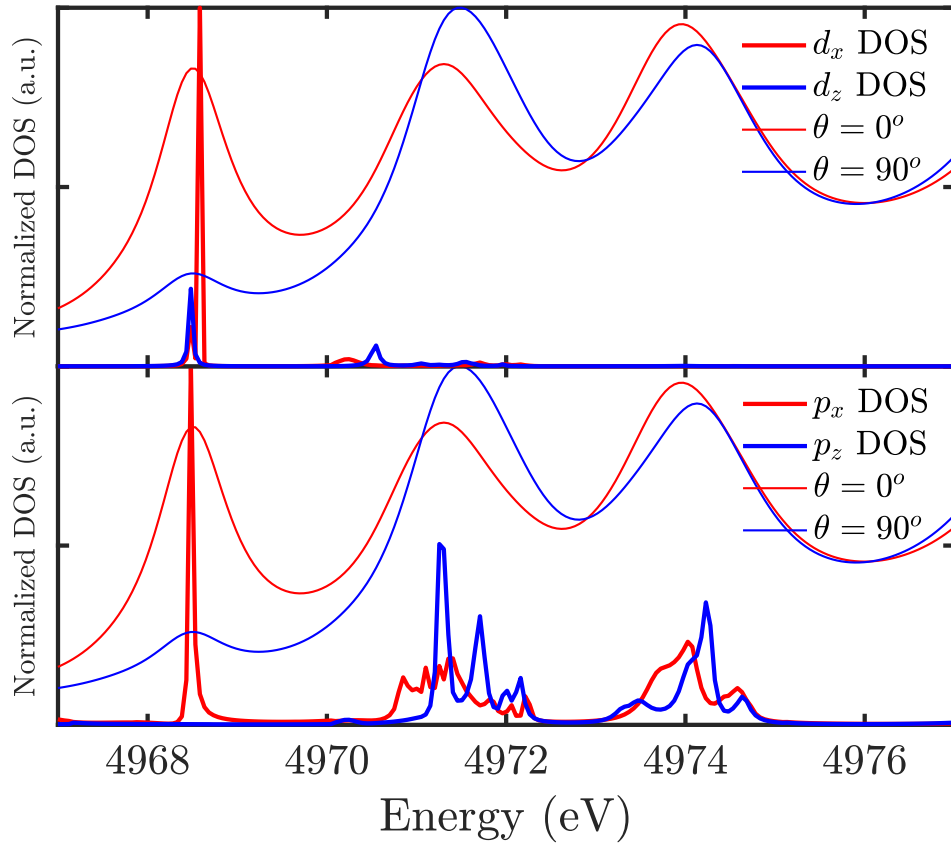
Figure 8.4 – Projected DOS along x and z in the pre-edge for a) p-orbitals and b) d-orbitals (thick lines) and calculated spectra for incidence angles $\theta = 0^\circ$ (red thin line) and $\theta = 90^\circ$ (blue thin line).
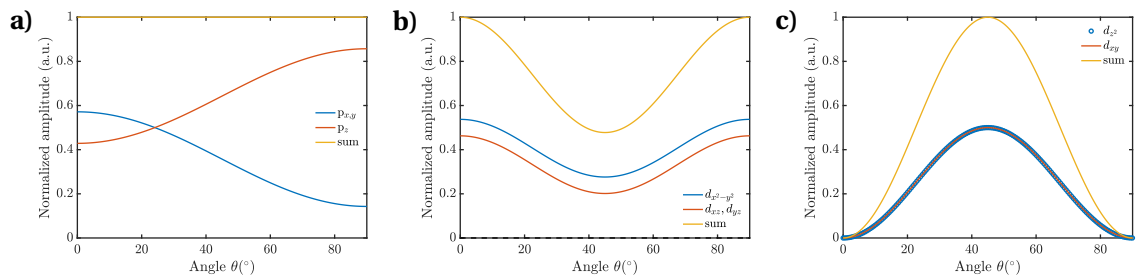
Figure 8.5 – Evolution of the a) dipolar and b) and c) quadrupolar cross-section with the angle of incidence θ in the configuration of the experiment for different final states.
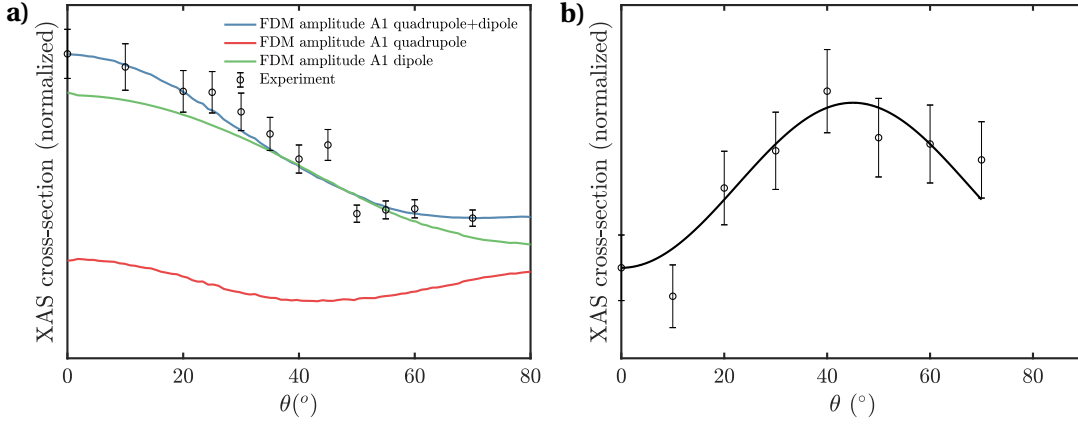
Figure 8.6 – a) Calculated evolution of the A1 peak amplitude with dipole (green curve), quadrupole (red curve) and sum of dipole and quadrupole contributions (blue curve). The experimental amplitudes of peak A1 are shown with black circles and the error bars correspond to the uncertainties provided by the fitting. b) Calculated evolution of the A2 peak amplitude (black line). The experimental amplitudes of peak A2 are shown with black circles and the error bars correspond to the uncertainties provided by the fitting.

Table 8.2 – Previous assignments of the final states of the pre-edge transitions of the Ti K-edge spectrum of anatase TiO$_2$. The orbitals with dominant contribution to the transition are emphasized in bold. $E1$ is for dipolar transitions and $E2$ for quadrupolar transitions. Off-site transitions are in red, on-site transitions are in black.

reference	A1	A2	A3	B
[406]	$E1$: $d_{x^2-y^2}(b_1)$, $p_x, p_y, d_{xz}, d_{yz}(e)$	$E1$: $p_z, d_{xy}(b_2)$, $p_x, p_y, d_{xz}, d_{yz}(e)$	$E1$: $p_z, d_{xy}(b_2)$, $d_{z^2}(a_1)$	$E1$: p, s
[404]	Frenkel exciton		$E1$: t_{2g}	$E1$: e_g
[412]	$E1$: $p(t_{2g})$, $E2$: $3d(t_{2g})$		$E1$: $p(e_g)$, $E1$: $p - 3d(t_{2g})$, $E2$: $3d(e_g)$	$E1$: $p_z, 3d(e_g)$
[410]	$E2$: t_{2g}		$E1$: t_{2g} $p_x, p_y, \mathbf{p_z}, d_{xy}, d_{xz}, d_{yz}$	$E1$: e_g $p_x, p_y, p_z, d_{x^2-y^2}, d_{z^2}$
This work	$E1$: $\mathbf{p_{x,y}}$, $E2$: $\mathbf{d_{xz}, d_{yz}}, d_{x^2-y^2}$	$E2$: $\mathbf{d_{z^2}}, d_{xy}$	$E1$: p_x, p_y, p_z	$E1$: p_x, p_y, p_z

8.5 Discussion

8.5.1 Local versus non-local character of the pre-edge transitions

Pre-edge transitions can originate either from on-site (localized) or off-site transitions involving neighbor Ti atoms of the absorber. Off-site transitions are dipole allowed due to the strong $p - d$ orbital hybridization [411]. This effect has been shown on NiO, an antiferromagnetic (AF) charge-transfer insulator, for which the transition to $3d$ orbitals of the majority spin of the absorber is only possible between Ti sites due to the AF ordering [16]. Hence, to disentangle between the local or non-local character of the pre-edge transitions in anatase TiO_2, we performed FDM calculations on clusters with increasing number of neighbour shells starting from an octahedral TiO_6 cluster with the same geometry and bond distances as in the bulk. The results are shown in Figure 8.7 with two orthogonal electric field orientations along [001] ($\theta = 90°$) and [010] ($\theta = 0°$).
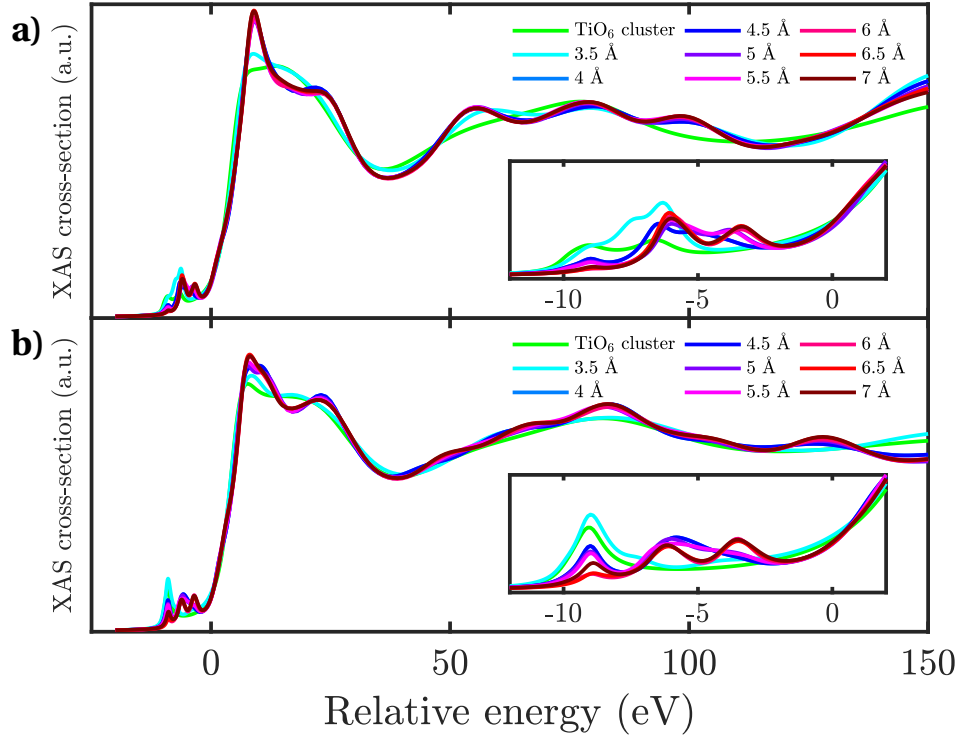
Figure 8.7 – Evolution of the calculated anatase XAS spectrum with cluster size for a) $\theta = 90°$ ($\hat{\epsilon} \parallel$ [001]), (b) $\theta = 0°$ ($\hat{\epsilon} \parallel$ [010]). The energy scale is relative to the Fermi level at -10 eV

The calculation for TiO_6 shows only A1 and A2 peaks meaning that they are mostly on-site transitions. This is consistent with the quadrupolar evolution of peak A2 which is only possible locally. The absence of peaks A3 and B suggests that they are mostly non-local transitions in agreement with Ref. [412]. Increasing the cluster size to 4 Å includes the second shell of Ti ions, which generates most of the A3 amplitude. This shows that similarly to NiO, an energy

gap opens between the on-site and off-site transitions to 3d orbitals of Ti and that A3 is mostly dipolar and strongly influenced by the intersite 3d − 4p hybridization. Peak B is missing for this cluster size which shows that it is due to a longer range interaction and can be reconstructed with a 5 Å cluster including the next shell of neighbor Ti atoms.

8.5.2 Origin of peak A2

The experimental angular evolution of the A2 amplitude (Figure 8.6b) matches a quadrupolar transition, qualitatively consistent with FDMNES calculations (Figure 8.2, inset). Since it has been shown that A2 is related to lattice defects [78, 281, 282, 403, 413, 414, 415], the question arises as to the physical details of this connection. Because of its purely quadrupolar character, one possible reason for the underestimated A2 amplitude in the theory is due to the fact that a perfect lattice has been considered. The occurrence of an oxygen vacancy in the vicinity of a Ti atom will lower the D$_{2d}$ symmetry and introduce $p − d$ orbital mixing in the pentacoordinated Ti atom increasing the transition amplitude while the angular dependence of the A2 peak remains mainly quadrupolar. In principle, this effect is also possible on the quadrupolar cross-section of peak A1 but may not be significant because of the strong dipole contribution already present in the perfect crystal. *Ab-initio* FDM calculations performed on octahedral TiO$_6$ and undercoordinated TiO$_5$ molecular clusters show an enhancement of A1 and A2 amplitudes when the oxygen vacancy is introduced at the apical or equatorial position with a stronger enhancement of A2 amplitude. This is fully compatible with our recent studies on photoexcited anatase and rutile TiO$_2$ nanoparticles [78, 281, 282], which show a transfer of spectral weight from anatase to amorphous.

8.6 Conclusion

In summary, a complementary approach using experimental LD measurements at the Ti K-edge of anatase TiO$_2$, *ab-initio* FDM calculations and spherical tensor analysis provides an unambiguous assignment of the pre-edge features. The distinction between on-site and off-site transitions is possible using different cluster sizes in the FDM calculations. The LD is visible well above the absorption edge due to the strong p-orbital polarization in a-TiO$_2$ which affects the amplitude of the EXAFS through an anisotropy of the single scattering terms. Surprisingly, a quadrupolar angular evolution is observed for peak A2. A connection between the unexpectedly large experimental amplitude of this peak is made with oxygen vacancies forming pentacoordinated Ti atoms, which adds a small amount of dipolar components via $p − d$ orbital mixing. Experiments are on-going to extend this work to rutile TiO$_2$.

The present results and analysis should be cast in the context of ongoing ultrafast X-ray spectroscopy studies at Free Electron Lasers [367, 395]. For materials such as TiO$_2$, the increased degree of detail that can be gathered from such sources was nicely illustrated in a recent paper by Obara et al. [326] who showed that the temporal response of the pure electronic feature (the edge) was much faster (~100 fs) than the response (~330 fs) of structural features such as

the above-edge XANES. The present work shows that by exploiting the angular dependence of some of the features, even up to the EXAFS region, one could get finer details about the structural dynamics, in particular in the case of non equivalent displacements of nearest neighbours. Work is in progress in this respect.

Conclusions and Future directions

In conclusion, this Thesis provides an overview of the photodynamics which can be investigated in band insulators and strongly correlated materials by femtosecond ultrafast ultraviolet (UV) spectroscopy and time-resolved X-ray absorption spectroscopy (TRXAS). The carrier cooling in semiconductors such as ZnO and MAPbBr$_3$ is of outmost importance for the implementation of these materials into optoelectronic devices. The ultrafast carrier cooling in ZnO converts efficiently the pump photon excess energy into lattice heat. In MAPbBr$_3$, the slow electron cooling is beneficial for the injection of hot charge carriers into electron transport materials (ETMs). However, we have observed that the formation of a bound state at the interface is limiting the injection efficiency. At the ZnO/N719 interface, the formation of an interfacial charge-transfer complex (ICTC) is confirmed which leads to a delayed electron injection into the ZnO substrate. The formation of the ICTC seems disconnected from the screening properties of the substrate and is likely due to the involvement of a trap state at the ZnO nanoparticle (NP) surface. The investigation of the transient response at the optical band gap of NiO essentially reproduces the observations made by others on different types of charge-transfer (CT) insulators such as cuprates [313, 314, 425]. The formation of a photoinduced absorption (PA) below the optical gap is characteristic of the dressing of the electronic excitations with bosonic modes occuring on ultrafast timescales and efficiently converting the electronic excitation into lattice heat. The fate of the electronic excitation has been investigated in detail by TRXAS which shows that photogenerated electrons localize in Ni 3d orbitals in less than 100 ps leading to a Ni-O bond elongation of ~7%. This can be associated to the formation of an electron-polaron. Finally the linear dichroism of the pre-edge features at the Ti K-edge of anatase TiO$_2$ has allowed the assignment of the final states involved in the corresponding transitions. This is supported by *ab initio* calculations and the derivation of the analytical angular XAS cross-section.

Some of the different projects investigated in this Thesis are currently being studied in more depth. The work on the electron injection between two solid state materials is extended to the gold-anatase TiO$_2$ interface which is relevant for a lot of applications in photocatalysis and immunotherapy. Especially, the focus is on the different excitation channels in the gold NPs which can inject electrons among the intraband, interband and plasmonic excitations. The first results show than even a low energy intraband excitation in gold can inject electrons into a-TiO$_2$ which confirms the results obtained recently by others [426].

The rich transient response observed on MAPbBr$_3$ in the UV will be generalized on other lead halide perovskite materials such as CsPbBr$_3$ and MAPbI$_3$ with the objective to find a global picture and assignment for the high order interband transitions in these materials. Especially, measuring in transient reflectivity of single crystals is also of interest since it allows more systematic studies and avoid sample fluctuations often encountered in thin films.

The electron cooling in ZnO will be completed by 2D UV experiments similarly to the work performed on a-TiO$_2$ [154] which provides access to a large range of pump photon excess energies and their influence on the electron cooling time. In this respect, a single crystal is more suitable than the colloidal solution used in this Thesis to get quantitative information. Complementary experiments of fluorescence up-conversion are also ongoing which due to the unavailability of tunable pump photon energy can only investigate the effect of increasing pump fluences on the cooling time of electrons.

The observation of electron localization and polaron formation in NiO calls for the determination of the polaron formation time. In order to achieve a subpicosecond time resolution, the experiment needs to be performed at a X-ray free-electron laser (FEL).

Finally, the strong LD in the pre-edge of anatase TiO$_2$ at the Ti K-edge offers the opportunity to investigate dynamical effects with a high selection of the final states investigated. A proposal has been submitted at a FEL to investigate the effect of the formation of self-trapped excitons [427, 428, 429, 430, 431] on the evolution of the pre-edge peak intensities along two orthogonal lattice orientations. The characterization of the ground state LD will be extended to rutile TiO$_2$ which has an inversion centre at the Ti centre and two inequivalent Ti sites in the lattice unit.

A Sample description

A.1 Dye N719

The ruthenium dye di-tetrabutylammonium cis-bis(isothiocyanato)bis(2,2´-bipyridyl-4,4´-dicarboxylato)ruthenium(II) (N719) was purchased from Solaronix. In the transient absorption spectroscopy (TAS) experiment of Chapter 5, N719 is dissolved in dimethylformamide (DMF) to achieve an optical density (OD) of 0.4 at a wavelength of 550 nm. The corresponding ultraviolet (UV)-Vis spectrum is depicted in Figure A.1 (green curve).

A.2 Bare wurtzite ZnO nanoparticles

Colloidal ZnO NPs in ethanol were purchased from Sigma-Aldrich (40 wt%, <130 nm particle size (dynamic light scattering (DLS)), Nano Sunguard^{TM} in ethanol II). The sample concentration was adapted from the commercial sample by dilution of 0.9 mL with 200 mL of absolute ethanol (Fischer Scientific, analytical reagent grade) to achieve ZnO concentration of 57 mmol/L (13 g/L) and an OD of ~1 at 360 nm. In Ref. [149], we reported the details of the sample characterization by means of X-ray diffraction (XRD), transmission electron microscopy (TEM) and X-ray absorption spectrum (XAS). Using these techniques, the crystallinity of the ZnO NPs, their rod-like shape and their average diameter of 17 ± 9 nm were demonstrated. The UV-Vis spectrum of the commercial solution is given in Figure A.1 (blue curve) and has been reported elsewhere [70, 149]. The spectrum exhibits a prominent and sharp exciton resonance around 365 nm [144].

A.3 N719-sensitized wurtzite ZnO nanoparticles

We used the ruthenium N719 dye as sensitizer adsorbed onto the ZnO NPs. To achieve a monolayer of dye on the NP at a concentration of 1.81×10^{-5} mol/L, a solution of 2.2 mg of N719 in 1 mL ethanol was mixed with the NP for one day. To ensure that a minimum amount of unbound N719 molecules remain, the solution was centrifugated two consecutive times with
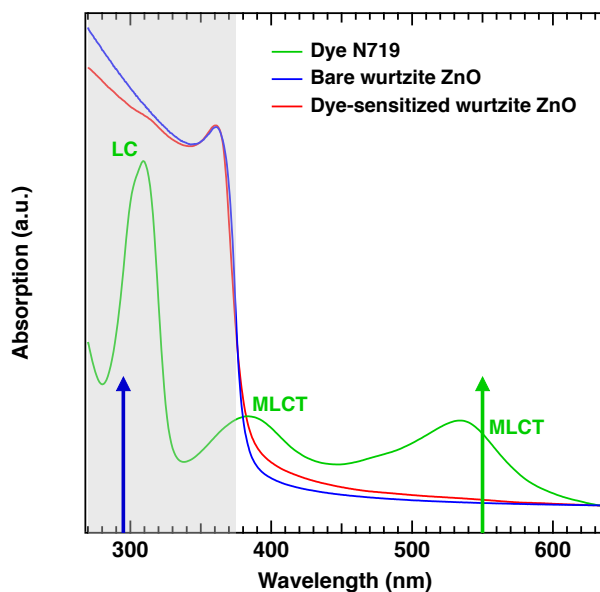
Figure A.1 – Steady-state absorption spectra of N719 dye (green curve) in DMF, the colloidal solution of wurtzite ZnO nanoparticles (NPs) (blue curve) in ethanol and the colloidal solution of dye-sensitized wurtzite ZnO NPs (red curve) in ethanol. The pump wavelength of 550 nm (2.25 eV) and 295 nm (4.20 eV) used for the experiment in Chapter 5 is indicated by the green and blue arrows respectively as well as the broadband UV region of the probe highlighted as a gray shaded area. The assignments of the metal-to-ligand charge-transfer (MLCT) bands and the ligand-centred (LC) band in N719 are also specified.
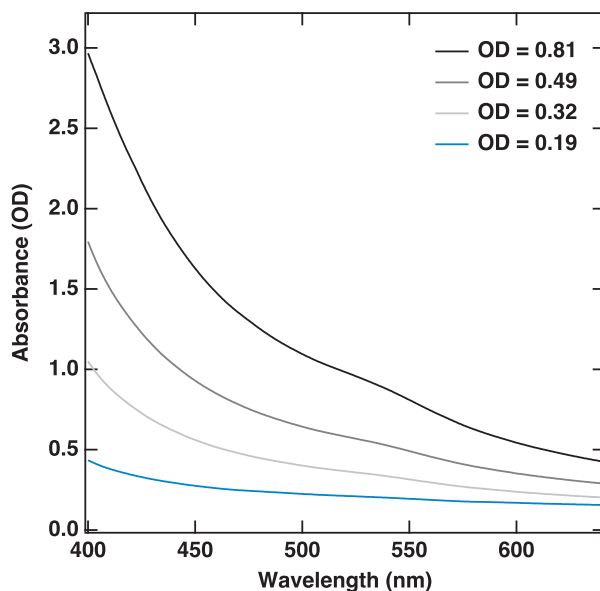
Figure A.2 – Steady-state absorption spectra of the colloidal solution of dye-sensitized wurtzite ZnO NPs in ethanol as a function of concentration (measured by the OD at 540 nm).

removal of the supernatant in between at 6000 rpm for half an hour. After the last supernatant removal, the NPs were resuspended in 100 mL of absolute ethanol to achieve an OD of ~2 at 360 nm. The UV-Vis spectrum of the solution is shown in Figure A.1 (red curve). Upon N719 dye absorption onto the ZnO NP surface, an overall increase of the absorption is observed below the optical gap with respect to bare ZnO NP. The MLCT transition at 540 nm becomes visible when the concentration of the sample is increased to reach an OD of ~0.5 at 540 nm (Figure A.2).
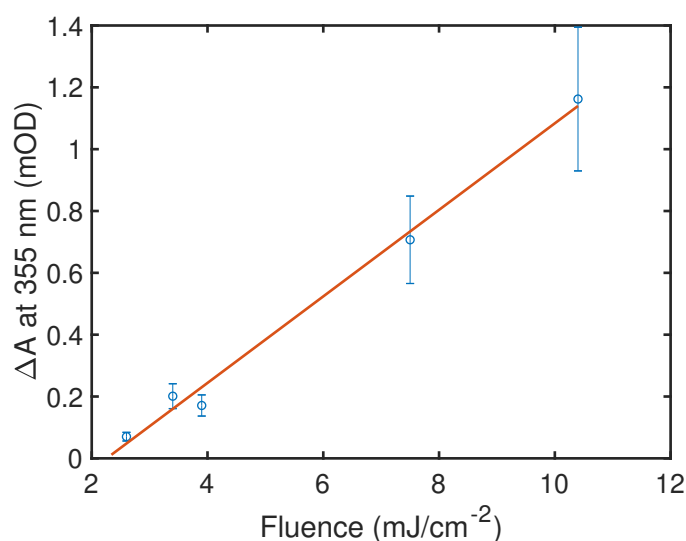
Figure A.3 – Evolution of the photobleach (PB) amplitude in ZnO NPs at 355 nm probe following 550 nm excitation for different pump fluences (blue circles) and linear fitting (red line). The linear evolution of the PB amplitude excludes two-photon absorption.

A.4 MAPbBr$_3$, MAPbBr$_3$/a-TiO$_2$ and a-TiO$_2$ thin films

The films of bare MAPbBr$_3$, MAPbBr$_3$/a-TiO$_2$ and a-TiO$_2$ were grown by spray pyrolysis in the group of Professor Guo[1] according to a procedure already introduced elsewhere [181]. Briefly, the quartz substrates were sequentially cleaned by ultrasonic treatment in detergent, de-ionized water, acetone and isopropyl alcohol. After drying, the cleaned substrates were further treated with UV-ozone for 25 min. The layer of a-TiO$_2$ was deposited onto the cleaned quartz substrate by spray pyrolysis using titanium didiopropoxide bis(acetylacetonate) (Sigma-Aldrich, 75wt% in isopropanol) precursor solution diluted in ethanol (1:39 v/v). During the spray pyrolysis, the quartz substrate was kept at 475°C on a hot plate and each spray was pumped out using an atomizer (Glakeller) with oxygen carrier gas. After the spray deposition was completed, the substrates were sintered at 475°C for 30 min. The MAPbBr$_3$ precursor

---

[1]Department of Photonics, National Cheng Kung University, Tainan, Taiwan

solution was prepared by mixing 0.015 g of MABr (Dyesol) with 0.0481 g of PbBr$_2$ (Sigma-Aldrich, 99.999%) in a dymethyl sulfoxide (DMSO) (Sigma-Aldrich, anhydrous) solution at 60°C and stirred for 12 h. The film of MAPbBr$_3$ perovskite was cast onto the quartz and quartz/a-TiO$_2$ substrates by a consecutive two-step spin-coating process at 500 rpm and 4000 rpm for 7 and 70 s, respectively. Additionally, chloroform solvent was added on the surface of the precursor film after 43 s during the spin coating. The MAPbBr$_3$ thin film was then annealed at 70°C on a hot plate for 10 min. The whole preparation of the perovskite layers are performed under inert nitrogen atmosphere with oxygen and moisture levels of less than 1 ppm.

The UV-Vis spectra of the three films are overlapped in Figure A.4a. The spectra of MAPbBr$_3$ and MAPbBr$_3$/a-TiO$_2$ show a well resolved Wannier-Mott exciton resonance observed in bulk-like materials or microcrystals around 2.4 eV [432]. The similarity between the UV-VIs spectra of the hybrid organic-inorganic lead halide perovskite (HOIP) layers deposited on quartz (MAPbBr$_3$) or a-TiO$_2$ (MAPbBr$_3$/a-TiO$_2$) shows that the perovskite crystals do not vary in size with different substrates in contrast to previous studies using quartz and mesoporous alumina respectively [433]. The electron injection between the MAPbBr$_3$ and a-TiO$_2$ layers can be observed from the ~60% fluorescence quenching of the green fluorescence after 400 nm excitation with respect to bare MAPbBr$_3$ (Figure A.4b) as usually reported [97, 216][2]. We can also conclude that pumping the perovskite at 400 nm as in the TAS experiments of Chapters 2 and 4 gives enough excess energy to the charge carriers to be injected into the a-TiO$_2$ substrate.
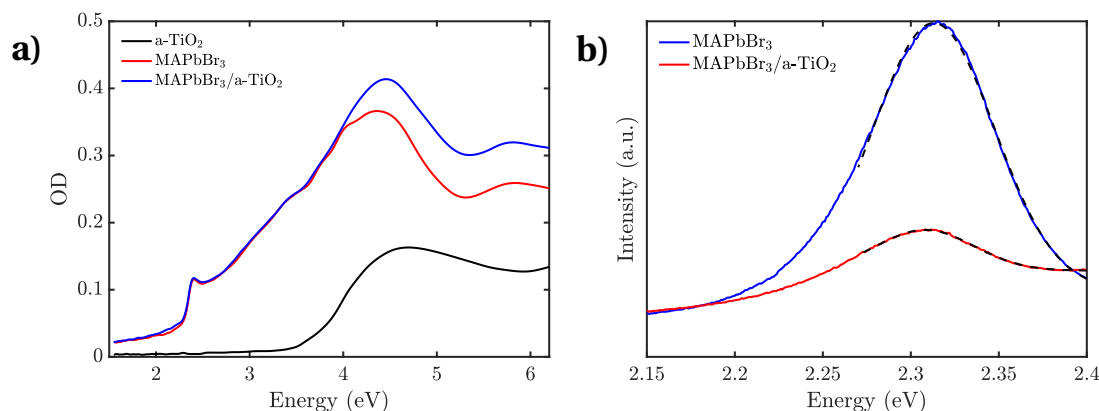
Figure A.4 – a) UV-Vis spectrum of the different films used for the TAS experiments performed in Chapters 2 and 4. b) Emission spectra of MAPbBr$_3$ (blue curve) and MAPbBr$_3$/a-TiO$_2$ (red curve) following 3.1 eV excitation. Gaussian fittings appear as black dashed lines.
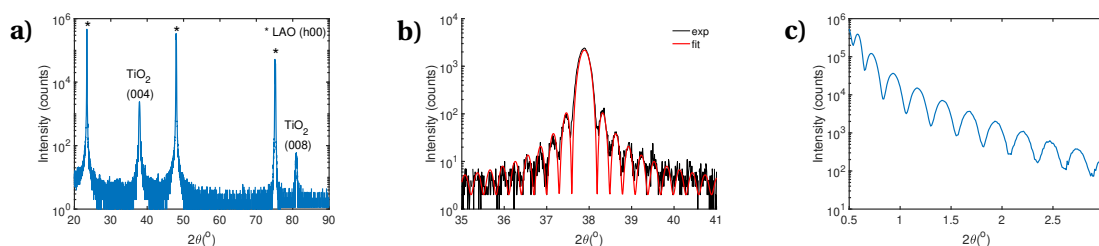
Figure A.5 – a) X-ray diffraction pattern from the (001)-anatase TiO$_2$ thin film, b) X-ray interferences in the region of diffraction peak (004), c) X-ray reflectometry showing a sample thickness of 32.8 ± 0.1 nm.

A.5 Anatase TiO$_2$ thin films

(001)-oriented epitaxial thin films of anatase TiO$_2$ are fabricated by pulse laser deposition (PLD) in the group of Thomas Lippert under the supervision of Daniele Pergolesi[3]. The vacuum chamber has a base pressure of about 10^{-5} Pa. A KrF excimer laser (Lambda Physik LPX 300, 25 ns pulses, $\lambda = 248$ nm) was used to ablate a target material of TiO$_2$ fabricated in our laboratory. Commercially available (100)-oriented LaAlO$_3$ (LAO) single crystal substrates ($10 \times 10 \times 0.5$ mm) were used as substrates. The target to substrate distance was set at 40 mm and the laser energy at the target was about 32 mJ on a spot area of about 1.6 mm^2 which gives an energy density of about 2.0 J/cm^2. The films were grown under oxygen partial pressure of 5 Pa. Platinum paste was used to provide the thermal contact between the substrate and the heating stage. The substrate temperature was about 610($\pm$10)°C, as measured with a pyrometer pointing at a Pt black spot near the substrate. XRD and X-ray reflectivity (XRR) (PANalytical X'pert Pro MPD with Cu Kα_1 radiation at 1.540 Å) analyses were used to investigate the crystalline structure of the films and for the calibration of the deposition rate, respectively. XRD shows the (001)-orientation of the deposited anatase TiO$_2$ thin film (Figure A.5a). Besides the (h00) reflexes of the substrate, only two diffraction peaks are visible, identified to the (004) and (008) reflexes of anatase TiO$_2$ (001)-oriented epitaxially on (100) LAO. Interferences fringes near the (004) diffraction peak are fitted to provide a film thickness of 31 ± 1 nm (Figure A.5b). The Kiessig fringes observed in XRR provide a sample thickness of 33 ± 1 nm (Figure A.5c) in agreement with XRD.

A.6 Nickel oxide (NiO) thin films

NiO (001) thin films were grown on MgO by chemical vapor deposition (35 nm thickness determined from XRR) by Rajesh Chopdekar at UC Davis. The samples were initially provided to Michael Porer in the group of Urs Staub in PSI.

---

[2]Note however that this does not mean that the overall quenching correponds to mobile electrons being injected into the bulk of the electron transport material (ETM) since injected charges can also be trapped at surface defects [218].

[3]Thin Film and Interfaces group, Paul Scherrer Institute, CH-5232 Villigen, Switzerland.

A.7   Nickel oxide (NiO) (101) single crystal

The (101) NiO was grown by chemical transport method in the EPFL Crystal Growth Facility lead by A. Magrez.

B | Estimate of the photogenerated and injected carrier densities in bare ZnO and ZnO/N719

B.1 Bare wurtzite ZnO nanoparticles

We calculate the number of excited electron-hole pairs per unit cell of wurtzite ZnO by taking into account a sample of nanoparticles (NPs), flowing in a quartz flow cell of thickness $l = 0.2$ mm with a mass concentration of ZnO in solution $c = 4.2$ g/L and an optical density of optical density (OD)$= 0.83$. Specifically, we consider the ultrafast broadband ultraviolet (UV) experiment in which the sample is pumped with a wavelength $\lambda_{pump} = 295$ nm at a repetition rate of $f = 10$ kHz and an average power $P = 65$ μW, The energy per pulse is $E_{pulse} = P/f$, corresponding to a number of photons per pulse of $N_{pulse} = E_{pulse}/E_{ph}$ with E_{ph} the energy of a single pump photon. The pump is focused on an area of $A_{foc} = \pi \times 45 \times 23$ μm$^2 = 3.25 \times 10^{-9}$ m^2, corresponding to a pumped volume of $V_{pump} = A_{foc} \times l = 6.5 \times 10^{-13}$ m^3. Since the radius of one NP is $R \sim 17$ nm, the volume can be estimated by approximating the NP to a sphere. This yields $V_{NP} = \frac{4}{3}\pi R^3 = 2.06 \times 10^{-23}$ m^3. The wurtzite ZnO density is $\rho = 5.61 \times 10^6$ g/m^3, and the mass of one NP is $M_{NP} = V_{NP} \times \rho = 1.2 \times 10^{-16}$ g. Given the mass concentration c, the number of NPs in the pumped volume is $N_{foc} = cV_{pump}10^3/M_{NP} = 2.37 \times 10^7$. The number of absorbed photons is $N_{abs} = (1 - T)N_{pulse}$, where $T = 10^{-OD} = 0.15$. Finally, the photoexcited carrier density n is calculated as the ratio between the total number of absorbed photons per NP N_{abs}/N_{foc} and the total illuminated volume $N_{foc} \times V_{pump}$ yielding $n = 5.2 \times 10^{18}$ cm^{-3}.

Table B.1 – Experimental conditions for the experiments performed on ZnO, di-tetrabutylammonium cis-bis(isothiocyanato)bis(2,2´-bipyridyl-4,4´-dicarboxylato)ruthenium(II) (N719) and ZnO/N719 in Chapter 5.

sample	pump wavelength (nm)	fluence (μJ.cm^{-3})	pump size (μm^2 FWHM)	excitation density (cm^{-3})
ZnO	295	63	90×46	5.2×10^{18}
N719	550	40	70×70	
ZnO/N719	550	740	70×70	3.9×10^{17}

B.2 Dye-sensitized ZnO nanoparticles

We calculate the electron injection density in the experiment with dye-sensitized wurtzite ZnO NPs. To this aim, we assume that all excited dye molecules inject electrons with a quantum yield of 1 in good approximation [267]. The N719 footprint at the NP surface is of the order of 2 nm in diameter. Given that the NP surface is $A_{NP} = 4\pi R^2 = 3.63 \times 10^{-15}$ m^2, the ratio between the NP surface and the dye footprint gives an estimate of the number of dye molecules per NP of ~1160. Approximately half of this number of molecules per NP is exposed to the incident pump beam which can be excited. This provides an injected electron density based on the number of NPs in the excited volume (2.37×10^7) and number of incident pump photons (5.33×10^{27}) of $n \sim 3.9 \times 10^{17}$ cm^{-3}.

The photobleach (PB) amplitude at the band gap is proportional to the number of photogenerated charges at the band edges [23]. The estimates of photoexcited density $n \sim 5.2 \times 10^{18}$ cm^{-3} in ZnO and injected electron density $n \sim 3.9 \times 10^{17}$ cm^{-3} in ZnO/N719 is consistent with the ratio of the PB amplitudes between bare ZnO NPs close to time 0 ($\Delta A = -12$ mOD, Figure 5.2c)) and the long time delay PB amplitude for ZnO/N719 ($\Delta A = -1.5$ mOD, Figure 5.2i)) of 8 with respect to the calculated ratio of charge densities of 13.

C MAPbBr$_3$ thin film

C.1   UV-Vis spectrum

The MAPbBr$_3$ thin films were provided by the group of Prof. Guo[1]. The UV-Vis spectrum of a thin film measured in transmission as well as the emission spectrum following 3.1 eV excitation are depicted in Figure C.1a. A Stokes shift of 86 meV is observed, larger than the ~50 meV observed in bulk perovskites [434, 435] meaning that the particles in the film are in a partial quantum confinement regime [432].
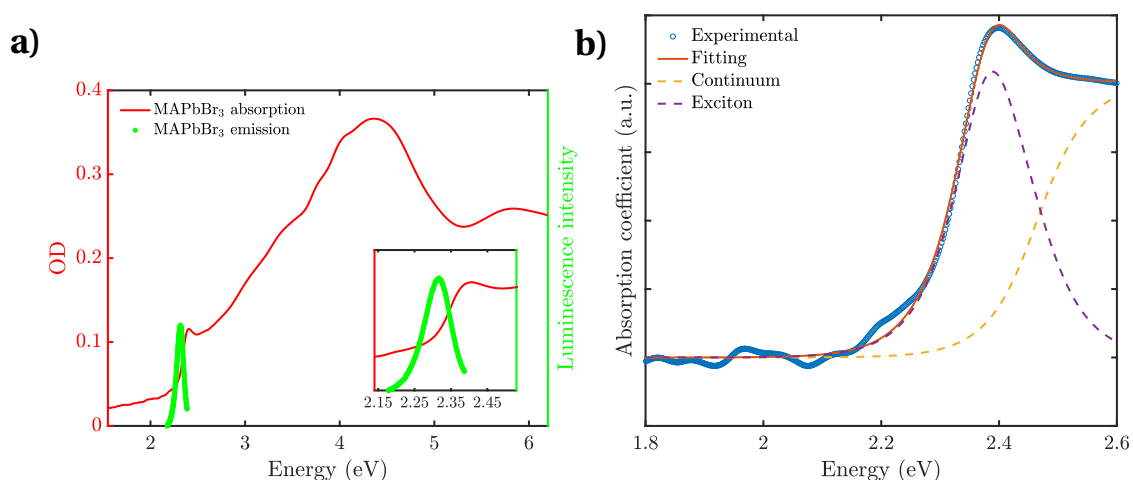
Figure C.1 – a) UV-Vis spectrum of MAPbBr$_3$ thin film measured in transmission (red curve) and emission spectrum following 3.1 eV excitation (green circles). b) UV-Vis spectrum of MAPbBr$_3$ thin film (blue circles), fitting of the spectrum with the convoluted Elliott formula C.2 (orange curve) and decomposition into exciton (dashed violet curve) and continuum (dashed yellow curve) absorption.

---

[1] Department of Photonics, National Cheng Kung University, Tainan, Taiwan

C.2 Analysis of the ground state UV-Vis spectrum with Elliott's theory

The ground state optical properties of MAPbBr$_3$ close to the optical gap are described by a superposition of Wannier exciton and continuum absorption. The original Elliott formula describing the absorption coefficient $\alpha(E)$ at a photon energy E of coexisting Wannier excitons and a continuum is given by [112]:

$$\alpha(E) = A\theta(E - E_g)\frac{\pi e^{\pi x}}{\sinh(\pi x)} + AR_{ex}\sum_{n_{ex}=1}^{\infty}\frac{4\pi}{n_{ex}^3}\delta\left(E - E_g + \frac{R_{ex}}{n_{ex}^2}\right) \tag{C.1}$$

with E_g the band gap, n_{ex} the principal quantum number, R_{ex} the exciton binding energy and $x = (E - E_g)/R_{ex}$ the normalized energy scale. θ and δ are the Heaviside and Dirac functions respectively. This equation is valid in the approximation that the exciton binding energy is much smaller than the energy gap and describes accurately the absorption coefficient near the band gap. To account for the inhomogeneous distribution of the particle sizes and thermal broadening, the spectrum is convoluted with a *sech* function similarly to the procedure developed by Sestu et al. [436] which provides,

$$\alpha(E) = A\sqrt{R_{ex}}\left[\sum_{n_{ex}}\frac{2R_{ex}}{n_{ex}^3}\text{sech}\left(\frac{E - E_g - \frac{R_{ex}}{n_{ex}^2}}{\Gamma}\right) + \int_{E_g}^{\infty}\text{sech}\left(\frac{E - x}{\Gamma}\right)\frac{1}{1 - e^{-2\pi\sqrt{\frac{R_{ex}}{x - E_g}}}}dE\right] \tag{C.2}$$

The equation C.2 is used to fit the MAPbBr$_3$ UV-Vis spectrum measured in transmission between 1.8 and 2.6 eV. The fitting is shown in Figure C.1b (orange curve) with the decomposition into exciton (violet dashed curve) and continuum (yellow dashed curve) absorption. The refined parameters ($n_{ex} = 10$ is kept constant) are given in Table C.1.

Table C.1 – Refined parameters from the fitting of the UV-Vis spectrum of MAPbBr$_3$ with equation C.2.

	R_{ex} (meV)	E_g (eV)	Γ (meV)
MAPbBr$_3$	80 ± 2	2.464 ± 0.004	54 ± 1

The band gap is ~70 meV larger than in MAPbBr$_3$ single crystal [175] but similar to NP samples due to a weak quantum confinement [97]. The fitted exciton binding energy falls into the range of reported values which spans from 15 to 100 meV at room temperature [6, 175, 436, 437].

C.3 Fluence dependence

A fluence dependence of the relative amplitude of PB2, PB3 and PB4 in MAPbBr$_3$ has been performed with 3.1 eV excitation. The spectral traces 1 ps after excitation are given in Figure

C.2a. PB3 around 3.87 eV follows a complex energy shift with increasing fluence first red-shifting between 0.8 and 4.0×10^{17} cm^{-3} followed by a blue-shift up to 14×10^{17} cm^{-3}. The evolution of the PB amplitude with excitation density is given in Figure C.2b. Only PB4 follows a linear behaviour with input power (blue circles) while PB2 (green circles) and PB3(red circles) are strongly non-linear and deviate from the linear regime at $\sim 2 \times 10^{17}$ cm^{-3} onward, an excitation density 50% larger than the power used in the experiments presented in Chapter 2.
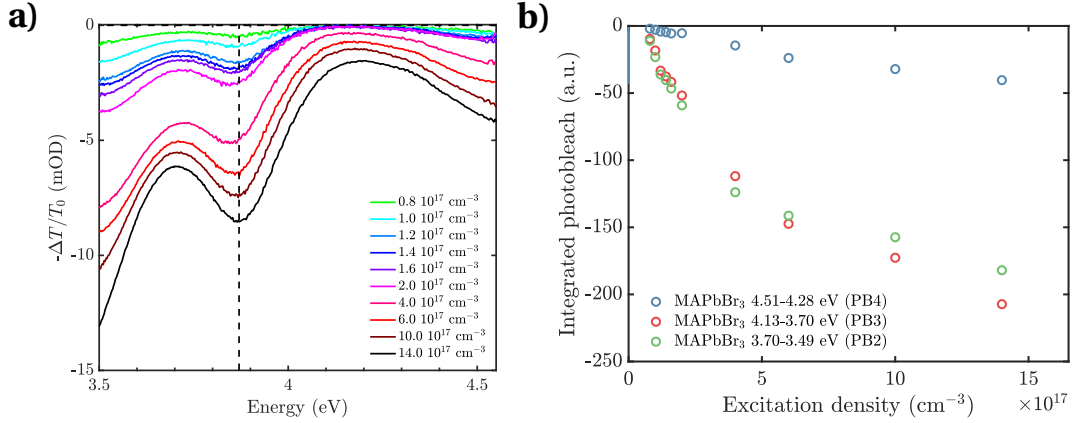
Figure C.2 – a) Fluence dependence in the UV following 3.1 eV excitation in MAPbBr$_3$ at different excitation densities. b) Evolution of the PB band integral in the PB2 (green circles), PB3 (red circles) and PB4 (blue circles) spectral regions with different excitation densities at 3.1 eV pump photon energy. Boundaries of the band integrals are in the legend.

C.4   Details about the transient transmission experiments

The experiment was performed at ambient pressure under inert nitrogen atmosphere for safety due to several reports of sample damaging under air exposure. However, it has recently been shown that standard air humidity exposure of the thin films does not lead to a change in photodynamics over several days [438].

The instrument response function (IRF) of the experiment performed on the MAPbBr$_3$ thin film in transmission (Chapter 2) is given in Figure C.3. It has been measured through a piece of quartz substrate of the same size and composition as the substrate on top of which the MAPbBr$_3$ thin film is deposited.

In order to exclude the contribution from the refractive index in the observed transient transmission signal on MAPbBr$_3$ thin film, a transient reflectivity experiment has been performed with 3.1 eV pump photons and the same excitation density. The pseudo-color coded energy-time map is given in Figure C.4. The transient signal compares well with the differential transmission signal in Figure 2.2b which shows that the differential transmission signal originates from changes in the absorption coefficient only [25].
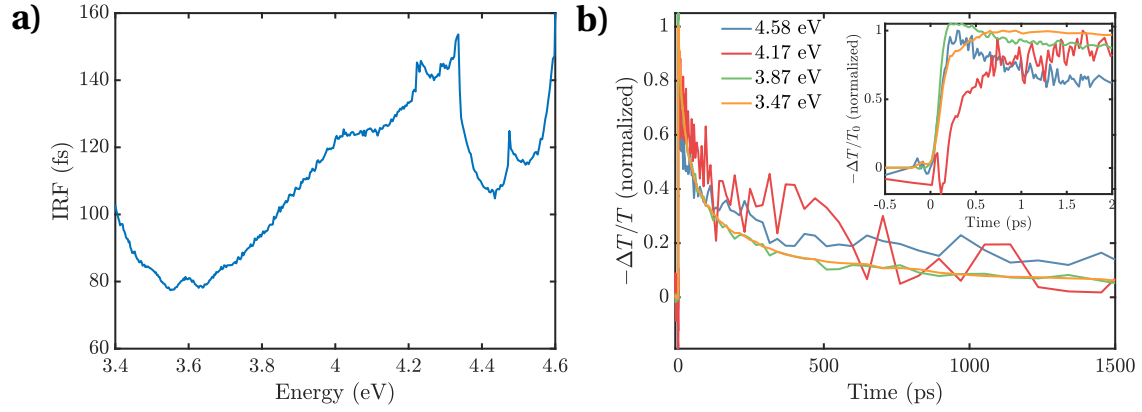
Figure C.3 – a) IRF of the differential transmission experiment on MAPbBr$_3$ thin film pumping at 3.1 eV and probing in the UV. b) Time traces at selected probe energies from MAPbBr$_3$ following 3.1 eV excitation.
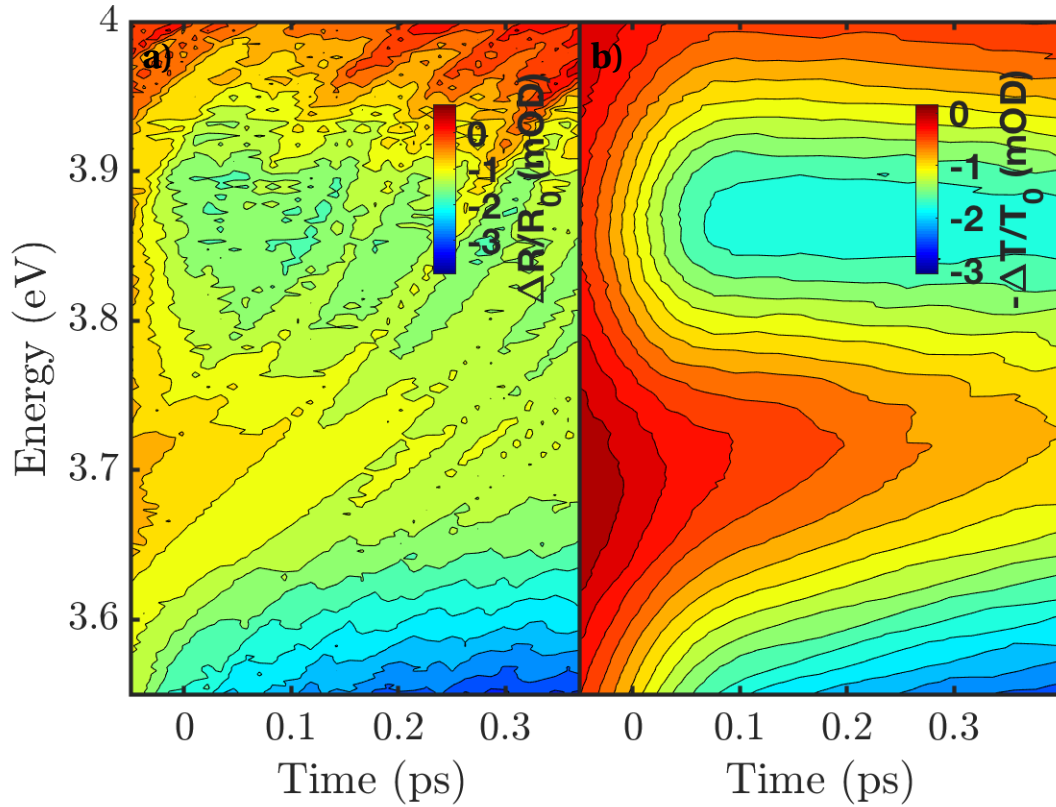
Figure C.4 – a) Transient reflectivity and b) differential transmission on MAPbBr$_3$ thin films following 3.1 eV excitation (density 1.7×10^{17} cm^{-3}).

Table C.2 – Summary of the energy position of the resonances retrieved by spectroscopic ellipsometry in the literature compared to the energy position of the PB on MAPbBr$_3$ in the UV following 3.1 eV excitation.

Reference	PB2 (eV)	PB3 (eV)	PB4 (eV)
[113]	3.58		4.55
[114]	3.52	3.88	4.46
[4]	3.41	3.91	5.12
[115]	3.42	3.92	4.36
[116]	3.42	3.95	4.47
our work	3.47	3.87	4.57

D TAS on MAPbBr$_3$ and MAPbBr$_3$/a-TiO$_2$ thin films in the Visible

D.1 Emission spectra from MAPbBr$_3$ and MAPbBr$_3$/a-TiO$_2$
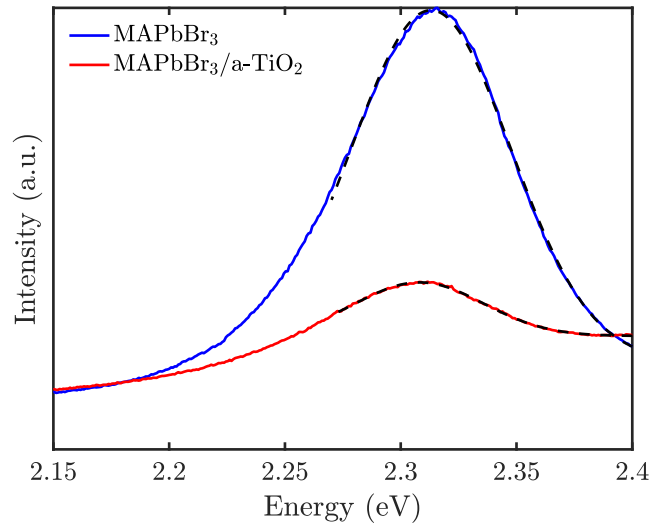
Figure D.1 – Emission spectra of MAPbBr$_3$ (blue curve) and MAPbBr$_3$/a-TiO$_2$ from 3.1 eV excitation. Black dashed lines are gaussian fittings.

The emission spectra of MAPbBr$_3$ and MAPbBr$_3$/a-TiO$_2$ are given in Figure D.1. The emission lines were fitted with gaussians to estimate the ratio of emission intensity between the two systems. The Gaussian is expressed as

$$G(E, A, E_0, \sigma, c) = \frac{A}{\sqrt{2\pi}\sigma} \exp\left(-\frac{(E - E_0)^2}{2\sigma^2}\right) + c \tag{D.1}$$

with full width at half maximum (FWHM) $= 2\sqrt{2\ln 2}\sigma$. The refined parameters are given in Table D.1. From the ratio between the integrals, MAPbBr$_3$/a-TiO$_2$ emission intensity is 10% of MAPbBr$_3$

Table D.1 – Refined parameters from the fitting of the emission spectra of MAPbBr$_3$ and MAPbBr$_3$/a-TiO$_2$ with a gaussian function.

sample	A	E_0 (eV)	FWHM (meV)
MAPbBr$_3$	1.4 ± 0.02	2.313 ± 0.001	81.1 ± 0.1
MAPbBr$_3$/a-TiO$_2$	0.172 ± 0.002	2.308 ± 0.001	65.2 ± 0.1

D.2 MAPbBr$_3$ differential transmission in the Visible

Energy-time maps for two comparable delivered pump fluences at 3.1 eV on MAPbBr$_3$ and MAPbBr$_3$/a-TiO$_2$ thin films are given in Figure D.2 (excitation density 1.7×10^{17} cm^{-3}). The differential transmission exhibits two photobleaches (PBs) labeled PB1 and PB2 as well as two photoinduced absorptions (PAs) labelled PA1 and PA2. The origin of the transient signal in the Visible has been extensively discussed in the case of MAPbI$_3$ [25, 39, 82, 118, 122, 126, 158, 439] but MAPbBr$_3$ has a similar transient reponse [39, 81, 82, 101, 117] close to its optical band gap. We briefly remind the origin of the PAs and PBs.

PB1 essentially has a Lorentzian lineshape and is assigned to the bleaching of the 1S Wannier-Mott excitation at the R-point [115] due to phase-space filling (PSF) by free charge carriers [3, 80, 84, 117, 118, 432, 440]. Different kinetic models have been tested to reproduce the decay time at PB1 which are depicted in Figure D.3a,b,c for MAPbBr$_3$ and D.3d,e,f for MAPbBr$_3$/a-TiO$_2$ (fitting equations in section D.3). It is clear that an exponential decay can be excluded from this analysis (Figure D.3a) while the transient signal can be described as a linear combination of bimolecular second order and Auger trimolecular third order kinetic laws in line with previous studies on MAPbBr$_3$ [117, 175] and MAPbI$_3$ [118]. The global evolution of the density of charge carriers n is given by,

$$-\frac{dn}{dt} = An^2 + Bn^3. \tag{D.2}$$

The negligible first order kinetic component discards exciton and trap-assisted recombinations.

PA1 is due to band gap renormalization (BGR) [97] which dominates over the Burstein-Moss (BM) blue-shift before the end of the charge carrier cooling step [158]. BGR on a faster timescale than cooling generates empty in-gap states which can be transiently populated [57]. The prompt appearance of PA1 shows the immediate renormalization of the electron and hole self-energy due to corrections of the exchange and hole correlation from the mobile charge carriers after photoexcitation [27]. The large amplitude difference between PA1 and PB1 in our experiment with respect to others [122] is related to the large pump excess energy as well as the P-polarization [25]. The PA1 lifetime is of the other of a few hundreds of femtoseconds similar to BGR lifetimes reported in FAPbBr$_3$ [211] and MAPbI$_3$ [38, 118, 441].
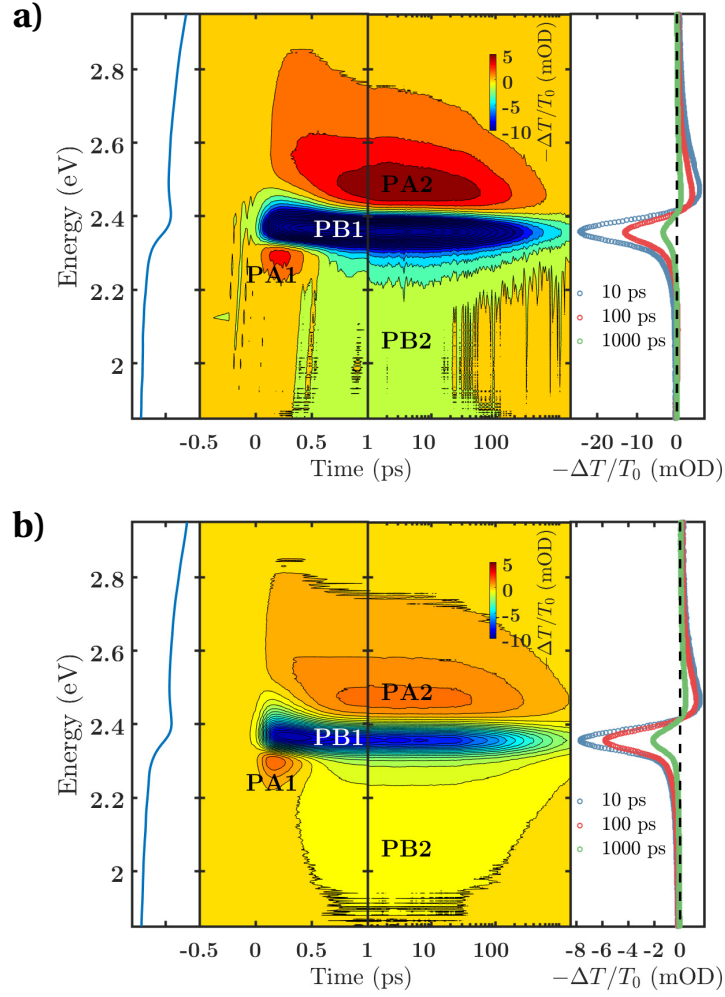
Figure D.2 – Differential transmission on a) MAPbBr$_3$ and b) MAPbBr$_3$/a-TiO$_2$ following 3.1 eV excitation (density 1.7×10^{17} cm^{-3}).

PA2 above the optical band gap is essentially due to the change in refractive index Δn as can be seen from the difference between transient transmission and transient reflectivity measurements where Δn plays a key role [25]. This effect is common in polar semiconductors with optical band gap in the Visible range such as GaAs [27], CdSe [442] or ZnSe [443]. Along the energy axis, the contribution from the change in absorption coefficient $\Delta \alpha$ to $-\Delta T/T_0$ is more pronounced closer the optical band gap while the contribution from Δn dominates at higher energies than the band gap [25]. Initially extending far above the optical band gap energy, PA2 moves progressively closer to the band edge over time as already reported [81, 432].

The progressively appearing negative tail PB2 extending well below the optical band gap has been already reported [175, 432] while it is sometimes absent [81, 117] suggesting that it is sample dependent. A consistent interpretation of its origin is related to exciton and hole

137
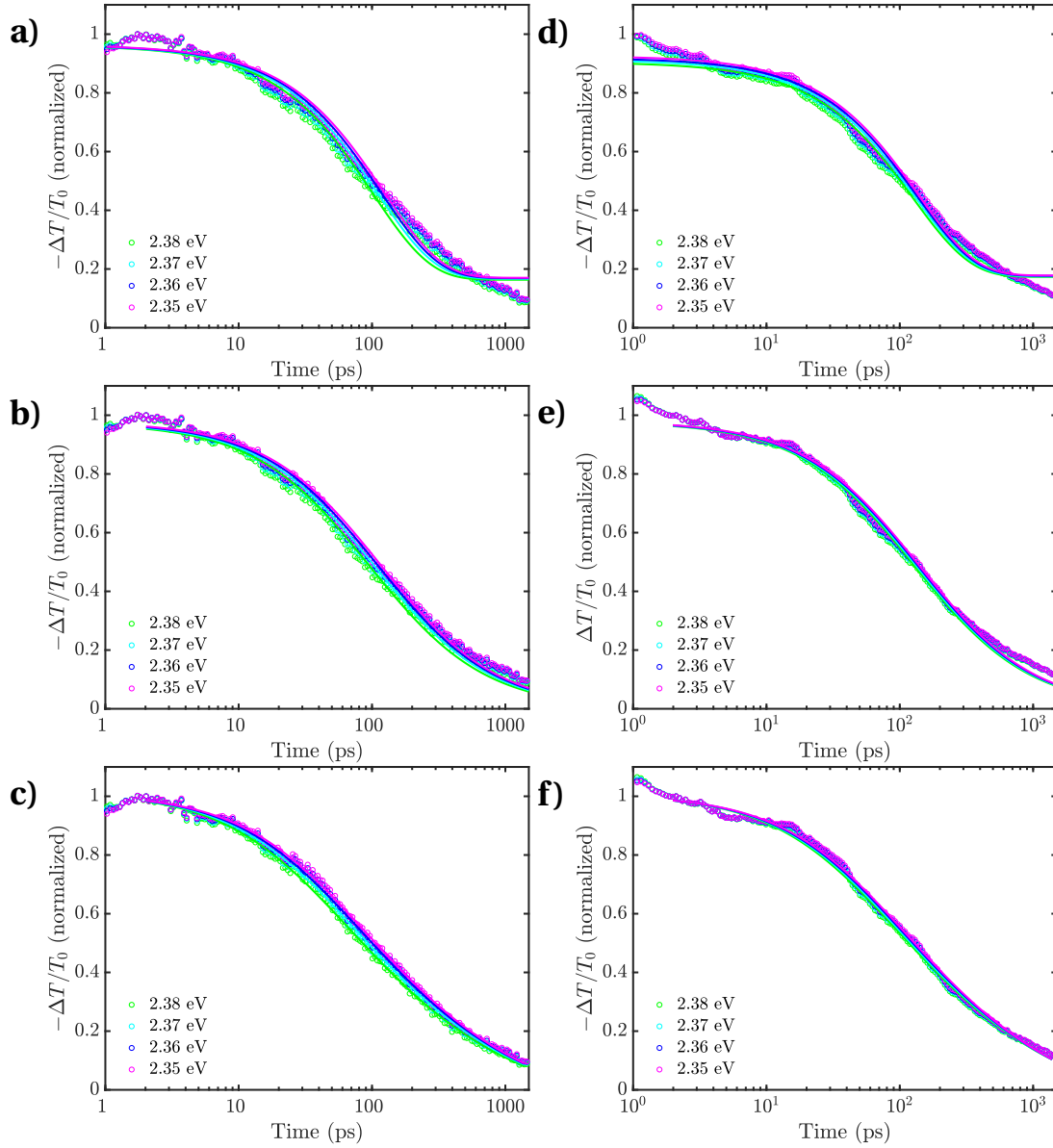
Figure D.3 – Kinetic models in the PB1 spectral region on MAPbBr$_3$ following 3.1 eV excitation: a) first order law, b) second order law and c) third order kinetic law. Kinetic models in the PB1 spectral region on MAPbBr$_3$/a-TiO$_2$: d) first order law, e) second order law and f) third order kinetic law.

traps [212] rather frequent in these solution processed hybrid organic-inorganic lead halide perovskite (HOIP) materials. Interestingly, the comparison between time traces taken in the PB1 and PB2 spectral regions give the same decay times while PB2 rises more slowly to reach its maximum amplitude (Figure D.4). It seems from this analysis that PB2 is an extension of PB1 in the in-gap spectral region. This result is fully consistent with the work of Zhu and coworkers who found similar recovery kinetics in MAPbI$_3$ for PB1 and PB2 but different rise times [212]. They have assigned this PB to self-trapped excitons [444] at the MAPbI$_3$ crystallite grain surface because of the stronger electron-phonon coupling. However, the recombination of a self-trapped exciton follows a monoexponential law while in our case a clear third order law describes the data (Figure D.3). Hence, PB2 involves three particles since it follows the same third order kinetic law as PB1. The exact nature of these states would require further investigation which is out of the scope of this Thesis.
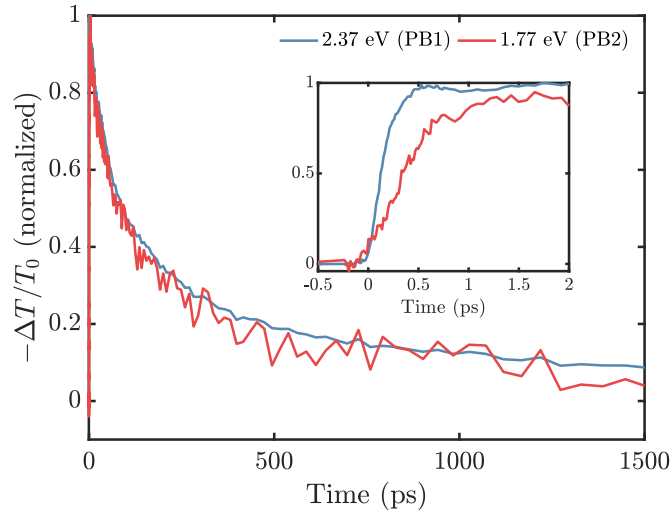
Figure D.4 – Comparison between the recovery time of the PB in the spectral region of PB1 (blue curve) and PB2 (red curve).

D.3   Kinetic laws

The integration of the kinetic laws at first, second and third order provides the equations D.3, D.4 and D.5 respectively which are used for the fittings of the time traces in Chapter 2 and this Appendix.

$$-\Delta T/T_0 = kn_0 e^{-At} + y_0 \text{ at first order} \tag{D.3}$$

$$-\Delta T/T_0 = \frac{kn_0}{n_0 B t + 1} + y_0 \text{ at second order} \tag{D.4}$$

$$-\Delta T/T_0 = \frac{kn_0}{\sqrt{2Cn_0^2 t + 1}} \text{ at third order} \tag{D.5}$$

In these expressions, the time constants are given by the parameters A, B and C in s^{-1}, $cm^3.s^{-1}$ and $cm^6.s^{-1}$ respectively. The amplitude is given by the factor k while the initial excitation density generated by the pump pulse is given by n_0 (in cm^{-3}).

D.4 Global analysis of MAPbBr$_3$ and MAPbBr$_3$/a-TiO$_2$ in the UV

A global analysis (GA) of the differential transmission in the UV is performed with the `Optimus` software [159]. The reconstructed energy-time maps for an increasing number of time constants are shown in Figure D.6 for MAPbBr$_3$ and Figure D.7 for MAPbBr$_3$/a-TiO$_2$. The decay associated spectrum (DAS) of the corresponding GA fittings are given in Figure D.8 for MAPbBr$_3$ (left column) and MAPbBr$_3$/a-TiO$_2$ (right column).

D.5 Differential transmission of MAPbBr$_3$ and MAPbBr$_3$/a-TiO$_2$ in the Visible

The usual way to infer electron injection at the HOIP/electron transport material (ETM) interface is from the initial faster recovery of PB1 due to a lower PSF at the conduction band (CB) minimum of the HOIP upon electron injection [106, 214] which is an indirect proof of electron injection [445, 446].

Spectral traces from differential transmissions experiments performed with 3.1 eV pump photon are shown in Figure D.9a, 1 ps after excitation (density 0.5×10^{17} cm^{-3}). We observe an absolute decrease of PB1 amplitude by ~35% in MAPbBr$_3$/a-TiO$_2$ with respect to bare MAPbBr$_3$. The comparison between the normalized time traces in the PB1 region is shown in Figure D.9b. Similarly to PB2 in the UV spectral range, the PB1 decay times of MAPbBr$_3$ and MAPbBr$_3$/a-TiO$_2$ are almost the same from the picosecond (ps) to nanosecond (ns) timescale under similar excitation conditions with a slightly slower decay for MAPbBr$_3$/a-TiO$_2$. It does not allow *a priori* saying that injection occurs at the interface. This is consistent with previous work at the MAPbI$_3$/a-TiO$_2$ interface looking at the kinetics in the PB1 spectral region [447]. Instead, a difference appears within the first 5 ps where the rise time in MAPbBr$_3$/a-TiO$_2$ is not bimodal contrary to MAPbBr$_3$ (inset in Figure D.9b). There are two possible explanations for this effect: (i) the delivered pump fluence to the sample is lower in MAPbBr$_3$/a-TiO$_2$ than
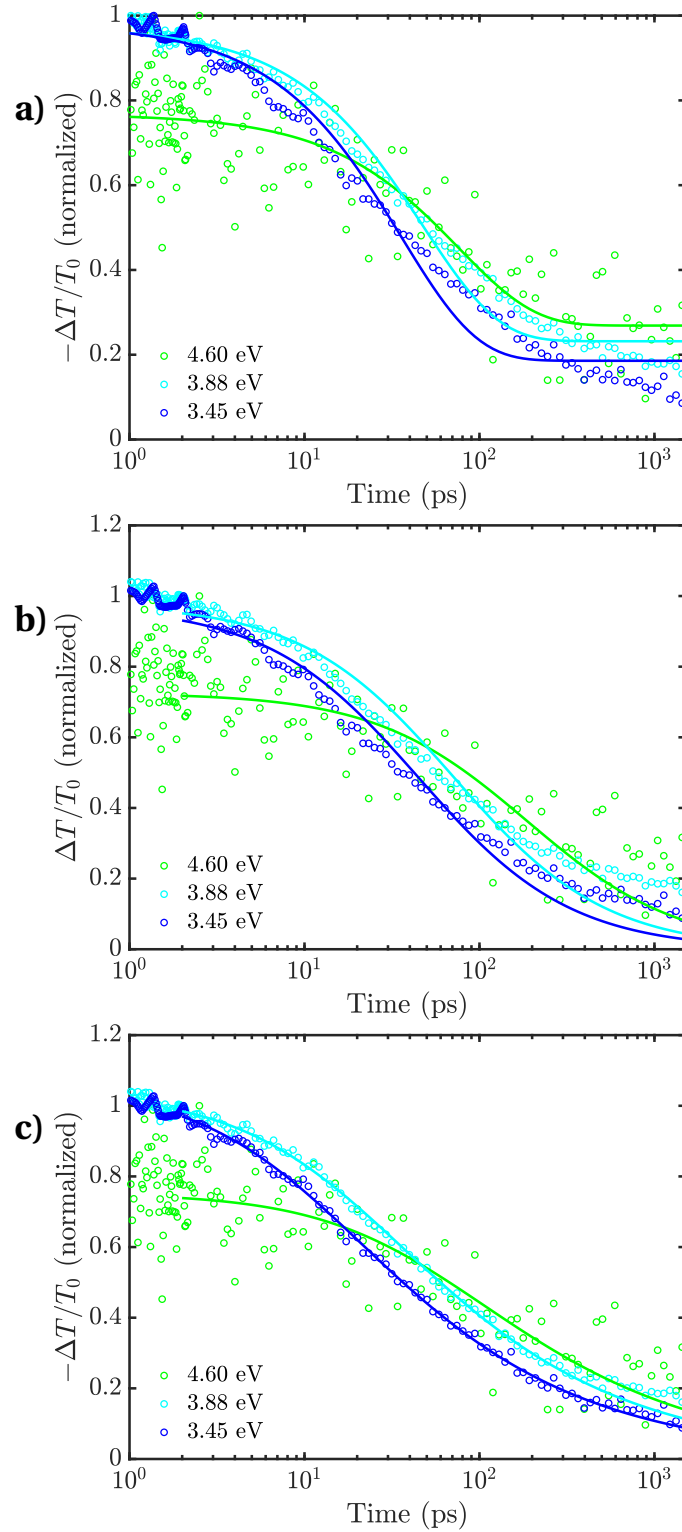
Figure D.5 – Kinetic models in the PB1, PB2 and PB3 spectral region in the ultraviolet (UV) on MAPbBr$_3$/a-TiO$_2$: a) first order law, b) second order law and c) third order kinetic law.
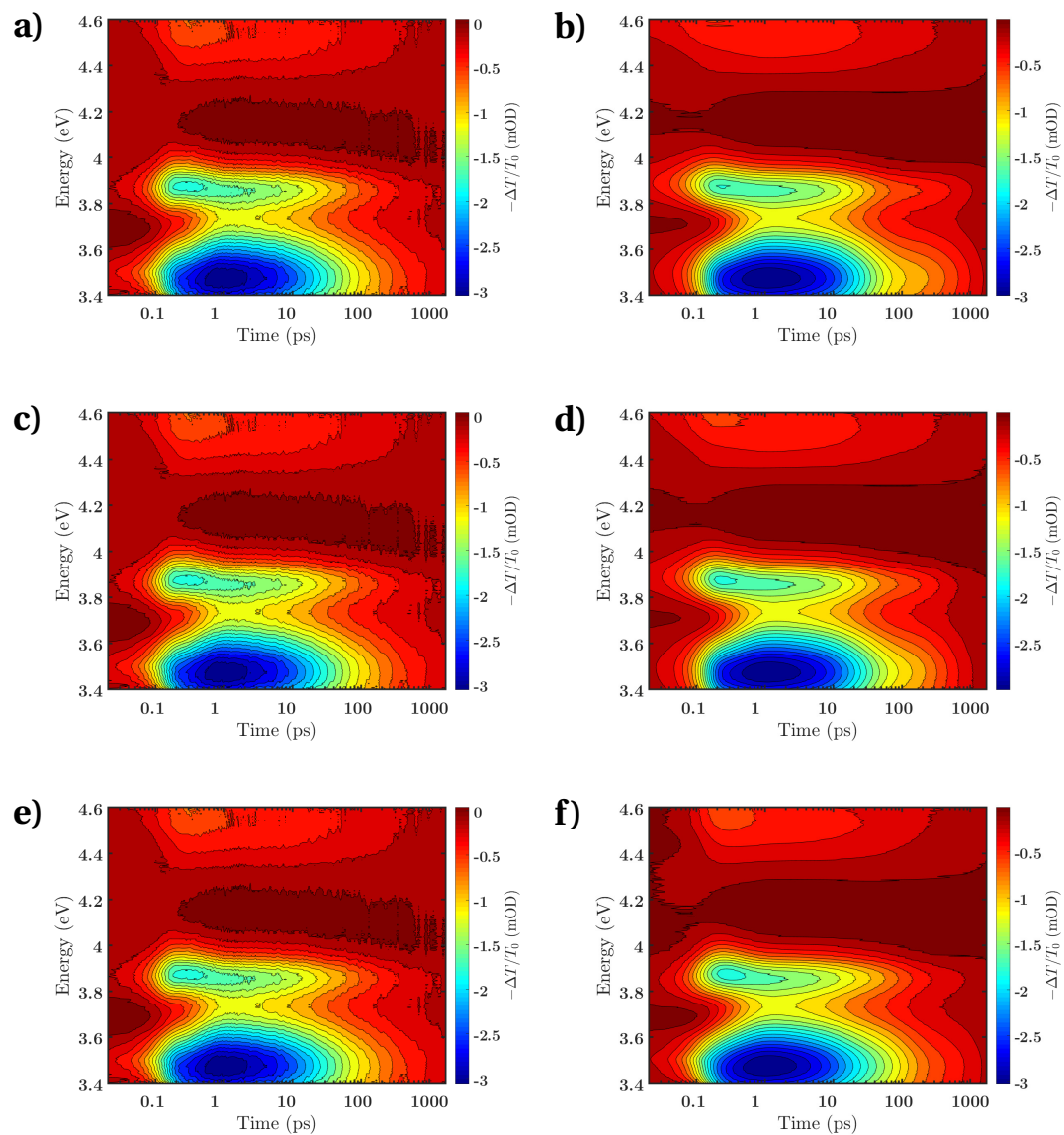
Figure D.6 – Experimental energy-time map of MAPbBr$_3$ (a, c and e are identical) and reconstructed maps from GA with b) three, d) four and f) five time constants.
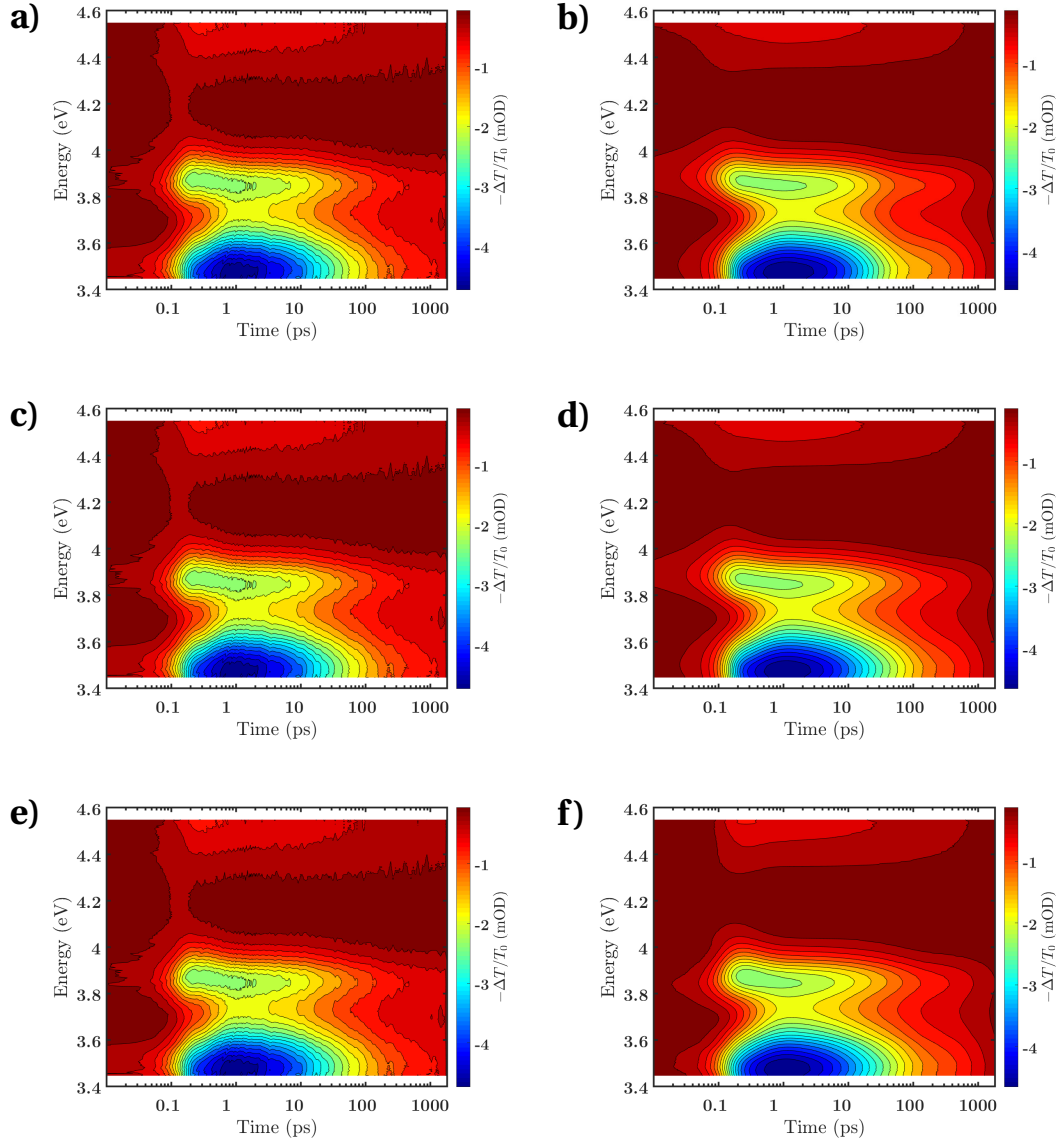
Figure D.7 – Experimental energy-time map of MAPbBr$_3$/a-TiO$_2$ (a, c and e are identical) and reconstructed maps from GA with b) three, d) four and f) five time constants.
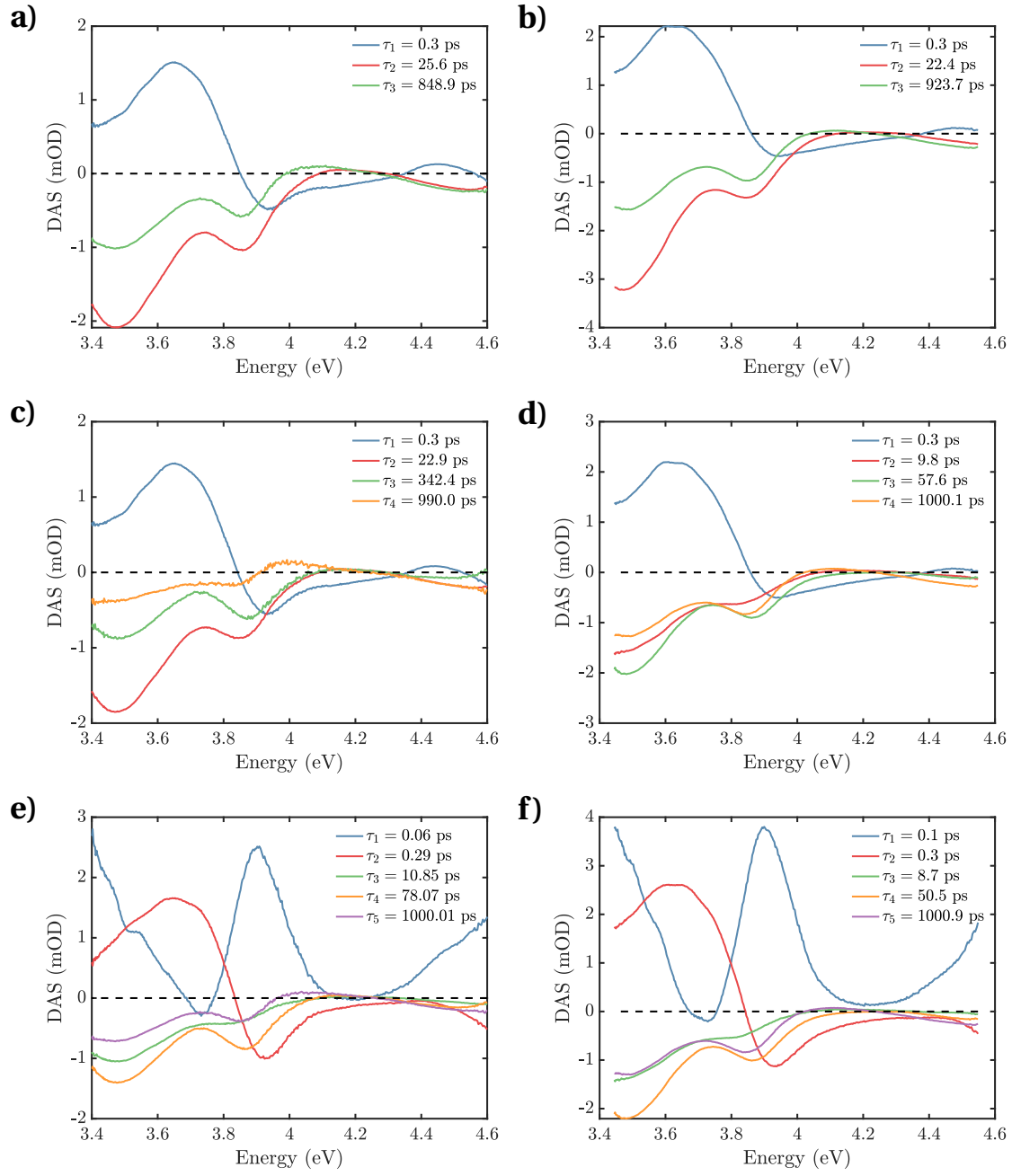
Figure D.8 – DAS of (left) MAPbBr$_3$ and (right) MAPbBr$_3$/a-TiO$_2$ with three (a,b), four (c,d) and five (e,f) time constants.

in MAPbBr$_3$ which fastens the cooling time [448], (ii) a prompt injection of hot charge carriers occurs which fastens the cooling time because of the smaller average energy to release by the electrons to cool down at the CB minimum [101]. The injection is also compatible with a slightly slower recovery time in MAPbBr$_3$/a-TiO$_2$ than in MAPbBr$_3$ observed in Figure D.9b. Since we have made sure that both experiments were performed at the same fluence, we interpret the result as a prompt injection of charge carriers into a-TiO$_2$ which leads to an apparently lower delivered pump fluence to the MAPbBr$_3$ layer. This experiment has been repeated at several pump fluences for both systems shown in Figure D.10a. Systematically, a faster rise time is observed in MAPbBr$_3$/a-TiO$_2$ which can be interpreted as the injection of hot charge-carriers into a-TiO$_2$. Hence, electron injection with Visible probe is rather difficult to observe for the current system since the presence of a-TiO$_2$ leads to minor changes in the kinetics on the nanosecond timescale and an apparently faster charge cooling time due to electron injection. The decrease of the absolute amplitude of PB1 in MAPbBr$_3$/a-TiO$_2$ certainly has one part originating from the electron injection but also probably because of a lower delivered fluence in the MAPbBr$_3$ layer due to the presence of a-TiO$_2$ which can act as a scatterer and a reflective layer. The best electron injection efficiencies into a-TiO$_2$ have been achieved with HOIP quantum dots (QDs) in which the discretization of the bands plays a key role in the efficiency of the injection process [101, 106, 440, 449].
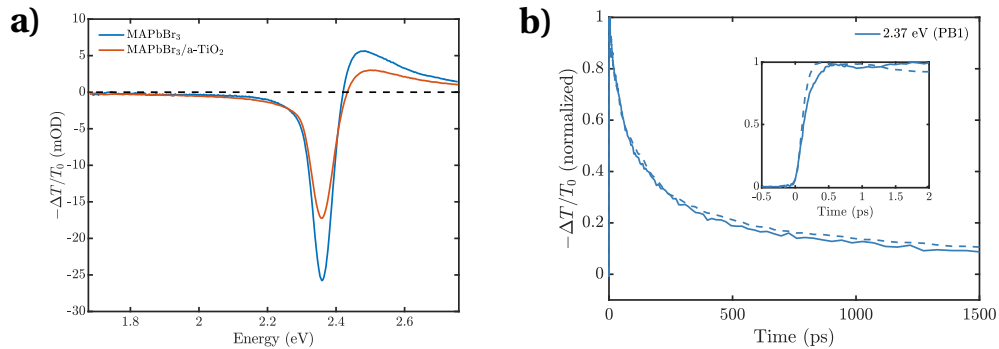
Figure D.9 – a) Comparison between the spectral traces of MAPbBr$_3$ (blue curve) and MAPbBr$_3$/a-TiO$_2$ (red curve) following 3.1 eV excitation at the same fluence, 1 ps after excitation. b) Comparison between normalized time traces in the PB1 region for MAPbBr$_3$ (continuous line) and MAPbBr$_3$/a-TiO$_2$ (dashed line).

Following these results, it seems that the electron injection occurs on a fast timescale of less than 1 ps since an effect of the a-TiO$_2$ layer is observed during the cooling. This is in contradiction with the long injection time on the 100 ps to nanosecond timescale retrieved in the UV in Chapter 4. However, the two experiments look at the injection process from a different perspective. The differential transmission in the Visible looks at the injection from the perspective of a decreased PSF in the HOIP layer while in the UV, one looks at the cooled injected electron at the bottom of the a-TiO$_2$ CB. A discrepancy between the two experiments is possible if intermediate states are involved at the interface which delay the diffusion of charge carriers into the ETM bulk (trap states, charge-transfer excitons (CTEs)) or if the presence of the ETM layer changes the morphology of the HOIP layer such that an extrinsic change of

dynamics is observed. The latter can be excluded on the basis of the remarkable agreement between the time traces measured at PB2 in MAPbBr$_3$ with and without a-TiO$_2$ at the same excitation density (Figure 4.2), which shows that in a spectral region where no contribution of a-TiO$_2$ is expected, the dynamics is intrinsic of MAPbBr$_3$. Hence, the effect of the interface onto the injection kinetics remains elusive and complementary experiments looking at the influence of the sample morphology may help understanding better the slow injection time into a-TiO$_2$. Clearly, the slow injection time rationalizes the recent discovery that charge transport occurs in the HOIP layer to the anode [88].
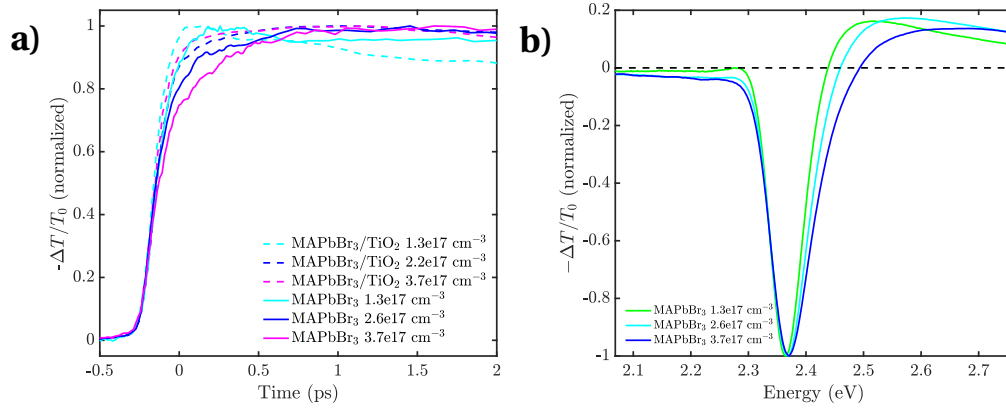
Figure D.10 – a) Evolution of the time traces measured in the PB1 spectral region for different excitation densities on MAPbBr$_3$ (continuous lines) and MAPbBr$_3$/a-TiO$_2$ (dotted lines). The time traces have been sign flipped for convenience. b) Evolution of the spectral traces 0.5 ps after excitation at 3.1 eV in MAPbBr$_3$ for different excitation densities.

Alternatively, the analysis of the carrier temperature over time can infer electron injection from a faster decrease of the average carrier temperature [101]. The PB1 high energy tail is directly related to the Fermi-Dirac (FD) distribution of the hot holes and electrons after thermalization, which can be approximated by a Maxwell-Boltzmann (MB) distribution at high carrier temperature. For a hot charge carrier distribution, the number of photons which can be emitted at energy E per unit energy step dE (and will be bleached in absorption at energy E) is given by [192],

$$N(E)dE \sim E^2 |M|^2 f_e f_h \rho_e \rho_h dE \tag{D.6}$$

where $N(E)$ is the number of bleached photons observed within dE from E, f_e and f_h are the electron and hole occupation numbers, ρ_e and ρ_h are the density of states (DOS) and $|M|^2$ is the excitation matrix element. The transient transmission $\Delta T/T_0$ is proportional to $N(E)$ and the electron and hole occupation numbers can be approximated by MB distribution such that,

$$-\frac{\Delta T}{T_0}(t, E) \propto E^2 \exp\left(\frac{E_f - E}{k_B T_c(t)}\right) \tag{D.7}$$

with E_f the Fermi energy, $T_c(t)$ the average carrier temperature at time t and k_B the Boltzmann

constant. Increasing the pump fluence generates a higher T_c which decays more slowly because of hot-phonon bottleneck effects. This generates a smoother exponential with a negative tail to the PB extending to higher and higher energies above the band gap as illustrated in Figure D.10b for MAPbBr$_3$. We have applied this analysis which has been used in a few studies [101, 158] on our datasets giving inconsistent results with a larger average carrier temperature in MAPbBr$_3$/a-TiO$_2$ than in MAPbBr$_3$.

D.6   Fluence dependence in the Visible

The differential transmission in the Visible with 3.1 eV excitation has been performed at different pump fluences. The evolution of the energy-time color-coded maps is shown in Figure D.11 for MAPbBr$_3$ and Figure D.12 for MAPbBr$_3$/a-TiO$_2$.
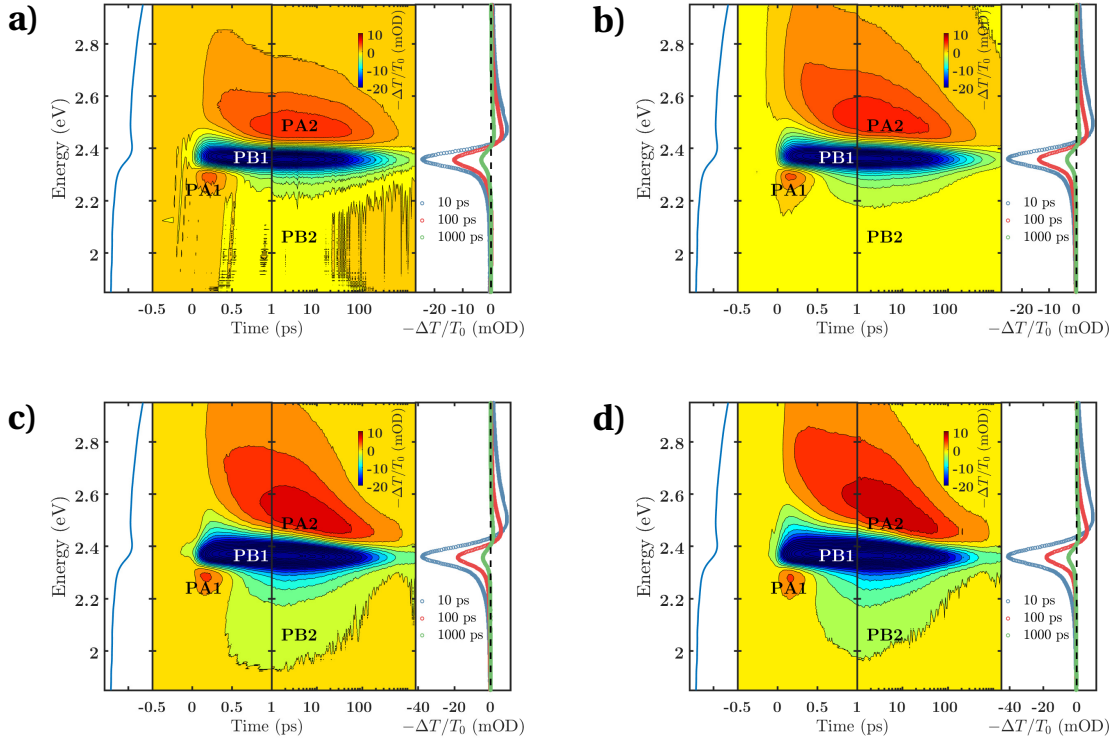
Figure D.11 – Evolution of the energy-time map of MAPbBr$_3$ with 3.1 eV pump photons and excitation densities: a) 1.3×10^{17} cm^{-3}, b) 2.6×10^{17} cm^{-3}, c) 3.7×10^{17} cm^{-3} and d) 5.6×10^{17} cm^{-3}.

D.7   Comparison of the time traces between MAPbBr$_3$ and MAPbBr$_3$/a-TiO$_2$

Time traces at single probe energy points in MAPbBr$_3$ and MAPbBr$_3$/a-TiO$_2$ are shown in Figure D.13 following 3.1 eV excitation at different probe energies. Contrary to band integrals,
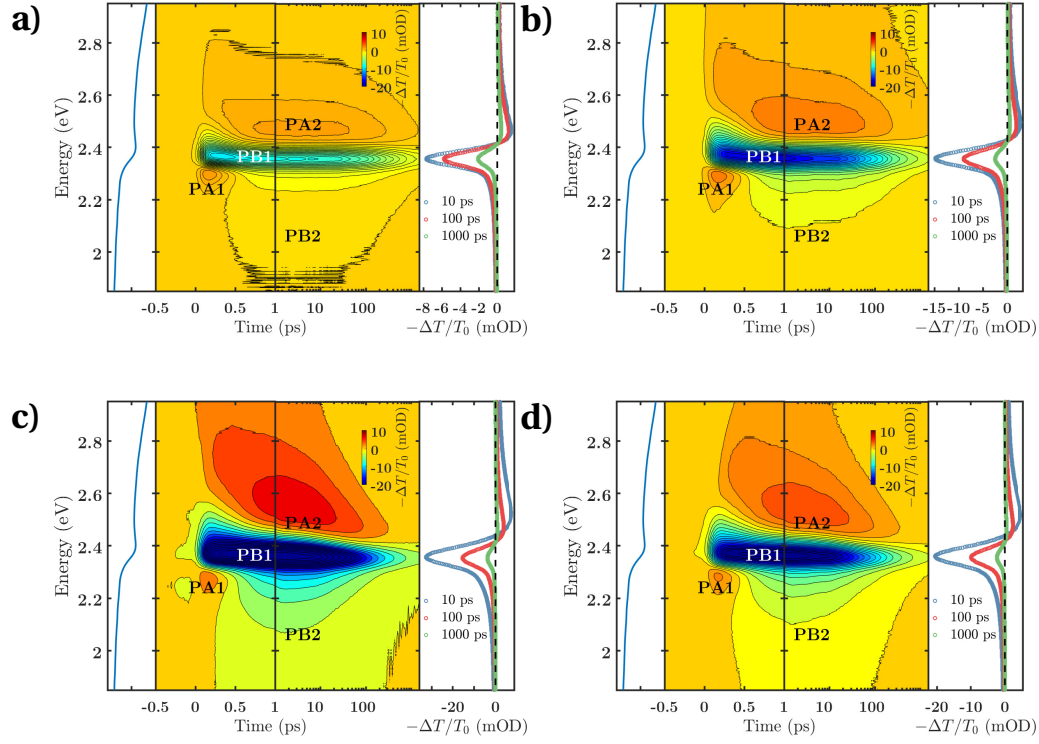
Figure D.12 – Evolution of the energy-time map of MAPbBr$_3$/a-TiO$_2$ with 3.1 eV pump photons and excitation densities: a) 1.1×10^{17} cm^{-3}, b) 2.2×10^{17} cm^{-3}, c) 3.7×10^{17} cm^{-3} and d) 5.6×10^{17} cm^{-3}.

time traces at given probe energies depend on the filling of the single particles states in the valence band (VB) and the CB. While the initial dynamics is similar for both systems (inset in Figure D.13), the dynamics differs on the picosecond to nanosecond timescale. First PB1 decays faster in MAPbBr$_3$/a-TiO$_2$ as a consequence of the decrease in the PSF contribution to the PB due to electron injection. At later times, PB1 recovers more slowly in MAPbBr$_3$/a-TiO$_2$ because of the charge separation which prevents charge carrier recombination and generates holes in the VB of MAPbBr$_3$ which contribute to PB1 for a longer time.

D.8 Transient signal in MAPbBr$_3$ normalized at PB1

In order to infer that the additional PB observed after the normalization at PB2 comes from the PB in a-TiO$_2$ (procedure described in chapter 4), the same procedure is followed in MAPbBr$_3$ for which no electron injection occurs which should not lead to an additional PB. The result is depicted in Figure D.14 (bottom panel) which gives a blurred image because of the similar decay kinetics in the PB2 and PB3 regions in the absence of electron injection.
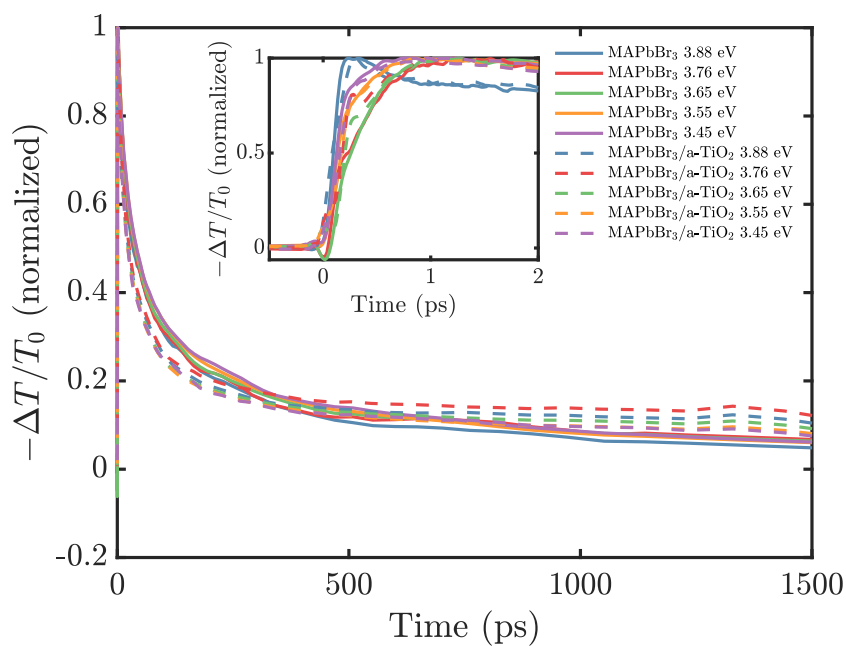
Figure D.13 – Comparison of the time traces obtained on MAPbBr$_3$ (continuous lines) and MAPbBr$_3$/a-TiO$_2$ (dashed lines) following 3.1 eV excitation at the same excitation density $(1.3 \times 10^{17} \text{ cm}^{-3})$.
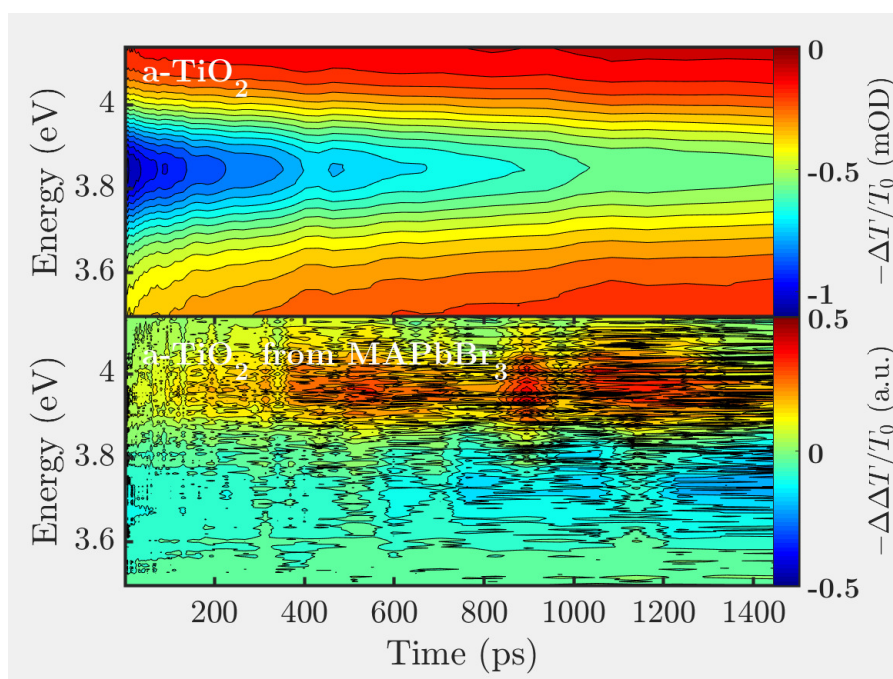
Figure D.14 – Color-coded energy-time map from (top) a-TiO$_2$ following 3.87 eV excitation and (bottom) MAPbBr$_3$ following 3.1 eV excitation and renormalized according to the procedure described in section 4.1.

D.9   Definition of a band integral

A band integral provides a difference in dipole strength ΔD which is given by,

$$\Delta D(t) = \int_{E_{min}}^{E_{max}} \frac{\Delta OD(E,t)}{E} dE \tag{D.8}$$

where E represents the probe photon energy between the lower and upper boundaries E_{min} and E_{max} respectively and t the time delay.

D.10   Analysis of the Burstein-Moss shift in MAPbBr$_3$ and MAPbBr$_3$/a-TiO$_2$

In the parabolic band approximation, an energy shift of the band gap is expected upon filling of the CB with electrons and the VB with holes according to [221],

$$E_g = E_g^0 + \frac{\hbar^2}{2m_{eh}^*}(3\pi^2 n_0)^{2/3} \tag{D.9}$$

with E_g^0 the ground state band gap, m_{eh}^* the reduced electron-hole effective mass ($m_{eh}^{*-1} = m_e^{*-1} + m_h^{*-1}$) and n_0 the density of photoexcited charges. Practically, the BM effect leads to the broadening of PB1 on the high energy side with increasing excitation density. The FWHM of PB1 can be used as a measure of the BM shift and thus the excitation density [221]. However, the dynamic BM applies after the charge carrier cooling. In the case of MAPbBr$_3$, we have checked the validity of the BM 2 ps after excitation by fitting the PB1 broadening at different excitation densities and plot the results in Figure D.15. The evolution of the band gap energy shift ($\Delta E_g = E_g - E_g^0$) is linear with the excitation density which shows the validity of the BM model. The same analysis on MAPbBr$_3$/a-TiO$_2$ also exhibits a linear behavior but surprisingly, the band gap shift is larger than in bare MAPbBr$_3$.
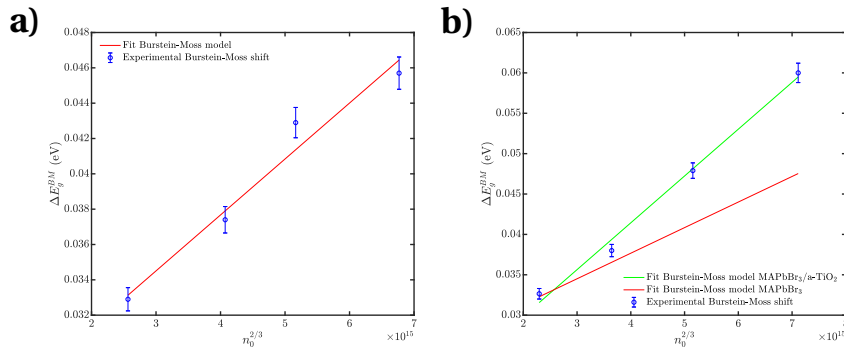
Figure D.15 – Fitted energy gap shift 2 ps after excitation in a) MAPbBr$_3$ and b) MAPbBr$_3$/a-TiO$_2$ against the estimated excitation density (circles with error bars). A linear fit shows the validity of the BM model and that the band gap shift evolves as $n_0^{2/3}$. The fit for MAPbBr$_3$ is displayed as a red curve and the fit for MAPbBr$_3$/a-TiO$_2$ is displayed as a green curve.

E TRXAS on NiO microparticles at the Ni K-edge

E.1 Sample preparation and characterization

NiO microparticles powder (325 mesh, 40 μm average diameter) has been purchased from Sigma-Aldrich. The microparticles were suspended in MilliQ water and sonicated for half an hour before the experiment. The solution was vigorously steered during the experiment to prevent agglomeration and deposition.

The UV-Vis spectrum of the microparticle suspension is provided in Figure E.1a. Excitation spectra are measured at the two emissions of NiO around 370 nm and 730 nm which reproduce the UV-Vis spectrum. The 355 nm pump photon energy used in the time-resolved X-ray absorption spectroscopy (TRXAS) is at the absorption onset which generates the same signal shape as with 266 nm excitation (Figure E.3b). We have also observed the same signal shape in transient reflectivity with 266 nm and 355 nm excitation in the deep-UV of NiO single crystals (see chapter 6) which shows that the band gap is indeed excited at 355 nm although not efficiently.

E.2 TRXAS: experimental conditions

The experimental conditions of the TRXAS experiment presented in Chapter 7 are given in Table E.1

E.3 X-ray energy calibration

The energy calibration was performed by measuring the X-ray absorption spectrum (XAS) spectrum in transmission of a thin Ni foil (~10 μm) with a Si diode couple to a current amplifier (variable gain DHPCA-100 from FEMTO). The Figure E.1b shows the first derivative of the measured foil XAS (blue curve) together with the tabulated XAS derivative spectrum (orange curve) [450]. A good agreement is observed in the X-ray absorption near-edge structure
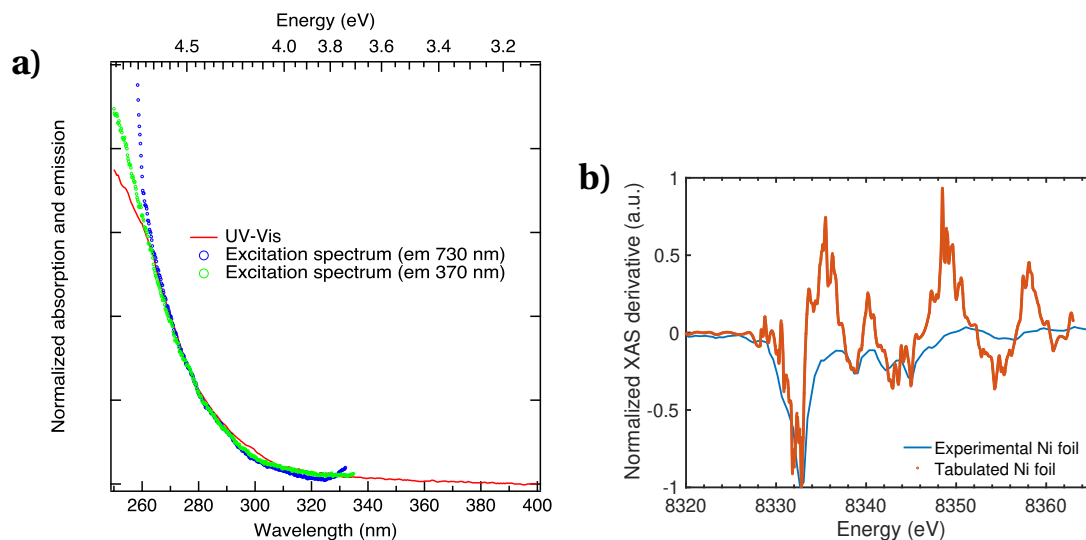
Figure E.1 – a) UV-Vis spectrum (red curve) and excitation spectra with detection at 370 nm (green circles) and 730 nm (blue circles) of a colloidal suspension of ∼170 mM NiO microparticles in MilliQ water. b) Energy calibration of the MicroXAS Si(111) monochromator with a Ni foil in transmission.

Table E.1 – Experimental parameters for the TRXAS experiment on NiO microparticles at the Ni K-edge. The excitation yield is an upper limit, estimated from the measurement of the absorbed laser power by the sample (see section E.4 for the details).

Parameter	Value
Laser repetition rate	260 kHz
Laser spot size	32 μm radius FWHM
Laser average power	700 mW
Laser fluence	81 mJ/cm^2
Energy per laser pulse	2.69 μJ
Photons per laser pulse	$4.81 \cdot 10^{12}$
Sample concentration (stiochiometric units of NiO)	170 mmol/L
Liquid jet thickness	200 μm
Excitation yield	4.6%

(XANES) between the derivative extrema which gets worse in the extended X-ray absorption fine structure (EXAFS) with the energy scale slightly expanded in our experimental data.

E.4 Estimate of the photoexcitation yield

Assuming the linearity of the signal with the peak power and the number of incident optical photons, the excitation yield f can be estimated from the relation,

$$f = \frac{N_{ph}}{F d c_{mol} N_A}(1 - 10^{-\epsilon_\lambda c_{mol} d}) \tag{E.1}$$

with N_{ph} the number of photons per pump pulse, F the beam waist, d the optical path length (liquid jet thickness), c_{mol} the molar concentration (in mol/m^3) and N_A the Avogadro number. A molar extinction coefficient of $\epsilon_{355\,nm}$ =29411 L/mol/m at 355 nm has been considered for the calculation of the excitation yield from the absorption cross section in a NiO single crystal [289]. From the experimental parameters in Table E.1, our excitation yield is less than 5% (upper limit due to the pump scattering from the sample).

E.5 Fluence depence on the TRXAS signal of NiO microparticles in solution

The linearity of the TRXAS signal with input pump fluence was checked at the Ni K-edge of NiO microparticles following 355 nm excitation at 100 ps time delay. The transient signals at three different fluences and a fit of the signal maximum absolute amplitude around 8.35 keV with absorbed power are given in Figure E.2. The dataset shows the linearity of the observed transient signal in the range of investigated pump fluences.
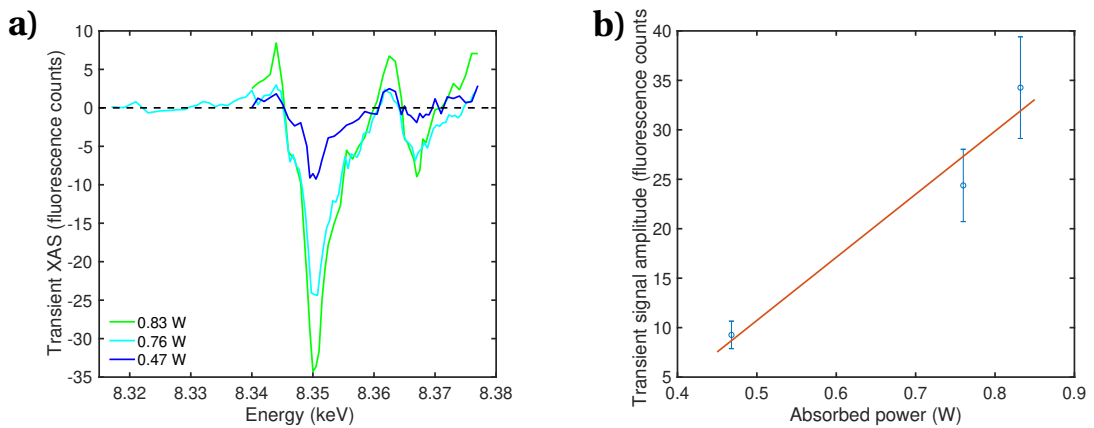
Figure E.2 – a) Evolution of the TRXAS signal of NiO microparticles following 355 nm excitation at three different pump powers. The time delay is 100 ps. b) Linear fitting of the signal absolute maximum amplitude at ~8350 eV with pump power.

E.6   **Comparison pump wavelength** 266 nm **and** 355 nm

Figure E.3b compares the transient spectra at the Ni K-edge of NiO following 266 and 355 nm excitation at 100 ps time delay. The transient is similar which indicates that it is independent of the pump photon energy. The larger noise in the transient with 266 nm pump photon energy is due to a lower average pump power (∼10 times less than with 355 nm excitation).

E.7   **Temporal evolution of the TRXAS signal of NiO microparticles in solution**

Spectral traces in the XANES of NiO at the Ni K-edge have been measured at different time delays after excitation which are shown in Figure E.3a.
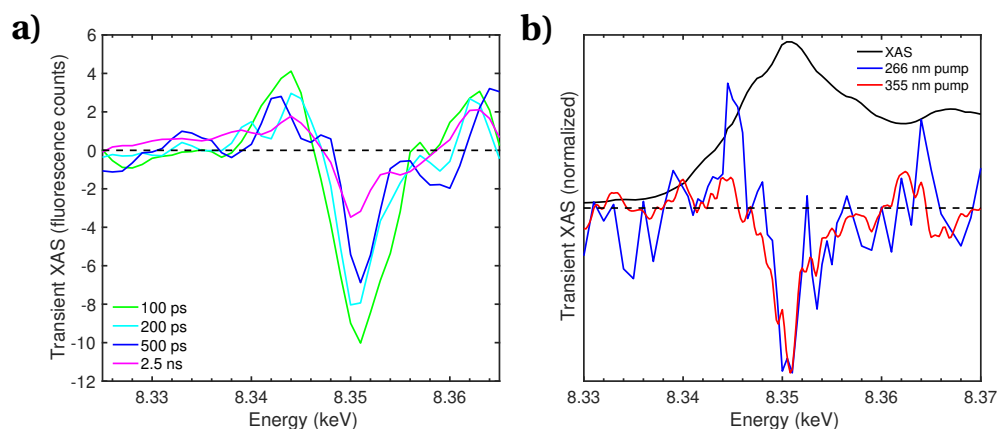
Figure E.3 – a) Temporal evolution of the Ni K-edge transient XAS signal in NiO at 100 ps (green curve), 200 ps (cyan curve), 500 ps (blue curve) and 2.5 ns (punk curve) after 355 nm excitation. b) Evolution of the transient signal for pump photon energies of 266 nm (blue curve) and 355 nm (red curve) at 100 ps time delay.

F XAS ab-initio calculations

The *ab initio* calculations of the XAS presented in this Thesis have been performed with the FDMNES package developed by Yves Joly and coworkers [451] and the XSpectra package developed by Matteo Calandra and coworkers [452] implemented in Quantum-Espresso [453]. The FDMNES package allows calculations both with the full multiple scattering (FMS) and finite difference method (FDM) which are implemented with full-relativistic description in the monoelectronic approximation within density functional theory (DFT)-local spin-density approximation (LSDA) [454] or with the Hubbard U correction (LSDA+U). The monoelectronic approach in the case of the K-edges is justified from the short lifetime of the photoelectron which can experience only the close surroundings of the absorbing atom and limit multiple scattering pathways. In addition, the interaction between the core-hole and the valence electrons is significantly weaker at the K-edge than the interaction with the $2p$ electrons at L-edges and for which a description with atomic multiplets is required [455]. In section F.1, we briefly describe the implementation of FDM and FMS calculations and some of the approximations made to get an accurate modelling of the XAS and TRXAS data. In section F.2, we discuss the implementation of pseudopotential based calculations with core-hole effects with the XSpectra package. Details of the calculations of the XANES and the EXAFS presented in chapter 7 are given in section F.3.

F.1 Calculations with FDMNES

F.1.1 FDM and FMS

The FMS is an inexpensive calculation method with respect to FDM. It requires that the crystal potential is modelled by non-overlapping spheres centred on the atoms, the so-called muffin-tin (MT) approximation. Hence the potential is spherical around the atoms, often modelled from atomic multiplet calculations for the different atoms in the ground state, while the interstitial potential region between the spheres is flat [456] (Figure F.1). The main limitation of this approximation is that it cannot account for the eventual potential anisotropy which is crucial in anatase TiO_2 for instance and for which full potential is required beyond the

spherical potential approximation. However, for NiO in its cubic phase, the calculations can be performed within the FMS-MT approximation. The propagation of the electron for each X-ray photon energy is performed with the Green formalism on the MT potential to provide the XAS spectrum.
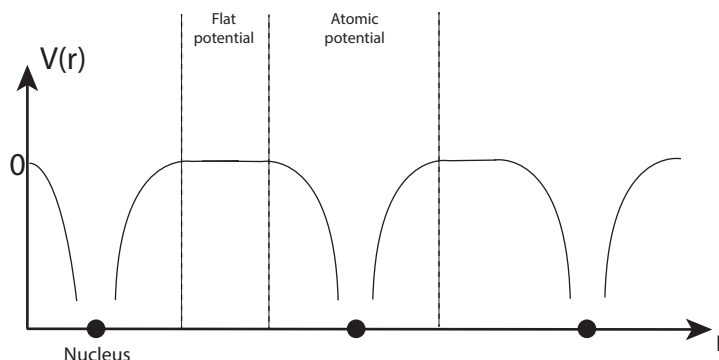
Figure F.1 – Schematic of the muffin-tin potential approximation used in FMS calculations. The potential is spherical around the atoms in the ground state while the interstitial potential region between the spheres is flat and conventionally set to zero.

The FDM overcomes the isotropic approximation of the atomic potential [457]. In this case, the potential is described within the local density approximation (LDA) and has been successfully implemented in FDMNES [369]. It decomposes the calculation into three different regions which are depicted in Figure F.2 and delimited by an outer sphere where the potential is considered constant. Inside the outer sphere and outside the atomic core regions, the FDM is used to solve the Schrödinger equation and get the XAS spectrum. Inside the atomic core regions, the expansion into spherical harmonics is used.

The Schrödinger equation solved with the FDM which has no requirement over the potential shape. Different possibilities for the description of the exchange-correlation potential are provided (Hedin-Lunqvist, Perdew,...). There is also the possibility to use non-spherical electronic densities, which is one important step beyond the MT approximation, for instance by populating specific $3d$ orbitals in transition metals.

More recent developments by J. Bourke and C. Chantler include an improvement in the code accuracy for FDM calculations [377]. The code includes thermal effects and electron/hole lifetimes and add background absorption from more loosely bound electrons but is currently limited to K-edge calculations.

F.1.2 Structure of the input file

The minimum inputs needed to start a FMS or FDM calculation are:

- the energy range to calculate around the Fermi energy
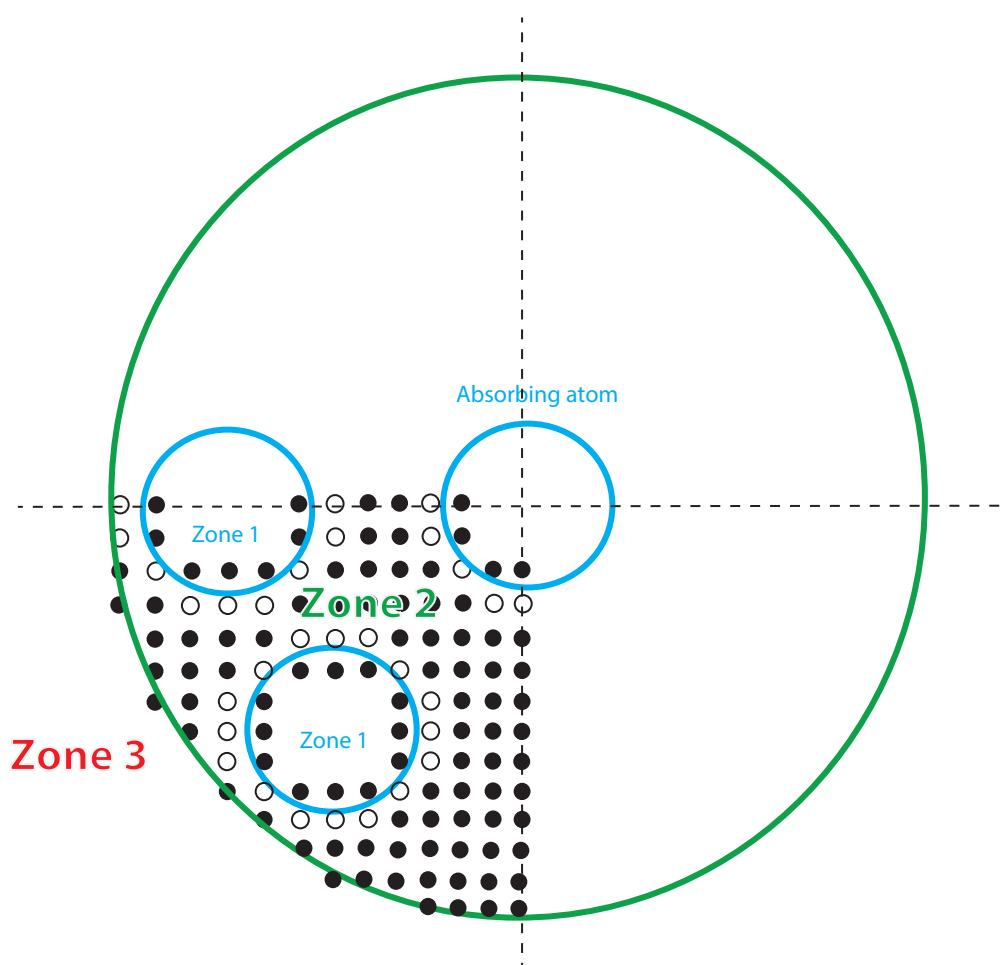
Figure F.2 – Splitting of the calculation into finite differences at different points in real space (circles). The calculation is performed differently in three spatial regions: zone 1) atomic cores, the potential is decomposed into spherical harmonics and the FDM is not used (blue region), zone 2) interstitial region, the FDM calculation is performed in this region (green region), zone 3) outer sphere, the potential is kept constant (green region). The calculation is performed in the minimum size region of the cluster sphere which can be reproduced by the symmetry operations of the crystal space group.

- the radius of the cluster (number of atoms which are explicitly considered in the calculation)

- the crystal structure: point group, unit cell dimension and angles, atomic positions in the unit cell, atomic numbers

- the atom absorbing the X-ray radiation and the ionized core orbital(choice of the X-ray edge)

In the case of a single crystal, the atomic positions are given by the crystal space group ($F_{m\bar{3}m}$ for NiO and $I_{4_1/amd}$ for TiO_2) which generates the crystal structure in the spatial limits given by the cluster radius. If not specified, the fundamental electronic structure of the atoms is used for the calculations. It may be beneficial to change the electronic configuration to an excited one in order to overcome some limitations of the package given by the core-hole implementation (*vide infra*). In the case of ionic compounds such as NiO, the electronic configuration of a given atom is in principle closer to the corresponding ion ($3d^8$). However, using such electronic configurations as starting point is not recommended and can greatly affect the convergence of the calculation. An alternative is to keep the atoms neutral with the correct number of electrons in the d shell but taking valence electrons into outer shells like $4s$ or $4p$ for a $3d$ transition metal which are spatially extended and for which the corresponding orbitals have a large overlap with the orbitals of neighboring atoms.

F.1.3   Calculation procedure

The calculation of the XAS cross-section is performed for each atom of a given type in the structure and the final spectrum is the average of the calculated spectra for each atom if no light field orientation is specified. This way, the information about the inequivalence between the sites is lost in the standard calculation but individual calculations can be performed for each site which has been done in the case of anatase TiO_2 (Chapter 8).

The novelty provided by FDMNES in addition to the implementation of the FDM is the possibility to perform self-consistent field (SCF) calculations [417]. In this case, the potential is recalculated after each iteration of the minimization of the system energy. SCF is computationally expensive but the calculation can be performed explicitly on a smaller cluster size than the one used for the description of the lattice. This calculation is performed on the unexcited cluster and provides an accurate description of the potential in the ground state. It is also possible to perform the same calculation in the "$Z+1$" approximation for the core-hole or any value of the screening which affects essentially the position of the quadrupolar transitions of the d-DOS at K-edges.

Finally, when the potential is known, the projected DOS of the final state is calculated which generates the spectrum after application of the selection rules and convolution. The experimental broadening has intrinsic (core-hole lifetime) and extrinsic origins (monochromator,

detector resolution, ...). The core-hole lifetime is usually energy dependent such that a standard description of the broadening is given by an *arctan* function:

$$\Gamma = \Gamma_{hole} + \Gamma_m \left(\frac{1}{2} + \frac{1}{\pi} \arctan \left(\frac{\pi}{3} \frac{\Gamma_m}{E_{Larg}} (e - \frac{1}{e^2}) \right) \right) \tag{F.1}$$

with $e = (E - E_F)/E_{cent}$ where Γ_m, E_{cent} and E_{Larg} are respectively the maximum broadening of the final state (on the high energy side), the centre and the broadening of the *arctan* function. The slope at the middle of the *arctan* rise is given by Γ_m/E_{Larg}. All these convolution parameters can be set independently or can even be fitted to the experimental data.

F.2 Calculations with XSpectra

In the case of NiO, the strongly correlated nature of the material required a specific description of the XAS including correlation effects. While a satisfactory agreement can be obtained with the FDM in the XANES and in the EXAFS regions, the pre-edge required the inclusion of the Hubbard U. The calculations of the XANES and pre-edge have been performed *ab initio* using the XSpectra package [452, 458] provided with Quantum-Espresso [453, 459]. The advantage of the calculation within XSpectra is the recent implementation of DFT+U methods for the XANES at the K-edge [16] which we use in this Thesis. Briefly, Troullier-Martins pseudopotentials are used [460] and the potential is computed self-consistently with the generalized gradient approximation (GGA)+U method [461]. The wavefunctions have been expanded with an energy cutoff of 140 Ry. The value of the Hubbard is $U = 7.6$ eV as suggested in Ref. [16]. For the calculation of the spin-polarized XAS cross-section with XSpectra, a supercell approach is used including core hole effects in the pseudopotential of the absorbing atom. The script requires the charge density calculated in the SCF-DFT+U calculation of the previous step and the core level wavefunction for the computation of the matrix elements. This is performed with the continued fraction [458] and the projected augmented wave (PAW) method [462]. The supercell is a 2 × 2 × 2 supercell of the magnetic cell (32 atoms). A 4 × 4 × 4 k-point grid is used for both the charge density and the continued fraction calculation. The absorbing atom is considered with a positive magnetic moment (spin up) meaning that the Ni nearest neighbors have a negative magnetic moment (spin down). A rhomboedral base is chosen for the calculation which forms a 3-fold rotation around the crystallographic c-axis. The primitive cell is a simple rhombohedron with vectors:

$$v_1 = a(t_x, -t_y, tz), \ v_2 = a(0, 2t_y, t_z), \ v_3 = a(-t_x, -t_y, t_z) \tag{F.2}$$

with a the cubic unit cell parameter and

$$t_x = \sqrt{\frac{1-c}{2}}, \ t_y = \sqrt{\frac{1-c}{6}}, \ t_z = \sqrt{\frac{1+2c}{3}} \tag{F.3}$$

The additional unit cell dimension to provide in this Bravais lattice is the $\cos \gamma$ between any pair of the unitary lattice vectors v_1, v_2 or v_3.

F.3 Simulation of the effect of lattice expansion on the XAS of NiO at the Ni K-edge

F.3.1 EXAFS

The ground state and excited state EXAFS are obtained by FMS calculations as implemented in the FDMNES package [368, 369]. Clusters of 7 Å radii are used with different Ni-O bond distances modelled by expanding the ground state lattice parameter. This cluster size is required to achieve convergence of the calculated ground state spectrum. The MT approximation is used and quadrupole and dipole matrix elements are included. The space group of NiO is $F_{m\bar{3}m}$ used in the calculation. The calculated spectrum is averaged over all possible polarizations. A gaussian convolution of 0.8 eV is included in the calculation to account for the experimental energy resolution. The ground state electronic configurations of nickel and oxygen were used to compute the atomic potentials. The calculation was not performed self-consistently. The Hedin-Lunqvist exchange correlation potential has been used.

F.3.2 XANES

Details for the calculations in the XANES with XSpectra are in section F.2. Figure F.3 shows the effect of lattice contraction onto the simulated TRXAS.
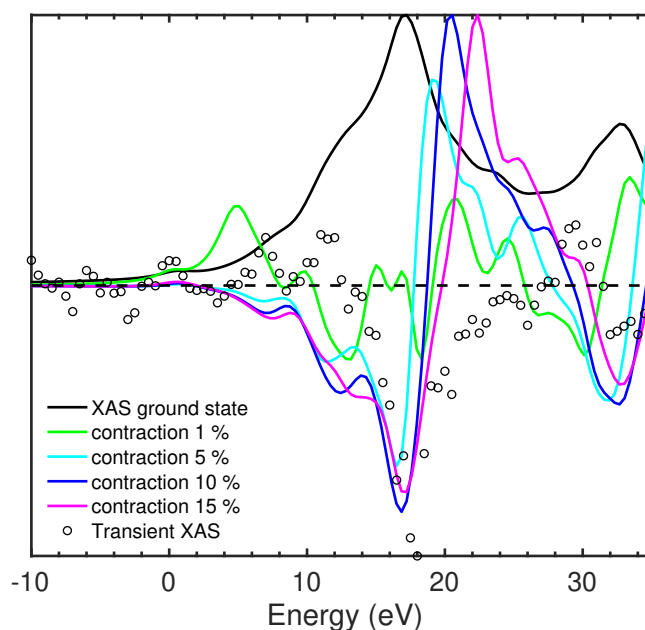
Figure F.3 – Simulated TRXAS spectra based on lattice contraction (colored curves), experimental transient 100 ps after excitation at 355 nm (black circles) and calculated ground state XAS (black line) at the Ni K-edge.

G Apparatus

G.1 UV-Vis spectra

The steady-state absorption spectra were recorded at room temperature using a commercial UV-VIS-NIR spectrometer (Shimadzu, UV-3600). For the measurements in solution, before measuring the absorption spectrum of the sample, a reference spectrum of the pure solvent was recorded to check its transparency in the investigated spectral range and to eventually correct the baseline from its absorption.

G.2 Fluorimetry

Emission and excitation spectra were measured with a Shimadzu RF-5301PC spectrofluorimeter.

G.3 Ellipsometry

The spectroscopic ellipsometry measurements were performed with a SE-2000 setup from Semilab equipped with a CCD array. For each measurement, 9 points were sampled in a square shape at the sample surface and compared to estimate the site-to-site fluctuations of the sample optical properties. The conversion between the ellipse Ψ and Δ parameters were performed with a homemade Matlab program.

G.4 TRXAS

TRXAS experiments performed in this Thesis have been performed at the SuperXAS and MicroXAS beamlines of the Swiss Light Source (SLS) at the Paul Scherrer Institute (PSI) in Switzerland. The properties of the SLS are described in section G.4.1. Details about the laser system and the detectors are given in section G.4.2. Finally, details about the liquid jet are

given in section G.4.2.

G.4.1 Properties of SLS and the MicroXAS beamline

Third generation synchrotrons such as the SLS gather high photon energies, high photon intensities, polarized and pulsed X-ray radiations which are key requirements for the experiments. The MicroXAS beamline is an undulator beamline which can provide hard X-rays in the range 3 to 23 keV with an average flux of 2×10^{12} photons/s for the 400 mA of the synchrotron current. The X-ray focus onto the sample can be tuned to $5 \times 5\ \mu m^2$ with a Kirkpatrick-Baez (KB) mirror system [463]. A top-up filling scheme allows low fluctuations of the synchrotron average current by regularly injecting electrons into the storage ring.

The SLS has an electron filling pattern made of 480 possible buckets filled or empty of electrons and spaced by 2 ns. In the hybrid filling configuration presented in Figure G.1, 390 buckets are filled with electrons (multibunch) and of the 90 remaining empty buckets, the camshaft corresponds to the 465th bucket and is filled with four times more current than the average multibunch current. The repetition rate of the synchrotron is 1.04 MHz which sets an upper limit for the data acquisition system (DAQ) rate for the experiments. The camshaft pulse duration is 70 ps which sets an upper limit for the time resolution of the experiment. Femtosecond time resolutions are nowadays provided by X-ray free-electron lasers (FELs).
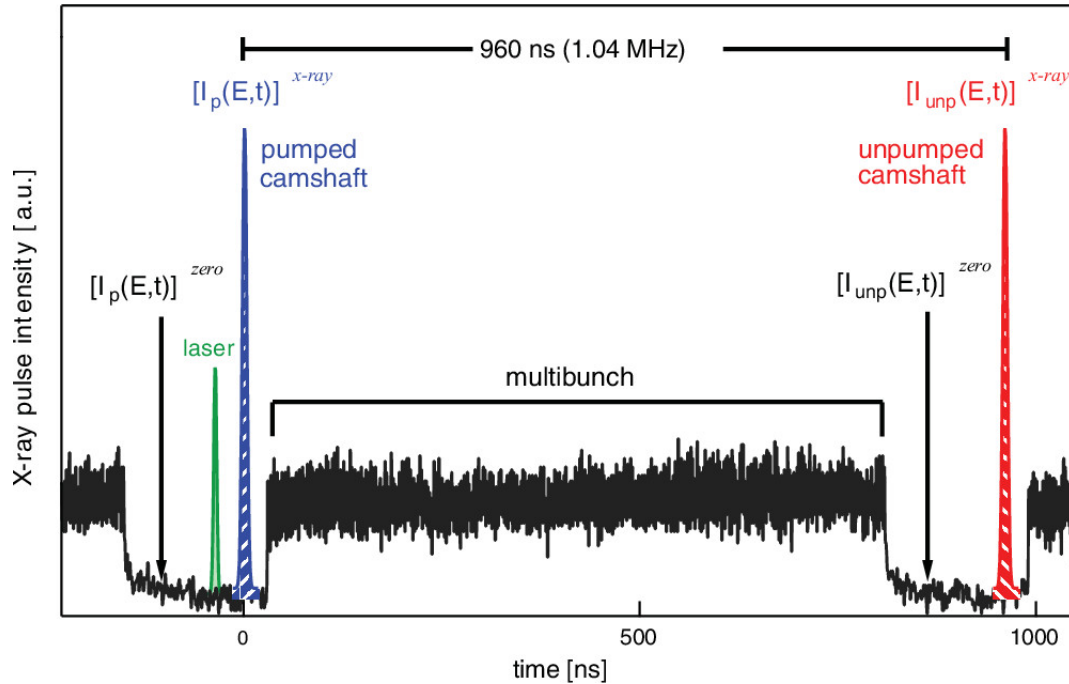
Figure G.1 – Hybrid filling pattern of the SLS decomposed into a multibunch of filled buckets spaced by 2 ns and one isolated camshaft pulse with 4 times more current than average. Reproduced from Ref. [17] with permission.

G.4.2 High-repetition rate TRXAS setup

The high repetition rate setup has been described in detail in Reference [17]. For the time-resolved experiments, only the camshaft from the ring is used which corresponds to ~1% of the average synchrotron flux. The pump pulse is provided by a high repetition rate Duetto Nd:YAG laser (Time Bandwidth). The tricky part of the setup is that the optical pump and the X-ray probe are delivered by two independent sources which need to be synchronized through the DAQ as already performed earlier at other synchrotron facilities [464, 465, 466, 467, 468]. The detail of the electronics is given in Figure G.2. Briefly, the master clock of the system is provided by an optical 1.04 MHz signal provided by the synchrotron which can be down converted to any repetition rate in the DAQ. This master triggering signal is split to the laser system (pulse picker at typically half the repetition rate of the experiment), to the detection scheme (for the track-and-hold (T&H)) and to the analog-to-digital converter (ADC) card. The fine time delay between the laser pulse and the X-ray pulse is introduced by the laser controller itself connected to a phase shifter receiving a 500 MHz radiofrequency (RF) signal from the synchrotron magnets which can change the delivery time over 2 ns.
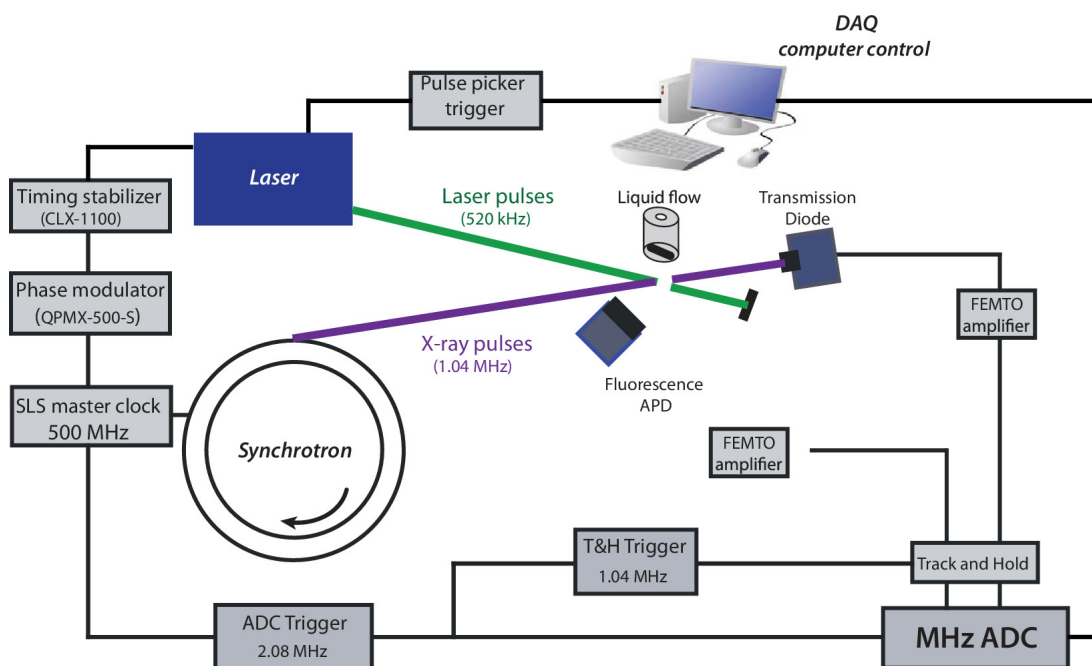
Figure G.2 – Diagram of the high-repetition rate TRXAS pump-probe setup. Reproduced from Ref. [17] with permission.

Two key steps of the experiments are the spatial and temporal overlap between the laser and the X-rays. The former is performed with a 50 μm pinhole and the latter with a 500 ps rise time diode.

Laser System: Duetto

The laser system used for the TRXAS experiments is a compact and mobile picosecond Duetto laser system produced by Time Bandwidth Products. The portability enables the installation of the laser at different beamlines of the SLS which offer different energy ranges and experimental conditions. The Duetto laser provides 10 ps pulses and a variable repetition-rate in the range between 200 kHz to 8.33 MHz in standard mode[1]. The laser consists of three main components: the oscillator and amplifier, a pulse-on-demand (PoD) unit and a non-linear optics (NLO) unit. The synchronization between the laser pulse delivery (pulse picker) and the X-ray pulse is performed with the electronic synchronization unit (CLX) reading both the pulse picker at the repetition rate of the experiment (pulse picker) and the fine time delay (phase shifter).

The Duetto laser system is a solid state neodynium-doped yttrium orthovanadate based amplified system which operates at a fundamental wavelength of 1064 nm. The oscillator and amplifier run at a repetition rate of 83.3 MHz. A Pockels cell releases the pulses from the cavity at any fraction of the internal frequency between 10 and 416, corresponding to outgoing pulse repetition rates of 8.33 MHz or 200 kHz respectively with an average output power greater than 12 W for the fundamental.

The CLX-1100 timing box stabilizes the relative phase between the RF and the intrinsic frequency by locking the phase of the laser oscillator to an input trigger with a jitter of < 400 fs.

The PoD unit is located between the amplifier and the NLO unit. It allows using the direct amplifier laser power or an internal Pockels cell as beam attenuator by applying an analog constant voltage signal with upper and lower limits given by transistor-transistor logic (TTL).

The NLO unit accepts the 1064 nm beam from the PoD. The output wavelength can be tuned by switching to a second harmonic generation (SHG) crystal resulting in 532 nm output wavelength or a combination of SHG and sum frequency generation (SFG) to perform 1064 and 532 nm mixing giving 355 nm laser output. We have recently implemented the 266 nm output by doubling 532 nm in a β-barium borate (BBO) crystal positioned in a oven at ~100°C to obtain average output power stability over ~3 hours at the high repetition rate of the laser [469]. The maximum output pulse energy depends on the laser repetition rate.

Laser optics

The optical setup is used to deliver the laser beam to the interaction zone of the liquid jet sample with the X-ray probe beam. Two steering mirrors after the laser provide full control over the beam position while the subsequent Schmidt-Cassegrain telescope (one divergent and one convergent lenses) magnifies the beam waist to get a better focus at the sample position. The beam is then steered over several mirrors and one periscope to level it at the sample

---

[1]The repetition rate can be lowered adapting the optics for large peak powers to prevent damaging.

height. A convex lens focusses the laser beam to a size of ~1.5 times the FWHM of the X-ray spot to ensure spatial overlap stability over the probe region. One of the last steering mirror is set on a motorized stage with Euler angles (Zaber T-MM-Series), which remotely adjusts the laser spot position on the sample while hard X-rays are present inside the experimental hutch.

Detectors and T&H

TRXAS requires rather fast detectors which can operate at high repetition rates with a large linear response over the incident X-ray flux and photon energy to adapt to the different edges investigated at MicroXAS. The TRXAS in transmission is measured with a silicon drift detector (SDD) photodiode (bias 150 volt) while the fluorescence is measured with two 1 cm^2 avalanche photodiodes (APDs) (bias -350 V to increase the sensitivity and the time resolution). Both diodes are shielded from the laser photons with 25 μm Be windows. The amplification of the detected current is a key step to achieve measurable signals. This is performed with a variable gain DHCPA-100 FEMTO current amplifier for the SDD transmission and a fixed gain HCA series FEMTO current amplifier for the APD in fluorescence.

The amplified signals are fed into T&H which hold the incoming current signal level long enough for the slower digitalization by the ADC to be performed.

Sample delivery

In this Thesis, TRXAS measurements are done exclusively on liquid samples flowing through a sheet jet (Figure G.3). The liquid jet nozzle consists of two sapphire pieces separated by spacers of 200 μm distance. The colloidal solution of nanoparticles (NPs) is flown through the jet nozzle by a peristaltic pump, creating a sheet of liquid. The sheet has the shape of an upside down triangle, with a laminar section close to the nozzle in the middle region of the jet (green triangle in Figure G.3). Although the peristaltic pump introduces a slow pulsation of the jet thickness at a frequency of a few Hz, it does not introduce a significant noise in the measurement because the fluctuations are way slower than the sampling time and are only observed as an average. The jet liquid is collected in a catcher and transferred back to the sample bottle. This way, a sample volume of ~50 mL can be flown for several hours provided that no damaging occurs.

Data Acquisition System

The laser pump/X-ray prove data is collected on a shot-to-shot basis, thus probing an excited state sample and a ground state sample in 4 μs with the laser running at a repetition rate of 260 kHz for the experiment on NiO microparticles (chapter 7). To correct for a possible detector offset, a baseline of the detector is taken for each shot. Over two synchrotron periods, this corresponds to four different signals being sampled (Figure G.1): two baseline offset signals $I_p(E, t)^{zero}$ and $I_{unp}(E, t)^{zero}$ with and without pump laser pulse respectively; and
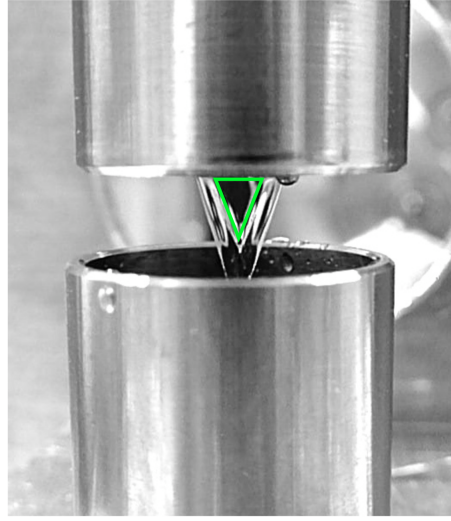
Figure G.3 – Picture of the liquid jet. The nozzle (top cylinder) contains two half cylindric sapphire pieces separated by ~200 µm spacer through which the liquid sample is pumped. The liquid is then collected by the catcher (bottom cylinder) and directed back to the sample container. The green lines indicate the laminar area on the jet stream, which is the most stable area and on which laser and X-ray beam are overlapped.

two signals from the camshaft $I_p(E,t)^{X-ray}$ and $I_{unp}(E,t)^{X-ray}$ with and without pump laser respectively. The transient signal at the X-ray energy E and time delay t after excitation is computed in transmission from,

$$\Delta A^T(E,t) = -\ln\left(\frac{I_p(E,t)^{X-ray} - I_p(E,t)^{zero}}{I_{unp}(E,t)^{X-ray} - I_{unp}(E,t)^{zero}}\right) \tag{G.1}$$

while the transient fluorescence signal in total fluorescence yield (TFY) is computed from,

$$\Delta A^F(E,t) = I_p(E,t)^{X-ray} - I_p(E,t)^{zero} - (I_{unp}(E,t)^{X-ray} - I_{unp}(E,t)^{zero}) \tag{G.2}$$

Note that none of the transient signals requires the *a priori* knowledge of the incident X-ray intensity $I_0(E)$ although it is highly recommended to use an APD to measure the incoming X-ray flux on a shot-to-shot basis[2]. Usually, the laser excitation does not result in 100% sample excitation. Hence the TRXAS signal contains a linear combination of the excited and unexcited species. To extract the component of the excited species, the knowledge about the excitation yield $f(t)$ is required which is related to the X-ray absorption coefficient $\mu(E)$ and $\mu^*(E)$[3] in the ground and excited state respectively according to,

$$\Delta A(E,t) = f(t)\cdot(\mu^*(E) - \mu(E)). \tag{G.3}$$

---

[2]This is easily done putting a thin Kapton foil into the beam and measuring the scattered photons with an APD.
[3]We make the assumption that a single excited state specie is formed upon excitation. Otherwise, different absorption coefficients need to be considered as well as the excitation yield of the different species.

It is often difficult to predict the excitation yield from the *a priori* knowledge of the absorption coefficient or molar extinction coefficient so that only an upper limit can be provided from the measurement of the average power delivered to the sample from the incident and transmitted average laser powers[4]. Information about the excited state absorption coefficient is useful especially in the EXAFS where atomic displacements upon laser excitation can be modelled directly from $\mu^*(E)$.

G.5   Transient absorption in the Visible: 1 kHz **system**

The 1 kHz laser system has been used for the transient absorption spectroscopy (TAS) experiments on MAPbBr$_3$, MAPbBr$_3$/a-TiO$_2$ and a-TiO$_2$ thin films in Chapters 2 and 4. We provide here the description of the setup.

A continous wave Nd:YVO$_4$ laser (Millennia Vs, Spectra Physics) is used to pump the Ti:Sapphire oscillator (Tsunami, Spectra Physics) with 3.9 W typical pump power. The mode-locked oscillator produces 800 nm pulses with a FWHM of ~20 nm, which are used as seed for the regenerative amplifier (Spitfire, Spectra Physics). The Ti:Sapphire crystal of the amplifier is pumped by a Nd:YLF pulsed laser (Quantronix) which delivers 200 ns pulses at 1 kHz with 8.5 W typical average power. The system delivers 800 nm pulses with a typical bandwidth of $15-20$ nm, duration of < 100 fs and pulse energy of 0.65 mJ at 1 kHz. Shot-to-shot noise, measured as the root mean square (RMS) on 1000 shots, is typically 2‰. After a telescope, which reduces the beam size by a factor 3, the beam is split in two parts, which are used to generate the pump and probe pulses.

The pump is generated by SHG of the fundamental through a 0.5 mm BBO (29.2°, type I). The pulse is focused at the sample position with a $f = 250$ mm parabola.

The broadband Visible probe is obtained by focusing a small fraction (~1 mW) of the 800 nm pulse in a continuously moving CaF$_2$ window. The transmitted broadband probe is coupled into an optical fiber and then into a homemade grating spectrometer. Finally, a charge-coupled device (CCD) array is positioned in the Fourier plane of the spectrograph to measure the spectrally-resolved intensity of the transmitted probe beam.

The single-shot detection scheme was previously described [470]. Briefly, the photodiode array is read out by a fast ADC for each probe pulse. The signal is computed from the different pump and unpumped measurements and averaged over a given number of shots in the computer.

---

[4]The exact calculation assumes that there are no other sources of optical power losses than the sample absorption which is often not the case for colloidal solutions of NP where the scattering is important.

G.6   Transient absorption in the deep-UV: 20 kHz **system**

The ultrafast broadband UV experiments have been performed with a setup providing tunable narrowband UV pump and broadband UV probe pulses in the range from 3.35 to 4.8 eV [110, 111].

First, a 20 kHz Ti:Sapphire laser regenerative amplifier (KMLabs, Halcyon+Wyvern500), provides 50 fs FWHM pulses at 1.55 eV with typically 0.7 mJ per pulse (12 W average power). Around 7 W are used to pump a non-collinear optical parametric amplifier (NOPA) (TOPAS white - Light Conversion) which provides sub-100 fs pulses with a very broad spectral coverage typically from 1.65 to 2.5 eV and 7 µJ in this broadband configuration. The narrowband configuration can provide pump powers of the order of 15 µJ. Around 60% of the NOPA output power is used to generate the narrowband pump pulses. In this line, the visible pulse goes through a chopper operating at 10 kHz, synchronized to the laser system and phase-locked manually via the detection of the transmitted intensity with a photodiode. The pump pulse can be used as such through an interference filter to select the excitation pump photon energy or can be frequency doubled through a BBO crystal to generate a UV pump pulse. Typical BBO thickness is less than 1 mm to keep the time duration of the pulse and because no further gain in doubling efficiency is usually observed for thick crystals after the double component and the seed have lost temporal overlap. The pump photon energy is controlled by phase-matching with a rotating stage set below the BBO. The typical bandwidth of the UV pump pulse is 20 meV and the excitation intensity follows the intensity profile of the NOPA output spectrum with pulse energy of the order of 100 nJ. The pump power is recorded on a shot-to-shot basis by a calibrated photodiode for each pump photon energy which allows the normalization of the data based on the average pump power. Alternatively, the harmonics of the Ti:Sapphire output can be generated with the remaining of the laser power through doubling (3.1 eV photons) and tripling lines (4.66 eV). This has the advantage to deliver large energy per pulse (several µJ) while keeping the temporal duration of the pump pulse around 50 fs. A half waveplate is often used to set the relative polarization between the pump and the probe at the magic angle (54.74°) to get rid off photoselection effects.

The remaining NOPA output is used to generate the broadband UV probe pulse with 1.7 eV bandwidth through an achromatic doubling scheme which has been developed in the group of Riedle [471, 472]. It comprises two fused silica prisms that spatially disperse and recollimate the Visible beam coming from the NOPA. The resulting spatially chirped beam is focused with a 90° off-axis parabolic mirror on a 200 µm thick BBO crystal. The frequency doubling of such broadband Visible pulse is made more complex since there is one phase-matching angle per frequency component. Hence the spatial chirp of the Visible beam and the different incident angles achieved by the parabola onto the BBO can match the phase-matching at all probe photon energies at the same time. The frequency-doubled beam is subsequently recollimated with another 90° off-axis parabola, recombined and recompressed with two additional CaF_2 prisms.

The pump and the probe pulses are focused onto the sample where they are spatially and temporally overlapped. The beam waists are typically around 80 μm for the pump and 20 μm for the probe which results in a homogeneous probing of an excited sample volume. The setup has been used alternatively in transmission or in reflection mode over the course of this Thesis.

After the sample, the reflected/transmitted broadband probe beam is focused in a multi-mode optical fiber (100 μm) which is coupled to the entrance slit of a 0.25 m imaging spectrograph (Chromex 250is). The beam is dispersed by a 150 grooves/mm holographic grating and imaged onto a multichannel detector consisting of a 512 pixel CMOS linear sensor (Hamamatsu S11105, 12.5 × 250 μm pixel size) with up to 50 MHz readout, so the maximum read-out rate per spectrum (almost 100 kHz) allows us to perform shot-to-shot detection easily. The described experimental setup typically offers a time resolution of 150 fs, but can be improved to 80 fs with the adoption of a chirp mirror or prism compressor in the pump line.

H Ellipsometry

H.1 Ellipsometry of anatase TiO$_2$ (001) thin films

The absorption coefficient of the thin films was obtained by spectroscopic ellipsometry. The main goal is to check the crystallinity of the sample from the position of the optical gap, the fluctuations of the optical properties at different positions of the sample surface and to estimate the thickness of the film from the spectral interferences below the gap. The absorption coefficient retrieved at 9 different positions of the sample surface 1 mm away from each other in a square lattice is depicted in Figure H.1a. The measurement is performed at 65°n incidence angle below the Brewster angle of 69.1° [473]. The ellipsometer beam focus at the sample surface is ~ 250 μm meaning that we are measuring fully independent spots.
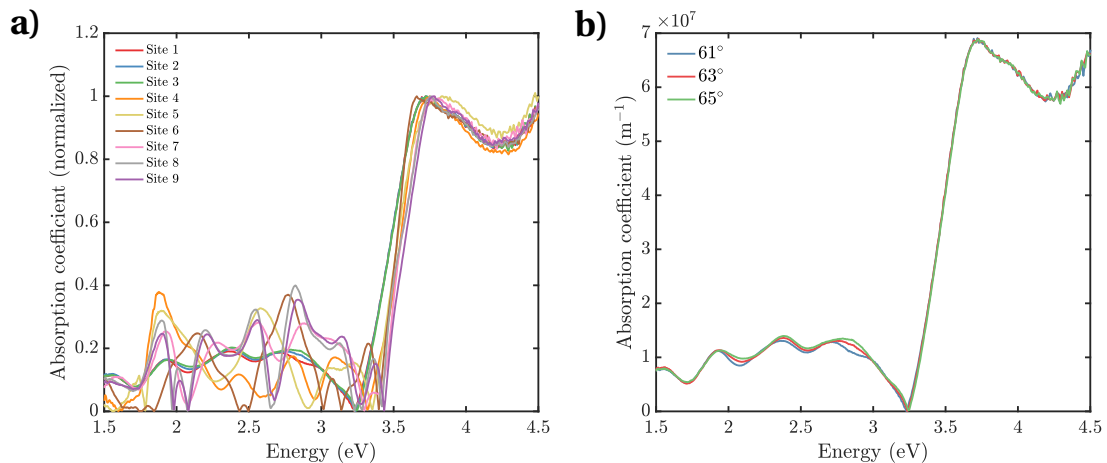
Figure H.1 – a) Absorption coefficient of anatase TiO$_2$ (001) crystalline thin film retrieved by spectroscopic ellipsometry at different positions on the film surface. b) Influence of the incidence angle on the absorption coefficient retrieved by spectroscopic ellipsometry.

The fluctuations of the absorption coefficient below the optical gap are due to sample thickness fluctuations which affect the spectral interferences [474]. The influence of the incident angle onto the sample surface was also varied to double check that the measurement was performed

171

below the Brewster angle and that no artefact was included because of polarization distortions of the reflected light. The absorption coefficient for three different incident angles is depicted in Figure H.1b and shows only minor differences below the optical gap where the change in beam size and sensitivity to the effective sample thickness can have an effect.

From the light focus at the sample surface and the reflected intensity, the ellipsometer can map the fluctuations of the altitude of the sample surface which is depicted in Figure H.2. The fluctuations seem quite large *a priori* considering the full map of the order of 60 nm. However, the map clearly shows a gradient of altitude from north to south which enhances the effect.
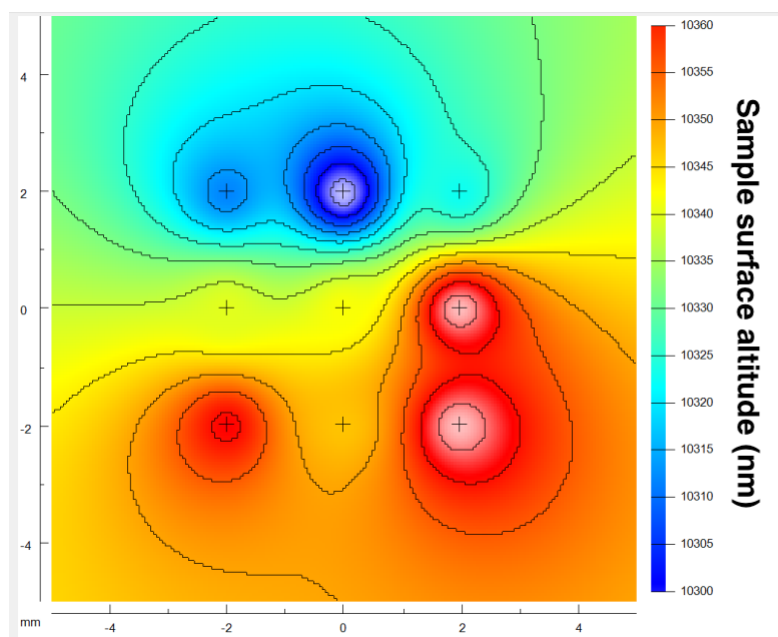
Figure H.2 – Mapping of the altitude at the anatase TiO_2 thin film surface. The altitude is a relative coordinate given by the ellipsometer in nanometer.

H.2 Ellipsometry of NiO (001)

The dielectric constants of NiO (001) were fitted with the Reffit software developed by Alexey Kuzmenko at the University of Geneva[1]. The software uses a model-independent Kramers-Kronig analysis to virtually any type of optical spectrum using an original Kramers-Kronig constrained variational technique [475]. A fast Marquard-Levenberg algorithm is used which is implement for the self-consistent fitting of multiple experiments [476].

For the fitting, a sum of two Tauc-Lorentz oscillators [477] and a Lorentzian lineshape (equations H.1 and H.2) have been used. The fitting is performed simultaneously and self-consistently

---

[1]https://sites.google.com/site/reffitprogram/home

on the experimental real part (ϵ_1) and imaginary part (ϵ_2) of the dielectric constant.

$$\epsilon_1(\omega) \sim \underbrace{1 + \sum_i \frac{\omega_{p,i}^2(\omega_{0,i}^2 - \omega^2)}{(\omega_{0,i}^2 - \omega^2)^2 + (\omega\Gamma_i)^2}}_{\text{Lorentz}} +$$

$$\sum_i \frac{A\Gamma_i a_{ln}}{2\pi\xi^4\alpha\omega_{0,i}} \ln\left(\frac{\omega_{0,i}^2 + \omega_{g,i}^2 + \alpha\omega_{g,i}}{\omega_{0,i}^2 + \omega_{g,i}^2 - \alpha\omega_{g,i}}\right) - \frac{Aa_{atan}}{\pi\xi^4\omega_{0,i}}\left(\pi - \arctan\left(\frac{2\omega_{g,i} + \alpha}{\Gamma_i}\right) + \arctan\left(\frac{\alpha - 2\omega_{g,i}}{\Gamma_i}\right)\right) +$$

$$\frac{4A\omega_{0,i}\omega_{g,i}(\omega^2 - \gamma^2)}{\pi\xi^4\alpha}\left(\arctan\left(\frac{\alpha + 2\omega_{g,i}}{\Gamma_i}\right) + \arctan\left(\frac{\alpha - 2\omega_{g,i}}{\Gamma_i}\right)\right)$$

$$-\frac{A\omega_{0,i}\Gamma_i(\omega^2 + \omega_{g,i}^2)}{\pi\xi^4\omega}\ln\left(\frac{|\omega - \omega_{g,i}|}{\omega + \omega_{g,i}}\right) +$$

$$\frac{2A\omega_{0,i}\Gamma_i\omega_{g,i}}{\pi\xi^4}\ln\left(\frac{|\omega - \omega_{g,i}|(\omega + \omega_{g,i})}{\sqrt{(\omega_{0,i}^2 - \omega_{g,i}^2) + \omega_{g,i}^2\Gamma_i^2}}\right) + \epsilon_{1,\infty}$$

(H.1)

and

$$\epsilon_2(\omega) = \underbrace{\sum_i \frac{\omega_{p,i}^2\omega\Gamma_i}{(\omega_{0,i}^2 - \omega^2)^2 + (\omega\Gamma_i)^2}}_{\text{Lorentz}} + \underbrace{\sum_i \frac{1}{\omega}\frac{A\omega_{0,i}\Gamma_i(\omega - \omega_{g,i})^2}{(\omega^2 - \omega_{0,i}^2) + \Gamma^2\omega^2}}_{\text{Tauc-Lorentz}} + \epsilon_{2,\infty} \text{ for } \omega > \omega_{g,i},$$

$$\epsilon_2(\omega) = \underbrace{\sum_i \frac{\omega_{p,i}^2\omega\Gamma_i}{(\omega_{0,i}^2 - \omega^2)^2 + (\omega\Gamma_i)^2}}_{\text{Lorentz}} \text{ for } \omega \leq \omega_{g,i}$$

(H.2)

with $a_{ln} = (\omega_g^2 - \omega_0^2)\omega^2 + \omega_g^2\Gamma - \omega_0^2(\omega_0^2 + 3\omega_g^2)$, $a_{atan} = (\omega^2 - \omega_0^2)(\omega_0^2 + \omega_g^2) + \omega_g^2\Gamma^2$, $\xi^4 = (\omega^2 - \gamma^2)^2 + \alpha^2\Gamma^2/4$, $\alpha = \sqrt{4\omega_0^2 - \Gamma^2}$ and $\gamma = \sqrt{\omega_0^2 - \Gamma/2}$.

I Crystal-symmetrization of the spherical tensors in the XAS cross-section of anatase TiO$_2$

First, the spherical tensors are symmetrized in the atomic frame and then in the crystal frame taking into account the possible inequivalent sites in the unit cell.

I.1 Derivation of the site-symmetrized spherical tensors of anatase in the site frame

The local point group of anatase is D$_{2d}$ (subgroup of the crystal point group D$_{4h}$) which contains 4 pure rotations and 2 rotoinversions. The angular evolution of the dipole and quadrupole cross-sections in this point group are the same as in the crystal point group D$_{4h}$ (equations 8.1 and 8.2). The site frame has the $\hat{z}$ axis chosen along the elongated axis of the TiO$_6$ octahedron and the $\hat{x}$ and $\hat{y}$ axes are chosen along the equatorial Ti$-$O bonds to form a direct frame. The site-symmetrized spherical tensor $\langle \sigma(l, m) \rangle$ in the site frame is given by:

$$\langle \sigma(l, m) \rangle = \frac{1}{|G'|} \sum_g \epsilon(g) \sum_{m'=-l}^{m'=l} \sigma(l, m') D^l_{m'm}(g) \tag{I.1}$$

with $|G'| = 6$ the number of rotoinversions and pure rotations in the site point group, g a rotoinversion in the site point group, and $D^l_{m'm}$ the Wigner-D matrix. The parity factor is $\epsilon(g) = -1$ when the spherical tensor is odd (dipole cross-section) and the symmetry operation g contains the inversion or $\epsilon(g) = 1$ otherwise. The Wigner-D matrix is expressed as:

$$D^l_{m'm}(g) = e^{-im'\alpha} d^l_{m'm}(\beta) e^{-im\gamma} \tag{I.2}$$

with Euler angles (α, β, γ) in ZYZ convention for the rotoinversion g of the site point group and d$^l_{m'm}$ is the reduced Wigner-D matrix with characteristic values $d^l_{m'm}(0) = \delta_{m,m'}$ and $d^l_{m'm} = (-1)^{l-m}\delta_{m',-m}$. This provides the following symmetrized dipolar spherical tensors in

the site frame:

$$\langle \sigma^D(0,0) \rangle = \frac{1}{6} \sum_g \epsilon(g) \sigma^D(0,0) D_{00}^0(g) = \frac{1}{3} \sigma^D(0,0)$$

$$\langle \sigma^D(2,0) \rangle = \frac{1}{6} \sum_g \sum_{m'=-2}^{m'=2} \epsilon(g) \sigma^Q(2,m') D_{m'0}^2(g) = \frac{1}{3} \sigma^D(2,0)$$

(I.3)

and the following quadrupolar spherical tensors,

$$\langle \sigma^Q(0,0) \rangle = \frac{1}{4} \sum_g \sigma^Q(0,0) D_{00}^0(g) = \sigma^Q(0,0)$$

$$\langle \sigma^Q(2,0) \rangle = \frac{1}{4} \sum_g \sum_{m'=-2}^{m'=2} \sigma^Q(2,m') D_{m'0}^2(g) = \sigma^Q(2,0)$$

$$\langle \sigma^Q(4,0) \rangle = \frac{1}{4} \sum_g \sum_{m'=-4}^{m'=4} \sigma^Q(4,m') D_{m'0}^4(g) = \sigma^Q(4,0)$$

$$\langle \sigma^Q(4,4) \rangle = \frac{1}{4} \sum_g \sum_{m'=-4}^{m'=4} \sigma^Q(4,m') D_{m'4}^4(g) = \sigma^Q(4,4)$$

(I.4)

I.2 From site-symmetrized spherical tensors to crystal-symmetrized spherical tensors

The coset method is a powerful way to calculate the spherical tensors averaged over the crystal from the spherical tensor symmetrized over a single site which has been developed by Brouder and coworkers [424]. The crystal-symmetrized tensor $\langle \sigma(l,m) \rangle_X$ of a given site is obtained from the site-symmetrized tensor $\langle \sigma(l,m) \rangle_S$ by the operation

$$\langle \sigma(l,m) \rangle_X = \frac{1}{n} \sum_{i=1}^{n} \sum_{m'=-l}^{m'=l} \epsilon(g_i) \langle \sigma(l,m) \rangle_S D_{m'm}^l(g_i^{-1})$$

(I.5)

with n the number of cosets. Briefly, since the atom at $(0,0,0)$ is equivalent to the site at $(1/2,1/2,1/2)$ by a pure lattice translation with the vector $(1/2,1/2,1/2)$, this gives a single coset (x,y,z). Consequently, the anatase unit cell contains two equivalent titanium atoms, the XAS cross-section of both atoms is the same and they cannot be distinguished. Thus, formula I.5 reduces to,

$$\langle \sigma(l,m) \rangle_X = \sum_{m'=-l}^{m'=l} \langle \sigma(l,m) \rangle_S D_{m'm}^l(0)$$

(I.6)

for anatase TiO$_2$ which cancels the terms $\langle \sigma^{Dr}(2,2) \rangle_X$, $\langle \sigma^{Qr}(2,2) \rangle_X$ and $\langle \sigma^{Qr}(4,2) \rangle_X$ while all the other non-zero spherical tensors are the same symmetrized in the site frame as in the crystal frame. We checked the equivalence between the sites with FDMNES calculations and both dipole and quadrupole components measured under any θ or ϕ angle have the

same cross-sections for both sites. We conclude that all the quadrupolar spherical tensors symmetrized in the crystal frame have the same value than the corresponding spherical tensors $\langle \sigma^Q(l,m) \rangle_X = \sigma^Q(l,m)$ while for the dipolar spherical tensors we have $\langle \sigma(l,m) \rangle_X = \frac{1}{3} \sigma^D(l,m)$. The symmetrized spherical tensors have to be used in equations 8.1 and 8.2 to obtain the angular evolution of the dipole and quadrupole cross-section.

I.3   Spherical tensors of anatase

final state	$\sigma^D(0,0)$	$\sigma^D(2,0)$
p_z	$8\pi^2/9$	$4\sqrt{2}\pi^2/9$
p_x	$8\pi^2/9$	$-4\sqrt{2}\pi^2/9$
p_y	$8\pi^2/9$	$-4\sqrt{2}\pi^2/9$

Table I.1 – Table of dipolar spherical tensors based on the final state reached by the transition from the Ni $1s$. Each element of the table must be multiplied by $\alpha\hbar\omega\delta(E_f - E_i - \hbar\omega)\xi_f^2$ where f is the final state reached by the transition which represents the integration of the radial parts of the wavefunctions.

final state	$\sigma^Q(0,0)$	$\sigma^Q(2,0)$	$\sigma^{Qr}(2,2)$	$\sigma^Q(4,0)$	$\sigma^{Qr}(4,4)$
d_{z^2}	$3/400$	$-3\sqrt{2/35}/80$	0	$9\sqrt{2/7}/400$	0
$d_{x^2-y^2}$	$3/400$	$3\sqrt{2/35}/80$	0	$3\sqrt{2/7}/800$	$3/(160\sqrt{5})$
d_{xy}	$3/400$	$3\sqrt{2/35}/80$	0	$3\sqrt{2/7}/800$	$-3/(160\sqrt{5})$
d_{xz}	$3/400$	$3\sqrt{2/35}/160$	$3\sqrt{3/35}/160$	$3\sqrt{2/7}/200$	0
d_{yz}	$3/400$	$3\sqrt{2/35}/160$	$-3\sqrt{3/35}/160$	$3\sqrt{2/7}/200$	0

Table I.2 – Table of quadrupolar spherical tensors based on the final state reached by the transition from the Ni $1s$. Each element of the table must be multiplied by $\alpha\hbar\omega k^2\delta(E_f - E_i - \hbar\omega)\xi_f^2$ where f is the final state reached by the transition which represents the integration of the radial parts of the wavefunctions.

I.3.1   Final expression of the dipole cross-section

$$\sigma^D(\hat{\epsilon}) = \sigma^D(0,0) - \frac{1}{\sqrt{2}}(3\cos^2\theta - 1)\sigma^D(2,0) \tag{I.7}$$

Final state is $\mathbf{p}_z$

$$\sigma^D(\hat{\epsilon}) = \alpha\hbar\omega\left(\frac{8\pi^2}{9} - 4\sqrt{2}\frac{\pi^2}{9}\frac{1}{\sqrt{2}}(3\cos^2\theta - 1)\right)\xi_{z^2}^2\delta(E_f - E_i - \hbar\omega) \tag{I.8}$$

177

then

$$\sigma^D(\hat{\epsilon}) = \alpha\hbar\omega\frac{4\pi^2}{3}(1 - \cos^2\theta)\xi_z^2\delta(E_f - E_i - \hbar\omega)$$
(I.9)

Final state is p$_x$ or p$_y$

$$\sigma^D(\hat{\epsilon}) = \alpha\hbar\omega\left(\frac{8\pi^2}{9} + 4\sqrt{2}\frac{\pi^2}{9}\frac{1}{\sqrt{2}}(3\cos^2\theta - 1)\right)\xi_{x,y}^2\delta(E_f - E_i - \hbar\omega)$$
(I.10)

then

$$\sigma^D(\hat{\epsilon}) = \alpha\hbar\omega\frac{4\pi^2}{9}(1 + 3\cos^2\theta)\xi_{x,y}^2\delta(E_f - E_i - \hbar\omega)$$
(I.11)

One can check that the sum of both dipolar components with p_z and $p_{x,y}$ final states, in the assumption that the overlap of the radial parts is such that $\xi_x^2 = \xi_y^2 = \xi_z^2$, gives $\sigma^D(\hat{\epsilon}) = \sigma^D(0,0) = \alpha\hbar\omega\frac{8\pi^2}{9}(\xi_x^2 + \xi_y^2 + \xi_z^2)\delta(E_f - E_i - \hbar\omega) = \alpha\hbar\omega\frac{8\pi^2}{3}\xi^2\delta(E_f - E_i - \hbar\omega), \forall\theta$ which is the total isotropic cross-section measured for an ensemble of randomly oriented nanoparticles or at the magic angle $\theta = \arccos\left(\frac{1}{3}\right)$.

I.3.2   Final expression of the quadrupole cross-section

$$\sigma^Q(\hat{\epsilon}, \hat{k}) = \sigma^Q(0,0) + \sqrt{\frac{5}{14}}(3\sin^2\theta\sin^2\psi - 1)\sigma^Q(2,0)$$
$$+ \frac{1}{\sqrt{14}}[35\sin^2\theta\cos^2\theta\cos^2\psi + 5\sin^2\theta\sin^2\psi - 4]\sigma^Q(4,0)$$
$$+ \sqrt{5}\sin^2\theta[(\cos^2\theta\cos^2\psi - \sin^2\psi)\cos4\phi - 2\cos\theta\sin\psi\cos\psi\sin4\phi]\sigma^{Qr}(4,4)$$
(I.12)

In the configuration of the experiment, $\psi = 0$ and $\phi = \pi/2$.

Final state is d$_{z^2}$

$$\sigma^Q(\hat{\epsilon}, \hat{k}) = \alpha\hbar\omega k^2\left\{\frac{3}{400} + \frac{3}{80}\sqrt{\frac{2}{35}}\sqrt{\frac{5}{14}} + \frac{9}{400}\sqrt{\frac{2}{7}}\frac{1}{\sqrt{14}}\left(35\sin^2\theta\cos^2\theta - 4\right)\right\}\xi_{z^2}^2\delta(E_f - E_i - \hbar\omega)$$
(I.13)

then

$$\sigma^Q(\hat{e}, \hat{k}) = \alpha\hbar\omega k^2 \left\{ \frac{3}{400} + \frac{3}{560} + \frac{9}{2800} \left(35\sin^2\theta\cos^2\theta - 4 \right) \right\} \xi_{z^2}^2 \delta(E_f - E_i - \hbar\omega) \tag{I.14}$$

Final state is d_{xy}

$$\sigma^Q(\hat{e}, \hat{k}) = \alpha\hbar\omega k^2 \{ \frac{3}{400} - \frac{3}{80}\sqrt{\frac{2}{35}}\sqrt{\frac{5}{14}} + \frac{3}{800}\sqrt{\frac{2}{7}}\frac{1}{\sqrt{14}} \left(35\sin^2\theta\cos^2\theta - 4 \right)$$
$$+ \frac{3}{160}\sqrt{5}\sqrt{5}\sin^2\theta\cos^2\theta \} \xi_{xy}^2 \delta(E_f - E_i - \hbar\omega) \tag{I.15}$$

then

$$\sigma^Q(\hat{e}, \hat{k}) = \alpha\hbar\omega k^2 \left\{ \frac{3}{400} - \frac{3}{560} + \frac{3}{5600} \left(35\sin^2\theta\cos^2\theta - 4 \right) + \frac{15}{160}\sin^2\theta\cos^2\theta \right\} \xi_{xy}^2 \delta(E_f - E_i - \hbar\omega) \tag{I.16}$$

Final state is $d_{x^2-y^2}$

$$\sigma^Q(\hat{e}, \hat{k}) = \alpha\hbar\omega k^2 \{ \frac{3}{400} - \frac{3}{80}\sqrt{\frac{2}{35}}\sqrt{\frac{5}{14}} + \frac{3}{800}\sqrt{\frac{2}{7}}\frac{1}{\sqrt{14}} \left(35\sin^2\theta\cos^2\theta - 4 \right)$$
$$- \frac{3}{160}\sqrt{5}\sqrt{5}\sin^2\theta\cos^2\theta \} \xi_{x^2-y^2}^2 \delta(E_f - E_i - \hbar\omega) \tag{I.17}$$

then

$$\sigma^Q(\hat{e}, \hat{k}) = \alpha\hbar\omega k^2 \left\{ \frac{3}{400} + \frac{3}{560} + \frac{3}{5600} \left(35\sin^2\theta\cos^2\theta - 4 \right) - \frac{15}{160}\sin^2\theta\cos^2\theta \right\} \xi_{x^2-y^2}^2 \delta(E_f - E_i - \hbar\omega) \tag{I.18}$$

Final state is d_{xz} or d_{yz}

$$\sigma^Q(\hat{e}, \hat{k}) = \alpha\hbar\omega k^2 \left\{ \frac{3}{400} - \frac{3}{160}\sqrt{\frac{2}{35}}\sqrt{\frac{5}{14}} - \frac{3}{200}\sqrt{\frac{2}{7}}\frac{1}{\sqrt{14}} \left(35\sin^2\theta\cos^2\theta - 4 \right) \right\} \xi_{xz,yz}^2 \delta(E_f - E_i - \hbar\omega) \tag{I.19}$$

then

$$\sigma^Q(\hat{\epsilon}, \hat{k}) = \alpha \hbar \omega k^2 \left\{ \frac{3}{400} - \frac{3}{1120} - \frac{3}{1400} \left(35 \sin^2 \theta \cos^2 \theta - 4 \right) \right\} \xi^2_{xz,yz} \delta(E_f - E_i - \hbar \omega) \quad \text{(I.20)}$$

Bibliography

[1] Frank C M Spoor, Stanko Tomic, Arjan J Houtepen, and Laurens D A Siebbeles. Broadband Cooling Spectra of Hot Electrons and Holes in PbSe Quantum Dots. *ACS Nano*, 11(6):6286–6294, May 2017.

[2] D S Chemla and DAB Miller. Room-Temperature Excitonic Nonlinear-Optical Effects in Semiconductor Quantum-Well Structures. *Journal of the Optical Society of America B-Optical Physics*, 2(7):1155–1173, 1985.

[3] Guichuan Xing, Nripan Mathews, Shuangyong Sun, Swee Sien Lim, Yeng Ming Lam, Michael Graetzel, Subodh Mhaisalkar, and Tze Chien Sum. Long-Range Balanced Electron- and Hole-Transport Lengths in Organic-Inorganic CH3NH3PbI3. *Science*, 342(6156):344–347, 2013.

[4] Paul F Ndione, Zhen Li, and Kai Zhu. Effects of alloying on the optical properties of organic–inorganic lead halide perovskite thin films. *Journal of Materials Chemistry C*, 4(33):7775–7782, 2016.

[5] Benoy Anand, Siddharth Sampat, Evgeny O Danilov, Weina Peng, Sara M Rupich, Yves J Chabal, Yuri N Gartstein, and Anton V Malko. Broadband transient absorption study of photoexcitations in lead halide perovskites: Towards a multiband picture. *Physical Review B*, 93(16):161205–5, April 2016.

[6] Xiao Chi, Kai Leng, Bo Wu, Dong Shi, Yufong Choy, Zhongxin Chen, Zhihui Chen, Xiaojiang Yu, Ping Yang, Qing-Hua Xu, Tze Chien Sum, Andrivo Rusydi, and Kian Ping Loh. Elucidating Surface and Bulk Emission in 3D Hybrid Organic-Inorganic Lead Bromide Perovskites. *Advanced Optical Materials*, 338:1800470–7, May 2018.

[7] V P Zhukov, P M Echenique, and E V Chulkov. Two types of excited electron dynamics in zinc oxide. *Physical Review B*, 82(9):094302–8, September 2010.

[8] V P Zhukov, V G Tyuterev, and E V Chulkov. Electron–phonon relaxation and excited electron distribution in zinc oxide and anatase. *Journal of Physics: Condensed Matter*, 24(40):405802, 2012.

[9] J D Ye, S L Gu, S M Zhu, S M Liu, Y D Zheng, R Zhang, and Y Shi. Fermi-level band filling and band-gap renormalization in Ga-doped ZnO. *Applied Physics Letters*, 86(19):192111–4, May 2005.

[10] J A Sans, J F Sánchez-Royo, and A Segura. Study of the bandgap renormalization in Ga-doped ZnO films by means of optical absorption under high pressure and photoelectron spectroscopy. *Superlattices and Microstructures*, 43(4):362–367, April 2008.

Bibliography

[11] M Usuda, N Hamada, T Kotani, and M van Schilfgaarde. All-electron GW calculation based on the LAPW method: Application to wurtzite ZnO. *Physical Review B*, 66(12):125101, 2002.

[12] Tae Dong Kang, Ho Suk Lee, and Hosun Lee. Optical properties of black NiO and CoO single crystals studied with spectroscopic ellipsometry. *Journal of the Korean Physical Society*, 50(3): 632–637, March 2007.

[13] Ayana Ghosh, Cayla M Nelson, Lina S Abdallah, and Stefan Zollner. Optical constants and band structure of trigonal NiO. *Journal of Vacuum Science & Technology A: Vacuum, Surfaces, and Films*, 33(6):061203–8, November 2015.

[14] R V Vedrinskii, V L Kraizman, A A Novakovich, Sh M Elyafi, S Bocharov, Th Kirchner, and G Dräger. Experimental and Theoretical Studies of Fine Structure in Polarized Ni K X-Ray Absorption Spectra of NiO Single Crystals. *physica status solidi (b)*, 226(1):203–217, July 2001.

[15] Matthea A Peck and Marjorie A Langell. Comparison of Nanoscaled and Bulk NiO Structural and Environmental Characteristics by XRD, XAFS, and XPS. *Chemistry of Materials*, 24(23):4483–4490, December 2012.

[16] C Gougoussis, M Calandra, A Seitsonen, Ch Brouder, A Shukla, and F Mauri. Intrinsic charge transfer gap in NiO from Ni K-edge x-ray absorption spectroscopy. *Physical Review B*, 79(4): 045118, January 2009.

[17] Frederico A Lima, Christopher J Milne, Dimali C V Amarasinghe, Mercedes Hannelore Rittmann-Frank, Renske M van der Veen, Marco Reinhard, Van-Thai Pham, Susanne Karlsson, Steven L Johnson, Daniel Grolimund, Camelia Borca, Thomas Huthwelker, Markus Janousch, Frank van Mourik, Rafael Abela, and Majed Chergui. A high-repetition rate scheme for synchrotron-based picosecond laser pump/x-ray probe experiments on chemical and biological systems in solution. *Review of Scientific Instruments*, 82(6):063111–17, 2011.

[18] Y Tokura and N Nagaosa. Orbital physics in transition-metal oxides. *Science*, 288(5465):462–468, April 2000.

[19] Peter W Milonni and Joseph H Eberly. *Laser Physics*. Milonni/Laser Physics. John Wiley & Sons, Hoboken, NJ, USA, April 2010.

[20] S L Shi, G Q Li, S J Xu, Y Zhao, and G H Chen. Green Luminescence Band in ZnO: Fine Structures, Electron–Phonon Coupling, and Temperature Effect. *The Journal of Physical Chemistry B*, 110 (21):10475–10478, June 2006.

[21] V P Zhukov, V G Tyuterev, E V Chulkov, and P M Echenique. Hole-Phonon Relaxation and Photo-catalytic Properties of Titanium Dioxide and Zinc Oxide: First-Principles Approach. *International Journal of Photoenergy*, 2014(14):1–12, 2014.

[22] L Banyai and S W Koch. A Simple Theory for the Effects of Plasma Screening on the Optical-Spectra of Highly Excited Semiconductors. *Zeitschrift für Physik B Condensed Matter*, 63(3): 283–291, 1986.

[23] Shaul Mukamel. *Principles of Nonlinear Optical Spectroscopy*. Oxford University Press, 1999.

[24] Z Vardeny and J Tauc. Picosecond coherence coupling in the pump and probe technique. *Optics Communications*, 39(6):396–400, 1981.

[25] Michael B Price, Justinas Butkus, Tom C Jellicoe, Aditya Sadhanala, Anouk Briane, Jonathan E Halpert, Katharina Broch, Justin M Hodgkiss, Richard H Friend, and Felix Deschler. Hot-carrier cooling and photoinduced refractive index changes in organic-inorganic lead halide perovskites. *Nature Communications*, 6:1–8, September 2015.

[26] H Haug, S W Koch, and M Lindberg. Optical Nonlinearities and Instabilities in Semiconductors. *Physica Scripta*, T13:178–183, February 2007.

[27] H Haug and S W Koch. *Quantum Theory of the Optical and Electronic Properties of Semiconductors*. World Scientific, April 1990.

[28] P Zu, Z K Tang, G K L Wong, M Kawasaki, A Ohtomo, H Koinuma, Y Segawa, and Tetsuya Hasegawa. Ultraviolet spontaneous and stimulated emissions from ZnO microcrystallite thin films at room temperature. *Solid State Communications*, 103(8):459–463, 1997. doi: 10.1016/S0038-1098(97)00216-0. URL http://linkinghub.elsevier.com/retrieve/pii/S0038109897002160.

[29] Rudi Berera, Rienk van Grondelle, and John T M Kennis. Ultrafast transient absorption spectroscopy: principles and application to photosynthetic systems. *Photosynthesis Research*, 101 (2-3):105–118, July 2009.

[30] Léon Van Hove. The Occurrence of Singularities in the Elastic Frequency Distribution of a Crystal. *Physical Review*, 89(6):1189–1193, 1953.

[31] Jagdeep Shah. Ultrafast studies of carrier relaxation in semiconductors and their microstructures. *Superlattices and Microstructures*, 6(3):293–302, 1989.

[32] Jagdeep Shah. Hot electrons and phonons under high intensity photoexcitation of semiconductors. *Solid-State Electronics*, 21(1):43–50, January 1978.

[33] Jagdeep Shah. *Ultrafast Spectroscopy of Semiconductors and Semiconductor Nanostructures*, volume 115 of *Springer Series in Solid-State Sciences*. Springer Science & Business Media, Berlin, Heidelberg, November 2013.

[34] D J Norris and M G Bawendi. Measurement and assignment of the size-dependent optical spectrum in CdSe quantum dots. *Physical Review B*, 53(24):16338–16346, 1996.

[35] Andreas Othonos, H M Van Driel, Jeff F Young, and Paul J Kelly. Correlation of hot-phonon and hot-carrier kinetics in Ge on a picosecond time scale. *Physical Review B*, 43(8):6682–6690, January 1991.

[36] H M Van Driel. Influence of hot phonons on energy relaxation of high-density carriers in germanium. *Physical Review B*, 19(11):5928–5932, January 1979.

[37] D Von Der Linde, J Kuhl, and H Klingenberg. Raman scattering from nonequilibrium LO phonons with picosecond resolution. *Physical Review Letters*, 44(23):1505–1508, January 1980.

[38] Ye Yang, David P Ostrowski, Ryan M France, Kai Zhu, Jao van de Lagemaat, Joseph M Luther, and Matthew C Beard. Observation of a hot-phonon bottleneck in lead-iodide perovskites. *Nature Photonics*, 10(1):53–59, 2015.

Bibliography

[39] Jianfeng Yang, Hongze Xia, Rui Sheng, Qingshan Ma, Jincheol Kim, Patrick Tapping, Takaaki Harada, Tak W Kee, Fuzhi Huang, Yi-Bing Cheng, Martin Green, Anita Ho-Baillie, Shujuan Huang, Santosh Shrestha, Robert Patterson, Gavin Conibeer, and Xiaoming Wen. Acoustic-optical phonon up-conversion and hot-phonon bottleneck in lead-halide perovskites. *Nature Communications*, 8:1–9, January 2017.

[40] Jeff F Young and H M Van Driel. Ambipolar diffusion of high-density electrons and holes in Ge, Si, and GaAs: Many-body effects. *Physical Review B*, 26(4):2147–2158, January 1982.

[41] J G Gay. Screening of excitons in semiconductors. *Physical Review B*, 4(8):2567–2575, January 1971.

[42] Jagdeep Shah, R F Leheny, and W Wiegmann. Low-temperature absorption spectrum in GaAs in the presence of optical pumping. *Physical Review B*, 16(4):1577–1580, January 1977.

[43] E Baldini, L Chiodo, A Dominguez, M Palummo, S Moser, M Yazdi-Rizi, G Auböck, B P P Mallett, H Berger, A Magrez, C Bernhard, M Grioni, A Rubio, and M Chergui. Strongly bound excitons in anatase TiO2 single crystals and nanoparticles. *Nature Communications*, 8(1):37, 2017.

[44] W F Brinkman and T M Rice. Electron-hole liquids in semiconductors. *Physical Review B*, 7(4):1508–1523, January 1973.

[45] Hideki Yukawa. On the Interaction of Elementary Particles I. *Proc. Phys. Math. Soc. Jap.*, 17:48–57, 1935.

[46] J Shah, R F Leheny, and C Lin. Dynamic Burstein shift in GaAs. *Solid State Communications*, 18(8):1035–1037, January 1976.

[47] R F Leheny, Jagdeep Shah, R L Fork, C V Shank, and A Migus. Dynamics of hot carrier cooling in photo-excited GaAs. *Solid State Communications*, 31(11):809–813, January 1979.

[48] Carlo Motta and Stefano Sanvito. Electron–Phonon Coupling and Polaron Mobility in Hybrid Perovskites from First Principles. *The Journal of Physical Chemistry C*, 122(2):1361–1366, January 2018.

[49] J Shah, B Deveaud, T C Damen, W T Tsang, A C Gossard, and P Lugli. Determination of Intervalley Scattering Rates in GaAs by Subpicosecond Luminescence Spectroscopy. *Physical Review Letters*, 59(19):2222–2225, 1987.

[50] J G Fujimoto, S G Shevel, and E P Ippen. Femtosecond Time-Resolved Exciton Dynamics in CdSe. *Solid State Communications*, 49(6):605–609, 1984.

[51] Victor I Klimov. Optical Nonlinearities and Ultrafast Carrier Dynamics in Semiconductor Nanocrystals. *The Journal of Physical Chemistry B*, 104(26):6112–6123, July 2000.

[52] C Burda, S Link, T C Green, and M A El-Sayed. New Transient Absorption Observed in the Spectrum of Colloidal CdSe Nanoparticles Pumped with High-Power Femtosecond Pulses. *The Journal of Physical Chemistry B*, 103(49):10775–10780, December 1999.

[53] S Hunsche, T Dekorsy, V Klimov, and H Kurz. Ultrafast dynamics of carrier-induced absorption changes in highly-excited CdSe nanocrystals. *Applied Physics B: Lasers and Optics*, 62(1):3–10, January 1996.

[54] Clemens Burda, Stephan Link, Mona B Mohamed, and Mostafa El-Sayed. The pump power dependence of the femtosecond relaxation of CdSe nanoparticles observed in the spectral range from visible to infrared. *The Journal of Chemical Physics*, 116(9):3828–3833, March 2002.

[55] Laura M Herz. Charge-Carrier Mobilities in Metal Halide Perovskites: Fundamental Mechanisms and Limits. *ACS Energy Letters*, 2(7):1539–1548, June 2017.

[56] Benjamin Lingnau. *Nonlinear and Nonequilibrium Dynamics of Quantum-Dot Optoelectronic Devices*. Springer Theses. Springer International Publishing, Cham, 2015.

[57] Andreas Othonos. Probing ultrafast carrier and phonon dynamics in semiconductors. *Journal of Applied Physics*, 83(4):1789–1830, February 1998.

[58] G H Wannier. The structure of electronic excitation levels in insulating crystals. *Physical Review*, 52(3):0191–0197, August 1937.

[59] G Dresselhaus. Effective Mass Approximation for Excitons. *Journal of Physics and Chemistry of Solids*, 1(1-2):14–22, 1956.

[60] J Frenkel. On the transformation of light into heat in solids. I. *Physical Review*, 37(1):17–44, January 1931.

[61] G Baldini and K Teegarden. Trapped exciton states in the alkali halides. *Journal of Physics and Chemistry of Solids*, 27(6-7):943–946, January 1966.

[62] W I Park, Y H Jun, S W Jung, and Gyu-Chul Yi. Excitonic emissions observed in ZnO single crystal nanorods. *Applied Physics Letters*, 82(6):964–966, February 2003.

[63] R L Greene, K K Bajaj, and D E Phelps. Energy-Levels of Wannier Excitons in GaAs-Ga1-XAlxAs Quantum-Well Structures. *Physical Review B*, 29(4):1807–1812, 1984.

[64] Eva A A Pogna, Margherita Marsili, Domenico De Fazio, Stefano Dal Conte, Cristian Manzoni, Davide Sangalli, Duhee Yoon, Antonio Lombardo, Andrea C Ferrari, Andrea Marini, Giulio Cerullo, and Deborah Prezzi. Photo-Induced Bandgap Renormalization Governs the Ultrafast Response of Single-Layer MoS2. *ACS Nano*, 10(1):1182–1188, December 2015.

[65] S B Nam, D C Reynolds, C W Litton, R J Almassy, T C Collins, and C M Wolfe. Free-Exciton Energy-Spectrum in GaAs. *Physical Review B*, 13(2):761–767, 1976.

[66] M Imada, A Fujimori, and Y Tokura. Metal-insulator transitions. *Reviews of Modern Physics*, 70 (4):1039–1263, 1998.

[67] D S Chemla, DAB Miller, P W Smith, A C Gossard, and W Wiegmann. Room-Temperature Excitonic Nonlinear Absorption and Refraction in GaAs/AlGaAs Multiple Quantum Well Structures. *Ieee Journal of Quantum Electronics*, 20(3):265–275, 1984.

[68] WH Knox, C Hirlimann, DA Miller, J Shah, DS Chemla, and CV Shank. Femtosecond excitation of nonthermal carrier populations in GaAs quantum wells. *Physical Review Letters*, 56(11): 1191–1193, March 1986.

[69] S Schmitt-Rink, D S Chemla, and D A B Miller. Theory of transient excitonic optical nonlinearities in semiconductor quantum-well structures. *Physical Review B*, 32(10):6601–6609, November 1985.

[70] Edoardo Baldini, Tania Palmieri, Thomas Rossi, Malte Oppermann, Enrico Pomarico, Gerald Auböck, and Majed Chergui. Interfacial Electron Injection Probed by a Substrate-Specific Excitonic Signature. *Journal of the American Chemical Society*, 139(33):11584–11589, August 2017.

[71] Y H Lee, A Chavez-Pirson, S W Koch, H M Gibbs, S H Park, J Morhange, A Jeffery, N Peyghambarian, L Banyai, A C Gossard, and W Wiegmann. Room-Temperature Optical Nonlinearities in GaAs. *Physical Review Letters*, 57(19):2446–2449, November 1986.

[72] David Emin. *Polarons.* Cambridge University Press, 2013.

[73] Peter Y Yu and Manuel Cardona. *Fundamentals of semiconductors: physics and materials properties; 3rd ed.*, volume 21. Springer, Dordrecht, 2005.

[74] Haiming Zhu, Kiyoshi Miyata, Yongping Fu, Jue Wang, Prakriti P Joshi, Daniel Niesner, Kristopher W Williams, Song Jin, and X Y Zhu. Screening in crystalline liquids protects energetic carriers in hybrid perovskites. *Science*, 353(6306):1409–1413, 2016.

[75] Tyler J S Evans, Kiyoshi Miyata, Prakriti P Joshi, Sebastian Maehrlein, Fang Liu, and X Y Zhu. Competition Between Hot-Electron Cooling and Large Polaron Screening in CsPbBr3 Perovskite Single Crystals. *The Journal of Physical Chemistry C*, 122(25):13724–13730, 2018.

[76] Kaibo Zheng, Mohamed Abdellah, Qiushi Zhu, Qingyu Kong, Guy Jennings, Charles A Kurtz, Maria E Messing, Yuran Niu, David J Gosztola, Mohammed J Al-Marri, Xiaoyi Zhang, Tönu Pullerits, and Sophie E Canton. Direct Experimental Evidence for Photoinduced Strong-Coupling Polarons in Organolead Halide Perovskite Nanoparticles. *The Journal of Physical Chemistry Letters*, 7(22):4535–4539, 2016.

[77] Fabio G Santomauro, Jakob Grilj, Lars Mewes, Georgian Nedelcu, Sergii Yakunin, Thomas Rossi, Gloria Capano, Andre Al Haddad, James Budarz, Dominik Kinschel, Dario S Ferreira, Giacomo Rossi, Mario Gutierrez Tovar, Daniel Grolimund, Valerie Samson, Maarten Nachtegaal, Grigory Smolentsev, Maksym V Kovalenko, and Majed Chergui. Localized holes and delocalized electrons in photoexcited inorganic perovskites: Watching each atomic actor by picosecond X-ray absorption spectroscopy. *Structural Dynamics*, 4(4):044002, 2016.

[78] James Budarz, Fabio G Santomauro, M Hannelore Rittmann-Frank, Chris J Milne, Thomas Huthwelker, Daniel Grolimund, Jochen Rittmann, Dominik Kinschel, Thomas Rossi, and Majed Chergui. Time-resolved Element-selective Probing of Charge Carriers in Solar Materials. *CHIMIA International Journal for Chemistry*, 71(11):768–772, November 2017.

[79] Xiaofan Deng, Xiaoming Wen, Rui Sheng, Shujuan Huang, Takaaki Harada, Tak W Kee, Martin A Green, and Anita Ho-Baillie. Ultrafast charge generation and relaxation dynamics in methylammonium lead bromide perovskites. In Benjamin J Eggleton and Stefano Palomba, editors, *SPIE Micro+Nano Materials, Devices, and Applications*, pages 966848–7. SPIE, December 2015.

[80] Xiaofan Deng, Xiaoming Wen, Shujuan Huang, Rui Sheng, Takaaki Harada, Tak W Kee, Martin Green, and Anita Ho-Baillie. Ultrafast Carrier Dynamics in Methylammonium Lead Bromide Perovskite. *The Journal of Physical Chemistry C*, 120(5):2542–2547, February 2016.

[81] Vinay Sharma, Sigalit Aharon, Itay Gdor, Chunfan Yang, Lioz Etgar, and Sanford Ruhman. New insights into exciton binding and relaxation from high time resolution ultrafast spectroscopy of CH3NH3PbI3 and CH3NH3PbBr3 films. *Journal of Materials Chemistry A: Materials for energy and sustainability*, 4(9):3546–3553, February 2016.

[82] Tufan Ghosh, Sigalit Aharon, Lioz Etgar, and Sanford Ruhman. Free Carrier Emergence and Onset of Electron–Phonon Coupling in Methylammonium Lead Halide Perovskite Films. *Journal of the American Chemical Society*, 139(50):18262–18270, 2017.

[83] Hiroki Kawai, Giacomo Giorgi, Andrea Marini, and Koichi Yamashita. The Mechanism of Slow Hot-Hole Cooling in Lead-Iodide Perovskite: First-Principles Calculation on Carrier Lifetime from Electron–Phonon Interaction. *Nano Letters*, 15(5):3103–3108, April 2015.

[84] Giulia Grancini, Daniele Viola, Yonghui Lee, Michael Saliba, Sanghyun Paek, Kyung Taek Cho, Simonetta Orlandi, Marco Cavazzini, Fernando Fungo, Mohammad I Hossain, Abdelhak Belaidi, Nouar Tabet, Gianluca Pozzi, Giulio Cerullo, and Mohammad Khaja Nazeeruddin. Femtosecond Charge-Injection Dynamics at Hybrid Perovskite Interfaces. *ChemPhysChem*, 18(17):2381–2389, July 2017.

[85] OSA, editor. *Charge Dynamics in Lead Bromide Perovskites Probed by Femtosecond Broadband Deep-UV Spectroscopy*, 2018.

[86] Michael M Lee, Joël Teuscher, Tsutomu Miyasaka, Takurou N Murakami, and Henry J Snaith. Efficient Hybrid Solar Cells Based on Meso-Superstructured Organometal Halide Perovskites. *Science*, 338(6107):643–647, 2012.

[87] Akihiro Kojima, Kenjiro Teshima, Yasuo Shirai, and Tsutomu Miyasaka. Organometal Halide Perovskites as Visible-Light Sensitizers for Photovoltaic Cells. *Journal of the American Chemical Society*, 131(17):6050–6051, May 2009.

[88] Samuel D Stranks and Henry J Snaith. Metal-halide perovskites for photovoltaic and light-emitting devices. *Nature Nanotechnology*, 10(5):391–402, May 2015.

[89] Sergii Yakunin, Mykhailo Sytnyk, Dominik Kriegner, Shreetu Shrestha, Moses Richter, Gebhard J Matt, Hamed Azimi, Christoph J Brabec, Julian Stangl, Maksym V Kovalenko, and Wolfgang Heiss. Detection of X-ray photons by solution-processed lead halide perovskites. *Nature Photonics*, 9 (7):444–U44, July 2015.

[90] Yang Zhou, Lu You, Shiwei Wang, Zhiliang Ku, Hongjin Fan, Daniel Schmidt, Andrivo Rusydi, Lei Chang, Le Wang, Peng Ren, Liufang Chen, Guoliang Yuan, Lang Chen, and Junling Wang. Giant photostriction in organic–inorganic lead halide perovskites. *Nature Communications*, 7:11193, April 2016.

[91] Wei Zhang, Giles E Eperon, and Henry J Snaith. Metal halide perovskites for energy applications. *Nature Energy*, 1(6):16048–8, May 2016.

[92] Eran Edri, Saar Kirmayer, David Cahen, and Gary Hodes. High Open-Circuit Voltage Solar Cells Based on Organic–Inorganic Lead Bromide Perovskite. *The Journal of Physical Chemistry Letters*, 4(6):897–902, March 2013.

[93] Eran Edri, Saar Kirmayer, Michael Kulbak, Gary Hodes, and David Cahen. Chloride Inclusion and Hole Transport Material Doping to Improve Methyl Ammonium Lead Bromide Perovskite-Based High Open-Circuit Voltage Solar Cells. *The Journal of Physical Chemistry Letters*, 5(3):429–433, February 2014.

[94] Bernard Wenger, Pabitra K Nayak, Xiaoming Wen, Sameer V Kesava, Nakita K Noel, and Henry J Snaith. Consolidation of the optoelectronic properties of CH3NH3PbBr3 perovskite single crystals. *Nature Communications*, 8(1):1–10, September 2017.

Bibliography

[95] Ajay Jha, Hong-Guang Duan, Vandana Tiwari, Pabitra K Nayak, Henry J Snaith, Michael Thorwart, and R J Dwayne Miller. Direct Observation of Ultrafast Exciton Dissociation in Lead Iodide Perovskite by 2D Electronic Spectroscopy. *ACS Photonics*, 5(3):852–860, December 2017.

[96] Valerio Sarritzu, Nicola Sestu, Daniela Marongiu, Xueqing Chang, Qingqian Wang, Maria Antonietta Loi, Francesco Quochi, Michele Saba, Andrea Mura, and Giovanni Bongiovanni. Perovskite Excitonics: Primary Exciton Creation and Crossover from Free Carriers to a Secondary Exciton Phase. *Advanced Optical Materials*, 6(3):1700839–8, December 2017.

[97] Hamzeh Telfah, Abdelqader Jamhawi, Meghan B Teunis, Rajesh Sardar, and Jinjun Liu. Ultrafast Exciton Dynamics in Shape-Controlled Methylammonium Lead Bromide Perovskite Nanostructures: Effect of Quantum Confinement on Charge Carrier Recombination. *The Journal of Physical Chemistry C*, 121(51):28556–28565, 2017.

[98] Jasmine P.H. Rivett, Liang Z. Tan, Michael B. Price, Sean A. Bourelle, Nathaniel J.L.K. Davis, James Xiao, Yatao Zou, Rox Middleton, Baoquan Sun, Andrew M. Rappe, Dan Credgington, and Felix Deschler. Long-lived polarization memory in the electronic states of lead-halide perovskites from local structural dynamics. *Nature Communications*, 9(1):1–8, 2018. ISSN 20411723. doi: 10.1038/s41467-018-06009-3. URL http://dx.doi.org/10.1038/s41467-018-06009-3.

[99] Thomas R. Hopper, Andrei Gorodetsky, Jarvist M. Frost, Christian Müller, Robert Lovrincic, and Artem A. Bakulin. Ultrafast Intraband Spectroscopy of Hot-Carrier Cooling in Lead-Halide Perovskites. *ACS Energy Letters*, 3(9):2199–2205, 2018. ISSN 23808195. doi: 10.1021/acsenergylett.8b01227.

[100] Tze Chien Sum and Nripan Mathews. Advancements in perovskite solar cells: photophysics behind the photovoltaics. *Energy & Environmental Science*, 7(8):2518–2534, 2014.

[101] Mingjie Li, Saikat Bhaumik, Teck Wee Goh, Muduli Subas Kumar, Natalia Yantara, Michael Grätzel, Subodh Mhaisalkar, Nripan Mathews, and Tze Chien Sum. Slow cooling and highly efficient extraction of hot carriers in colloidal perovskite nanocrystals. *Nature Communications*, 8:14350, 2017.

[102] V Klimov, P H Bolivar, and H Kurz. Hot-Phonon Effects in Femtosecond Luminescence Spectra of Electron-Hole Plasmas in CdS. *Physical Review B*, 52(7):4728–4731, 1995.

[103] W Z Lin, R W Schoenlein, J G Fujimoto, and E P Ippen. Femtosecond Absorption Saturation Studies of Hot Carriers in GaAs and AlGaAs. *Ieee Journal of Quantum Electronics*, 24(2):267–275, February 1988.

[104] H Fröhlich. Localized Versus Band Model of Electrons in Solids. *Helvetica Physica Acta*, 41(6-7):838–&, 1968.

[105] K Wu, J Chen, J R McBride, and T Lian. Efficient hot-electron transfer by a plasmon-induced interfacial charge-transfer transition. *Science*, 349(6248):632–635, 2015.

[106] Kaifeng Wu, Guijie Liang, Qiongyi Shang, Yueping Ren, Degui Kong, and Tianquan Lian. Ultrafast Interfacial Electron and Hole Transfer from CsPbBr3 Perovskite Quantum Dots. *Journal of the American Chemical Society*, 137(40):12792–12795, September 2015.

[107] Masaki Shirayama, Hideyuki Kadowaki, Tetsuhiko Miyadera, Takeshi Sugita, Masato Tamakoshi, Masato Kato, Takemasa Fujiseki, Daisuke Murata, Shota Hara, Takurou N Murakami, Shohei Fujimoto, Masayuki Chikamatsu, and Hiroyuki Fujiwara. Optical Transitions in Hybrid Perovskite Solar Cells: Ellipsometry, Density Functional Theory, and Quantum Efficiency Analyses for CH3NH3PbI3. *Physical Review Applied*, 5(1):3586–25, January 2016.

[108] Davide Sangalli, Stefano Dal Conte, Cristian Manzoni, Giulio Cerullo, and Andrea Marini. Nonequilibrium optical properties in semiconductors from first principles: A combined theoretical and experimental study of bulk silicon. *Physical Review B*, 93(19):189–13, May 2016.

[109] R G Wheeler and J O Dimmock. Exciton Structure and Zeeman Effects in Cadmium Selenide. *Physical Review*, 125(6):1805–&, 1962.

[110] Gerald Auböck, Cristina Consani, Frank van Mourik, and Majed Chergui. Ultrabroadband femtosecond two-dimensional ultraviolet transient absorption. *Optics letters*, 37(12):2337, 2012.

[111] Gerald Auböck, Cristina Consani, Roberto Monni, Andrea Cannizzo, Frank van Mourik, and Majed Chergui. Femtosecond pump/supercontinuum-probe setup with 20 kHz repetition rate. *Review of Scientific Instruments*, 83(9):093105–6, 2012.

[112] R J Elliott. Intensity of Optical Absorption by Excitons. *Physical Review*, 108(6):1384–1389, 1957.

[113] Mohd Sharizal Alias, Ibrahim Dursun, Makhsud I Saidaminov, Elhadj Marwane Diallo, Pawan Mishra, Tien Khee Ng, Osman M Bakr, and Boon S Ooi. Optical constants of CH3NH3PbBr3 perovskite thin films measured by spectroscopic ellipsometry. *Optics Express*, 24(15):16586–9, 2016.

[114] Aurélien M A Leguy, Pooya Azarhoosh, M Isabel Alonso, Mariano Campoy-Quiles, Oliver J Weber, Jizhong Yao, Daniel Bryant, Mark T Weller, Jenny Nelson, Aron Walsh, Mark van Schilfgaarde, and Piers R F Barnes. Experimental and theoretical optical properties of methylammonium lead halide perovskites. *Nanoscale*, 8(12):6317–6327, 2016.

[115] Ji-Sang Park, Sukgeun Choi, Yong Yan, Ye Yang, Joseph M Luther, Su-Huai Wei, Philip Parilla, and Kai Zhu. Electronic Structure and Optical Properties of α-CH3NH3PbBr3 Perovskite Single Crystal. *The Journal of Physical Chemistry Letters*, 6(21):4304–4308, November 2015.

[116] Masato Kato, Takemasa Fujiseki, Tetsuhiko Miyadera, Takeshi Sugita, Shohei Fujimoto, Masato Tamakoshi, Masayuki Chikamatsu, and Hiroyuki Fujiwara. Universal rules for visible-light absorption in hybrid perovskite materials. *Journal of Applied Physics*, 121(11):115501–15, March 2017.

[117] Ye Yang, Mengjin Yang, Zhen Li, Ryan Crisp, Kai Zhu, and Matthew C Beard. Comparison of Recombination Dynamics in CH3NH3PbBr3 and CH3NH3PbI3 Perovskite Films: Influence of Exciton Binding Energy. *The Journal of Physical Chemistry Letters*, 6(23):4688–4692, December 2015.

[118] M Tuan Trinh, Xiaoxi Wu, Daniel Niesner, and X Y Zhu. Many-body interactions in photo-excited lead iodide perovskite. *Journal of Materials Chemistry A: Materials for energy and sustainability*, 3(17):9285–9290, April 2015.

[119] Guichuan Xing, Bo Wu, Shi Chen, Julianto Chua, Natalia Yantara, Subodh Mhaisalkar, Nripan Mathews, and Tze Chien Sum. Interfacial Electron Transfer Barrier at Compact TiO2/CH3NH3PbI3 Heterojunction. *Small*, 11(29):3606–3613, August 2015.

Bibliography

[120] Tze Chien Sum, Nripan Mathews, Guichuan Xing, Swee Sien Lim, Wee Kiang Chong, David Giovanni, and Herlina Arianita Dewi. Spectral Features and Charge Dynamics of Lead Halide Perovskites: Origins and Interpretations. *Accounts of Chemical Research*, 49(2):294–302, February 2016.

[121] Swee Sien Lim, Wee Kiang Chong, Ankur Solanki, Herlina Arianita Dewi, Subodh Mhaisalkar, Nripan Mathews, and Tze Chien Sum. Modulating carrier dynamics through perovskite film engineering. *Physical Chemistry Chemical Physics*, 18(39):27119–27123, 2016.

[122] Joseph S Manser and Prashant V Kamat. Band filling with free charge carriers in organometal halide perovskites. *Nature Photonics*, 8(9):737–743, 2014.

[123] Arianna Marchioro. *Interfacial Charge Transfer Dynamics in Solid-State Hybrid Organic-Inorganic Solar Cells*. PhD thesis, EPFL, June 2014.

[124] Piotr Piatkowski, Boiko Cohen, Francisco Javier Ramos, Maria Di Nunzio, Mohammad Khaja Nazeeruddin, Michael Grätzel, Shahzada Ahmad, and Abderrazzak Douhal. Direct monitoring of ultrafast electron and hole dynamics in perovskite solar cells. *Physical Chemistry Chemical Physics*, 17(22):14674–14684, 2015.

[125] G Grancini, M Maiuri, D Fazzi, A Petrozza, H-J Egelhaaf, D Brida, G Cerullo, and G Lanzani. Hot exciton dissociation in polymer solar cells. *Nature Materials*, 12(1):29–33, December 2012.

[126] Johannes M Richter, Federico Branchi, Franco Valduga de Almeida Camargo, Baodan Zhao, Richard H Friend, Giulio Cerullo, and Felix Deschler. Ultrafast carrier thermalization in lead iodide perovskite probed with two-dimensional electronic spectroscopy. *Nature Communications*, 8(1):376, August 2017.

[127] Kevin G Stamplecoskie, Joseph S Manser, and Prashant V Kamat. Dual nature of the excited state in organic-inorganic lead halide perovskites. *Energy & Environmental Science*, 8(1):208–215, December 2014.

[128] Kannatassen Appavoo, Wanyi Nie, Jean-Christophe Blancon, Jacky Even, Aditya D Mohite, and Matthew Y Sfeir. Ultrafast optical snapshots of hybrid perovskites reveal the origin of multiband electronic transitions. *Physical Review B*, 96(19):195308–9, November 2017.

[129] D O Demchenko, N Izyumskaya, M Feneberg, V Avrutin, U Ozgur, R Goldhahn, and H Morkoc. Optical properties of the organic-inorganic hybrid perovskite CH3NH3PbI3: Theory and experiment. *Physical Review B*, 94(7):075206–9, August 2016.

[130] Philipp Löper, Michael Stuckelberger, Bjoern Niesen, Jérémie Werner, Miha Filipič, Soo-Jin Moon, Jun-Ho Yum, Marko Topič, Stefaan De Wolf, and Christophe Ballif. Complex Refractive Index Spectra of CH3NH3PbI3 Perovskite Thin Films Determined by Spectroscopic Ellipsometry and Spectrophotometry. *The Journal of Physical Chemistry Letters*, 6(1):66–71, December 2014.

[131] P Lautenschlager, S Logothetidis, L Via, and M Cardona. Ellipsometric studies of the dielectric function of Cd1−xMnxTe alloys. *Physical Review B*, 32(6):3811–3818, September 1985.

[132] Yutaka Toyozawa, Masaharu Inoue, Teturo Inui, Makoto Okazaki, and Eiichi Hanamura. Coexistence of Local and Band Characters in the Absorption Spectra of Solids I. Formulation. *Journal of the Physical Society of Japan*, 22(6):1337–1349, June 1967.

[133] Makoto Okazaki, Masaharu Inoue, Yutaka Toyozawa, Teturo Inui, and Eiichi Hanamura. Coexistence of Local and Band Characters in the Absorption Spectra of Solids. II. Calculations for the Simple Cubic Lattice. *Journal of the Physical Society of Japan*, 22(6):1349–1361, June 1967.

[134] M Saliba, T Matsui, K Domanski, J Y Seo, A Ummadisingu, S M Zakeeruddin, J P Correa-Baena, W R Tress, A Abate, A Hagfeldt, and M Grätzel. Incorporation of rubidium cations into perovskite solar cells improves photovoltaic performance. *Science*, 354(6309):206–209, 2016.

[135] Haibo Zeng, Guotao Duan, Yue Li, Shikuan Yang, Xiaoxia Xu, and Weiping Cai. Blue Luminescence of ZnO Nanoparticles Based on Non-Equilibrium Processes: Defect Origins and Emission Controls. *Advanced Functional Materials*, 20(4):561–572, February 2010.

[136] C Klingshirn and H Haug. Optical properties of highly excited direct gap semiconductors. *Physics Reports*, 70(5):315–398, 1981.

[137] A Redondo-Cubero, A Hierro, J M Chauveau, K Lorenz, G Tabares, N Franco, E Alves, and E Muñoz. Single phase a-plane MgZnO epilayers for UV optoelectronics: substitutional behaviour of Mg at large contents. *CrystEngComm*, 14(5):1637–1640, 2012.

[138] Motoaki Iwaya, Shinji Terao, Nobuaki Hayashi, Takayuki Kashima, Hiroshi Amano, and Isamu Akasaki. Realization of crack-free and high-quality thick $Al_xGa_{1-x}N$ for UV optoelectronics using low-temperature interlayer. *Applied Surface Science*, 159:405–413, January 2000.

[139] Karin Keis, Lionel Vayssieres, Sten-Eric Lindquist, and Anders Hagfeldt. Nanostructured ZnO electrodes for photovoltaic applications. *Nanostructured Materials*, 12(1-4):487–490, 1999.

[140] Dongxu Zhao, Yichun Liu, Dezhen Shen, Youming Lu, Jiying Zhang, and Xiwu Fan. Photoluminescence properties of MgxZn1−xO alloy thin films fabricated by the sol-gel deposition method. *Journal of Applied Physics*, 90(11):5561–5563, December 2001.

[141] U Ozgur, Y I Alivov, C Liu, A Teke, M A Reshchikov, S Dogan, V Avrutin, S J Cho, and H Morkoc. A comprehensive review of ZnO materials and devices. *Journal of Applied Physics*, 98(4), 2005.

[142] J Phillips. *Bonds and Bands in Semiconductors.* Elsevier, December 2012.

[143] M Topsakal, S Cahangirov, E Bekaroglu, and S Ciraci. First-principles study of zinc oxide honeycomb structures. *Physical Review B*, 80(23):177–14, December 2009.

[144] A Mang, K Reimann, and S Rubenacke. Band-Gaps, Crystal-Field Splitting, Spin-Orbit-Coupling, and Exciton Binding-Energies in ZnO Under Hydrostatic-Pressure. *Solid State Communications*, 94(4):251–254, April 1995.

[145] T S Kim, C J Youn, and T S Jeong. Splitting of the valence band for polycrystalline ZnO. *Journal of the Korean Physical Society*, 38(1):42–46, January 2001.

[146] H Gerischer. Charge transfer processes at semiconductor-electrolyte interfaces in connection with problems of catalysis. *Surface Science*, 18(1):97–122, January 1969.

[147] H Gerischer, M E Michel-Beyerle, F Rebentrost, and H Tributsch. Sensitization of charge injection into semiconductors with large band gap. *Electrochimica Acta*, 13(6):1509–1515, January 1968.

[148] An-Jen Cheng, Yonhua Tzeng, Yi Zhou, Minseo Park, Tsung-hsueh Wu, Curtis Shannon, Dake Wang, and Wonwoo Lee. Thermal chemical vapor deposition growth of zinc oxide nanostructures for dye-sensitized solar cell fabrication. *Applied Physics Letters*, 92(9):092113–4, March 2008.

Bibliography

[149] T Rossi, T J Penfold, M H Rittmann-Frank, M Reinhard, J Rittmann, C N Borca, D Grolimund, C J Milne, and M Chergui. Characterizing the Structure and Defect Concentration of ZnO Nanoparticles in a Colloidal Solution. *The Journal of Physical Chemistry C*, 118(33):19422–19430, August 2014.

[150] B H Bransden and C J Joachain. *Physics of Atoms and Molecules; 2nd ed.* Prentice-Hall, Harlow, 2003.

[151] V P Zhukov and E V Chulkov. Ab initio approach to the excited electron dynamics in rutile and anatase TiO2. *Journal of Physics: Condensed Matter*, 22(43):435802–9, October 2010.

[152] Stefano Baroni, Stefano de Gironcoli, Andrea Dal Corso, and Paolo Giannozzi. Phonons and related crystal properties from density-functional perturbation theory. *Reviews of Modern Physics*, 73(2):515–562, April 2001.

[153] F Marsiglio and J P Carbotte. Eliashberg theory and the high T_c oxides. *Solid State Communications*, 63(5):419–423, January 1987.

[154] Edoardo Baldini, Tania Palmieri, Enrico Pomarico, Gerald Auböck, and Majed Chergui. Clocking the Ultrafast Electron Cooling in Anatase Titanium Dioxide Nanoparticles. *ACS Photonics*, 5(4): 1241–1249, 2018.

[155] C V Shank, R L Fork, R F Leheny, and J Shah. Dynamics of Photoexcited GaAs Band-Edge Absorption with Subpicosecond Resolution. *Physical Review Letters*, 42(2):112–115, 1979.

[156] Jagdeep Shah and R C C Leite. Radiative Recombination from Photoexcited Hot Carriers in GaAs. *Physical Review Letters*, 22(24):1304–1307, December 1969.

[157] K G Saw, N M Aznan, F K Yam, S S Ng, and S Y Pung. New Insights on the Burstein-Moss Shift and Band Gap Narrowing in Indium-Doped Zinc Oxide Thin Films. *PLoS ONE*, 10(10):e0141180–17, October 2015.

[158] Jianhui Fu, Qiang Xu, Guifang Han, Bo Wu, Cheng Hon Alfred Huan, Meng Lee Leek, and Tze Chien Sum. Hot carrier cooling mechanisms in halide perovskites. *Nature Communications*, 8(1):1–9, October 2017.

[159] Chavdar Slavov, Helvi Hartmann, and Josef Wachtveitl. Implementation and Evaluation of Data Analysis Strategies for Time-Resolved Optical Spectroscopy. *Analytical Chemistry*, 87(4): 2328–2336, February 2015.

[160] Gabriel F Dorlhiac, Clyde Fare, and Jasper J van Thor. PyLDM - An open source package for lifetime density analysis of time-resolved spectroscopic data. *PLOS Computational Biology*, 13 (5):e1005528–15, May 2017.

[161] Nur P Damayanti, Ana Paula Craig, and Joseph Irudayaraj. A hybrid FLIM-elastic net platform for label free profiling of breast cancer. *The Analyst*, 138(23):7127–8, 2013.

[162] D C Reynolds, D C Look, B Jogai, J E Hoelscher, R E Sherriff, M T Harris, and M J Callahan. Time-resolved photoluminescence lifetime measurements of the Γ5 and Γ6 free excitons in ZnO. *Journal of Applied Physics*, 88(4):2152–2153, August 2000.

192

[163] Christophe Bauer, Gerrit Boschloo, Emad Mukhtar, and Anders Hagfeldt. Ultrafast relaxation dynamics of charge carriers relaxation in ZnO nanocrystalline thin films. *Chemical Physics Letters*, 387(1-3):176–181, March 2004.

[164] YP Varshni. Eigenenergies and oscillator strengths for the Hulthén potential. *Physical Review A*, 41(9):4682–4689, May 1990.

[165] Manuel Cardona and Gunther Harbeke. Optical Properties and Band Structure of Wurtzite-Type Crystals and Rutile. *Physical Review*, 137(5A):A1467–A1476, 1965.

[166] S Kedenburg, M Vieweg, T Gissibl, and H Giessen. Linear Refractive Index and Absorption Measurements of Nonlinear Optical Liquids in the Visible and Near-infrared Spectral Region. *Optical Materials Express*, 2(11):1588–1611, 2012.

[167] S Shokhovets, O Ambacher, B K Meyer, and G Gobsch. Anisotropy of the momentum matrix element, dichroism, and conduction-band dispersion relation of wurtzite semiconductors. *Physical Review B*, 78(3):6487–18, July 2008.

[168] W Y Liang and A D Yoffe. Transmission Spectra of ZnO Single Crystals. *Physical Review Letters*, 20(2):59–&, 1968.

[169] G E Jellison and L A Boatner. Optical functions of uniaxial ZnO determined by generalized ellipsometry. *Physical Review B*, 58(7):3586–3589, 1998.

[170] Anderson Janotti and Chris G Van de Walle. Fundamentals of zinc oxide as a semiconductor. *Reports on Progress in Physics*, 72(12):126501, December 2009.

[171] Aline L Schoenhalz, Jeverson T Arantes, Adalberto Fazzio, and Gustavo M Dalpian. Surface and Quantum Confinement Effects in ZnO Nanocrystals. *The Journal of Physical Chemistry C*, 114 (43):18293–18297, October 2010.

[172] André Schleife, Claudia Rödl, Frank Fuchs, Karsten Hannewald, and Friedhelm Bechstedt. Optical Absorption in Degenerately Doped Semiconductors: Mott Transition or Mahan Excitons? *Physical Review Letters*, 107(23):236405–5, November 2011.

[173] Marijn A M Versteegh, A J van Lange, H T C Stoof, and Jaap I Dijkhuis. Observation of preformed electron-hole Cooper pairs in highly excited ZnO. *Physical Review B*, 85:195206, May 2012.

[174] Sun-Kyun Lee, Bong-Joon Kwon, Yong-Hoon Cho, Hang-Ju Ko, and Takafumi Yao. Excitonic transition dynamics on front and back surfaces of ZnO thin films. *Physical Review B*, 84(20): 139–5, November 2011.

[175] Ye Yang, Yong Yan, Mengjin Yang, Sukgeun Choi, Kai Zhu, Joseph M Luther, and Matthew C Beard. Low surface recombination velocity in solution-grown CH3NH3PbBr3 perovskite single crystal. *Nature Communications*, 6(1):183, 2015.

[176] K Ozawa, K Sawada, and Y Shirotori. Angle-resolved photoemission study of the valence band structure of ZnO (1010). *Journal of Physics: Condensed Matter*, 17(8):1271–1278, 2005.

[177] Linda Y Lim, Stephan Lany, Young Jun Chang, Eli Rotenberg, Alex Zunger, and Michael F Toney. Angle-resolved photoemission and quasiparticle calculation of ZnO: The need for d band shift in oxide semiconductors. *Physical Review B*, 86(23):235113, December 2012.

Bibliography

[178] M V Ryzhkov, S I Rumyantsev, V M Markushev, Ch M Briskina, and A P Tarasov. Edge Luminescence of ZnO Films. *Journal of Applied Spectroscopy*, 81(5):877–880, November 2014.

[179] S Hunsche, K Leo, H Kurz, and K Kohler. Exciton Absorption Saturation by Phase-Space Filling - Influence of Carrier Temperature and Density. *Physical Review B*, 49(23):16565–16568, 1994.

[180] Moongoo Choi, Koo-Chul Je, Sang-Youp Yim, and Seung-Han Park. Relative strength of the screened Coulomb interaction and phase-space filling on exciton bleaching in multiple quantum well structures. *Physical Review B*, 70(8):13–4, August 2004.

[181] Tsung-Yu Chiang, Gang-Lun Fan, Jun-Yuan Jeng, Kuo-Cheng Chen, Peter Chen, Ten-Chin Wen, Tzung-Fang Guo, and Ken-Tsung Wong. Functional p-Type, Polymerized Organic Electrode Interlayer in CH3NH3PbI3 Perovskite/Fullerene Planar Heterojunction Hybrid Solar Cells. *ACS Applied Materials & Interfaces*, 7(44):24973–24981, November 2015.

[182] S W Koch, S Schmitt-Rink, and H Haug. Theory of Optical Nonlinearities in InSb. *physica status solidi (b)*, 106(1):135–140, January 1981.

[183] P C Ou, J H Lin, and W F Hsieh. Spectral dependence of transient reflectance in a ZnO epitaxial film at room temperature. *Applied Physics B*, 106(2):399–404, September 2011.

[184] S Shokhovets, G Gobsch, and O Ambacher. Conduction band parameters of ZnO. *Superlattices and Microstructures*, 39(1-4):299–305, January 2006.

[185] S Shokhovets, L Spieß, and G Gobsch. Spectroscopic ellipsometry of wurtzite ZnO and GaN: Examination of a special case. *Journal of Applied Physics*, 107(2):023509–11, January 2010.

[186] N T Pelekanos, J Ding, M Hagerott, A V Nurmikko, H Luo, N Samarth, and J K Furdyna. Quasi-two-dimensional excitons in (Zn,Cd)Se/ZnSe quantum wells: Reduced exciton LO-phonon coupling due to confinement effects. *Physical Review B*, 45(11):6037–6042, January 1992.

[187] Jiaguang Han, Zhiyuan Zhu, Sanith Ray, Abul K Azad, Weili Zhang, Mingxia He, Shihong Li, and Yiping Zhao. Optical and dielectric properties of ZnO tetrapod structures at terahertz frequencies. *Applied Physics Letters*, 89(3):031107–4, July 2006.

[188] Yefan Chen, N T Tuan, Yusaburo Segawa, Hang-Ju Ko, Soon-ku Hong, and Takafumi Yao. Stimulated emission and optical gain in ZnO epilayers grown by plasma-assisted molecular-beam epitaxy with buffers. *Applied Physics Letters*, 78(11):1469–1471, March 2001.

[189] T Jesper Jacobsson, Sviatlana Viarbitskaya, Emad Mukhtar, and Tomas Edvinsson. A size dependent discontinuous decay rate for the exciton emission in ZnO quantum dots. *Physical Chemistry Chemical Physics*, 16(27):13849–13857, 2014.

[190] D Von Der Linde and R Lambrich. Direct measurement of hot-Electron relaxation by picosecond spectroscopy. *Physical Review Letters*, 42(16):1090–1093, January 1979.

[191] J F Ryan, R A Taylor, A J Turberfield, Angela Maciel, J M Worlock, A C Gossard, and W Wiegmann. Time-resolved photoluminescence of two-dimensional hot carriers in GaAs-AlGaAs heterostructures. *Physical Review Letters*, 53(19):1841–1844, January 1984.

[192] Kathleen Kash and Jagdeep Shah. Carrier energy relaxation in In0.53Ga0.47As determined from picosecond luminescence studies. *Applied Physics Letters*, 45(4):401–403, August 1984.

194

[193] D Zanato, N Balkan, B K Ridley, G Hill, and W J Schaff. Hot electron cooling rates via the emission of LO-phonons in InN. *Semiconductor Science and Technology*, 19(8):1024–1028, June 2004.

[194] Aishi Yamamoto, Takeo Kido, Takenari Goto, Yefan Chen, Takafumi Yao, and Atsuo Kasuya. Dynamics of photoexcited carriers in ZnO epitaxial thin films. *Applied Physics Letters*, 75(4): 469–471, July 1999.

[195] E Hendry, M Koeberg, and M Bonn. Exciton and electron-hole plasma formation dynamics in ZnO. *Physical Review B*, 76(4):045214–6, July 2007.

[196] X M Wen, J A Davis, D McDonald, L V Dao, P Hannaford, V A Coleman, H H Tan, C Jagadish, K Koike, S Sasa, M Inoue, and M Yano. Ultrafast dynamics in ZnO/ZnMgO multiple quantum wells. *Nanotechnology*, 18(31):315403–6, July 2007.

[197] Hsu-Cheng Hsu and Wen-Feng Hsieh. Excitonic polaron and phonon assisted photoluminescence of ZnO nanowires. *Solid State Communications*, 131(6):371–375, August 2004.

[198] S J Xu, Shi-Jie Xiong, and S L Shi. Resonant coupling of bound excitons with LO phonons in ZnO: Excitonic polaron states and Fano interference. *The Journal of Chemical Physics*, 123(22): 221105–6, December 2005.

[199] Hikmet Sezen, Honghui Shang, Fabian Bebensee, Chengwu Yang, Maria Buchholz, Alexei Nefedov, Stefan Heissler, Christian Carbogno, Matthias Scheffler, Patrick Rinke, and Christof Wöll. Evidence for photogenerated intermediate hole polarons in ZnO. *Nature Communications*, 6(1): 6901, April 2015.

[200] N Peyghambarian, H M Gibbs, J L Jewell, A Antonetti, A Migus, D Hulin, and A Mysyrowicz. Blue Shift of the Exciton Resonance Due to Exciton-Exciton Interactions in a Multiple-Quantum-Well Structure. *Physical Review Letters*, 53(25):2433–2436, 1984.

[201] L Schultheis, J Kuhl, A Honold, and CW Tu. Ultrafast phase relaxation of excitons via exciton-exciton and exciton-electron collisions. *Physical Review Letters*, 57(13):1635–1638, September 1986.

[202] A Cannizzo, O Bräm, G Zgrablic, A Tortschanoff, A Ajdarzadeh Oskouei, F van Mourik, and M Chergui. Femtosecond fluorescence upconversion setup with broadband detection in the ultraviolet. *Optics letters*, 32(24):3555–3557, December 2007.

[203] Malte Oppermann, Natalia Nagornova, Aurelio Oriana, Edoardo Baldini, Lars Mewes, Benjamin Bauer, Tania Palmieri, Thomas Rossi, Frank van Mourik, and Majed Chergui. The LOUVRE Laboratory: State-of-the-Art Ultrafast Ultraviolet Spectroscopies for Molecular and Materials Science. *CHIMIA International Journal for Chemistry*, 71(5):288–294, May 2017.

[204] M Grätzel. Photoelectrochemical cells. *Nature*, 414(6861):338–344, 2001.

[205] Michael Grätzel. Recent Advances in Sensitized Mesoscopic Solar Cells. *Accounts of Chemical Research*, 42(11):1788–1798, November 2009.

[206] H Zhou, Q Chen, G Li, S Luo, T b Song, H S Duan, Z Hong, J You, Y Liu, and Y Yang. Interface engineering of highly efficient perovskite solar cells. *Science*, 345(6196):542–546, 2014.

Bibliography

[207] Nam Joong Jeon, Jun Hong Noh, Young Chan Kim, Woon Seok Yang, Seungchan Ryu, and Sang Il Seok. Solvent engineering for high-performance inorganic–organic hybrid perovskite solar cells. *Nature Materials*, 13(9):897–903, July 2014.

[208] James M Ball, Michael M Lee, Andrew Hey, and Henry J Snaith. Low-temperature processed meso-superstructured to thin-film perovskite solar cells. *Energy & Environmental Science*, 6(6):1739–5, 2013.

[209] Jing Leng, Junxue Liu, Jun Zhang, and Shengye Jin. Decoupling Interfacial Charge Transfer from Bulk Diffusion Unravels Its Intrinsic Role for Efficient Charge Extraction in Perovskite Solar Cells. *The Journal of Physical Chemistry Letters*, 7(24):5056–5061, November 2016.

[210] Holly F Zarick, Abdelaziz Boulesbaa, Alexander A Puretzky, Eric M Talbert, Zachary R DeBra, Naiya Soetan, David B Geohegan, and Rizia Bardhan. Ultrafast carrier dynamics in bimetallic nanostructure-enhanced methylammonium lead bromide perovskites. *Nanoscale*, 9(4):1475–1483, 2017.

[211] M Ibrahim Dar, Marius Franckevičius, Neha Arora, Kipras Redeckas, Mikas Vengris, Vidmantas Gulbinas, Shaik Mohammed Zakeeruddin, and Michael Grätzel. High photovoltage in perovskite solar cells: New physical insights from the ultrafast transient absorption spectroscopy. *Chemical Physics Letters*, 683:211–215, September 2017.

[212] Xiaoxi Wu, M Tuan Trinh, Daniel Niesner, Haiming Zhu, Zachariah Norman, Jonathan S Owen, Omer Yaffe, Bryan J Kudisch, and X Y Zhu. Trap States in Lead Iodide Perovskites. *Journal of the American Chemical Society*, 137(5):2089–2096, February 2015.

[213] Raihana Begum, Manas R Parida, Ahmed L Abdelhady, Banavoth Murali, Noktan M Alyami, Ghada H Ahmed, Mohamed Nejib Hedhili, Osman M Bakr, and Omar F Mohammed. Engineering Interfacial Charge Transfer in CsPbBr3 Perovskite Nanocrystals by Heterovalent Doping. *Journal of the American Chemical Society*, 139(2):731–737, January 2017.

[214] Feng Liu, Yaohong Zhang, Chao Ding, Taro Toyoda, Yuhei Ogomi, Teresa S Ripolles, Shuzi Hayase, Takashi Minemoto, Kenji Yoshino, Songyuan Dai, and Qing Shen. Ultrafast Electron Injection from Photoexcited Perovskite CsPbI3 QDs into TiO2 Nanoparticles with Injection Efficiency near 99%. *The Journal of Physical Chemistry Letters*, 9(2):294–297, 2018.

[215] Carlito S Ponseca Jr., Tom J Savenije, Mohamed Abdellah, Kaibo Zheng, Arkady Yartsev, Tobjörn Pascher, Tobias Harlang, Pavel Chabera, Tönu Pullerits, Andrey Stepanov, Jean-Pierre Wolf, and Villy Sundström. Organometal Halide Perovskite Solar Cell Materials Rationalized: Ultrafast Charge Generation, High and Microsecond-Long Balanced Mobilities, and Slow Recombination. *Journal of the American Chemical Society*, 136(14):5189–5192, April 2014.

[216] Carlito S Ponseca Jr., Eline M Hutter, Piotr Piatkowski, Boiko Cohen, Torbjörn Pascher, Abderrazzak Douhal, Arkady Yartsev, Villy Sundström, and Tom J Savenije. Mechanism of Charge Transfer and Recombination Dynamics in Organo Metal Halide Perovskites and Organic Electrodes, PCBM, and Spiro-OMeTAD: Role of Dark Carriers. *Journal of the American Chemical Society*, 137(51):16043–16048, December 2015.

[217] Neha Arora, M Ibrahim Dar, Mojtaba Abdi-Jalebi, Fabrizio Giordano, Norman Pellet, Gwénolé Jacopin, Richard H Friend, Shaik Mohammed Zakeeruddin, and Michael Grätzel. Intrinsic and Extrinsic Stability of Formamidinium Lead Bromide Perovskite Solar Cells Yielding High Photovoltage. *Nano Letters*, 16(11):7155–7162, November 2016.

[218] A Marchioro, J Teuscher, D Friedrich, M Kunst, R van de krol, Thomas Moehl, M Grätzel, and Jacques-Edouard Moser. Unravelling the mechanism of photoinduced charge transfer processes in lead iodide perovskite solar cells. *Nature Photonics*, 8(3):250–255, 2014.

[219] Edoardo Baldini. *Nonequilibrium Dynamics of Collective Excitations in Quantum Materials*. Springer, March 2018.

[220] Tetsuro Katayama, Harunobu Suenaga, Tomoki Okuhata, Sadahiro Masuo, and Naoto Tamai. Unraveling the Ultrafast Exciton Relaxation and Hidden Energy State in CH3NH3PbBr3 Nanoparticles. *The Journal of Physical Chemistry C*, 122(9):5209–5214, 2018.

[221] Prashant V Kamat, Nada M Dimitrijevic, and A J Nozik. Dynamic Burstein-Moss shift in semiconductor colloids. *The Journal of Physical Chemistry*, 93(8):2873–2875, 1989.

[222] Laura M Herz. Charge-Carrier Dynamics in Organic-Inorganic Metal Halide Perovskites. *Annual Review of Physical Chemistry*, 67(1):65–89, May 2016.

[223] Bo Wu, Huy Tiep Nguyen, Zhiliang Ku, Guifang Han, David Giovanni, Nripan Mathews, Hong Jin Fan, and Tze Chien Sum. Discerning the Surface and Bulk Recombination Kinetics of Organic–Inorganic Halide Perovskite Single Crystals. *Advanced Energy Materials*, 6(14):1–9, 2016. ISSN 16146840. doi: 10.1002/aenm.201600551.

[224] Zhyrair Gevorkian, Vladimir Gasparian, and Yurii Lozovik. Large diffusion lengths of excitons in perovskite and TiO2 heterojunction. *Applied Physics Letters*, 108(5):15–17, 2016. ISSN 00036951. doi: 10.1063/1.4941242. URL http://dx.doi.org/10.1063/1.4941242.

[225] L. Forro, O. Chauvet, D. Emin, L. Zuppiroli, H. Berger, and F. Lévy. High mobility n-type charge carriers in large single crystals of anatase (TiO2). *Journal of Applied Physics*, 75(1):633–635, 1994. ISSN 00218979. doi: 10.1063/1.355801.

[226] E. Hendry, M. Koeberg, B. O'Regan, and M. Bonn. Local field effects on electron transport in nanostructured TiO2revealed by terahertz spectroscopy. *Nano Letters*, 6(4):755–759, 2006. ISSN 15306984. doi: 10.1021/nl0600225.

[227] Marine E F Bouduban, Fabrizio Giordano, Arnulf Rosspeintner, Joël Teuscher, Eric Vauthey, Michael Grätzel, and Jacques-E Moser. Inter-Domain Charge Transfer as a Rationale for Superior Photovoltaic Performances of Mixed Halide Lead Perovskites. *arXiv.org*, August 2018.

[228] Marine E F Bouduban, Andrés Burgos-Caminal, Rachele Ossola, Joël Teuscher, and Jacques-E Moser. Energy and charge transfer cascade in methylammonium lead bromide perovskite nanoparticle aggregates. *Chemical Science*, 8(6):4371–4380, May 2017.

[229] Yiling Song, Cong Zhang, Weiwei Liu, Xiaohong Li, Hua Long, Kai Wang, Bing Wang, and Peixiang Lu. High-efficiency energy transfer in perovskite heterostructures. *Optics Express*, 26(14):18448–18456, 2018.

[230] Le Quang Phuong, Yasuhiro Yamada, Masaya Nagai, Naoki Maruyama, Atsushi Wakamiya, and Yoshihiko Kanemitsu. Free Carriers versus Excitons in CH3NH3PbI3 Perovskite Thin Films at Low Temperatures: Charge Transfer from the Orthorhombic Phase to the Tetragonal Phase. *The Journal of Physical Chemistry Letters*, 7(13):2316–2321, June 2016.

[231] Brian O'Regan and Michael Grätzel. A low-cost, high-efficiency solar cell based on dye-sensitized colloidal TiO2 films. *Nature*, 353(6346):737–740, 1991.

[232] P L Washington, H C Ong, J Y Dai, and R P H Chang. Determination of the optical constants of zinc oxide thin films by spectroscopic ellipsometry. *Applied Physics Letters*, 72(25):3261–3263, June 1998.

[233] A B Djurišić, Y Chan, and E H Li. The optical dielectric function of ZnO. *Applied Physics A*, 76(1): 37–43, January 2003.

[234] Lubomir Spanhel and Marc A Anderson. Semiconductor clusters in the sol-gel process: quantized aggregation, gelation, and crystal growth in concentrated zinc oxide colloids. *Journal of the American Chemical Society*, 113(8):2826–2833, April 1991.

[235] Hong Ye, Philippe M Fauchet, S Mathukumar, and Yicheng Lu. Femtosecond spectroscopy in ZnO with tunable UV pulses. In *Ultrafast Phenomena in Semiconductors V*, 2001.

[236] Olivier Bräm, Fabrizio Messina, Ahmed M El-Zohry, Andrea Cannizzo, and Majed Chergui. Polychromatic femtosecond fluorescence studies of metal–polypyridine complexes in solution. *Chemical Physics*, 393(1):51–57, January 2012.

[237] Gerald Auböck and Majed Chergui. Sub-50-fs photoinduced spin crossover in [Fe(bpy)3]2+. *Nature Chemistry*, 7(8):1–5, July 2015.

[238] Akihiro Namekawa and Ryuzi Katoh. Exciton annihilation in dye-sensitized nanocrystalline semiconductor films. *Chemical Physics Letters*, 659(C):154–158, August 2016.

[239] A N Tarnovsky, W Gawelda, M Johnson, C Bressler, and M Chergui. Photexcitation of Aqueous Ruthenium(II)-tris-(2,2'-bipyridine) with High-Intensity Femtosecond Laser Pulses. *The Journal of Physical Chemistry B*, 110(51):26497–26505, December 2006.

[240] Marijn A M Versteegh, Tim Kuis, H T C Stoof, and Jaap I Dijkhuis. Ultrafast screening and carrier dynamics in ZnO: Theory and experiment. *Physical Review B*, 84(3):035207–19, July 2011.

[241] Noh Soo Han, Hyeong Seop Shim, Joo Hee Seo, Sun Young Kim, Seung Min Park, and Jae Kyu Song. Defect states of ZnO nanoparticles: Discrimination by time-resolved photoluminescence spectroscopy. *Journal of Applied Physics*, 107(8):084306, 2010.

[242] T Koida, S F Chichibu, A Uedono, A Tsukazaki, M Kawasaki, T Sota, Y Segawa, and H Koinuma. Correlation between the photoluminescence lifetime and defect density in bulk and epitaxial ZnO. *Applied Physics Letters*, 82(4):532–534, January 2003.

[243] C J Milne, J Szlachetko, T J Penfold, F Santomauro, A Britz, W Gawelda, G Doumy, A-M March, S H Southworth, J Rittmann, M Chergui, and R Abela. Time-resolved X-ray absorption and emission spectroscopy on ZnO nanoparticles in solution. In *19th International Conference on Ultrafast Phenomena*, page 09.Wed.D.1, Washington, D.C., 2014. OSA.

[244] Thomas J Penfold, Jakub Szlachetko, Fabio G Santomauro, Alexander Britz, Wojciech Gawelda, Gilles Doumy, Anne Marie March, Stephen H Southworth, Jochen Rittmann, Rafael Abela, Majed Chergui, and Christopher J Milne. Revealing hole trapping in zinc oxide nanoparticles by time-resolved X-ray spectroscopy. *Nature Communications*, 9(1):1–9, January 2018.

[245] Priti Tiwana, Pablo Docampo, Michael B Johnston, Henry J Snaith, and Laura M Herz. Electron Mobility and Injection Dynamics in Mesoporous ZnO, SnO2, and TiO2 Films Used in Dye-Sensitized Solar Cells. *ACS Nano*, 5(6):5158–5166, June 2011.

[246] David Stockwell, Ye Yang, Jier Huang, Chantelle Anfuso, Zhuangqun Huang, and Tianquan Lian. Comparison of Electron-Transfer Dynamics from Coumarin 343 to TiO2, SnO2, and ZnO Nanocrystalline Thin Films: Role of Interface-Bound Charge-Separated Pairs. *The Journal of Physical Chemistry C*, 114(14):6560–6566, April 2010.

[247] H Němec, J Rochford, O Taratula, E Galoppini, P Kužel, T Polívka, A Yartsev, and V Sundström. Influence of the Electron-Cation Interaction on Electron Mobility in Dye-Sensitized ZnO and TiO2 Nanocrystals: A Study Using Ultrafast Terahertz Spectroscopy. *Physical Review Letters*, 104 (19):197401–4, May 2010.

[248] Neil A Anderson, Xin Ai, and Tianquan Lian. Electron Injection Dynamics from Ru Polypyridyl Complexes to ZnO Nanocrystalline Thin Films. *The Journal of Physical Chemistry B*, 107(51): 14414–14421, December 2003.

[249] Akihiro Furube, Ryuzi Katoh, and Kohjiro Hara. Electron injection dynamics in dye-sensitized semiconductor nanocrystalline films. *Surface Science Reports*, 69(4):389–441, December 2014.

[250] John B Asbury, Encai Hao, Yongqiang Wang, Hirendra N Ghosh, and Tianquan Lian. Ultrafast Electron Transfer Dynamics from Molecular Adsorbates to Semiconductor Nanocrystalline Thin Films. *The Journal of Physical Chemistry B*, 105(20):4545–4557, May 2001.

[251] Katrin R Siefermann, Chaitanya D Pemmaraju, Stefan Neppl, Andrey Shavorskiy, Amy A Cordones, Josh Vura-Weis, Daniel S Slaughter, Felix P Sturm, Fabian Weise, Hendrik Bluhm, Matthew L Strader, Hana Cho, Ming-Fu Lin, Camila Bacellar, Champak Khurmi, Jinghua Guo, Giacomo Coslovich, Joseph S Robinson, Robert A Kaindl, Robert W Schoenlein, Ali Belkacem, Daniel M Neumark, Stephen R Leone, Dennis Nordlund, Hirohito Ogasawara, Oleg Krupin, Joshua J Turner, William F Schlotter, Michael R Holmes, Marc Messerschmidt, Michael P Minitti, Sheraz Gul, Jin Z Zhang, Nils Huse, David Prendergast, and Oliver Gessner. Atomic-Scale Perspective of Ultrafast Charge Transfer at a Dye–Semiconductor Interface. *The Journal of Physical Chemistry Letters*, 5 (15):2753–2759, 2014.

[252] Akihiro Furube, Ryuzi Katoh, Kohjiro Hara, Shigeo Murata, Hironori Arakawa, and M Tachiya. Ultrafast Stepwise Electron Injection from Photoexcited Ru-Complex into Nanocrystalline ZnO Film via Intermediates at the Surface. *The Journal of Physical Chemistry B*, 107(17):4162–4166, May 2003.

[253] Mario Borgwardt, Martin Wilke, Thorsten Kampen, Sven Mähl, Manda Xiao, Leone Spiccia, Kathrin M Lange, Igor Yu Kiyan, and Emad F Aziz. Charge Transfer Dynamics at Dye-Sensitized ZnO and TiO2 Interfaces Studied by Ultrafast XUV Photoelectron Spectroscopy. *Scientific Reports*, 6:1–7, April 2016.

[254] István Robel, Masaru Kuno, and Prashant V Kamat. Size-Dependent Electron Injection from Excited CdSe Quantum Dots into TiO2 Nanoparticles. *Journal of the American Chemical Society*, 129(14):4136–4137, April 2007.

[255] Lars Dworak, Sina Roth, and Josef Wachtveitl. Charge Transfer-Induced State Filling in CdSe Quantum Dot–Alizarin Complexes. *The Journal of Physical Chemistry C*, 121(5):2613–2619, 2017.

[256] R A Marcus and Norman Sutin. Electron transfers in chemistry and biology. *Biochimica et Biophysica Acta (BBA) - Reviews on Bioenergetics*, 811(3):265–322, 1985.

[257] R A Marcus. On the Theory of Electron-Transfer Reactions. VI. Unified Treatment for Homogeneous and Electrode Reactions. *The Journal of Chemical Physics*, 43(2):679–701, July 1965.

[258] Liang-Hong Guo, Shaul Mukamel, and George McLendon. Photophysical Probes of a Protein/Semiconductor Electrode Interface. *Journal of the American Chemical Society*, 117(1):546–547, January 1995.

[259] Andrea Listorti, Brian O'Regan, and James R Durrant. Electron Transfer Dynamics in Dye-Sensitized Solar Cells. *Chemistry of Materials*, 23(15):3381–3399, August 2011.

[260] Li-Hong Yu, Jing-Yu Xi, Kin Cheung Lo, Lucy Jane Antrobus, David Lee Phillips, and Wai Kin Chan. Transient Absorption of N719 and its Electron Transfer Kinetics on ZnO Nanoparticles Surface. *Journal of Inorganic and Organometallic Polymers and Materials*, 25(1):169–175, October 2014.

[261] John B Asbury, Yongqiang Wang, and Tianquan Lian. Multiple-Exponential Electron Injection in Ru(dcbpy)2(SCN)2 Sensitized ZnO Nanocrystalline Thin Films. *The Journal of Physical Chemistry B*, 103(32):6643–6647, August 1999.

[262] Anders Hagfeldt and Michael Graetzel. Light-Induced Redox Reactions in Nanocrystalline Systems. *Chemical reviews*, 95(1):49–68, January 1995.

[263] Christophe Bauer, Gerrit Boschloo, Emad Mukhtar, and Anders Hagfeldt. Electron Injection and Recombination in Ru(dcbpy)2(NCS)2 Sensitized Nanostructured ZnO. *The Journal of Physical Chemistry B*, 105(24):5585–5588, June 2001.

[264] Christian Strothkämper, Andreas Bartelt, Philipp Sippel, Thomas Hannappel, Robert Schütz, and Rainer Eichberger. Delayed Electron Transfer through Interface States in Hybrid ZnO/Organic-Dye Nanostructures. *The Journal of Physical Chemistry C*, 117(35):17901–17908, August 2013.

[265] Jodi M Szarko, Antje Neubauer, Andreas Bartelt, Liana Socaciu-Siebert, Frank Birkner, Klaus Schwarzburg, Thomas Hannappel, and Rainer Eichberger. The Ultrafast Temporal and Spectral Characterization of Electron Injection from Perylene Derivatives into ZnO and TiO2 Colloidal Films. *The Journal of Physical Chemistry C*, 112(28):10542–10552, June 2008.

[266] Akihiro Furube, Ryuzi Katoh, Toshitada Yoshihara, Kohjiro Hara, Shigeo Murata, Hironori Arakawa, and M Tachiya. Ultrafast Direct and Indirect Electron-Injection Processes in a Photoexcited Dye-Sensitized Nanocrystalline Zinc Oxide Film: The Importance of Exciplex Intermediates at the Surface. *The Journal of Physical Chemistry B*, 108(33):12583–12592, August 2004.

[267] Ryuzi Katoh, Akihiro Furube, Toshitada Yoshihara, Kohjiro Hara, Gaku Fujihashi, Shingo Takano, Shigeo Murata, Hironori Arakawa, and M Tachiya. Efficiencies of Electron Injection from Excited N3 Dye into Nanocrystalline Semiconductor (ZrO2, TiO2, ZnO, Nb 2O5, SnO2, In2O3) Films. *The Journal of Physical Chemistry B*, 108(15):4818–4822, April 2004.

[268] H Yoshikawa and S Adachi. Optical constants of ZnO. *Japanese Journal of Applied Physics*, 36(10):6237–6243, October 1997.

[269] Maofeng Dou and Clas Persson. Comparative study of rutile and anatase SnO2 and TiO2: Band-edge structures, dielectric functions, and polaron effects. *Journal of Applied Physics*, 113(8):083703–11, February 2013.

[270] R J Gonzalez, R Zallen, and H Berger. Infrared reflectivity and lattice fundamentals in anatase TiO2. *Physical Review B*, 55(11):7014–7017, 1997.

[271] T Busani and R A B Devine. Dielectric and infrared properties of TiO2 films containing anatase and rutile. *Semiconductor Science and Technology*, 20(8):870–875, July 2005.

[272] Hisashi Fukuda, Seigo Namioka, Miho Miura, Yoshihiro Ishikawa, Masaki Yoshino, and Shigeru Nomura. Structural and Electrical Properties of Crystalline TiO2 Thin Films Formed by Metalorganic Decomposition. *Japanese Journal of Applied Physics*, 38(Part 1, No. 10):6034–6038, 1999.

[273] Stefan Neppl, Andrey Shavorskiy, Ioannis Zegkinoglou, Matthew Fraund, Daniel S Slaughter, Tyler Troy, Michael P Ziemkiewicz, Musahid Ahmed, Sheraz Gul, Bruce Rude, Jin Z Zhang, Anton S Tremsin, Per-Anders Glans, Yi-Sheng Liu, Cheng Hao Wu, Jinghua Guo, Miquel Salmeron, Hendrik Bluhm, and Oliver Gessner. Capturing interfacial photoelectrochemical dynamics with picosecond time-resolved X-ray photoelectron spectroscopy. *Faraday Discussions*, 171:219–241, November 2014.

[274] Guangfen Wu, Zi Li, Xu Zhang, and Gang Lu. Charge Separation and Exciton Dynamics at Polymer/ZnO Interface from First-Principles Simulations. *The Journal of Physical Chemistry Letters*, 5(15):2649–2656, July 2014.

[275] K Virkki, E Tervola, M Ince, T Torres, and N V Tkachenko. Comparison of electron injection and recombination on TiO2 nanoparticles and ZnO nanorods photosensitized by phthalocyanine. *Royal Society Open Science*, 5(7):180323–10, July 2018.

[276] E. M. Kaidashev, M. Lorenz, H. Von Wenckstern, A. Rahm, H. C. Semmelhack, K. H. Han, G. Benndorf, C. Bundesmann, H. Hochmuth, and M. Grundmann. High electron mobility of epitaxial ZnO thin films on c-plane sapphire grown by multistep pulsed-laser deposition. *Applied Physics Letters*, 82(22):3901–3903, 2003. ISSN 00036951. doi: 10.1063/1.1578694.

[277] Tammy P. Chou, Qifeng Zhang, and Guozhong Cao. Effects of dye loading conditions on the energy conversion efficiency of ZnO and TiO2 dye-sensitized solar cells. *Journal of Physical Chemistry C*, 111(50):18804–18811, 2007. ISSN 19327447. doi: 10.1021/jp076724f.

[278] Th Dittrich, E. A. Lebedev, and J. Weidmann. Electron drift mobility in porous TiO2(anatase). *Physica Status Solidi (A) Applied Research*, 165(2), 1998. ISSN 00318965. doi: 10.1002/(SICI) 1521-396X(199802)165:2<R5::AID-PSSA99995>3.0.CO;2-9.

[279] Bin Ding, Shi-Yu Huang, Qian-Qian Chu, Yan Li, Chengxin Li, Changjiu Li, and Guan-Jun Yang. Low-temperature SnO2-modified TiO2 yields record efficiency for normal planar perovskite solar modules. *Journal of Materials Chemistry A: Materials for energy and sustainability*, 6(22): 10233–10242, 2018.

[280] Guanglan Liao, Zhiyong Liu, Bo Sun, Xingyue Liu, Jinghui Han, Haibo Ye, Yuxue Tu, Chen Chen, Tielin Shi, and Zirong Tang. 15cells using TiO2/SnO2 bilayer as electron transport layer. *Journal of Materials Chemistry A: Materials for energy and sustainability*, 6(17):7409–7419, 2018.

[281] M Hannelore Rittmann-Frank, Chris J Milne, Jochen Rittmann, Marco Reinhard, Thomas J Penfold, and Majed Chergui. Mapping of the Photoinduced Electron Traps in TiO2 by Picosecond X-ray Absorption Spectroscopy. *Angewandte Chemie International Edition*, 53(23):5858–5862, May 2014.

[282] F G Santomauro, A Lübcke, J Rittmann, E Baldini, A Ferrer, M Silatani, P Zimmermann, S Grübel, J A Johnson, S O Mariager, P Beaud, D Grolimund, C Borca, G Ingold, S L Johnson, and M Chergui. Femtosecond X-ray absorption study of electron localization in photoexcited anatase TiO2. *Scientific Reports*, 5:1–6, September 2015.

[283] Lalita Chauhan, A K Shukla, and K Sreenivas. Dielectric and magnetic properties of Nickel ferrite ceramics using crystalline powders derived from DL alanine fuel in sol–gel auto-combustion. *Ceramics International*, 41(7):8341–8351, August 2015.

[284] Yanan Wang, Xinjiang Cui, Youquan Deng, and Feng Shi. Catalytic hydrogenation of aromatic rings catalyzed by Pd/NiO. *RSC Adv.*, 4(6):2729–2732, 2014.

[285] Hai Yang Peng, Yong Feng Li, Wei Nan Lin, Yu Zhan Wang, Xing Yu Gao, and Tom Wu. Deterministic conversion between memory and threshold resistive switching via tuning the strong electron correlation. *Scientific Reports*, 2:1–6, June 2012.

[286] Congcong Zhao, Cheng Chen, Fanglin Du, and Jinmin Wang. Template synthesis of NiO ultrathin nanosheets using polystyrene nanospheres and their electrochromic properties. *RSC Adv.*, 5(48): 38533–38537, April 2015.

[287] D S Dalavi, N S Harale, I S Mulla, V K Rao, V B Patil, I Y Kim, J H Kim, and P S Patil. Nanoporous network of nickel oxide for ammonia gas detection. *Materials Letters*, 146(C):103–107, May 2015.

[288] H A Alperin. Neutron Diffraction Investigation of the Magnetic Structure of Nickel Oxide. *Journal of Applied Physics*, 31(5):S354, 1960.

[289] R Newman and R Chrenko. Optical Properties of Nickel Oxide. *Physical Review*, 114(6):1507–1513, June 1959.

[290] Jeffrey McKay and Victor Henrich. Structure of Valence and Conduction Levels in NiO. *Physical Review Letters*, 53(24):2343–2346, 1984.

[291] G Sawatzky and J Allen. Magnitude and Origin of the Band Gap in NiO. *Physical Review Letters*, 53(24):2339–2342, 1984.

[292] S Hüfner, P Steiner, I Sander, F Reinert, and H Schmitt. The optical gap of NiO. *Zeitschrift für Physik B Condensed Matter*, 86(2):207–215, June 1992.

[293] Z X Shen, C Shih, O Jepsen, W Spicer, I Lindau, and J Allen. Aspects of the correlation effects, antiferromagnetic order, and translational symmetry of the electronic structure of NiO and CoO. *Physical Review Letters*, 64(20):2442–2445, 1990.

[294] Z X Shen, R S List, D S Dessau, B O Wells, O Jepsen, A J Arko, R Barttlet, C K Shih, F Parmigiani, J C Huang, and PAP Lindberg. Electronic-Structure of NiO - Correlation and Band Effects. *Physical Review B*, 44(8):3604–3626, 1991.

[295] Atsushi Fujimori, Fujio Minami, and Satoru Sugano. Multielectron satellites and spin polarization in photoemission from Ni compounds. *Physical Review B*, 29(9):5225–5227, 1984.

[296] Atsushi Fujimori and Fujio Minami. Valence-band photoemission and optical absorption in nickel compounds. *Physical Review B*, 30(2):957–971, 1984.

[297] Roland Gillen and John Robertson. Accurate screened exchange band structures for the transition metal monoxides MnO, FeO, CoO and NiO. *Journal of Physics-Condensed Matter*, 25(16):165502–9, April 2013.

[298] O Bengone, M Alouani, P Blöchl, and J Hugel. Implementation of the projector augmented-wave LDA U method: Application to the electronic structure of NiO. *Physical Review B*, 62(24):16392–16401, 2000.

[299] Chi-Cheng Lee, H C Hsueh, and Wei Ku. Dynamical linear response of TDDFT with LDA+U functional: Strongly hybridized Frenkel excitons in NiO. *Physical Review B*, 82(8):081106–4, August 2010.

[300] Claudia Rödl and Friedhelm Bechstedt. Optical and energy-loss spectra of the antiferromagnetic transition metal oxides MnO, FeO, CoO, and NiO including quasiparticle and excitonic effects. *Physical Review B*, 86(23):235122, December 2012.

[301] Sergey V Faleev, Mark van Schilfgaarde, and Takao Kotani. All-Electron Self-Consistent GW Approximation: Application to Si, MnO, and NiO. *Physical Review Letters*, 93(12):126406–4, September 2004.

[302] X Ren, I Leonov, G Keller, M Kollar, I Nekrasov, and D Vollhardt. LDA+DMFT computation of the electronic spectrum of NiO. *Physical Review B*, 74(19):195114–8, November 2006.

[303] J Kuneš, V Anisimov, A Lukoyanov, and D Vollhardt. Local correlations and hole doping in NiO: A dynamical mean-field study. *Physical Review B*, 75(16):165115–4, April 2007.

[304] J Kuneš, V Anisimov, S Skornyakov, A Lukoyanov, and D Vollhardt. NiO: Correlated Band Structure of a Charge-Transfer Insulator. *Physical Review Letters*, 99(15):156404–4, October 2007.

[305] T Schuler, D Ederer, S Itza-Ortiz, G Woods, T Callcott, and J Woicik. Character of the insulating state in NiO: A mixture of charge-transfer and Mott-Hubbard character. *Physical Review B*, 71(11):115113, March 2005.

[306] J Zaanen, G A Sawatzky, and J W Allen. Band gaps and electronic structure of transition-metal compounds. *Physical Review Letters*, 55(4):418–421, July 1985.

[307] E E Salpeter and H A Bethe. A Relativistic Equation for Bound-State Problems. *Physical Review*, 84(6):1232–1242, 1951.

[308] N F Mott. The Basis of the Electron Theory of Metals, with Special Reference to the Transition Metals. *Proceedings of the Physical Society of London Section A*, 62(355):416–422, 1949.

[309] David Adler and Julius Feinleib. Electrical and optical properties of narrow-band materials. *Physical Review B-Solid State*, 2(8):3112–3134, 1970.

[310] H Ishii, Y Ishiwata, R Eguchi, and Y Harada. Resonant Soft X-Ray Emission Spectroscopy of NiO across the Ni L2, 3 Thresholds. *Journal of the Physical Society of Japan*, 70(6):1813–1816, 2001.

[311] Masahiko Matsubara, Takayuki Uozumi, Akio Kotani, and Jean Claude Parlebas. Charge Transfer Excitation in Resonant X-ray Emission Spectroscopy of NiO. *Journal of the Physical Society of Japan*, 74(7):2052–2060, July 2005.

[312] Je-Luen Li, G M Rignanese, and Steven G Louie. Quasiparticle energy bands of NiO in the GW approximation. *Physical Review B*, 71(19):193102, 2005.

[313] H Okamoto, T Miyagoe, K Kobayashi, H Uemura, H Nishioka, H Matsuzaki, A Sawa, and Y Tokura. Ultrafast charge dynamics in photoexcited Nd2CuO4 and La2CuO4 cuprate compounds investigated by femtosecond absorption spectroscopy. *Physical Review B*, 82(6):060513–4, August 2010.

[314] H Okamoto, T Miyagoe, K Kobayashi, H Uemura, H Nishioka, H Matsuzaki, A Sawa, and Y Tokura. Photoinduced transition from Mott insulator to metal in the undoped cuprates Nd2CuO4 and La2CuO4. *Physical Review B*, 83(12):125102–10, March 2011.

[315] Fabio Novelli, Vittorio Cataudella, Martina Esposito, Ignacio Vergara, Federico Cilento, Enrico Sindici, Adriano Amaricci, Claudio Giannetti, Dharmalingam Prabhakaran, Simon Wall, Andrea Perucchi, Stefano Dal Conte, Giulio Cerullo, Massimo Capone, Andrey Mishchenko, Markus Gr uuml ninger, Naoto Nagaosa, Fulvio Parmigiani, Giulio De Filippis, and Daniele Fausti. Witnessing the formation and relaxation of dressed quasi-particles in a strongly correlated electron system. *Nature Communications*, 5:1–8, September 2014.

[316] S Dal Conte, L Vidmar, D Golez, M Mierzejewski, G Soavi, S Peli, F Banfi, G Ferrini, R Comin, B M Ludbrook, L Chauviere, N D Zhigadlo, H Eisaki, M Greven, S Lupi, A Damascelli, D Brida, M Capone, J Bonca, G Cerullo, and C Giannetti. Snapshots of the retarded interaction of charge carriers with ultrafast fluctuations in cuprates. *Nature Physics*, 11(5):421–426, March 2015.

[317] Denis Golež, Martin Eckstein, and Philipp Werner. Dynamics of screening in photodoped Mott insulators. *Physical Review B*, 92(19):195123–17, November 2015.

[318] Wang Jifang, E S Fisher, and M H Manghnzmi. Elastic Constants of Nickel Oxide. *Chinese Physics Letters*, 8(3):153–156, April 2009.

[319] L Huber, A Ferrer, T Kubacka, T Huber, and C Dornes. Coherent acoustic perturbation of second-harmonic generation in NiO. *Physical Review B*, 92(9):094304, 2015.

[320] M R Notis, R M Spriggs, and W C Hahn. Elastic Moduli of Pressure-Sintered Nickel Oxide. *Journal of Geophysical Research*, 76(29):7052–&, 1971.

[321] T Miyamoto, Y Matsui, T Terashige, T Morimoto, N Sono, H Yada, S Ishihara, Y Watanabe, S Adachi, T Ito, K Oka, A Sawa, and H Okamoto. Probing ultrafast spin-relaxation and precession dynamics in a cuprate Mott insulator with seven-femtosecond optical pulses. *Nature Communications*, 9 (1):3948, September 2018.

[322] Claudio Giannetti, Massimo Capone, Daniele Fausti, Michele Fabrizio, Fulvio Parmigiani, and Dragan Mihailovic. Ultrafast optical spectroscopy of strongly correlated materials and high-temperature superconductors: a non-equilibrium approach. *Advances in Physics*, 65(2):58–238, July 2016.

[323] Andreas Mann, Edoardo Baldini, Antonio Tramontana, Ekaterina Pomjakushina, Kazimierz Conder, Christopher Arrell, Frank van Mourik, José Lorenzana, and Fabrizio Carbone. Probing the electron-phonon interaction in correlated systems with coherent lattice fluctuation spectroscopy. *Physical Review B*, 92(3):035147–8, July 2015.

[324] Edoardo Baldini, Andreas Mann, Simone Borroni, Christopher Arrell, Frank van Mourik, and Fabrizio Carbone. A versatile setup for ultrafast broadband optical spectroscopy of coherent collective modes in strongly correlated quantum systems. *Structural Dynamics*, 3(6):064301–12, November 2016.

[325] J Pattanayak and K D Becker. On the Temperature-Dependence of the Optical-Absorption Edge in Nickel-Oxide. *Physica Status Solidi B-Basic Solid State Physics*, 188(2):833–842, April 1995.

[326] Yuki Obara, Hironori Ito, Terumasa Ito, Naoya Kurahashi, Stephan Thürmer, Hiroki Tanaka, Tetsuo Katayama, Tadashi Togashi, Shigeki Owada, Yo-ichi Yamamoto, Shutaro Karashima, Junichi Nishitani, Makina Yabashi, Toshinori Suzuki, and Kazuhiko Misawa. Femtosecond time-resolved X-ray absorption spectroscopy of anatase TiO2 nanoparticles using XFEL. *Structural Dynamics*, 4(4):044033–19, July 2017.

[327] Sai Bai, Motao Cao, Yizheng Jin, Xinliang Dai, Xiaoyong Liang, Zhizhen Ye, Min Li, Jipeng Cheng, Xuezhang Xiao, Zhongwei Wu, Zhouhui Xia, Baoquan Sun, Ergang Wang, Yueqi Mo, Feng Gao, and Fengling Zhang. Low-Temperature Combustion-Synthesized Nickel Oxide Thin Films as Hole-Transport Interlayers for Solution-Processed Optoelectronic Devices. *Advanced Energy Materials*, 4(6):1301460–6, November 2013.

[328] Jong H Kim, Po-Wei Liang, Spencer T Williams, Namchul Cho, Chu-Chen Chueh, Micah S Glaz, David S Ginger, and Alex K Y Jen. High-Performance and Environmentally Stable Planar Heterojunction Perovskite Solar Cells Based on a Solution-Processed Copper-Doped Nickel Oxide Hole-Transporting Layer. *Advanced Materials*, 27(4):695–701, November 2014.

[329] Jesse R Manders, Sai-Wing Tsang, Michael J Hartel, Tzung-Han Lai, Song Chen, Chad M Amb, John R Reynolds, and Franky So. Solution-Processed Nickel Oxide Hole Transport Layers in High Efficiency Polymer Photovoltaic Cells. *Advanced Functional Materials*, 23(23):2993–3001, January 2013.

[330] Jun-Yuan Jeng, Kuo-Cheng Chen, Tsung-Yu Chiang, Pei-Ying Lin, Tzung-Da Tsai, Yun-Chorng Chang, Tzung-Fang Guo, Peter Chen, Ten-Chin Wen, and Yao-Jane Hsu. Nickel Oxide Electrode Interlayer in CH3NH3PbI3 Perovskite/PCBM Planar-Heterojunction Hybrid Solar Cells. *Advanced Materials*, 26(24):4107–4113, March 2014.

[331] Shogo Mori, Shunya Fukuda, Seiichi Sumikura, Yoshihiro Takeda, Yoshiaki Tamaki, Eiji Suzuki, and Takao Abe. Charge-Transfer Processes in Dye-Sensitized NiO Solar Cells. *The Journal of Physical Chemistry C*, 112(41):16134–16139, September 2008.

[332] Long Hu, Jun Peng, Weiwei Wang, Zhe Xia, Jianyu Yuan, Jialing Lu, Xiaodong Huang, Wanli Ma, Huaibing Song, Wei Chen, Yi-Bing Cheng, and Jiang Tang. Sequential Deposition of CH3NH3PbI3 on Planar NiO Film for Efficient Planar Perovskite Solar Cells. *ACS Photonics*, 1(7):547–553, July 2014.

[333] Kuo-Chin Wang, Po-Shen Shen, Ming-Hsien Li, Shi Chen, Ming-Wei Lin, Peter Chen, and Tzung-Fang Guo. Low-Temperature Sputtered Nickel Oxide Compact Thin Film as Effective Electron Blocking Layer for Mesoscopic NiO/CH3NH3PbI3 Perovskite Heterojunction Solar Cells. *ACS Applied Materials & Interfaces*, 6(15):11851–11858, July 2014.

[334] Stefan Hüfner. *Photoelectron Spectroscopy*, volume 82 of *Principles and Applications*. Springer Science & Business Media, Berlin, Heidelberg, November 2013.

Bibliography

[335] B.H. Brandow. Electronic structure of mott insulators. *Advances in Physics*, 26(5):651–808, 1977. doi: 10.1080/00018737700101443. URL https://doi.org/10.1080/00018737700101443.

[336] K Terakura, T Oguchi, A R Williams, and J Kübler. Band theory of insulating transition-metal monoxides: Band-structure calculations. *Physical Review B*, 30(8):4734–4747, 1984.

[337] K Terakura, A R Williams, T Oguchi, and J Kubler. Transition-Metal Monoxides: Band or Mott Insulators. *Physical Review Letters*, 52(20):1830–1833, January 1984.

[338] D E Eastman and J L Freeouf. Photoemission Partial State Densities of Overlapping p and d States for NiO, CoO, FeO, MnO, and Cr2O3. *Physical Review Letters*, 34(7):395–398, 1975.

[339] M Taguchi, M Matsunami, Y Ishida, R Eguchi, A Chainani, Y Takata, M Yabashi, K Tamasaku, Y Nishino, T Ishikawa, Y Senba, H Ohashi, and S Shin. Revisiting the Valence-Band and Core-Level Photoemission Spectra of NiO. *Physical Review Letters*, 100(20):206401–4, May 2008.

[340] J Weinen, T C Koethe, C F Chang, S Agrestini, D Kasinathan, Y F Liao, H Fujiwara, C Schüßler-Langeheine, F Strigari, T Haupricht, G Panaccione, F Offi, G Monaco, S Huotari, K D Tsuei, and L H Tjeng. Polarization dependent hard X-ray photoemission experiments for solids: Efficiency and limits for unraveling the orbital character of the valence band. *Journal of Electron Spectroscopy and Related Phenomena*, 198:6–11, January 2015.

[341] S Billinge, Th Proffen, V Petkov, and J Sarrao. Evidence for charge localization in the ferromagnetic phase of La1-xCaxMnO3 from high real-space-resolution x-ray diffraction. *Physical Review B - Condensed Matter and Materials Physics*, 62(2):1203–1211, January 2000.

[342] Peter Baum, Ding Shyue Yang, and Ahmed H Zewail. 4D visualization of transitional structures in phase transformations by electron diffraction. *Science*, 318(5851):788–792, November 2007.

[343] Ding Shyue Yang, Changshi Lao, and Ahmed H Zewail. 4D electron diffraction reveals correlated unidirectional behavior in zinc oxide nanowires. *Science*, 321(5896):1660–1664, September 2008.

[344] W S Lee, Y D Chuang, R G Moore, and Y Zhu. Phase fluctuations and the absence of topological defects in a photo-excited charge-ordered nickelate. *Nature Communications*, 3:838, 2012. doi: 10.1038/ncomms1837. URL http://www.nature.com/ncomms/journal/v3/n5/abs/ncomms1837.html.

[345] Jacinto Sa, Yves Kayser, Christopher J Milne, Daniel Luis Abreu Fernandes, and Jakub Szlachetko. Temperature-programmed reduction of NiO nanoparticles followed by time-resolved RIXS. *Physical Chemistry Chemical Physics*, 16(17):7692–7696, April 2014.

[346] M A van Veenendaal and G A Sawatzky. Doping dependence of Ni 2p x-ray-absorption spectra of MxNi1-xO (M=Li,Na). *Physical Review B*, 50(16):11326–11331, 1994.

[347] G van der Laan, J Zaanen, G A Sawatzky, R Karnatak, and J M Esteva. Comparison of x-ray absorption with x-ray photoemission of nickel dihalides and NiO. *Physical Review B*, 33(6):4253–4263, 1986.

[348] A Kuzmin, N Mironova, and J Purans. The influence of pd mixing and magnetic interactions on the pre-edge peak intensity at the Co (Ni) K absorption edge in solid solutions. *Journal of Physics: Condensed Matter*, 9(24):5277–5286, January 1999.

[349] J García, J Blasco, M G Proietti, and M Benfatto. Analysis of the x-ray-absorption near-edge-structure spectra of La1-xNdxNiO3 and LaNi1-xFexO3 perovskites at the nickel K edge. *Physical Review B*, 52(22):15823–15828, December 1995.

[350] L A Grunes. Study of the K edges of 3d transition metals in pure and oxide form by x-ray-absorption spectroscopy. *Physical Review B*, 27(4):2111–2131, February 1983.

[351] Frank de Groot, Gyorgy Vanko, and Pieter Glatzel. The 1s x-ray absorption pre-edge structures in transition metal oxides. *Journal of Physics: Condensed Matter*, 21(10):104207–8, February 2009.

[352] P Le Fevre, H Magnan, D Chandesris, J Jupille, S Bourgeois, A Barbier, W Drube, T Uozumi, and A Kotani. Hard X-ray resonant electronic spectroscopy in transition metal oxides. *Nuclear Instruments and Methods in Physics Research Section A: Accelerators, Spectrometers, Detectors and Associated Equipment*, 547(1):176–186, July 2005.

[353] J P Hill, C C Kao, and D F McMorrow. K-edge resonant x-ray magnetic scattering from a transition-metal oxide: NiO. *Physical Review B*, 55(14):R8662–R8665, April 1997.

[354] S J Li, Z Y Wu, T D Hu, Y N Xie, J Zhang, T Liu, C R Natoli, E Paris, and A Marcelli. A study of the pre-edge X-ray absorption fine structures in Ni monoxide. *Physica Scripta*, T115:223–225, 2005.

[355] D Norman, K B Garg, and P J Durham. The X-ray Absorption Near Edge Structure of transition metal oxides: A one-electron interpretation. *Solid State Communications*, 56(10):895–898, 1985.

[356] Farrel W Lytle, Robert B Greegor, and Armand J Panson. Discussion of x-ray-absorption near-edge structure: Application to Cu in the high-Tc superconductors La1.8Sr0.2CuO4 and YBa2Cu3O7. *Physical Review B*, 37(4):1550–1562, February 1988.

[357] Peter Kizler. X-ray-absorption near-edge structure spectra for bulk materials: Multiple-scattering analysis versus a phenomenological approach. *Physical Review B*, 46(17):10540–10546, November 1992.

[358] A Kuzmin, J Purans, and A Rodionov. X-ray absorption spectroscopy study of the Ni K edge in magnetron-sputtered nickel oxide thin films. *Journal of Physics: Condensed ...*, 9(32):6979–6993, 1997.

[359] A Kuzmin, J Purans, and R Kalendarev. Ab initio calculations of the Ni K-edge XANES in NicMg1-cO solid solutions. *physica status solidi (c)*, 2(1):665–668, January 2005.

[360] H Modrow, S Bucher, J J Rehr, and A L Ankudinov. Calculation and interpretation of K-shell x-ray absorption near-edge structure of transition metal oxides. *Physical Review B*, 67(3):035123–10, January 2003.

[361] S Hüfner and T Riesterer. Electronic structure of NiO. *Physical Review B*, 33(10):7267–7269, 1986.

[362] M Calandra, J P Rueff, C Gougoussis, D Céolin, M Gorgoi, S Benedetti, P Torelli, A Shukla, D Chandesris, and Ch Brouder. K-edge x-ray absorption spectra in transition-metal oxides beyond the single-particle approximation: Shake-up many-body effects. *Physical Review B*, 86 (16):165102–6, October 2012.

[363] E Klevak, J J Kas, and J J Rehr. Charge transfer satellites in x-ray spectra of transition metal oxides. *Physical Review B*, 89(8):085123–7, February 2014.

Bibliography

[364] J C Woicik, J M Ablett, N F Quackenbush, A K Rumaiz, C Weiland, T C Droubay, and S A Chambers. Experimental assignment of many-electron excitations in the photoionization of NiO. *Physical Review B*, 97:245142, June 2018.

[365] Per Olov Löwdin. On the Non-Orthogonality Problem Connected with the Use of Atomic Wave Functions in the Theory of Molecules and Crystals. *The Journal of Chemical Physics*, 18(3): 365–375, March 1950.

[366] Ashish Chhaganlal Gandhi, Jayashree Pant, Swarada D Pandit, Sunanda K Dalimbkar, Ting-Shan Chan, Chia-Ling Cheng, Yuan-Ron Ma, and Sheng Yun Wu. Short-Range Magnon Excitation in NiO Nanoparticles. *The Journal of Physical Chemistry C*, 117(36):18666–18674, August 2013.

[367] Majed Chergui. Time-resolved X-ray spectroscopies of chemical systems: New perspectives. *Structural Dynamics*, 3(3):031001–13, May 2016.

[368] Yves Joly, Delphine Cabaret, Hubert Renevier, and Calogero R Natoli. Electron Population Analysis by Full-Potential X-Ray Absorption Simulations. *Physical Review Letters*, 82(11):2398–2401, March 1999.

[369] Y Joly. X-ray absorption near-edge structure calculations beyond the muffin-tin approximation. *Physical Review B*, 63(12):111–10, March 2001.

[370] Florian Pielmeier and Franz J Giessibl. Spin Resolution and Evidence for Superexchange on NiO(001) Observed by Force Microscopy. *Physical Review Letters*, 110(26):266101–5, June 2013.

[371] J A Dawson, Y Guo, and J Robertson. Energetics of intrinsic defects in NiO and the consequences for its resistive random access memory performance. *Applied Physics Letters*, 107(12):122110, September 2015.

[372] Françoise Hippert, Erik Geissler, Jean Louis Hodeau, Eddy Lelièvre-Berna, and Jean-René Regnard. *Neutron and X-ray Spectroscopy*. Springer Science & Business Media, July 2006.

[373] Jeroen A van Bokhoven and Carlo Lamberti. *X-Ray Absorption and X-Ray Emission Spectroscopy*. Theory and Applications. John Wiley & Sons, March 2016.

[374] P. Debye. Interferenz von röntgenstrahlen und wärmebewegung. *Annalen der Physik*, 348(1): 49–92, 1913. doi: 10.1002/andp.19133480105. URL https://onlinelibrary.wiley.com/doi/abs/10.1002/andp.19133480105.

[375] Ivar Waller. Zur Frage der Einwirkung der Wärmebewegung auf die Interferenz von Röntgen-strahlen. *Zeitschrift für Physik*, 17(1):398–408, December 1923.

[376] G Dalba and P Fornasini. EXAFS Debye - Waller factor and thermal vibrations of crystals. *Journal of Synchrotron Radiation*, 4(4):243–255, July 1997.

[377] J D Bourke, C T Chantler, and Y Joly. FDMX: extended X-ray absorption fine structure calculations using the finite difference method. *Journal of Synchrotron Radiation*, 23(2):551–559, February 2016.

[378] Hungru Chen and John H Harding. Nature of the hole states in Li-doped NiO. *Physical Review B*, 85(11):115127, 2012.

[379] J B Goodenough, D G Wickham, and W J Croft. Some magnetic and crystallographic properties of the system Li+xNi++1−2xni+++xO. *Journal of Physics and Chemistry of Solids*, 5(1-2):107–116, January 1958.

[380] Ingrid J Pickering, Graham N George, Joseph T Lewandowski, and Allan J Jacobson. Nickel K-edge x-ray absorption fine structure of lithium nickel oxides. *Journal of the American Chemical Society*, 115(10):4137–4144, 1993.

[381] W C Mackrodt, N M Harrison, V R Saunders, N L Allan, and M D Towler. Direct evidence of O(p) holes in Li-doped NiO from Hartree-Fock calculations. *Chemical Physics Letters*, 250(1):66–70, February 1996.

[382] W C Mackrodt and D S Middlemiss. A hybrid Hartree–Fock density functional theory study of Li xNi 1 xO. *Journal of Physics: Condensed Matter*, 16(27):S2811–S2825, June 2004.

[383] P Kuiper, G Kruizinga, J Ghijsen, G A Sawatzky, and H Verweij. Character of Holes in LixNi1−xO and Their Magnetic Behavior. *Physical Review Letters*, 62(10):1214–1214, 1989.

[384] Fabien Tran, Peter Blaha, Karlheinz Schwarz, and Pavel Novák. Hybrid exchange-correlation energy functionals for strongly correlated electrons: Applications to transition-metal monoxides. *Physical Review B*, 74(15):171–10, October 2006.

[385] I G Austin, A J Springth, and B A Smith. Hopping and Narrow-Band Polaron Conduction in NiO and CoO. *Physics Letters*, 21(1):20–22, 1966.

[386] I G Austin, B D Clay, and C E Turner. Optical absorption of small polarons in semiconducting NiO and CoO in the near and far infra-red. *Journal of Physics C: Solid State Physics*, 1(5):1418–1434, October 1968.

[387] V I Sokolov, V A Pustovarov, V N Churmanov, V Yu Ivanov, N B Gruzdev, P S Sokolov, A N Baranov, and A S Moskvin. Unusual x-ray excited luminescence spectra of NiO suggest self-trapping of the d-d charge-transfer exciton. *Physical Review B*, 86(11):1884–10, September 2012.

[388] J A Aramburu, P García Fernández, M T Barriuso, and M Moreno. Big off-center displacements of ions in insulators: The Jahn-Teller ion Ni+ in CaF2. *Physical Review B*, 67(2):1–4, January 2003.

[389] Rajdeep Sensarma, David Pekker, Ehud Altman, Eugene Demler, Niels Strohmaier, Daniel Greif, Robert Jördens, Leticia Tarruell, Henning Moritz, and Tilman Esslinger. Lifetime of double occupancies in the Fermi-Hubbard model. *Physical Review B*, 82(22):224302–16, December 2010.

[390] Philipp Werner and Martin Eckstein. Effective doublon and hole temperatures in the photo-doped dynamic Hubbard model. *Structural Dynamics*, 3(2):023603–13, March 2016.

[391] G Wellein, H Röder, and H Fehske. Polarons and bipolarons in strongly interacting electron-phonon systems. *Physical Review B*, 53(15):9666–9675, 1996.

[392] D Muñoz Ramo, A L Shluger, J L Gavartin, and G Bersuker. Theoretical Prediction of Intrinsic Self-Trapping of Electrons and Holes in Monoclinic HfO2. *Physical Review Letters*, 99(15):277–4, October 2007.

[393] Sharareh Sayyad and Martin Eckstein. Coexistence of excited polarons and metastable delocalized states in photoinduced metals. *Physical Review B*, 91(10):644–13, March 2015.

[394] Kazuya Shinjo and Takami Tohyama. Photoinduced absorptions inside the Mott gap in the two-dimensional extended Hubbard model. *Physical Review B*, 96(19):195141–6, November 2017.

[395] Rafael Abela, Paul Beaud, Jeroen A van Bokhoven, Majed Chergui, Thomas Feurer, Johannes Haase, Gerhard Ingold, Steven L Johnson, Gregor Knopp, Henrik Lemke, Chris J Milne, Bill Pedrini, Peter Radi, Gebhard Schertler, Jörg Standfuss, Urs Staub, and Luc Patthey. Perspective: Opportunities for ultrafast science at SwissFEL. *Structural Dynamics*, 4(6):061602–26, November 2017.

[396] Daniel I Khomskii. *Basic Aspects of the Quantum Theory of Solids*. Order and Elementary Excitations. Cambridge University Press, September 2010.

[397] Marina Freitag, Joël Teuscher, Yasemin Saygili, Xiaoyu Zhang, Fabrizio Giordano, Paul Liska, Jianli Hua, Shaik M Zakeeruddin, Jacques-E Moser, Michael Grätzel, and Anders Hagfeldt. Dye-sensitized solar cells for efficient power generation under ambient lighting. *Nature Photonics*, 11 (6):372–378, 2017.

[398] Kazuya Nakata and Akira Fujishima. TiO2 photocatalysis: Design and applications. *Journal of Photochemistry & Photobiology, C: Photochemistry Reviews*, 13(3):169–189, 2012.

[399] K Suenaga, M Tencé, C Mory, C Colliex, H Kato, T Okazaki, H Shinohara, K Hirahara, S Bandow, and S Iijima. Element-Selective Single Atom Imaging. *Science*, 290(5500):2280–2282, December 2000.

[400] Jacob F Sherson, Christof Weitenberg, Manuel Endres, Marc Cheneau, Immanuel Bloch, and Stefan Kuhr. Single-atom-resolved fluorescence imaging of an atomic Mott insulator. *Nature*, 467(7311):68–72, February 2010.

[401] C J Milne, T J Penfold, and M Chergui. Recent experimental and theoretical developments in time-resolved X-ray spectroscopies. *Coordination Chemistry Reviews*, 277-278:44–68, October 2014.

[402] Christian Brouder, Delphine Cabaret, Amélie Juhin, and Philippe Sainctavit. Effect of atomic vibrations on the x-ray absorption spectra at the Kedge of Al in α-Al2O3 and of Ti in TiO2 rutile. *Physical Review B*, 81(11):432–6, March 2010.

[403] Vittorio Luca. Comparison of Size-Dependent Structural and Electronic Properties of Anatase and Rutile Nanoparticles. *The Journal of Physical Chemistry C*, 113(16):6367–6380, 2009.

[404] R Brydson, H Sauer, W Engel, J M Thomass, E Zeitler, N Kosugi, and H Kuroda. Electron energy loss and X-ray absorption spectroscopy of rutile and anatase: a test of structural sensitivity. *Journal of Physics: Condensed Matter*, 1(4):797–812, January 1999.

[405] T Uozumi, K Okada, A Kotani, O Durmeyer, J P Kappler, E Beaurepaire, and J C Parlebas. Experimental and Theoretical Investigation of the Pre-Peaks at the Ti K-Edge Absorption-Spectra in TiO2. *EPL (Europhysics Letters)*, 18(1):85–90, 1992.

[406] Z Y Wu, G Ouvrard, P Gressier, and C R Natoli. Ti and O K edges for titanium oxides by multiple scattering calculations: Comparison to XAS and EELS spectra. *Physical Review B*, 55(16):10382–10391, April 1997.

[407] David W Fischer. X-Ray Band Spectra and Molecular-Orbital Structure of Rutile TiO2. *Physical Review B*, 5(11):4219–4226, June 1972.

[408] M F Ruiz-Lopez and A Munoz-Paez. A theoretical study of the XANES spectra of rutile and anatase. *Journal of Physics: Condensed Matter*, 3(45):8981–8990, 1991.

[409] F Farges, G E Brown, and J J Rehr. Ti K-edge XANES studies of Ti coordination and disorder in oxide compounds: Comparison between theory and experiment. *Physical Review B*, 56(4): 1809–1819, 1997.

[410] C A Triana, C Moyses Araujo, R Ahuja, G A Niklasson, and T Edvinsson. Electronic transitions induced by short-range structural order in amorphous TiO2. *Physical Review B*, 94(16):165129–9, October 2016.

[411] Takashi Yamamoto. Assignment of pre-edge peaks in K-edge x-ray absorption spectra of 3d transition metal compounds: electric dipole or quadrupole? *X-Ray Spectrometry*, 37(6):572–584, November 2008.

[412] Delphine Cabaret, Amélie Bordage, Amélie Juhin, Mounir Arfaoui, and Emilie Gaudry. First-principles calculations of X-ray absorption spectra at the K-edge of 3d transition metals: an electronic structure analysis of the pre-edge. *Physical Chemistry Chemical Physics*, 12(21):5619–17, 2010.

[413] Lin X Chen, Tijana Rajh, Zhiyu Wang, and Marion C Thurnauer. XAFS Studies of Surface Structures of TiO2 Nanoparticles and Photocatalytic Reduction of Metal Ions. *The Journal of Physical Chemistry B*, 101(50):10688–10697, 1997.

[414] Vittorio Luca, Samitha Djajanti, and Russell F Howe. Structural and Electronic Properties of Sol–Gel Titanium Oxides Studied by X-ray Absorption Spectroscopy. *The Journal of Physical Chemistry B*, 102(52):10650–10657, December 1998.

[415] Tracey L Hanley, Victor Luca, Ingrid Pickering, and Russell F Howe. Structure of Titania Sol–Gel Films: A Study by X-Ray Absorption Spectroscopy. *The Journal of Physical Chemistry B*, 106(6): 1153–1160, February 2002.

[416] Hengzhong Zhang, Bin Chen, Jillian F Banfield, and Glenn A Waychunas. Atomic structure of nanometer-sized amorphous TiO2. *Physical Review B*, 78(21):528–12, December 2008.

[417] Y Joly, O Bunău, J E Lorenzo, R M Galéra, S Grenier, and B Thompson. Self-consistency, spin-orbit and other advances in the FDMNES code to simulate XANES and RXD experiments. *Journal of Physics: Conference Series*, 190(1):012007–13, November 2009.

[418] N F M Henry and K Lonsdale. *International Tables for X-ray Crystallography*, volume 1. The Kynoch Press, 1969.

[419] C Brouder, J P Kappler, and E Beaurepaire. Theory and application of angle resolved X-ray absorption spectra. *Conference Proceedings - 2nd European Conference on Progress in X-ray Synchrotron Radiation Research*, 25:19–22, 1990.

[420] B.L. Henke, E.M. Gullikson, and J.C. Davis. X-ray interactions: Photoabsorption, scattering, transmission, and reflection at e = 50-30,000 ev, z = 1-92. *Atomic Data and Nuclear Data Tables*, 54(2):181 – 342, 1993. ISSN 0092-640X. doi: https://doi.org/10.1006/adnd.1993.1013. URL http://www.sciencedirect.com/science/article/pii/S0092640X83710132.

Bibliography

[421] R Carboni, S Giovannini, G Antonioli, and F Boscherini. Self-absorption correction strategy for fluorescence-yield soft x-ray near edge spectra. *Physica Scripta*, 2005(T115):986, 2005.

[422] L Hedin and B I Lundqvist. Explicit local exchange-correlation potentials. *Journal of Physics C: Solid State Physics*, 4(14):2064–2083, March 2001.

[423] C Brouder. Angular dependence of X-ray absorption spectra. *Journal of Physics: Condensed Matter*, 2(3):701–738, 1990.

[424] Christian Brouder, Amélie Juhin, Amélie Bordage, and Marie-Anne Arrio. Site symmetry and crystal symmetry: a spherical tensor analysis. *Journal of Physics: Condensed Matter*, 20(45): 455205–16, October 2008.

[425] K Matsuda, I Hirabayashi, K Kawamoto, T Nabatame, T Tokizaki, and A Nakamura. Femtosecond Spectroscopic Studies of the Ultrafast Relaxation Process in the Charge-Transfer State of Insulating Cuprates. *Physical Review B*, 50(6):4097–4101, 1994.

[426] Daniel C Ratchford, Adam D Dunkelberger, Igor Vurgaftman, Jeffrey C Owrutsky, and Pehr E Pehrsson. Quantification of Efficient Plasmonic Hot-Electron Injection in Gold Nanoparticle–TiO2 Films. *Nano Letters*, 17(10):6047–6055, September 2017.

[427] N Hosaka, T Sekiya, and S Kurita. Excitonic state in anatase TiO2 single crystal. *Journal of Luminescence*, 72-4:874–875, June 1997.

[428] C P Saini, A Barman, D Banerjee, O Grynko, S Prucnal, M Gupta, D M Phase, A K Sinha, D Kanjilal, W Skorupa, and A Kanjilal. Impact of Self-Trapped Excitons on Blue Photoluminescence in TiO2 Nanorods on Chemically Etched Si Pyramids. *The Journal of Physical Chemistry C*, 121(21): 11448–11454, May 2017.

[429] H Tang, K Prasad, R Sanjinès, P E Schmid, and F Lévy. Electrical and optical properties of TiO2 anatase thin films. *Journal of Applied Physics*, 75(4):2042–2047, February 1994.

[430] H Tang, F Lévy, H Berger, and P E Schmid. Urbach tail of anatase TiO2. *Physical Review B*, 52(11): 7771–7774, September 1995.

[431] M Watanabe and T Hayashi. Time-resolved study of self-trapped exciton luminescence in anatase TiO2 under two-photon excitation. *Journal of Luminescence*, 112(1-4):88–91, April 2005.

[432] Giulia Grancini, Guglielmo Lanzani, and Aron Walsh. Role of microstructure in the electron–hole interaction of hybrid lead halide perovskites. *Nature Photonics*, 9(10):695–701, 2015.

[433] Ajay Ram Srimath Kandada and Annamaria Petrozza. Photophysics of Hybrid Lead Halide Perovskites: The Role of Microstructure. *Accounts of Chemical Research*, 49(3):536–544, March 2016.

[434] Zhen-Yu Zhang, Hai-Yu Wang, Yan-Xia Zhang, Ya-Wei Hao, Chun Sun, Yu Zhang, Bing-Rong Gao, Qi-Dai Chen, and Hong-Bo Sun. The Role of Trap-assisted Recombination in Luminescent Properties of Organometal Halide CH3NH3PbBr3 Perovskite Films and Quantum Dots. *Scientific reports*, 6(1):1–7, May 2016.

[435] Feng Zhang, Haizheng Zhong, Cheng Chen, Xian-gang Wu, Xiangmin Hu, Hailong Huang, Junbo Han, Bingsuo Zou, and Yuping Dong. Brightly Luminescent and Color-Tunable Colloidal CH3NH3PbX3(X = Br, I, Cl) Quantum Dots: Potential Alternatives for Display Technology. *ACS Nano*, 9(4):4533–4542, February 2015.

[436] Nicola Sestu, Michele Cadelano, Valerio Sarritzu, Feipeng Chen, Daniela Marongiu, Roberto Piras, Marina Mainas, Francesco Quochi, Michele Saba, Andrea Mura, and Giovanni Bongiovanni. Absorption F-Sum Rule for the Exciton Binding Energy in Methylammonium Lead Halide Perovskites. *The Journal of Physical Chemistry Letters*, 6(22):4566–4572, October 2015.

[437] Yasuhiro Yamada, Takumi Yamada, and Yoshihiko Kanemitsu. Free Carrier Radiative Recombination and Photon Recycling in Lead Halide Perovskite Solar Cell Materials. *Bulletin of the Chemical Society of Japan*, 90(10):1129–1140, October 2017.

[438] Jeffrey A Christians, Pierre A Miranda Herrera, and Prashant V Kamat. Transformation of the Excited State and Photovoltaic Efficiency of CH3NH3PbI3 Perovskite upon Controlled Exposure to Humidified Air. *Journal of the American Chemical Society*, 137(4):1530–1538, January 2015.

[439] ChuanXiang Sheng, Chuang Zhang, Yaxin Zhai, Kamil Mielczarek, Weiwei Wang, Wanli Ma, Anvar Zakhidov, and Z Valy Vardeny. Exciton versus Free Carrier Photogeneration in Organometal Trihalide Perovskites Probed by Broadband Ultrafast Polarization Memory Dynamics. *Physical Review Letters*, 114(11):591–5, March 2015.

[440] Qinghui Liu, Yinghui Wang, Ning Sui, Yanting Wang, Xiaochun Chi, Qianqian Wang, Ying Chen, Wenyu Ji, Lu Zou, and Hanzhuang Zhang. Exciton Relaxation Dynamics in Photo-Excited CsPbI3 Perovskite Nanocrystals. *Scientific reports*, 6(1):1–6, July 2016.

[441] Kai Chen, Alex J Barker, Francis L C Morgan, Jonathan E Halpert, and Justin M Hodgkiss. Effect of Carrier Thermalization Dynamics on Light Emission and Amplification in Organometal Halide Perovskites. *The Journal of Physical Chemistry Letters*, 6(1):153–158, January 2015.

[442] K I Kang, A D Kepner, S V Gaponenko, S W Koch, Y Z Hu, and N Peyghambarian. Confinement-Enhanced Biexciton Binding-Energy in Semiconductor Quantum Dots. *Physical Review B*, 48 (20):15449–15452, 1993.

[443] M Umlauff, H Kalt, C Klingshirn, M Scholl, J Sollner, and M Heuken. Laser Processes and Optical Nonlinearities in ZnSe Heterostructures. *Physical Review B*, 52(7):5063–5069, 1995.

[444] R T Williams and K S Song. The self-trapped exciton. *Journal of Physics and Chemistry of Solids*, 51(7):679–716, 1990.

[445] Karel Žídek, Kaibo Zheng, Carlito S Ponseca Jr., Maria E Messing, L Reine Wallenberg, Pavel Chabera, Mohamed Abdellah, Villy Sundström, and Tönu Pullerits. Electron Transfer in Quantum-Dot-Sensitized ZnO Nanowires: Ultrafast Time-Resolved Absorption and Terahertz Study. *Journal of the American Chemical Society*, 134(29):12110–12117, July 2012.

[446] Bill Pandit, Tulashi Luitel, Dustin R Cummins, Arjun K Thapa, Thad Druffel, Frank Zamborini, and Jinjun Liu. Spectroscopic Investigation of Photoinduced Charge-Transfer Processes in FTO/TiO2/N719 Photoanodes with and without Covalent Attachment through Silane-Based Linkers. *The Journal of Physical Chemistry A*, 117(50):13513–13523, December 2013.

[447] Hui-Seon Kim, Chang-Ryul Lee, Jeong-Hyeok Im, Ki-Beom Lee, Thomas Moehl, Arianna Marchioro, Soo-Jin Moon, Robin Humphry-Baker, Jun-Ho Yum, Jacques-E Moser, Michael Grätzel, and Nam-Gyu Park. Lead Iodide Perovskite Sensitized All-Solid-State Submicron Thin Film Mesoscopic Solar Cell with Efficiency Exceeding 9%. *Scientific reports*, 2:583–7, August 2012.

Bibliography

[448] Elinore M L D de Jong, Genki Yamashita, Leyre Gomez, Masaaki Ashida, Yasufumi Fujiwara, and Tom Gregorkiewicz. Multiexciton Lifetime in All-Inorganic CsPbBr3 Perovskite Nanocrystals. *The Journal of Physical Chemistry C*, 121(3):1941–1947, January 2017.

[449] Apurba De, Navendu Mondal, and Anunay Samanta. Hole Transfer Dynamics from Photoexcited Cesium Lead Halide Perovskite Nanocrystals: 1-Aminopyrene as Hole Acceptor. *The Journal of Physical Chemistry C*, 122(25):13617–13623, 2018.

[450] Center for X-ray optics and advanced light source. X-ray Data Booklet, 2001.

[451] O Bunău and Y Joly. Self-consistent aspects of x-ray absorption calculations. *Journal of Physics: Condensed Matter*, 21(34):345501–12, August 2009.

[452] Christos Gougoussis, Matteo Calandra, Ari P Seitsonen, and Francesco Mauri. First-principles calculations of x-ray absorption in a scheme based on ultrasoft pseudopotentials: From α-quartz to high-Tc compounds. *Physical Review B*, 80(7):33–8, August 2009.

[453] Paolo Giannozzi, Stefano Baroni, Nicola Bonini, Matteo Calandra, Roberto Car, Carlo Cavazzoni, Davide Ceresoli, Guido L Chiarotti, Matteo Cococcioni, Ismaila Dabo, Andrea Dal Corso, Stefano de Gironcoli, Stefano Fabris, Guido Fratesi, Ralph Gebauer, Uwe Gerstmann, Christos Gougoussis, Anton Kokalj, Michele Lazzeri, Layla Martin-Samos, Nicola Marzari, Francesco Mauri, Riccardo Mazzarello, Stefano Paolini, Alfredo Pasquarello, Lorenzo Paulatto, Carlo Sbraccia, Sandro Scandolo, Gabriele Sclauzero, Ari P Seitsonen, Alexander Smogunov, Paolo Umari, and Renata M Wentzcovitch. QUANTUM ESPRESSO: a modular and open-source software project for quantum simulations of materials. *Journal of Physics: Condensed Matter*, 21(39): 395502–20, September 2009.

[454] G L Oliver and J P Perdew. Spin-density gradient expansion for the kinetic energy. *Physical Review A*, 20(2):397–403, 1979.

[455] Frank de Groot. Multiplet effects in X-ray spectroscopy. *Coordination Chemistry Reviews*, 249 (1-2):31–63, January 2005.

[456] J C Slater. Wave Functions in a Periodic Potential. *Physical Review*, 51(10):846–851, 1937.

[457] G E Kimball and G H Shortley. The Numerical Solution of Schrödinger's Equation. *Physical Review*, 45(11):815–820, 1934.

[458] Mathieu Taillefumier, Delphine Cabaret, Anne-Marie Flank, and Francesco Mauri. X-ray absorption near-edge structure calculations with the pseudopotentials: Application to the K-edge in diamond and α-quartz. *Physical Review B*, 66(19):701–8, November 2002.

[459] P Giannozzi, O Andreussi, T Brumme, O Bunău, M Buongiorno Nardelli, M Calandra, R Car, C Cavazzoni, D Ceresoli, M Cococcioni, N Colonna, I Carnimeo, A Dal Corso, S de Gironcoli, P Delugas, R A DiStasio Jr, A Ferretti, A Floris, G Fratesi, G Fugallo, R Gebauer, U Gerstmann, F Giustino, T Gorni, J Jia, M Kawamura, H-Y Ko, A Kokalj, E Küçükbenli, M Lazzeri, M Marsili, N Marzari, F Mauri, N L Nguyen, H-V Nguyen, A Otero-de-la Roza, L Paulatto, S Poncé, D Rocca, R Sabatini, B Santra, M Schlipf, A P Seitsonen, A Smogunov, I Timrov, T Thonhauser, P Umari, N Vast, X Wu, and S Baroni. Advanced capabilities for materials modelling with Quantum ESPRESSO. *Journal of Physics: Condensed Matter*, 29(46):465901–31, October 2017.

[460] N Troullier and José Luriaas Martins. Efficient pseudopotentials for plane-wave calculations. *Physical Review B*, 43(3):1993–2006, 1991.

[461] Heather J Kulik, Matteo Cococcioni, Damian A Scherlis, and Nicola Marzari. Density Functional Theory in Transition-Metal Chemistry: A Self-Consistent Hubbard U Approach. *Physical Review Letters*, 97(10):435–4, September 2006.

[462] P E Blochl. Projector augmented-wave method. *Physical Review B*, B50(24):17953–17979, 1994.

[463] P Kirkpatrick and A V Baez. Formation of Optical Images by X-Rays. *Journal of the Optical Society of America*, 38(9):766–774, 1948.

[464] L X Chen. Probing transient molecular structures with time-resolved pump/probe XAFS using synchrotron X-ray sources. *Journal of Electron Spectroscopy and Related Phenomena*, 119(2-3): 161–174, August 2001.

[465] Christian Bressler, Melanie Saes, Majed Chergui, Daniel Grolimund, Rafael Abela, and Philip Pattison. Towards structural dynamics in condensed chemical systems exploiting ultrafast time-resolved x-ray absorption spectroscopy. *The Journal of Chemical Physics*, 116(7):2955–2966, February 2002.

[466] Melanie Saes, Frank van Mourik, Wojciech Gawelda, Maik Kaiser, Majed Chergui, Christian Bressler, Daniel Grolimund, Rafael Abela, Thornton E Glover, Philip A Heimann, Robert W Schoenlein, Steven L Johnson, Aaron M Lindenberg, and Roger W Falcone. A setup for ultrafast time-resolved x-ray absorption spectroscopy. *Review of Scientific Instruments*, 75(1):24–8, 2004.

[467] Lin X Chen. Probing Transient Molecular Structures in Photochemical Processes Using Laser-Initiated Time-Resolved X-ray Absorption Spectroscopy. *Annual Review of Physical Chemistry*, 56(1):221–254, May 2005.

[468] M Chergui. Picosecond and femtosecond X-ray absorption spectroscopy of molecular systems. *Acta Crystallographica Section A Foundations of Crystallography*, 66(2):229–239, February 2010.

[469] S Chaitanya Kumar, J Canals Casals, Junxiong Wei, and M Ebrahim-Zadeh. High-power, high-repetition-rate performance characteristics of β-BaB2O4 for single-pass picosecond ultraviolet generation at 266 nm. *Optics Express*, 23(21):28091–13, 2015.

[470] C Bonati. *Ultrafast carrier and lattice dynamics in semiconductor and metal nanocrystals*. PhD thesis, EPFL, 2007.

[471] Peter Baum, Stefan Lochbrunner, and Eberhard Riedle. Tunable sub-10-fs ultraviolet pulses generated by achromatic frequency doubling. *Optics letters*, 29(14):1686–1688, July 2004.

[472] P Baum, S Lochbrunner, and E Riedle. Generation of tunable 7-fs ultraviolet pulses: achromatic phase matching and chirp management. *Applied Physics B*, 79(8):1027–1032, November 2004.

[473] J R DeVore. Refractive Indices of Rutile and Sphalerite. *JOSA*, 41(6):416–419, June 1951.

[474] O S Heavens. Optical properties of thin films. *Reports on Progress in Physics*, 23(1):1–65, 1960.

[475] A. B. Kuzmenko. Kramers-Kronig constrained variational analysis of optical spectra. *Review of Scientific Instruments*, 76(8):1–9, 2005. ISSN 00346748. doi: 10.1063/1.1979470.

Bibliography

[476] Mark K. Transtrum and James P. Sethna. Improvements to the Levenberg-Marquardt algorithm for nonlinear least-squares minimization. *arXiv.org*, (2), 2012. URL http://arxiv.org/abs/1201.5885.

[477] G E Jellison and F A Modine. Parameterization of the optical functions of amorphous materials in the interband region. *Applied Physics Letters*, 69(3):371–4, 1996.

Reproduction of images - Copyright

Chapter 1: Basic concepts of semiconductor physics and time-resolved spectroscopy

- Figure 1.4: Reproduced from [1] (Figure under Creative Common License).

- Figure 1.5: Curve reproduced from [2].

Chapter 2: Photodynamics in methylammonium lead bromide perovskite (MAPbBr$_3$)

- Figure 2.5: Adapted with permission from [3], Copyright American Association for the Advancement of Science.

- Figure 2.6: Reproduced from [3] with permission, Copyright American Association for the Advancement of Science.

- Figure 2.7: Reproduced with permission from [5] (License # RNP/18/SEP/007900).

- Figure 2.8: Reproduced with permission from [5] (License # RNP/18/SEP/007901).

- Figure 2.9: The UV-Vis spectrum of MAPbI$_3$ is adapted from [4]. The differential transmission spectrum of MAPbI$_3$ is reproduced from [5].

- Figure 2.11: Adapted with permission from [6] (License # 4432070660202).

Chapter 3: Photodynamics in colloidal suspensions of ZnO nanoparticles

- Figure 3.1: Reproduced with permission from [7]. (License # RNP/18/SEP/008018)

- Figure 3.8b: The theory curve (red) is reproduced from [7].

Chapter 5: Charge injection between ZnO and N719

- Figure 5.1: Image under CC license.

- Figure 5.6: UV-Vis spectra of Ga:ZnO are adapted from [9] for doping densities $<10^{20}$ cm^{-3} and from Ref. [10] for doping densities $>10^{20}$ cm^{-3}.

- Figure 5.7: The band structure of wurtzite ZnO has been adapted from Ref. [11].

Chapter 6: Transient reflectivity in the deep-UV of a prototypical charge-tranfer insulator: Nickel Oxide (NiO)

- Figure H.2: The red trace is reproduced from [12] and the black trace from [13].

- Figure 6.2b: Reproduced with permission from [13].

Chapter 7: Electron localization upon optical band gap excitation in NiO microparticles investigated by time-resolved X-ray absorption spectroscopy at the Ni K-edge

- Figure 7.1: Curves are reproduced from [14] in the XANES and [15] in the EXAFS.

- Figure 7.2a: Spectrum of the single crystal is reproduced from Ref. [16].

- Figure 7.3: Curves are reproduced from [16].

Appendix G: Apparatus

- Figure G.1: Reproduced from Ref. [17] with permission (License #4483320943527).

- Figure G.2: Reproduced from Ref. [17] with permission (License #4483320987383).

Address: 1 Chemin d'Auniéres, Résidence Véga
74500 Evian-les-Bains
France
Mobile: +33(0)633773309
Mail: t.rossi@epfl.ch
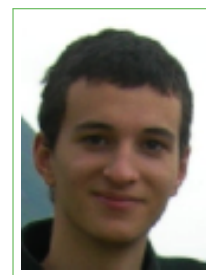
Thomas Rossi

Personal Information

○ OrcID: 0000-0002-7448-8948

○ ResearcherID: R-1164-2017

○ Google Scholar ID: Thomas Charles Henry Rossi

Academic Background

PhD

Sep. 2014 - Aug. 2018   **Ultrafast Optical and X-ray Spectroscopy of Transition Metal Oxides and Interfaces**, Swiss Light Source, Paul Scherrer Institüt, Villigen, Switzerland and Ecole Polytechnique Fédérale de Lausanne, Lausanne, Switzerland, supervisor: Pr. Majed Chergui.

Master

Sep. 2010 - Aug. 2012   **Material Science Major Chemistry**, *Ecole Normale Supérieure, Lyon, France*, Magna Cum Laude.

Bachelor

Sep. 2007 - Aug. 2010   **Material Science Major Chemistry**, *Ecole Normale Supérieure, Lyon, France*, Summa Cum Laude.

Graduate and Undergraduate Internships

Mar. 2012 - Sep. 2012   **New Insigths into the Structural and Electronic Properties of Zinc Oxide Nanoparticles in Solution**, *mark: 19/20*, Swiss Light Source, Paul Scherrer Institüt, Villigen, Switzerland and Ecole Polytechnique Fédérale de Lausanne, Lausanne, Switzerland, supervisors: Pr. Majed Chergui, Dr. Chris Milne and Dr. Hannelore Rittmann-Franck.

May 2011 - Sep. 2011   **Theoretical Study of an Interference Effect in the Optical Spectra of Octahedral Transition Metal Complexes**, *mark: 18/20*, Université de Montréal, Montréal, Canada, supervisor: Pr. Christian Reber.

Jun. 2010 - **Synthesis and Characterization of a Second Generation Ionic Liquid: Bistriflu-**
Aug. 2010 **oromethylsulfonylimidure of N,N-methyloctylpyrrolydinium**, *mark: 14/20*, Université de Savoie, Le Bourget-Du-Lac, France, supervisors: Pr. Micheline Draye and Dr. Grégory Chatel.

National Competitive Exam

Sep. 2012 - **Agrégation (High-Level Teaching Competitive Exam)**, *Physical Sciences Major*
Aug. 2013 *Chemistry*, France, ranking: 16th of $\sim$700 candidates.

Work Experience

Sep. 2013 - **Secondary School Teacher**, *Physics and Chemistry*, Lycée Berthollet, Annecy, France.
Aug. 2014

Student Supervision

○ Kevin Maik Jablonka, student in exchange from Munich University to EPFL, Switzerland, project: Anisotropy of the Exciton Photodynamics in Zinc Oxide Single Crystals. From the 15th of February 2018 to the 15th of June 2018.

Teaching Activities

Sep. 2017 - **Teaching Assistant**, *Molecular Physics*, First Year Fundamental Physics Master,
Jan. 2018 Swiss Federal Institute of Technology, Lausanne, Switzerland.

Sep. 2016 - **Teaching Assistant**, *Molecular Physics*, First Year Fundamental Physics Master,
Jan. 2017 Swiss Federal Institute of Technology, Lausanne, Switzerland.

Sep. 2015 - **Teaching Assistant and Final Exam Supervisor**, *Solid Mechanics and Point Mechan-*
Jan. 2016 *ics*, First Year Civil Engineering and Environmental Engineering, Swiss Federal Institute of Technology, Lausanne, Switzerland.

Sep. 2014 - **Teaching Assistant**, *Solid Mechanics and Point Mechanics*, First Year Civil Engineer-
Jan. 2015 ing, Swiss Federal Institute of Technology, Lausanne, Switzerland.

Honors and Awards

Oct. 2017 **Teaching Excellence**, *Molecular Physics lecture*, EPFL, Lausanne, Switzerland.

Jul. 2011 **Best Presentation**, *Annual Symposium Of Inorganic Chemistry*, Montreal University, Montreal, Canada.

Personal Skills

Languages

English   fluent

French	mother tongue
Spanish	B2 level
Italian	basic

Computational

Adobe Illustrator, Adobe Photoshop, Matlab, Microsoft Office, LaTeX

Publications

[1] M. Oppermann, B. Bauer, T. Rossi, J. Helbing, and M. Chergui. Ultrafast Broadband Circular Dichroism in the Deep-UV. *In Press Optica*, 2018.

[2] E. Baldini, T. Palmieri, T. Rossi, M. Oppermann, E. Pomarico, G. Auböck, and M. Chergui. Interfacial Electron Injection Probed by a Substrate-Specific Excitonic Signature. *Journal of the American Chemical Society*, 139(33):11584–11589, 2017.

[3] J. Budarz, F. G. Santomauro, M. H. Rittmann-Frank, C. J. Milne, T. Huthwelker, D. Grolimund, J. Rittmann, D. Kinschel, T. Rossi, and M. Chergui. Time-resolved Element-selective Probing of Charge Carriers in Solar Materials. *CHIMIA International Journal for Chemistry*, 71(11):768–772, 2017.

[4] M. Oppermann, N. Nagornova, A. Oriana, E. Baldini, L. Mewes, B. Bauer, T. Palmieri, T. Rossi, F. van Mourik, and M. Chergui. The LOUVRE Laboratory: State-of-the-Art Ultrafast Ultraviolet Spectroscopies for Molecular and Materials Science. *CHIMIA International Journal for Chemistry*, 71(5):288–294, 2017.

[5] F. G. Santomauro, J. Grilj, L. Mewes, G. Nedelcu, S. Yakunin, T. Rossi, G. Capano, A. Al Haddad, J. Budarz, D. Kinschel, D. S. Ferreira, G. Rossi, M. G. Tovar, D. Grolimund, V. Samson, M. Nachtegaal, G. Smolentsev, M. V. Kovalenko, and M. Chergui. Localized Holes and Delocalized Electrons in Photoexcited Inorganic Perovskites: Watching each Atomic Actor by Picosecond X-ray Absorption Spectroscopy. *Structural Dynamics*, 4(4):044002, 2016.

[6] T. Rossi, T. J. Penfold, M. H. Rittmann-Frank, M. Reinhard, J. Rittmann, C. N. Borca, D. Grolimund, C. J. Milne, and M. Chergui. Characterizing the Structure and Defect Concentration of ZnO Nanoparticles in a Colloidal Solution. *The Journal of Physical Chemistry C*, 118(33):19422–19430, 2014.

[7] G. Chatel, C. Goux-Henry, A. Mirabaud, T. Rossi, N. Kardos, B. Andrioletti, and M. Draye. H2O2/NaHCO3-Mediated Enantioselective Epoxidation of Olefins in NTf2-Based Ionic Liquids and Under Ultrasound. *Journal of Catalysis*, 291:127–132, 2012.

Proceedings

[8] T. Rossi, L. Wang, M. Oppermann, P. Chen, Y.-H. Chiang, M.-C. Tsai, T.-F. Guo, and M. Chergui. Cooling Dynamics of Electrons in MAPbBr3 Probed in the Deep-UV. In *in press Ultrafast Phenomena XXI*. 2018.

Talks given at International Conferences

[9] T. Rossi, L. Wang, M. Oppermann, P. Chen, Y.-H. Chiang, M.-C. Tsai, T.-F. Guo, and M. Chergui. Charge-Carrier Dynamics in MAPbBr3 Probed by Femtosecond Broadband Deep-UV Spectroscopy. In *Ultrafast Phenomena XXI*. Hamburg, Germany, 2018.

[10] T. Rossi, M. Oppermann, B. Bauer, A. Magrez, M. Porer, E. Baldini, and M. Chergui. Deep-UV Dynamics of Nickel Oxide Single Crystals. In *School on UV and X-ray spectroscopies of correlated electron systems*. Les Houches, France, 2017.

Submitted Publications

[11] <u>T. Rossi</u>, D. Grolimund, M. Nachtegaal, N. Ohannessian, D. Pergolesi, T. Lippert, and M. Chergui. XAS Linear Dichroism at the Ti K-edge of TiO2 Anatase Single Crystal. *submitted*, 2018.

In Preparation

[12] <u>T. Rossi</u>, K. Jablonka, M. Oppermann, and M. Chergui. Charge Carrier Cooling in ZnO Nanoparticles Investigated by Transient Absorption Spectroscopy in the Deep-UV. *in preparation*.

[13] <u>T. Rossi</u>, D. Kinschel, J. Budarz, G. Rossi, F. Santomauro, and M. Chergui. Charge Localization in NiO Microparticles Probed by Time-Resolved X-ray Absorption Spectroscopy. *in preparation*.

[14] <u>T. Rossi</u>, L. Wang, M. Oppermann, P. Chen, Y.-H. Chiang, M.-C. Tsai, T.-F. Guo, and M. Chergui. Charge Dynamics in MAPbBr3 Investigated by Broadband Visible/UV Transient Absorption Spectroscopy. *in preparation*.

[15] <u>T. Rossi</u>, L. Wang, M. Oppermann, P. Chen, Y.-H. Chiang, M. C. Tsai, T.-F. Guo, and M. Chergui. Charge Injection at the Perovskite/Anatase Interface Probed in the Deep-UV. *in preparation*.